

NASA Conference Publication 2311

18TH AEROSPACE MECHANISMS SYMPOSIUM

(NASA-CP-2311) THE 18TH AEROSPACE
MECHANISMS SYMPOSIUM (NASA) 321 P
HC A14/MF A01

CSC 20K

G3/39

N84-25078
THRU
N84-25096
Unclas
13421

*Proceedings of a symposium held at
Goddard Space Flight Center
Greenbelt, Maryland
May 2-4, 1984*



NASA Conference Publication 2311

18TH AEROSPACE MECHANISMS SYMPOSIUM

Proceedings of a symposium sponsored by
National Aeronautics and Space Administration,
the California Institute of Technology, and
Lockheed Missiles and Space Company, Inc.,
and held at Goddard Space Flight Center
Greenbelt, Maryland
May 2-4, 1984

NASA
National Aeronautics
and Space Administration
Scientific and Technical
Information Branch

PREFACE

This NASA Conference Publication includes the proceedings of the 18th Aerospace Mechanisms Symposium held at the National Aeronautics and Space Administration (NASA) Goddard Space Flight Center on May 2, 3, and 4, 1984. The symposium was sponsored by NASA, California Institute of Technology, and Lockheed Missiles and Space Company, Inc.

The object of the symposium was to provide a forum for the interchange of information among those active in the field of mechanisms technology. For this purpose, 18 papers were presented on aeronautics and spaceflight, with special emphasis on actuators and aerospace applications for ground support equipment, latches, connectors, and other mechanisms for large space structures. The papers were prepared by engineers from a broad aerospace background that included participants from the United States aerospace industry, NASA, Europe, and Asia.

The efforts of the review committee, the session chairmen, and the speakers that contributed to the technical excellence and professional character of the conference are especially appreciated.

The use of trade names or names of manufacturers in this publication does not constitute an official endorsement of these products or manufacturers, either expressed or implied, by NASA.

PRECEDING PAGE BLANK NOT FILMED

CONTENTS

Preface	iii
Organizing and Reviewing Committee	vii
Program	ix
1. THE DESIGN AND DEVELOPMENT OF A RELEASE MECHANISM FOR SPACE SHUTTLE LIFE-SCIENCE EXPERIMENTS Howard M. Jones and Robert G. Daniell	1
2. ACTUATOR DEVELOPMENT FOR THE INSTRUMENT POINTING SYSTEM (IPS) Klaus Suttner	15
3. A PASSIVELY CONTROLLED APPENDAGE DEPLOYMENT SYSTEM FOR THE SAN MARCO D/L SPACECRAFT William E. Lang, Harold P. Frisch, and Deborah A. Schwartz	29
4. DESIGN AND OPERATION OF A DEPLOYABLE TRUSS STRUCTURE Koryo Miura	49
5. DESIGN AND TEST OF A LOW-TEMPERATURE LINEAR DRIVER/RATE CONTROLLER Charles H. Lowry	65
6. EVOLUTION FROM A HINGE ACTUATOR MECHANISM TO AN ANTENNA DEPLOYMENT MECHANISM FOR USE ON THE EUROPEAN LARGE COMMUNICATIONS SATELLITE (L-SAT/OLYMPUS) Martin D. De'Ath	79
7. THE IMPORTANCE OF THERMAL-VACUUM TESTING IN ACHIEVING HIGH RELIABILITY OF SPACECRAFT MECHANISMS K. Parker	93
8. IMPROVING SLIPRING PERFORMANCE Donald N. Matteo	111
9. THE DESIGN AND DEVELOPMENT OF TWO-FAILURE TOLERANT MECHANISMS FOR THE SPACEBORNE IMAGING RADAR (SIR-B) ANTENNA S. J. Presas	131
10. INHERENT PROBLEMS IN DESIGNING TWO-FAILURE TOLERANT ELECTROMECHANICAL ACTUATORS Stephen Hornyak	155
11. PASSIVE SUN SEEKER/TRACKER AND A THERMALLY ACTIVATED POWER MODULE Clete J. Siebert and Fred A. Morris	171

12.	THE DESIGN AND DEVELOPMENT OF A SOLAR TRACKING UNIT	187
	Irby W. Jones and James B. Miller	
13.	ANTENNA TRACKING MECHANISM FOR GEOSTATIONARY SATELLITES	203
	Colin M. Francis	
14.	SPACELAB 4 - PRIMATE EXPERIMENT SUPPORT HARDWARE	215
	Paul R. Fusco and Richard J. Peyran	
15.	DESIGN OF A PRECISION ETALON POSITION CONTROL SYSTEM FOR A CRYOGENIC SPECTROMETER	243
	J. -N. Aubrun, K. R. Lorell, D. F. Zacharie, and J. B. Thatcher	
16.	THE ELECTRON ECHO 6 MECHANICAL DEPLOYMENT SYSTEMS	263
	Stewart C. Meyers, James E. Steffen, Perry R. Malcolm, and John R. Winckler	
17.	SEPARATION AND STAGING MECHANISMS FOR THE INDIAN SLV-3 LAUNCH VEHICLE	277
	M. K. Abdul Majeed, K. Natarajan, and V. K. Krishnankutty	
18.	SMART MOTOR TECHNOLOGY	301
	Douglas T. Packard and Donald E. Schmitt	

ORGANIZING AND REVIEWING COMMITTEE

The papers presented at the Symposium were selected and reviewed by the Organizing Committee. Each author is responsible for the content and the technical accuracy of their respective paper. The committee was composed of the following members:

General Chairman--Charles W. Coale, Lockheed Missiles and Space Company, Inc.

Operations Chairman--Joseph F. Wilson, Lockheed Missiles and Space Company, Inc.

Administrative Chairman--David F. Welch, California Institute of Technology

Host Chairman--Frank T. Martin, National Aeronautics and Space Administration, Goddard Space Flight Center

Committee Members

Richard H. Bentall, European Space Technology Center

Tom F. Bonner, NASA/Langley Research Center

Kenneth C. Curry, Jet Propulsion Laboratory

Charles R. Darwin, NASA/Marshall Space Flight Center

David F. Engelbert, NASA/Ames Research Center

Otto H. Fedor, NASA/Kennedy Space Center

Harvey H. Horiuchi, Jet Propulsion Laboratory

Allen J. Louviere, NASA/Johnson Space Center

Peter A. Minderman, NASA/Kennedy Space Center

James B. Sterett, Jr., NASA/Marshall Space Flight Center

Bowden W. Ward, Jr., NASA/Goddard Space Flight Center

Nathan D. Watson, NASA/Langley Research Center

Special Consultant

Alfred L. Rinaldo, Lockheed Missiles and Space Company, Inc. (Retired)

PROGRAM

WEDNESDAY, MAY 2, 1984

10:00-12:00 REGISTRATION AND COFFEE SOCIAL
Auditorium, Bldg. 8, NASA Goddard Space Flight Center

12:00 LUNCH

1:00 AFTERNOON SESSIONS
INTRODUCTORY REMARKS
Mr. Frank T. Martin, Host Chairman
NASA Goddard Space Flight Center
Dr. Charles W. Coale, General Chairman
Lockheed Missiles & Space Co.

WELCOME
Dr. Noel W. Hinners, Center Director
NASA Goddard Space Flight Center

SESSION I
Mr. Otto H. Fedor, Session Chairman
NASA John F. Kennedy Space Center, FL

MECHANICAL FAILURE IN THE OPTICAL LINESCAN
SYSTEM CARRIED ON THE DEFENSE METEOROLOGICAL
SATELLITE
A. J. Arnold, The Aerospace Corp., Los Angeles, CA

THE DESIGN AND DEVELOPMENT OF A RELEASE
MECHANISM FOR SPACE SHUTTLE LIFE-SCIENCE
EXPERIMENTS
Howard M. Jones and Robert G. Daniell, Spar Aero-
space Limited, Weston, Ontario, Canada

BRITISH AEROSPACE MECHANISMS FOR INTELSAT VI
Geoffrey J. Sturtivant, British Aerospace Dynamics
Group, Stevenage, Herts, England

ACTUATOR DEVELOPMENT FOR THE INSTRUMENT POINTING
SYSTEM (IPS)
Klaus Suttner, Dornier System GmbH,
Friedrichshafen, West Germany

COFFEE BREAK

PRECEDING PAGE PLANK NOT FILMED

SESSION II

Mr. Louis K. Kiraly, Session Chairman
NASA Lewis Research Center, Cleveland, OH

A PASSIVELY CONTROLLED APPENDAGE DEPLOYMENT SYSTEM
FOR THE SAN MARCO D/L SPACECRAFT

William E. Lang, Harold P. Frisch, and Deborah
A. Schwartz, NASA Goddard Space Flight Center,
Greenbelt, MD

DESIGN AND OPERATION OF A DEPLOYABLE TRUSS STRUC-
TURE

Koryo Miura, The Institute of Space and Astro-
nautical Science, Tokyo, Japan

DESIGN AND TEST OF A LOW TEMPERATURE LINEAR
DRIVER/RATE CONTROLLER

Charles H. Lowry, Rockwell International, Space
Transportation and Systems Group, Downey, CA

EVOLUTION FROM A HINGE ACTUATOR MECHANISM TO AN
ANTENNA DEPLOYMENT MECHANISM FOR USE ON THE EURO-
PEAN LARGE COMMUNICATIONS SATELLITE (L-SAT/OLYMPUS)

Martin D. De'Ath, British Aerospace Dynamics Group,
Stevenage, Herts, England

7:30-9:30 EVENING SOCIAL GATHERING
Ballroom, Sheraton Hotel (New Carrollton)

THURSDAY, MAY 3, 1984

8:30 MORNING SESSIONS
Auditorium Bldg. 8, NASA Goddard Space Flight Center

SESSION III

Lt. Col. Ted Schroeder, Session Chairman
Air Force Space Technology Center,
Kirkland AFB, NM

THE IMPORTANCE OF THERMAL-VACUUM TESTING IN ACHIEV-
ING HIGH RELIABILITY OF SPACECRAFT MECHANISMS

K. Parker, European Space Tribology Laboratory,
Risley, England

IMPROVING SLIPRING PERFORMANCE

Donald N. Matteo, General Electric Co., Space
Systems Division, Philadelphia, PA

THE DESIGN AND DEVELOPMENT OF TWO-FAILURE TOLERANT
MECHANISMS FOR THE SPACEBORNE IMAGING RADAR (SIR-B)
ANTENNA

S. J. Presas, Ball Aerospace Systems Division,
Boulder, CO

INHERENT PROBLEMS IN DESIGNING TWO-FAILURE TOLERANT
ELECTROMECHANICAL ACTUATORS

Stephen Hornyak, General Dynamics, Convair Division,
San Diego, CA

COFFEE BREAK

SESSION IV

Prof. Charles R. Hayleck, Jr., Session Chairman
University of Maryland, College Park, MD

PASSIVE SUN SEEKER/TRACKER AND A THERMALLY ACTIV-
ATED POWER MODULE

Clete J. Siebert and Fred A. Morris, Martin
Marietta Aerospace, Denver, CO

THE DESIGN AND DEVELOPMENT OF A SOLAR TRACKING
UNIT

Irby W. Jones and James B. Miller, NASA Langley
Research Center, Hampton, VA

ANTENNA TRACKING MECHANISM FOR GEOSTATIONARY SATEL-
LITES

Colin M. Francis, Ford Aerospace and Communications
Corp., Palo Alto, CA

- 12:30 TOUR OF PAUL E. GARBER FACILITY
Mr. Bowden W. Ward, Jr., Tour Chairman
NASA Goddard Space Flight Center
- 1:00 LUNCHEON AT THE FACILITY
- 2:00 TOUR
- 4:30 RETURN TO HOTEL AND GSFC
- EVENING SOCIAL ACTIVITIES
Ballroom, Sheraton Hotel (New Carrollton)
- 7:15 SOCIAL HOUR
- 8:15 SYMPOSIUM BANQUET
- 9:00 AWARDS

9:15 INTRODUCTION OF BANQUET SPEAKER
Mr. Robert J. Herzberg, Chief Scientist,
Space Systems Division, Lockheed Missiles & Space Co.

BANQUET SPEAKER
Mr. Frank J. Ceppolina, NASA Goddard Space Flight Center:
"The Solar Maximum Repair Mission"

FRIDAY, MAY 4, 1984

8:30 MORNING SESSIONS

SESSION V

Mr. James B. Sterett, Jr., Session Chairman
NASA George C. Marshall Space Flight Center, AL

SPACELAB 4 - PRIMATE EXPERIMENT SUPPORT HARDWARE
Paul R. Fusco and Richard J. Peyran, NASA Ames
Research Center, Moffett Field, CA

DESIGN OF A PRECISION ETALON POSITION CONTROL
SYSTEM FOR A CRYOGENIC SPECTROMETER
J. -N. Aubrun, K. R. Lorell, D. F. Zacharie, and
J. B. Thatcher, Lockheed Palo Alto Research Lab-
oratories, Palo Alto, CA

THE ELECTRON ECHO 6 MECHANICAL DEPLOYMENT SYSTEMS
Stewart C. Meyers, NASA Goddard Space Flight
Center, Greenbelt, MD, and James E. Steffen and
Perry R. Malcolm, University of Minnesota,
Minneapolis, MN

SEPARATION AND STAGING MECHANISMS FOR THE INDIAN
SLV-3 LAUNCH VEHICLE
M. K. Abdul Majeed, K. Natarajan, and V. K.
Krishnankutty, Indian Space Research Organisation,
Vikram Sarabhai Space Centre, Trivandrum, India

COFFEE BREAK

SESSION VI

Dr. Richard H. Bentall, Session Chairman
European Space Research & Technology Centre,
Nordwijk, The Netherlands

SMART MOTOR TECHNOLOGY
Douglas T. Packard, Jet Propulsion Laboratory,
Pasadena, CA and Donald E. Schmitt, Lockheed
Missiles & Space Co., Sunnyvale, CA

N84
25079

UNCLAS

[N84 25079

THE DESIGN AND DEVELOPMENT OF A RELEASE MECHANISM
FOR SPACE SHUTTLE LIFE-SCIENCE EXPERIMENTS

Howard M. Jones and Robert G. Daniell

ABSTRACT

This paper describes the design, the development, and the testing of a release mechanism for use in two Life Science Experiments on the Spacelab 1, 4, and D1 missions. The mechanism is a self-latching ball-lock device actuated by a linear solenoid. An unusual feature is the tapering of the ball-lock plunger to give it a near-constant breakout force for release under a wide range of loads. The selection of the design, based on the design requirements, is discussed. A number of problems occurred during development and test, including problems caused by human factors that became apparent after initial delivery for crew-training sessions. These problems and their solutions are described to assist in the design and testing of similar mechanisms.

INTRODUCTION

The Spacelab Vestibular Experiments are designed to investigate changes in vestibular functions during weightless conditions and space motion sickness.

The Otolith Spinal Reflex or "Hop and Drop" Experiment tests the effects of alterations in Otolith organ contributions to leg muscle activity in specific experimental situations, each involving a different motion of the subject. Hopping and unexpected fall tests will be conducted on-orbit in Spacelab and on the ground before and after flight. The on-orbit tests employ elastic cords to provide the forces necessary to keep the subject in place while hopping, or to propel him towards the floor in the falls.

In the fall test section of the Otolith Spinal Reflex Experiment it is necessary to release the subject without warning, so that he will accelerate towards the floor under the influence of the extended cord assemblies. The release mechanism used in this test incorporates some unique design features and is the subject of this paper.

The fall test configuration on Spacelab 1 is shown in Figure 1.

REQUIREMENTS

- Function: sudden and smooth release of subject without audible or visible warning under a wide range of loads and voltages (0 to 100 Kg, 19 to 32 V)
- Release Delay: not to exceed 0.1 second from command until subject starts to fall and to be very consistent for a given load and voltage

ORIGINAL PAGE IS
OF POOR QUALITY

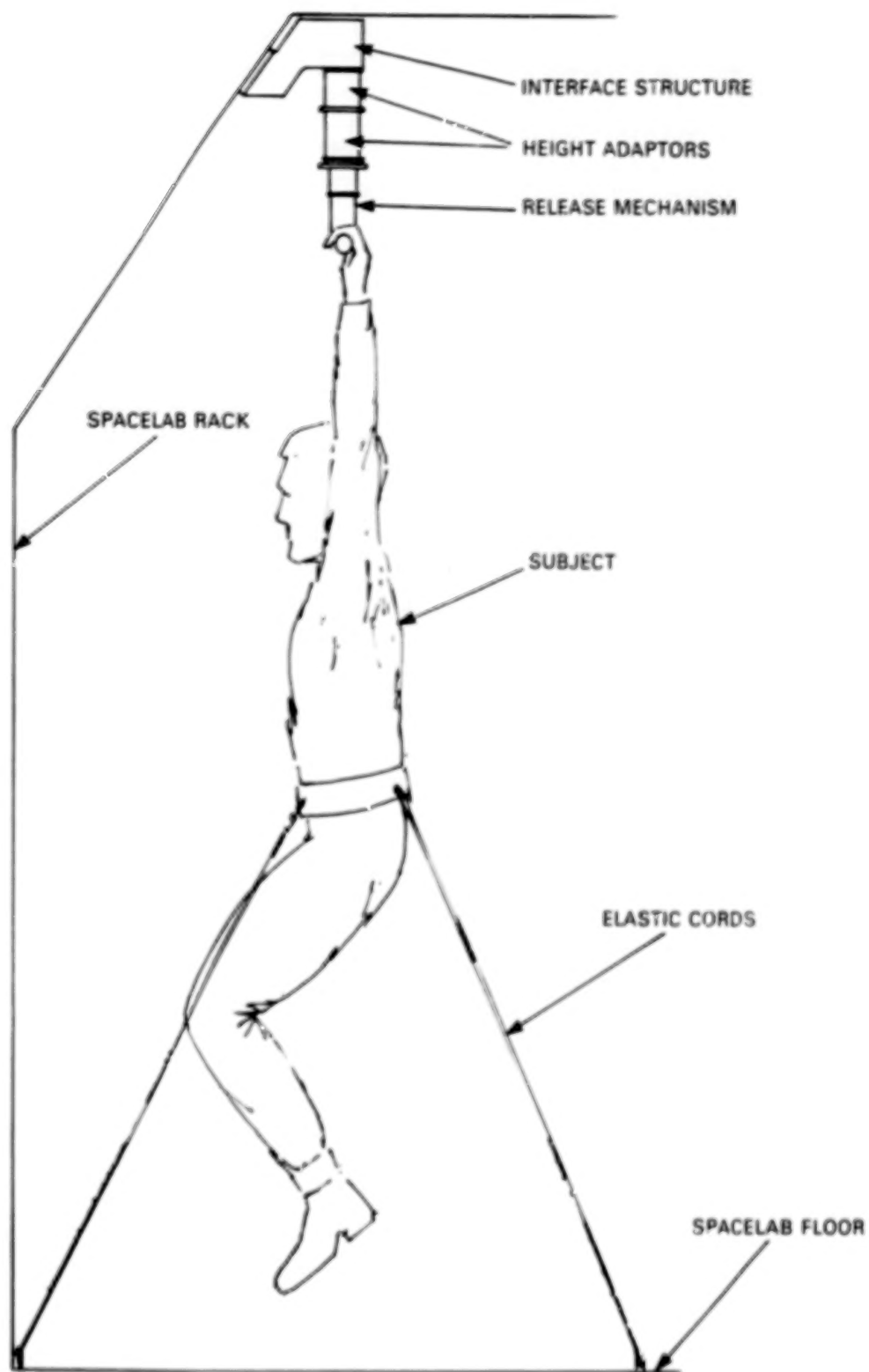


Figure 1. Fall Test Configuration

- To be self latching in the retention position
- Low weight (2.5 Kg), size, and power consumption (40 W at 24 V)
- To be reusable immediately after each release
- No stored energy devices that could impact crew safety
- Lifetime: 1,500 release cycles under a specified load profile, before refurbishment

DESIGN

Various design approaches were initially considered. The main problem was to achieve release under high external load within the mass, power, time and safety constraints.

Pyrotechnic and pneumatic devices offer the best force/weight ratio but would violate the reusability and safety requirements for the Spacelab interior.

The release delay of a linear actuator employing an electric motor with reduction gearing and a lead screw was found to be excessive and the subject would obtain an audible advanced warning of the release.

It was eventually determined that a solenoid-actuated ball-lock mechanism would meet the performance and safety requirements and would provide a compact, low-power design, with a low number of moving parts.

The active part of the release mechanism is a handlebar providing a two-handed grip and carrying a solenoid-actuated ball-lock pin vertically mounted at its center point. The mating part is an outer sleeve with a semi-circular cross-section groove that is attached to the Spacelab structure.

On latch-up, the three balls are radially locked into the groove in the fixed outer sleeve and the load imparted by the subject under the influence of the extended cord assemblies is taken by the balls in shear. The plunger is held in the extended position by a compression coil spring. When energized, the solenoid withdraws a plunger and permits the balls to collapse toward the pin centre and out of the groove, which allows the ball lock pin to slide out of the outer sleeve under the influence of the axial load.

A large solenoid force, however, was predicted for release under high load because of high friction on the plunger caused by the clamping action of the balls. In addition, the release characteristics of the mechanism would vary considerably as a function of load. This problem was solved by using a tapered plunger with a half-cone angle equal to the arctangent of the predicted coefficient of friction. The plunger which was neutral under load, needed only a small force to release.

The principle is illustrated in Figure 2.

The flight-standard release mechanism is shown in Figure 3.

A development model was manufactured and tested using a spring gage instead of a solenoid so that the release forces could be measured under a wide range of loads. A series of plungers with various taper angles were tested and an optimum angle selected.

The theoretical and measured plunger release forces are shown in Figure 4 and Figure 5 for various loads and plunger taper angles.

The solenoid used for the release mechanism involved modification of a standard bought out unit for two reasons:

1. Replacement of unacceptable materials with those approved by NASA for manned spaceflight applications
2. Performance improvement (particularly the force capability at the fully-extended position)

The performance before and after modification is shown in Figure 6.

DEVELOPMENT PROBLEMS AND SOLUTIONS

Design modification resulted from development testing in three areas:

- Release characteristics
- Retention characteristics
- Lubrication life

The following paragraphs describe these areas.

Release Characteristics

The unit exhibited occasional failure to release when the solenoid was energized because of:

- Insufficient solenoid force
- Excessive retention spring force
- Lubricant failure
- Unexpected mechanism kinematics

Investigation of the first three items resulted in minor improvements but the problem was not completely solved.

A thorough review of the mechanism design was then conducted and a potential jamming mode of the mechanism was predicted by analysis. This mode involved the latch-up kinematics of the mechanism as shown in Figure 7.

ORIGINAL PAGE 19
OF POOR QUALITY

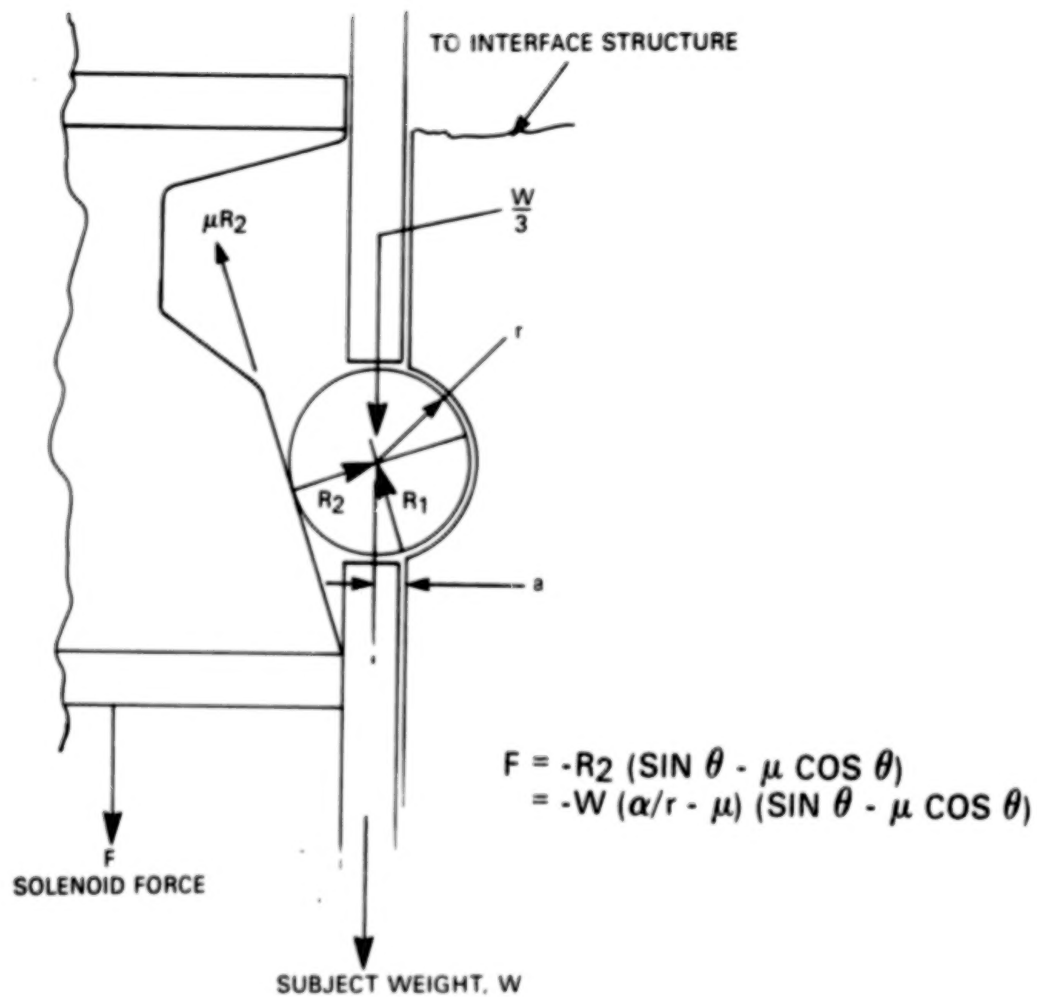


Figure 2. Principle of Release Mechanism

ORIGINAL PAGE 19
OF POOR QUALITY

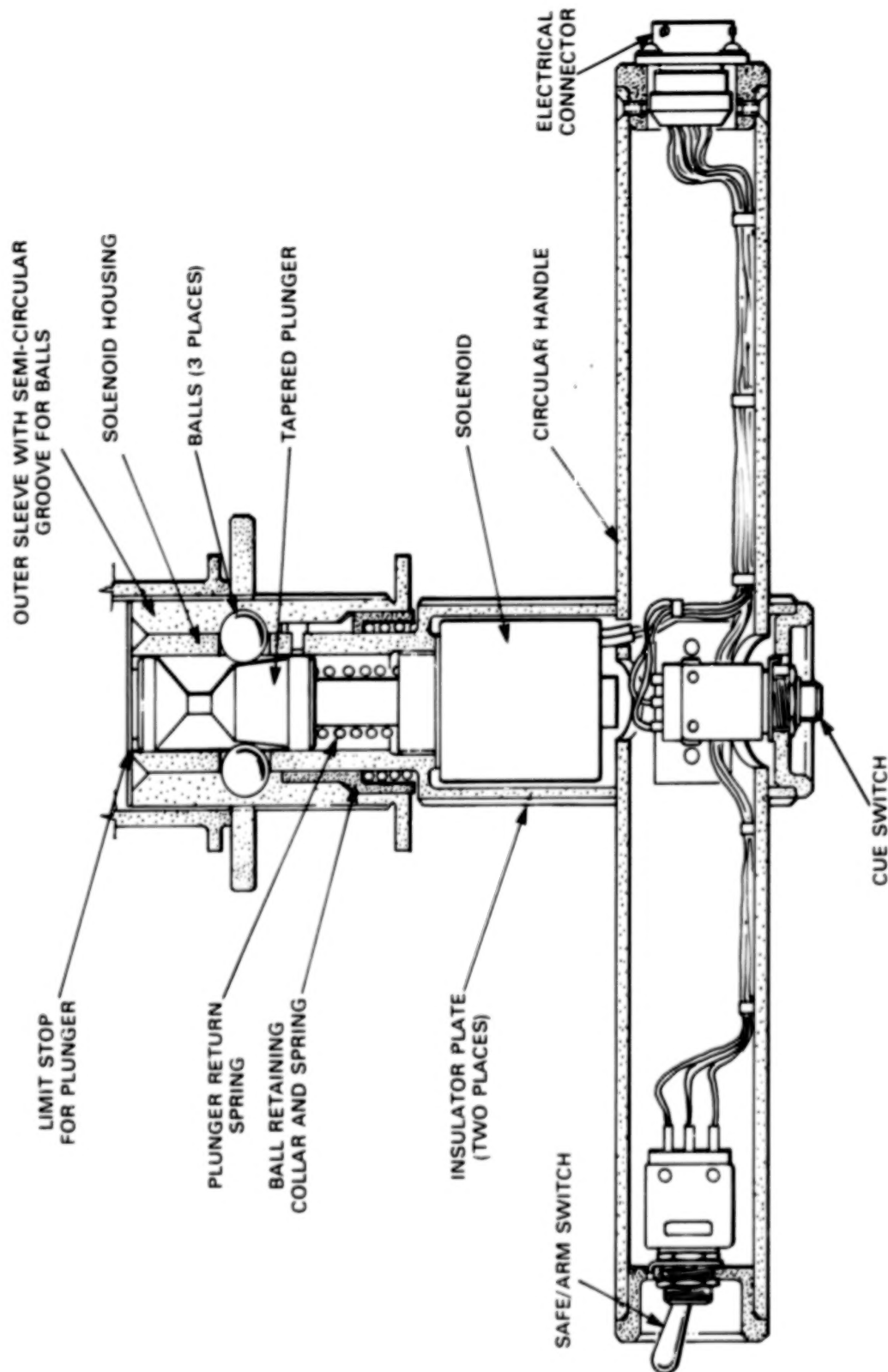


Figure 3. Release Mechanism Flight Unit

ORIGINAL PAGE 19
OF POOR QUALITY

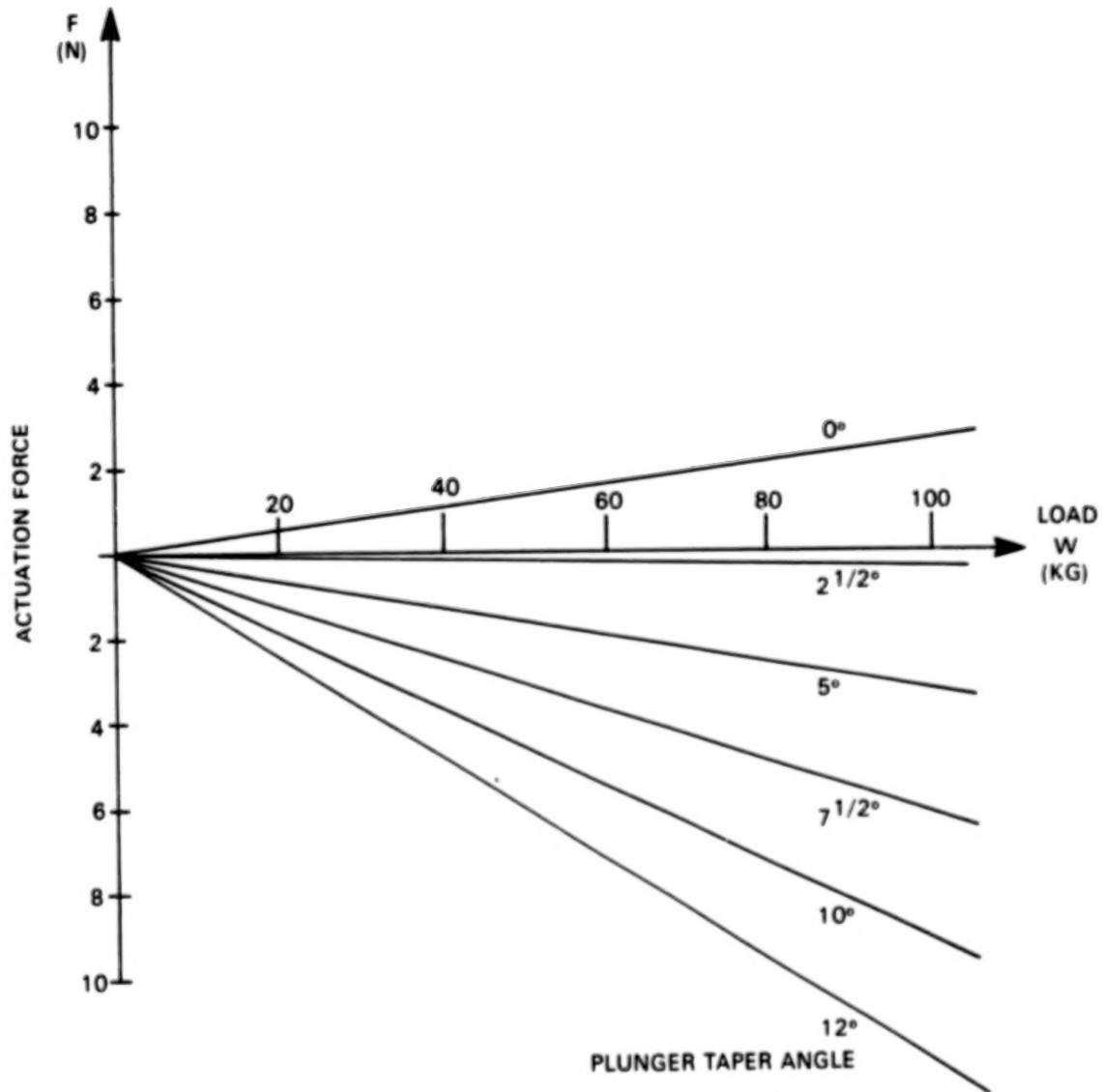


Figure 4. Theoretical Performance of Release Mechanism

ORIGINAL PAGE IS
OF POOR QUALITY

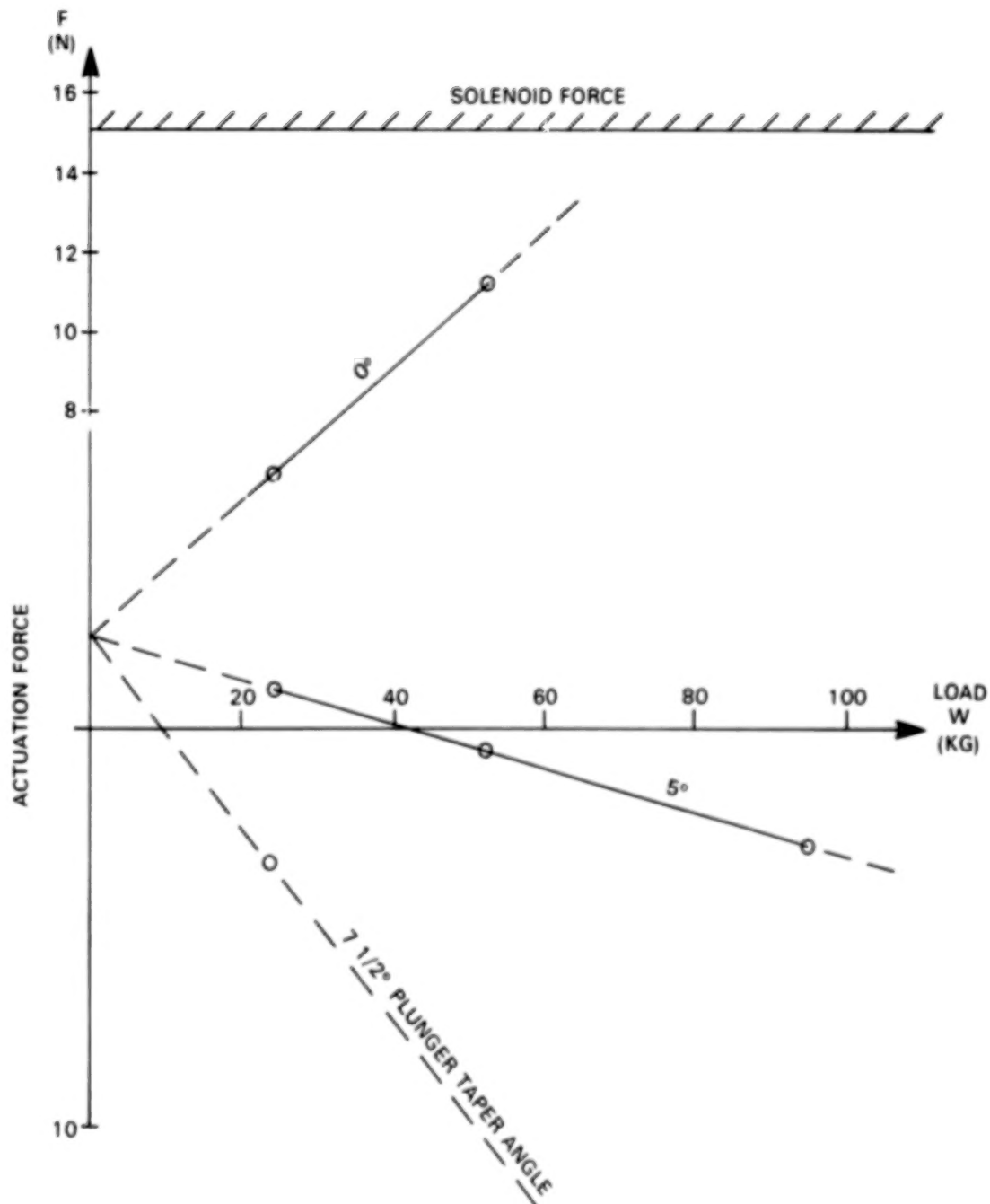


Figure 5. Test Performance of Release Mechanism

ORIGINAL PAGE 19
OF POOR QUALITY

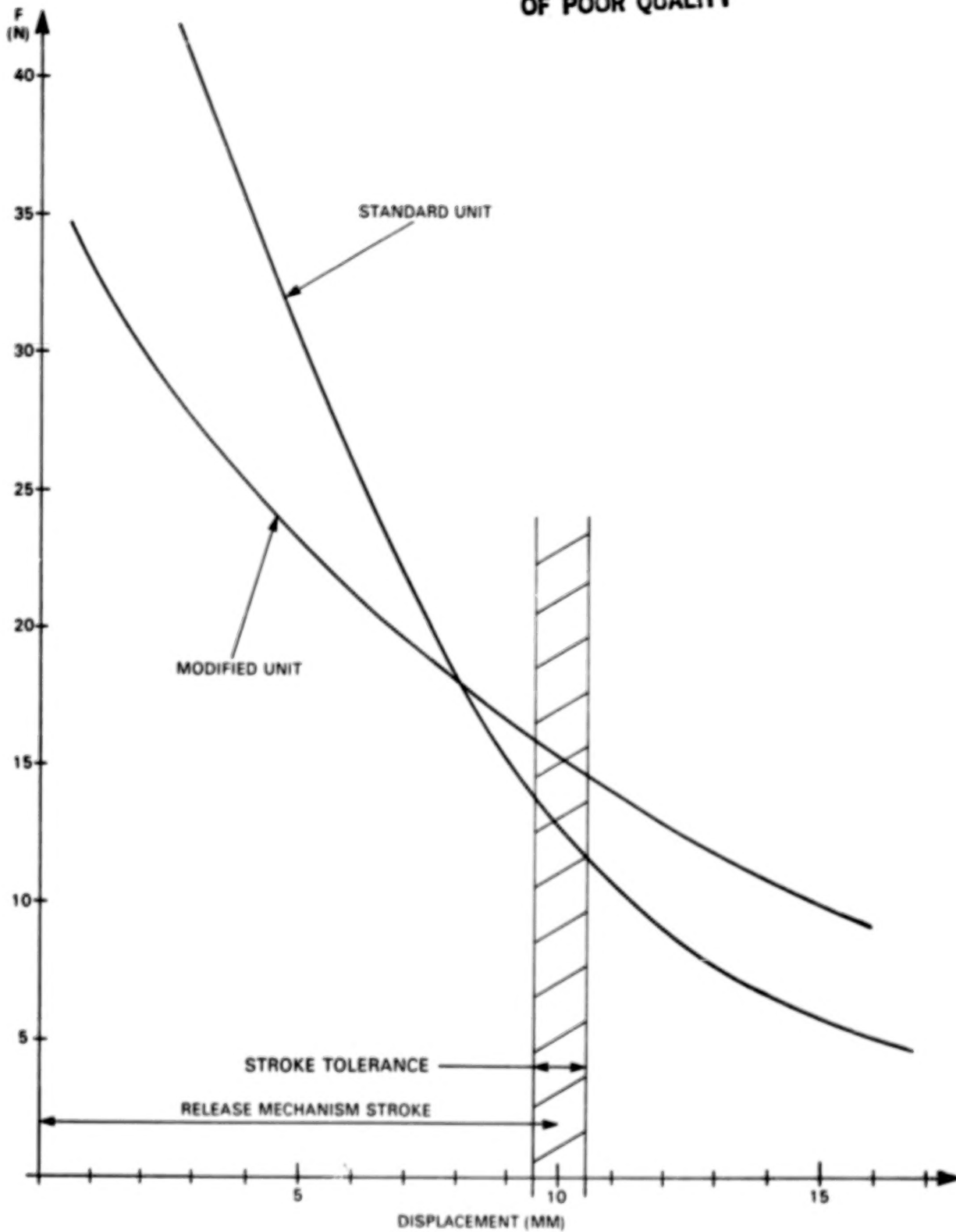
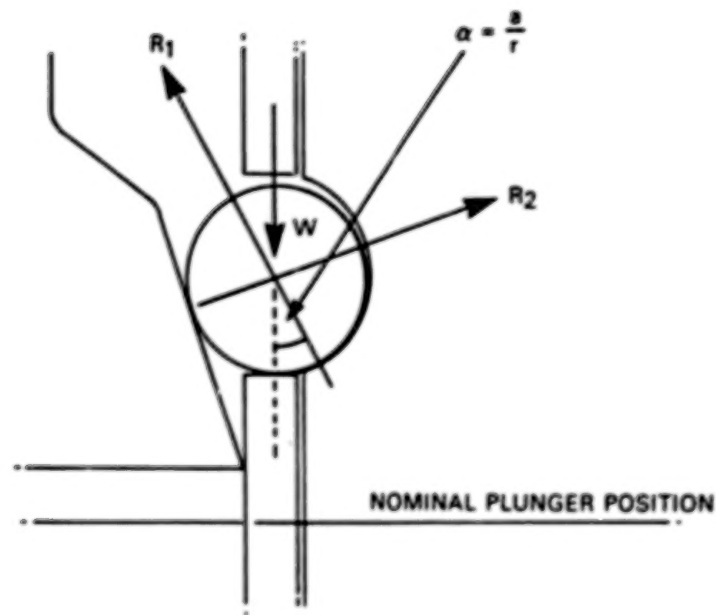
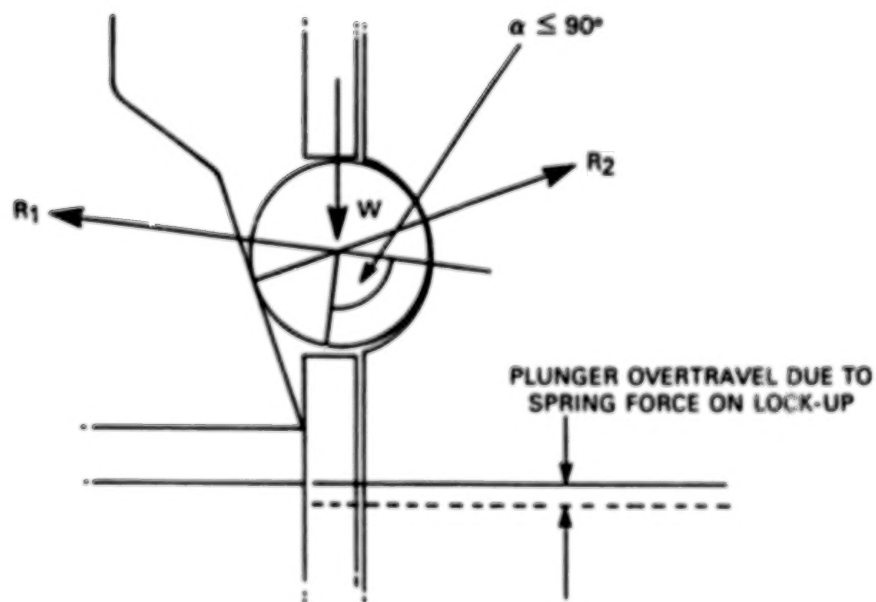


Figure 6. Solenoid Characteristics

ORIGINAL PAGE IS
OF POOR QUALITY



(a) NOMINAL LOCK-UP GEOMETRY



(b) JAMMING MODE LOCK-UP GEOMETRY

Figure 7. Lock-up Kinematics of Release Mechanism

Because of the spring force and plunger momentum, overtravel of the plunger could force the balls into the back of the groove altering the contact angle for the reaction force R_1 .

Because
$$R_1 = \frac{W}{\cos \phi}$$

R_1 becomes very large as ϕ approaches 90° .

When R_1 is very large, two effects cause very large resistance forces on the plunger.

- Side loads on the plunger caused by differential ball reactions become significant and cause high reaction forces at the plunger journals
- The reaction force on the plunger, R_2 becomes large enough to cause rapid lubricant wear allowing sticking of the balls to the plunger

These effects were eliminated by installing a limit stop for the plunger which prevented it from reaching the overtravel condition

Retention Characteristics

Figure 5 shows that the plunger tends to release by itself at higher loads and that a retaining force is required. Several iterations were required to obtain the correct spring force (if too large a force was used, the solenoid could not release). If a minimum spring force was used, uncommanded release could occur when the mechanism was shaken or rotated under full load. When the release performance problems previously described were solved, it was found that a stronger spring could be used and the retention performance was improved correspondingly. Continued rotation of the mechanism with respect to the groove, however, eventually caused uncommanded release because the motion of the balls allowed slip of the plunger. This was not considered a serious problem for this application.

Lubrication Life

The active parts of the mechanism are made from hardened corrosion-resistant steel. Dry lubricants based on molybdenum disulphide are used to prevent galling and to avoid the problems of wet lubricants in an unsealed mechanism, (e.g., contamination risk when mechanism is separated). The plunger is coated with a solid film lubricant per MIL-L-46010 to provide low friction and relatively high contact stress capacity when sliding against the balls. A high rate of wear of this lubricant was observed during initial testing.

When the release performance problems were eliminated as previously mentioned, a considerable improvement in the plunger lubricant life was obtained because the contact stresses of the balls on the plunger had been reduced.

A further improvement that was obtained by adding to the experiment procedure involved rotating the plunger about its centerline occasionally so that the new lubricant was contacted by the balls.

TESTING

Performance Testing

Initially, a simple pass/fail test was used, based on completion of a large number of releases without jamming at normal voltage (i.e., worst-case specification values). To allow the timely detection of problems, however, a characterization test was adopted to determine the performance margins of the release mechanism.

Two methods of defining release performance were used:

- Testing at reduced voltage
- Measuring release delay

The relationship between supply voltage and release force is illustrated in Figure 8. If the voltage is reduced until consistent release no longer occurs, the resistive forces in the mechanism can be determined. If these are significantly higher than predicted a potential problem in the mechanism exists.

Measurements of release delay can be made using an accelerometer mounted on the solenoid housing or by recording the solenoid current profile which dips when the plunger moves. Both have been used and provide an accurate indication of the time between switching voltage to the solenoid and motion of the release mechanism. Both the average value and the consistency of the delay provide a good indication of the health of the mechanism.

Environmental Tests

The following environmental tests were performed by NASA, Johnson Space Center and the Massachusetts Institute of Technology, Laboratory for Space Experiments:

- Electromagnetic compatibility (EMC)
- Vibration of stowed release mechanism
- Thermal cycling
- Toxicity and outgassing

Life Test

A Life Test of one release mechanism was performed and an operating life factor of 4 was demonstrated in relation to mission, ground testing, and crew training operations. At the end of this test the unit was still operating normally.

ORIGINAL PAGE 13
OF POOR QUALITY

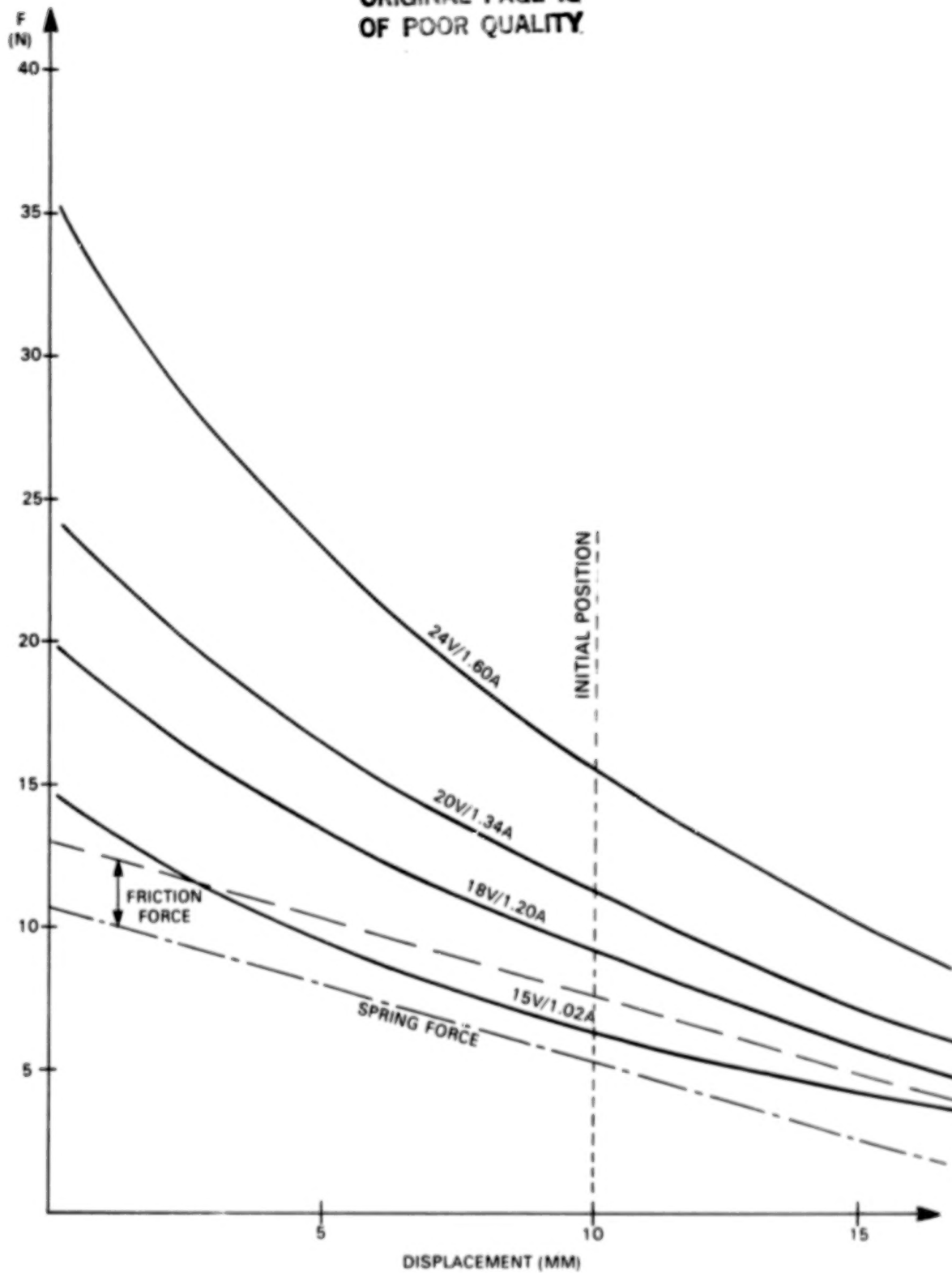


Figure 8. Solenoid Force at Various Supply Voltages

CONCLUSIONS

Three flight units have been delivered for use in Life Science Experiments on the Spacelab 1, D1, and 4 missions.

The unit used on Spacelab 1 (STS-9), which flew in November and December 1983, performed satisfactorily.

The Spacelab D1 and 4 missions are due in June 1985 (STS-26) and December 1985 (STS-32).

The mechanism described in this paper is suitable for other applications requiring quick release under load, with release delay independent of load and supply voltage, low-power consumption, and immediate reusability.

ACKNOWLEDGEMENT

The work described in this paper was performed under contract to the Defence and Civil Institute of Environmental Medicine (DCIEM), Downsview, Ontario, Canada. The authors would like to thank Dr. K.E. Money of DCIEM for his valuable support.

N84
25080

UNCLAS

ACTUATOR DEVELOPMENT FOR THE
INSTRUMENT POINTING SYSTEM (IPS)

Klaus Suttner*

ABSTRACT

This paper gives a brief introduction to the mechanisms of the instrument pointing system (IPS). Particular emphasis is placed on the actuators which are necessary for operating the IPS. The actuators are described as follows:

- Two linear actuators that clamp the gimbals down during ascent and descent
- Two linear actuators that attach the payload to the IPS during the mission, and release it into the payload clamps
- One rotational actuator that opens and closes the payload clamps
- Three identical drive units that represent the three orthogonal-gimbal axes and are the prime movers for pointing

Design features, manufacturing problems, test performance, and results are presented in this paper.

HISTORY

In 1972, Dornier under the sponsorship of the European Space Agency, began investigating the feasibility of an instrument pointing system (IPS) to be flown on a Spacelab Pallet on board the Space Shuttle. The task of IPS would be to support solar, stellar, and Earth sensing payloads during launch and landing, and to point them on-orbit, with arc-sec accuracy.

The design phase started in 1976 and until 1980 the qualification programme was proceeding successfully. Because increased Shuttle mechanical environment and changed Shuttle and Spacelab requirements did not allow the original concept to continue, a rigorous redesign was initiated that resulted in the totally new construction shown in Figure 1. Only a few parts of the original concept survive in the new design, although the experience gained from the previous phase was very useful for the new start. See Figure 2.

Since that time the new IPS has almost completed its qualification programme and the activities for the July 1984 delivery are proceeding.

*Dornier System GmbH, Friedrichshafen, West Germany

ORIGINAL PAGE 19
OF POOR QUALITY

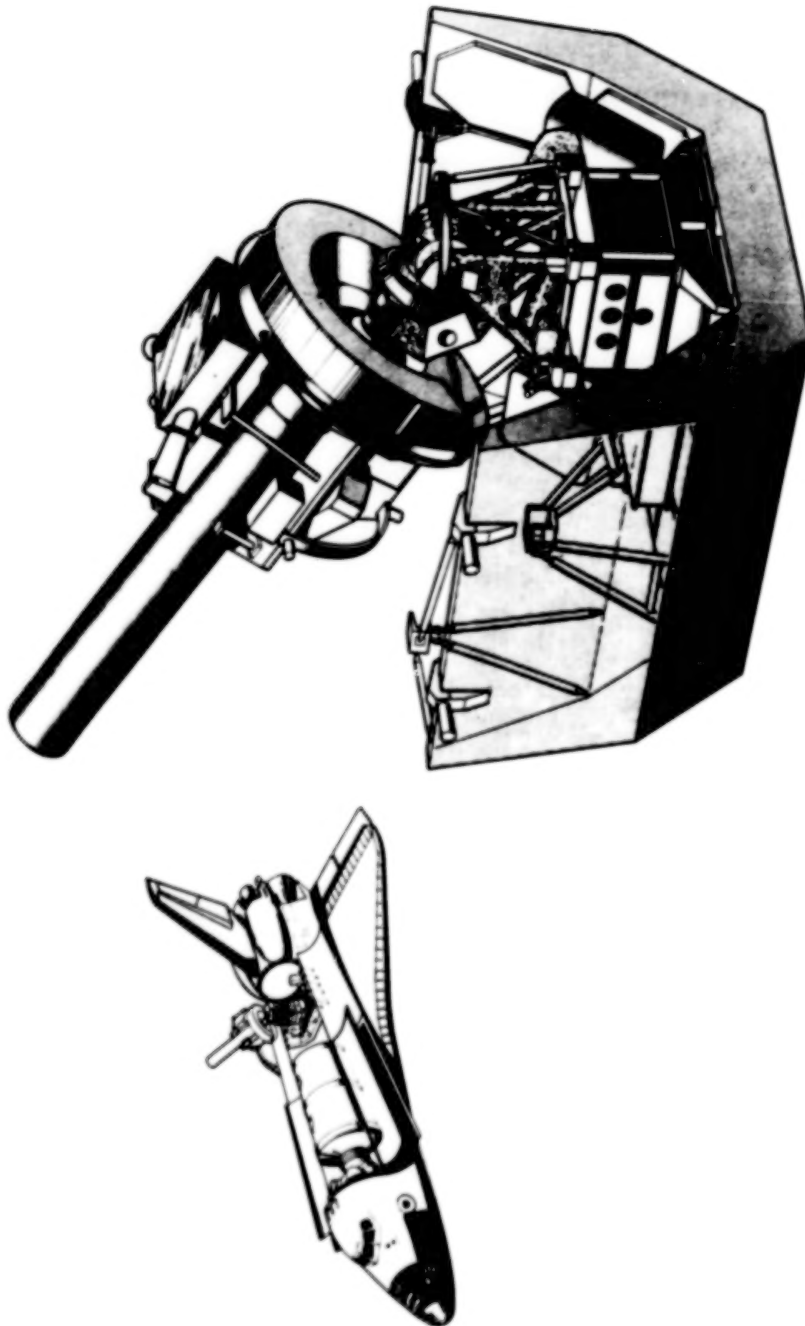


Figure 1. Configuration of IPS

ORIGINAL PAGE 19
OF POOR QUALITY

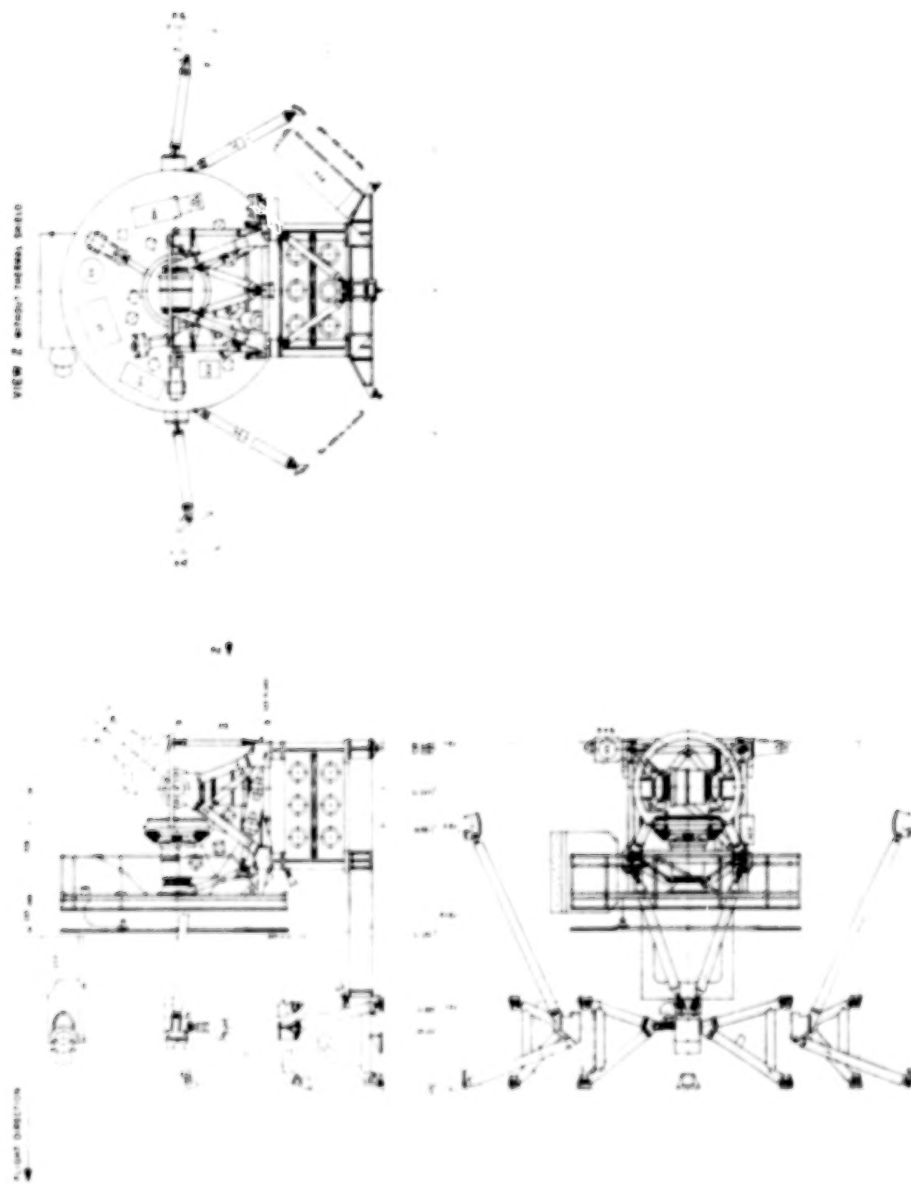


Figure 2. Three-Sided View of IPS

PERFORMANCE DATA

The IPS is designed to include a wide range of payloads for solar, stellar, or Earth sensing missions. To cover all imaginable demands of potential users very severe requirements had to be observed and fulfilled by an adequate layout. The main features of the IPS are:

- a. IPS weight--1200 kg
- b. Payload data (max)
 - Weight--3000 kg
 - Diameter--3 m
 - Length--3 m
- c. Pointing precision--2 arc-sec normal to line of sight--15 arc-sec around line of sight
- d. Usable viewing angle-- $\pm 60^\circ$ half-cone angle; $\pm 180^\circ$ around line of sight
- e. Lifetime--10 years or 50 missions

MECHANICAL CONFIGURATION

Three drive units form the orthogonal axes of the gimbal system. Structural members connect them mutually with the pallet and the payload.

The gimbal latch mechanism, driven by one of a pair of linear actuators, fixes the gimbal system rigidly to the mounting structure during ascent and descent. For the mission, the latch opens to allow the gimbals to be moved. Normal operation requires only one actuator for safe locking in the launch and landing configuration; the second actuator is a backup if the first should fail. The latching concept consists of two hooks attached to the movable gimbals and two cranks driven by the actuators, which catch and pull the hooks down to the structure.

During ascent and descent, the payload is separate/ from the gimbal system. The payload gimbal separation mechanism is used for attaching the payload to the gimbals. One of a second pair of linear actuators activates this mechanism. The actuator pulls the payload out of its clamps, which have been previously opened, and provides a rigid connection between the payload and the gimbals by means of a cable and pulley system. When the cables are released by the main actuator or in a failure case by the redundant actuator, leaf springs push the payload away from the gimbals back into the clamps.

The three clamps are V-shaped housings with a sliding keybolt that closes the opening, each capable of accommodating one of three trunnions bolted to the payload. The keybolts are operated simultaneously by flexible rotational shafts driven by one rotational actuator.

LINEAR ACTUATOR

Performance requirements are as follows:

- 18 Vdc, 1.9A-maximum
- 120-mm stroke
- 6000-N force
- -30° to +70° operating temperature
- 2800 cycles under ambient and orbit environment

Design Description

A design that used a dc brush motor driving a harmonic drive gear and a threaded shaft/nut assembly was chosen to meet the previous requirements (Figure 3). Titanium was selected for the structural parts owing to its good stress-to-weight ratio and the thermal requirements.

The frameless dc motor turns at approximately 200 rpm, depending on the applied load. The rotor is bolted to the wave generator of the harmonic drive gear, which reduces the speed by a ratio of 1:78. The output of the gear is transmitted by a hollow shaft to a rotating nut in which a nonrotating threaded shaft, with a pitch of 8 mm, can move longitudinally. The shaft is attached to a plunger sliding in a tubular section of the housing.

A prism fixed to the plunger penetrates a slot of the outer housing and prevents the plunger and subsequently the shaft from rotating. Also the slopes of the prism operate the actuator endswitches.

With the exception of the harmonic drive, all rotating parts are mounted on deep groove ball bearings of the same size. Races and balls are manufactured from AISI 440 C CEVM, and the cages from phenolic resin impregnated with Fomblin oil Z 25. This lubricant is also used for the harmonic drive and the nut/shaft assembly.

Fabrication Problems

Because of mass restrictions, it was necessary to machine the parts down to the absolute minimum, which led to very expensive, lightweight filigree parts.

Computer calculations taking temperature influences and applied loads into account led to extremely close tolerances for the ball bearing fits. Even under these conditions smooth running and proper performance had to be guaranteed.

Test Performance

For qualification testing, one qualification model actuator was built in addition to the four flight models. A normal test programme with vibration, thermal-vacuum, life-cycle and functional performance tests will be used to qualify the actuator.

ORIGINAL PAGE 19
OF POOR QUALITY

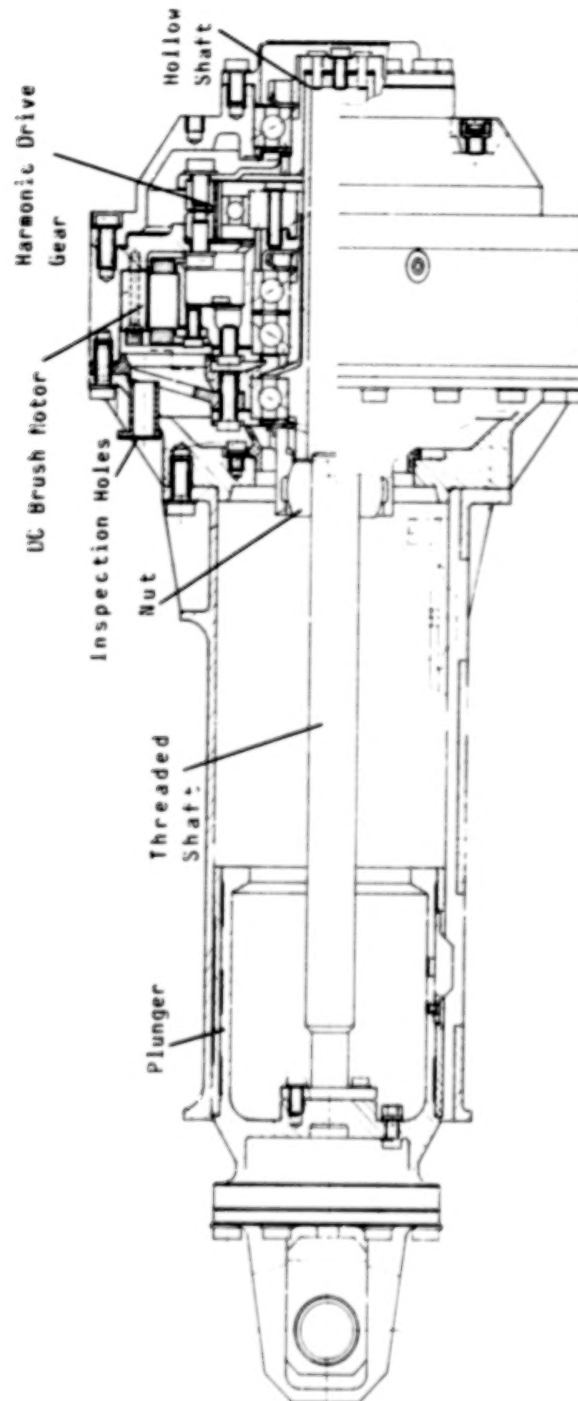


Figure 3. Linear Actuator

Problems

Originally Dornier intended to hermetically seal the entire actuator; the gaps between the flanges were equipped with O-rings, and the sliding plunger was connected with the housing by a metal bellows. This seal was difficult to maintain because:

- The atmosphere inside the actuator must contain a carefully controlled amount of moisture which is required to achieve good motor brush performance
- The rubber seals become hard at low temperatures and leak under temperature gradients between the flanges
- The welded bellows cracked during the vibration test

After this experience the motor manufacturer was requested to provide motor brushes capable of operating in vacuum. Their positive answer encouraged Dornier to abandon the sealed concept.

During the thermal-vacuum testing however, the brushes failed after the low-temperature test. To find a suitable brush material, an investigation was begun but it was not successful. Brushes were subsequently declared as life-limited items that have to be inspected regularly, and exchanged if necessary, and the mechanical design was modified to ease inspection and replacement.

Owing to the very short lifetime achievable by the brushes--little more than one 7-day mission--the search for more durable brushes is continuing with the aim of increasing the number of missions using the same brush set.

ROTATIONAL ACTUATOR

Performance requirements are as follows:

- 18 Vdc, 3.6-A maximum
- Two motors in one housing
- 60 revolutions cw and ccw at three outlets
- 2.4 Nm maximum at each of the three outlets simultaneously
- -25° to +90°C operating temperature
- 1400 cycles under ambient and orbit environment
- Manual operation must be possible

Design Description

The rotational actuator (Figure 4) consists of two major parts: the motor housing and the gear box.

Two dc brush motors are mounted on a single common shaft inside the motor housing. The motors and shaft bearings are the same as those used in the linear actuators.

ORIGINAL PAGE IS
OF POOR QUALITY

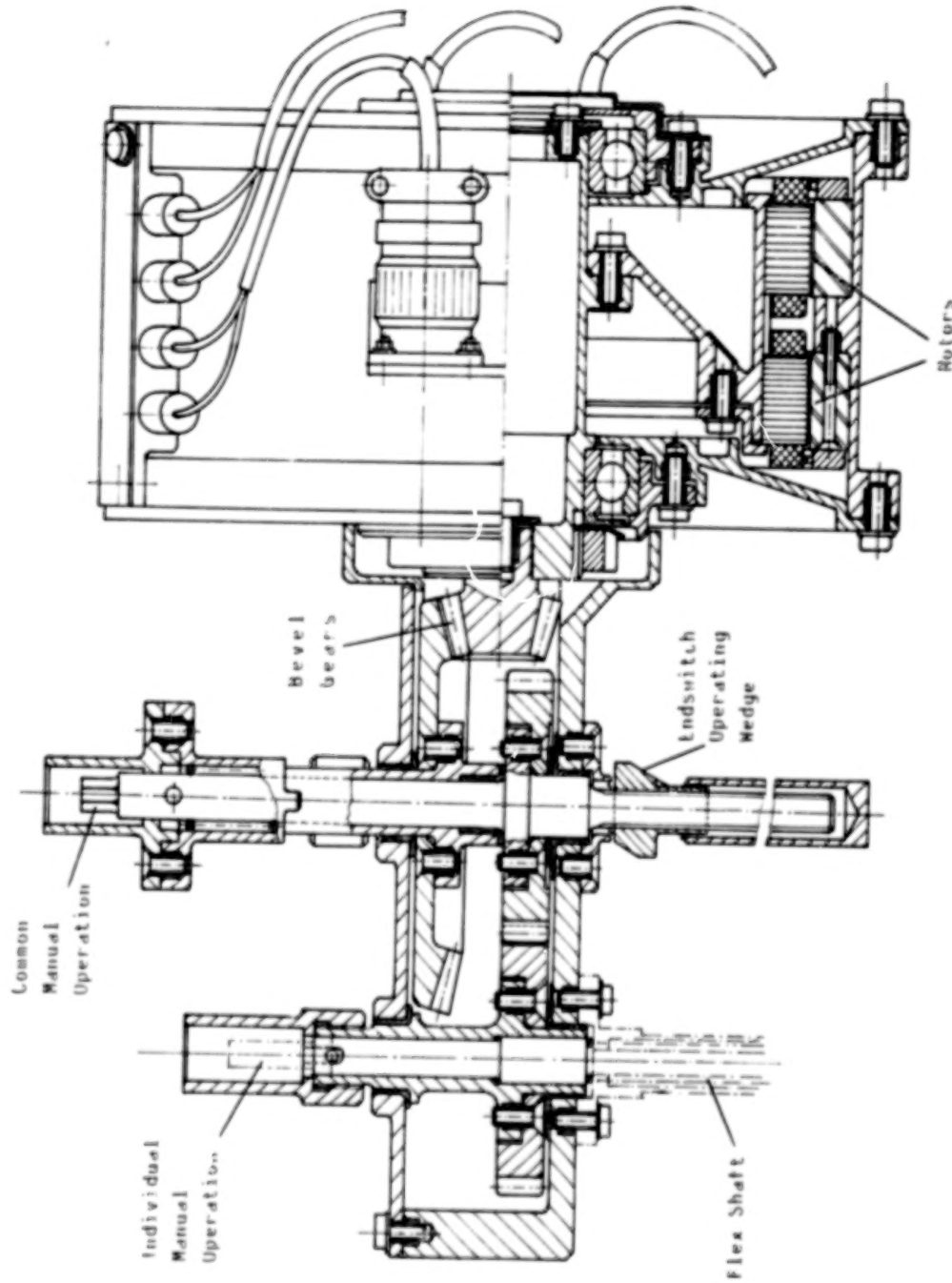


Figure 4. Rotational Actuator

A bevel drive gear located at the end of the shaft is in contact with a bevel crown wheel, both located inside the gear box. This first gear stage reduces the motor speed by four. To distribute the motion to the three payload clamp flex shafts a spur gear with a central wheel and three adjacent wheels is used.

The wheel shafts are mounted on dry lubricated journal bearings.

In an emergency, the flex shafts can be manually operated either individually or by the common central shaft, using a special torque limited detachable crank tool.

At the two extreme positions of the keybolt in the payload clamps, the motor is switched off by two sets of endswitches (not shown in Figure 4). The switches are operated by wedges sliding along a threaded spindle which extends from the central gear shaft.

Test Performance

One qualification model actuator will undergo the qualification programme of vibration, thermal-vacuum, life cycle, and functional performance tests. A set of flexible shafts will be tested in parallel.

To simulate the mechanical actuating forces, either a payload clamp or load simulators using a thread/nut assembly and springs may be used. The simulator is designed to perform under ambient and vacuum conditions.

Problems

Because the same motors were used as in the linear actuator, this assembly had similar motor brush problems. Operation of the payload clamps requires fewer motor revolutions, so a higher number of missions between brush exchanges can be anticipated.

GIMBAL DRIVE UNIT

Performance requirements are as follows:

- 18 Vdc, 9 A-maximum
- 15 Nm torque maximum
- 2 arc-sec pointing accuracy
- -10° to +80°C operating temperature
- 25.2 kN axial load; 43.5 kN and 13 kNm lateral
- 30000 cycles over $\pm 180^\circ$ and 500,000 cycles over $\pm 5^\circ$ under orbit environment
- Infinite number of revolutions of the bare drive, equipped with cable feed through $\pm 60^\circ$ to $\pm 193^\circ$.
- 200 signal and 290 power lines across each drive unit

Design Description

The main active elements of the IPS gimbal system are the drive units. Three drive units form the three axes and provide

- The capability to carry the loads of ascent, descent, and ground operations
- Sufficient angular freedom
- Low friction torques over the whole travel
- Generation of torque to move the gimbals
- Position indication
- Passage for approximately 500 electric leads

When the IPS was redesigned, the drive units were also significantly reconfigured (Figure 5). Whereas in principal most of the functions remained the same, the drive units were simplified and some of the functions removed and separately allocated.

The main differences are:

<u>Old</u>	<u>New</u>
a. Load by pass for: <ul style="list-style-type: none">• Unloading the bearings• Active emergency braking• Self aligning to zero• Locking for ascent	a. No load by pass, instead: <ul style="list-style-type: none">• Sufficiently dimensioned bearings• External passive end stop• External guiding slots• External gimbal latch mechanism
b. Cable follow-up with spirally wound special flat-band cables	b. Cable feedthrough with normal cables running axially through the hollow shaft
c. Numerous parts, complicated function, hermetic sealing necessary	c. Fewer parts, simple function capable of operating under ambient and vacuum conditions
d. Small bearings requiring auxiliary bearing for ground operation and an offloading device	d. Bigger bearings with no extra measures required
e. Bearings with expensive titanium carbide coated tungsten balls	e. Normal stainless-steel bearings
f. "Soft" shaft with changing diameters and cutouts, set together from several pieces	f. One solid stiff shaft

ORIGINAL PAGE 19
OF POOR QUALITY

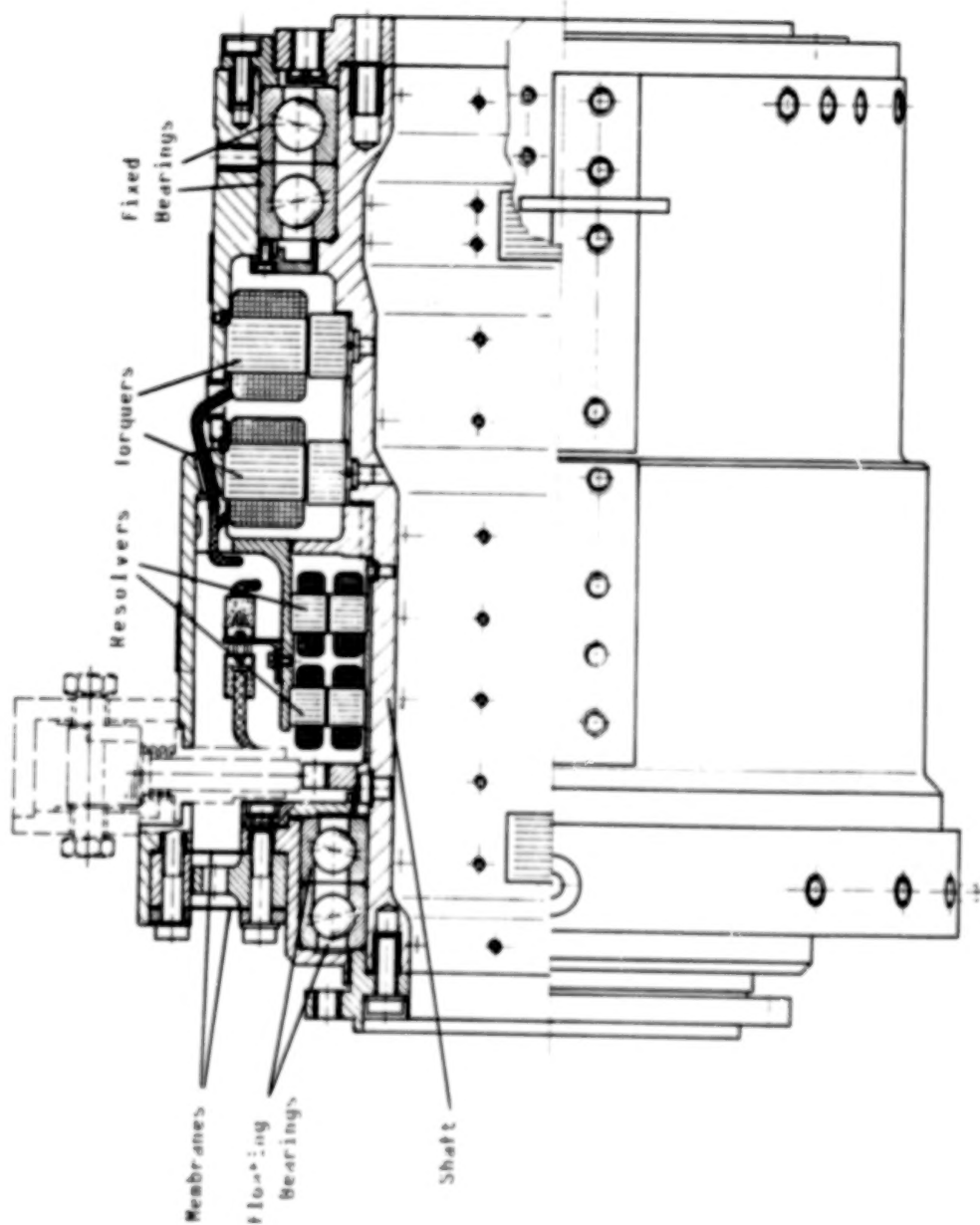


Figure 5. Drive Unit

The new drive unit features two pairs of angular contact ball bearings arranged in a face-to-face configuration. Races and balls are manufactured from AISI 400 C - CEVM, with ABEC 7 (ISO 4) tolerances, the cages from phenolic resin with 2-percent porosity. The bearings are lubricated with Fomblin oil Z 25.

The larger diameter pair are rigidly fixed carrying both axial and radial loads, and the smaller pair are mounted on membranes and float axially.

The frameless brushless dc torque motors, the only items taken over from the previous design, use a samarium cobalt permanent magnet rotor and a sine and cosine winding in the stator.

Two resolvers, matching the torquers in number of polepairs and windings, provide the torquer position and speed-control signals. Two singlespeed resolvers, integrated within the previously mentioned resolvers, determine the angle between shaft and housing.

Torquers and resolvers are mutually aligned by locator pins in shaft and housing, respectively. The cable feedthrough is not shown in Figure 5. Almost 500 signal and power leads run axially through the hollow shaft, with power and signal leads separated by a concentric metal tube. This arrangement has to allow a rotation of up to $\pm 193^\circ$ without a significant increase of torque.

Fabrication Problems

For weight and thermal reasons, the housing, the shaft, and the flanges of the drive units have been made from titanium. Highly accurate machines (partially with air bearings) were used to turn the bearing fits. The tolerances of these were calculated by computer in close cooperation with the bearing manufacturer. Tolerances of better than $6 \mu\text{m}$ in diameter and $3 \mu\text{m}$ in roundness were necessary.

In one case a kind of memory behaviour of the titanium was observed caused by an unfavourable clamping of the workpiece. To recover the out-of-tolerance part the distorted area was chemically nickel plated and remachined.

Test Performance

Besides the electrical and vibration tests, special attention was directed to the torque behavior of the drives. The old drive unit concept was designed for the lowest possible torque, which resulted in very small bearings with their attendant disadvantages, as previously described. New investigations into the control loop, however, revealed that the total system performance was not affected by higher torques. To determine these torques with and without a cable feedthrough under different environments, special test equipment was designed.

The drive unit is mounted on a rotating vertical axis turntable, driven by an electric motor through a 6000:1 speed reducer. The speed and position are monitored by a tachogenerator and a potentiometer, respectively.

The drive unit shaft is attached to a piezoelectric torque transducer. The whole assembly is mounted in a tubular structure that can be placed, completely, into a thermal-vacuum chamber. By rotating the turntable, the net resistance torque of the drive unit, with or without cable feedthrough, is indicated on the torque transducer. To cover the requirements for both pointing and slewing modes of operation, test runs were made for both small and large angles of rotation. The measurements revealed a torque of approximately 0.5 Nm for the bare drive unit without the cable feedthrough and approximately 4 Nm with the cables installed at $+193^\circ$. Under cold temperature influence, a slight torque increase of about 5 percent was observed.

A life cycle test was also performed in this test rig. The motor and the torque transducer were decoupled and the internal dc torquers were activated by a control and measuring unit consisting of a normal programmable desk computer with a subsequent power stage. The shaft position was monitored by the internal resolvers. During this test, $\pm 180^\circ$ cycles equalling 30,000 revolutions and 500,000 cycles of $\pm 5^\circ$ at extreme temperatures were performed and revealed no change in torque.

A fatigue and a quasistatic load test was conducted that used a vibrator on which the housing was fixed and a mass dummy of 160 kg attached to the shaft by a 420-mm long stiff beam. Accelerations of up to 20 g for a duration equivalent to 200 missions were applied, which yielded an axial force of 25 kN and a bending moment of 13 kNm.

Final resolver zero and stability checks and torque tests did not show deviations from the former results.

After these qualifications tests, the cable feedthrough was checked for cable breakage and insulator damaged with positive results. Thereafter, the cables were stripped and inspected, but no damage or abrasion was found.

The drive unit is fully qualified and without any reservations and showed its ability to meet all requirements and to operate successfully in the IPS.

CONCLUSIONS

The active mechanisms for the IPS are partially qualified: some tests are still running.

The mechanical performance of the linear and rotational actuators is proven; as their capability for meeting the requirements has been demonstrated. The remaining brush problem is under investigation. It is not likely a brush can be found that survives the entire required lifetime, but the aim, however, is to provide brushes for at least a limited number of missions.

The drive unit was fully qualified in an extensive test programme. In addition, the three flight units have been successfully acceptance tested and are integrated in the IPS.

No severe problems can be reported from the other IPS subsystems. The system integration is currently under way. After the final integration of IPS, some system tests are planned. At present, no complications are anticipated so scheduled delivery of the first IPS to ESA is planned for July 1984. A second IPS will be delivered to NASA half a year later.

We hope that the IPS will provide scientists with a precise tool on which to mount their instruments and to obtain accurate observations and measurements, enabling them to increase our knowledge of the world and the universe.

N84.
25081

UNCLAS

A PASSIVELY CONTROLLED APPENDAGE DEPLOYMENT SYSTEM
FOR THE SAN MARCO D/L SPACECRAFT

by

William E. Lang, Harold P. Frisch, and Deborah A. Schwartz*

Abstract

The need for adding deployable inertia booms to the San Marco D/L spacecraft developed from a critical spin stability and weight margin problem which became apparent when the flight spacecraft was well into the final integration phase. Available options reduced to either despin of the system followed by deployment at reduced speed or deployment at the final stage spin rate of approximately 115 rpm. Spinning deployment involves transition to a lower energy state which the deployment mechanism must accommodate. The configuration dictated that the add-on boom units attach to existing pitch and yaw axis interfaces and fold back within a restrictive heat shield envelope.

As a single axis hinge design could not accommodate high-speed deployment, concepts where the boom hinge assembly can also rotate about the spacecraft radial pitch or yaw axis were studied in depth. This paper describes the analytical simulation of deployment dynamics of these 2-axis concepts as well as the evolution of practical designs for the add-on boom units.

With the boom free to swing back in response to Coriolis forces as well as outwards in response to centrifugal forces, the kinematics of motion are complex but admit the possibility of absorbing deployment energy in frictional or other damping devices about the radial axis, where large amplitude motions can occur and where the design envelope allows more available volume.

An acceptable range can be defined for frictional damping for any given spin rate. Inadequate damping allows boom motions which strike the spacecraft; excessive damping may cause the boom to swing out and latch with damaging violence. The acceptable range is a design parameter and must accommodate spin rate tolerance and also the tolerance and repeatability of the damping mechanisms.

Introduction

The San Marco D/L is the latest of a series of spacecraft in an international cooperative program involving NASA and the Italian Centro Ricerche Aerospaziali (CRA). The spacecraft is to be launched by a Scout rocket from a site off the east coast of Africa with the primary mission being to study the equatorial region upper atmosphere. The spacecraft is larger than its predecessors and similar in general configuration, having a

*Guidance and Control Branch, NASA/Goddard Space Flight Center, Greenbelt, Maryland

quasi-spherical lightweight outer shell coupled via load sensors to a rigid and comparatively massive central body to evaluate atmospheric drag. It contains other scientific instruments, is spin stabilized, and has 4 wire antennae which deploy radially, plus two "STEM" type antennae which extend along the spin axis.

It will also have deployable inertia booms which are needed because of a critical spin stability and weight margin problem which became apparent when the flight spacecraft was well into the final integration phase. The evolution of this problem and the development of the add-on boom units intended to solve it are the subjects of this paper.

All San Marco spacecraft needed a so-called triaxial mass balance to accommodate the primary drag balance experiment. The mass centers of the inner body and outer shell must both be essentially coincident with each other and with the geometric center and the center of pressure of the outer shell. Also, the products of inertia about all 3 reference axes of the drag balance experiment, and especially about the spacecraft spin axis, must be minimized. Reference 1 discusses the subject of triaxial balancing. Spin balance of the spacecraft about the spin axis of the final stage booster is a concurrent requirement, complicated by the logistic sequence that the spacecraft is balanced in Rome, Italy, the booster is balanced in Wallops Island, Virginia, and they are never mated and aligned until final assembly at the equatorial launch site, where balance of the final assembly cannot be done.

There is also the basic spin stability requirement that the spin axis be a major principal axis with moment of inertia greater than pitch or yaw axes. In this case, an extra inertia ratio margin was needed to accommodate the spin axis antenna extension, but some offsetting margin reduction results from radial wire antenna deployment. The mission sequence is spin up, booster ignition, burn out, separation, coast, radial boom deployment (in stages) and finally spin axis boom extension, with spin stability needed throughout the sequence.

Evolution of the Problem

As the flight spacecraft integration became relatively complete, weight and moment of inertia measurements were made with disconcerting results. The projected weight was more than expected and allowed little margin below maximum vehicle capability for the planned orbit. Also, the projected moment of inertia ratio was unfavorable and could not be corrected by adding mass within the weight margin, or within the outer shell, as the inner body was a densely packed configuration. Furthermore, mass moment checks showed considerable static unbalance about all 3 axes and dynamic spin balance about any axis had not yet been done.

It was felt on the basis of earlier San Marco experience that up to 4 percent of total spacecraft weight should be budgeted for triaxial balancing and even with an inertially favorable moment of inertia ratio this would have made the weight margin very critical.

Available options were considered, and, other than unacceptable expedients such as removing experiments from the spacecraft, reduced to developing add-on deployable inertia boom units attached to the existing pitch and yaw axis handling fixture interfaces. These 4 booms would fold back within the restrictive heat shield envelope and might require a preliminary yo-yo despin device in order to survive deployment.

This would correct the inertia ratio problem. The balance problem was to be reconsidered after making spin balance measurements about all 3 axes so that the extent to which necessary corrections could be vectorially combined within the outer shell envelope could be evaluated.

Thinking on boom designs rapidly polarized to either a simple, single hinge axis design which would need a yo-yo device, or more sophisticated ideas with multiple hinge axis degrees of freedom, frictional energy absorbing devices, and complex deployment dynamics which might not need a yo-yo or which would at least survive if the yo-yo did not work. It was decided to proceed with both concepts in parallel and with detailed design of the "simple boom," pending better resolution of the actual weight margin after balancing.

After more spacecraft integration, revised weight and moment of inertia measurements and the first spin balance measurements were performed. Various strategies for unbalance correction were tried with due consideration for practical limitations on where the structure allowed weights to be located. The most obvious correction considering mass moment and product of inertia components separately and correcting by adding weights at structurally convenient locations, needed about 9 Kg. Vector combination of these components reduced the weight required to 6.2 Kg at the expense of more inconvenient positioning of correction weights.

Meanwhile, an additional constraint was imposed on the boom design. It had been determined that the degree of shading that the deployed booms would cause to the solar cell panels was acceptable. However, the radial deployed position of 2 of the booms would violate the required field of view of a major onboard experiment, and it was required that the booms be skewed 7 degrees in the pitch/yaw plane. This could be done, but added some weight to the boom structure due to the need for a wedge shaped attachment flange, and necessitated the development of new spacecraft handling devices and procedures.

The question of spacecraft handling logistics and boom alignment merits discussion as a separate but related problem area. The San Marco is balanced using stub arbors attached to the booster interface and to a dummy forward interface, for the spin axis, or to accurate orthogonal holes in the structure for the pitch and yaw axes. These pitch and yaw interface holes have two other functions. They are used to screw in radial lifting handle bars for spacecraft lifting and rotation. They are also used to attach the add-on inertia boom units or rather the attachment flanges for the booms.

Figure 1 shows a sectional view of the boom attachment to the spacecraft.

ORIGINAL PAGE 19
OF POOR QUALITY

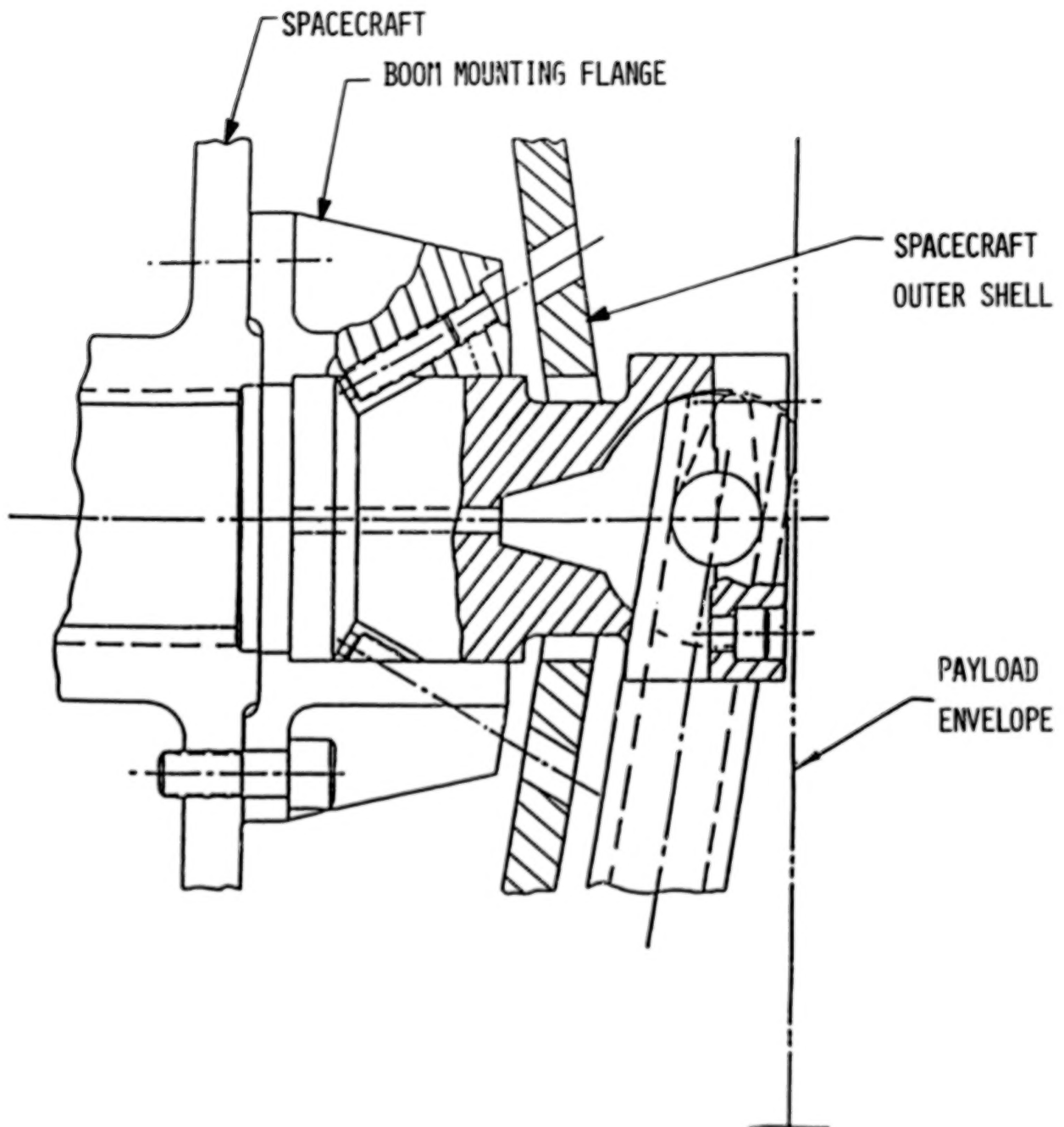


Figure 1. Boom Attachment to Spacecraft

Figures 2, 3, and 4 show other features of the boom system. The flange which is the actual interface to the spacecraft is wedge-shaped and skews the boom 7 degrees. Before the flanges are installed, the radial threaded holes in the spacecraft structural frame are used to attach and accurately align the balancing arbors and also to insert radial handles for spacecraft lifting and pitch rotation. The boom flanges are to be installed and aligned after balancing, but there is a need for handling about a lateral axis after the boom flanges are installed and aligned and the original handles cannot be used because of the 7 degree skew, so new handles are needed, made with a 7 degree skew and to fit into the sockets for the boom hubs. The boom hubs and booms can be removed from the flange sockets and are aligned and secured by angled set screws accessible through holes in the spacecraft outer shell. Thus, the booms can and must be assembled and/or removed with the outer shell in place since the outer hubs are larger than the holes in the outer shell.

The spacecraft balancing requirements make it necessary that the deployed position of the booms be controlled as accurately as possible and be repeatable after several test deployments and the final flight deployment. A limit of 3 mm deviation of boom tip location from nominal, in any direction, was established as the practical limit of feasible manufacturing tolerance control for slender booms almost a meter long. As the desired control of residual unbalance implied no more than 1 mm tip location deviation, it is necessary to accurately measure and/or control the tip alignment to this level of accuracy as a mass property status input. Tip alignment control is to be by shims under the boom attachment flanges; therefore, the flanges should not be removed after alignment. Boom deflection due to gravity is to be considered or negated during boom tip alignment operations. The boom tip location requirements, as well as the need for minimum boom weight, were important design factors for the booms.

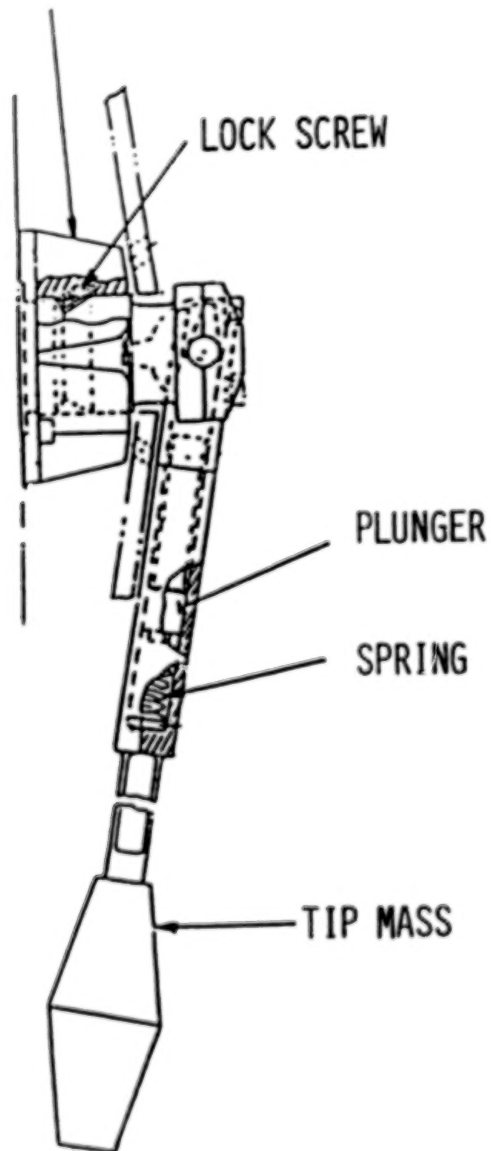
Analysis of Boom Deployment Dynamics

The configuration dictated that the inertia booms be folded down to 9 degrees past vertical, skewed back 15 degrees to clear the spacecraft umbilical tunnel, and that the deployed booms be in the pitch-yaw plane but skewed 7 degrees from radial in the direction of spin. All booms were to be 0.836 m long, with a tip mass to be as required for mass property control, but not expected to exceed 1 Kg. The pre-deployment spin rate would be approximately 115 rpm without yo-yo despin or 38 rpm if a yo-yo were used. In either event, deployment would reduce the spin rate by about 10 percent and impose Coriolis forces during deployment as well as high stresses at lock-in to deployed position.

Spinning deployment involves transition to a lower energy state, with conservation of angular momentum, and as it became apparent that a single hinge design could not withstand high-speed deployment, concepts where the boom hinge assembly could also rotate about another axis orthogonal to the hinge axis were studied in depth. This second axis as well as the hinge axis would have to be skewed 7 degrees from the spacecraft radial axis to accommodate deployed position requirements.

ORIGINAL PAGE 19
OF POOR QUALITY

ATTACHMENT FLANGE



ATTACHMENT FLANGE

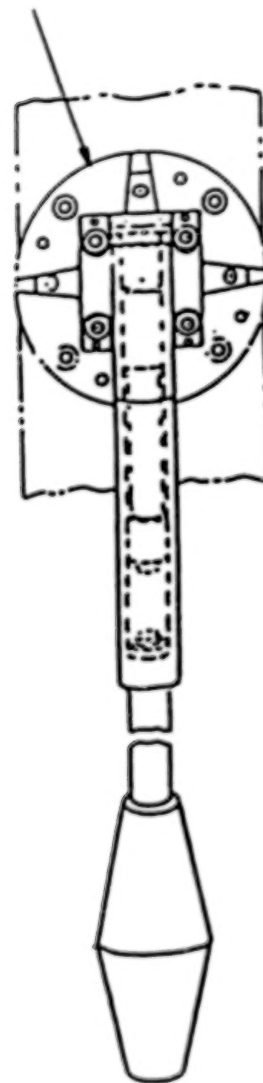


Figure 2. Inertia Boom Assembly

ORIGINAL PAGE 19
OF POOR QUALITY

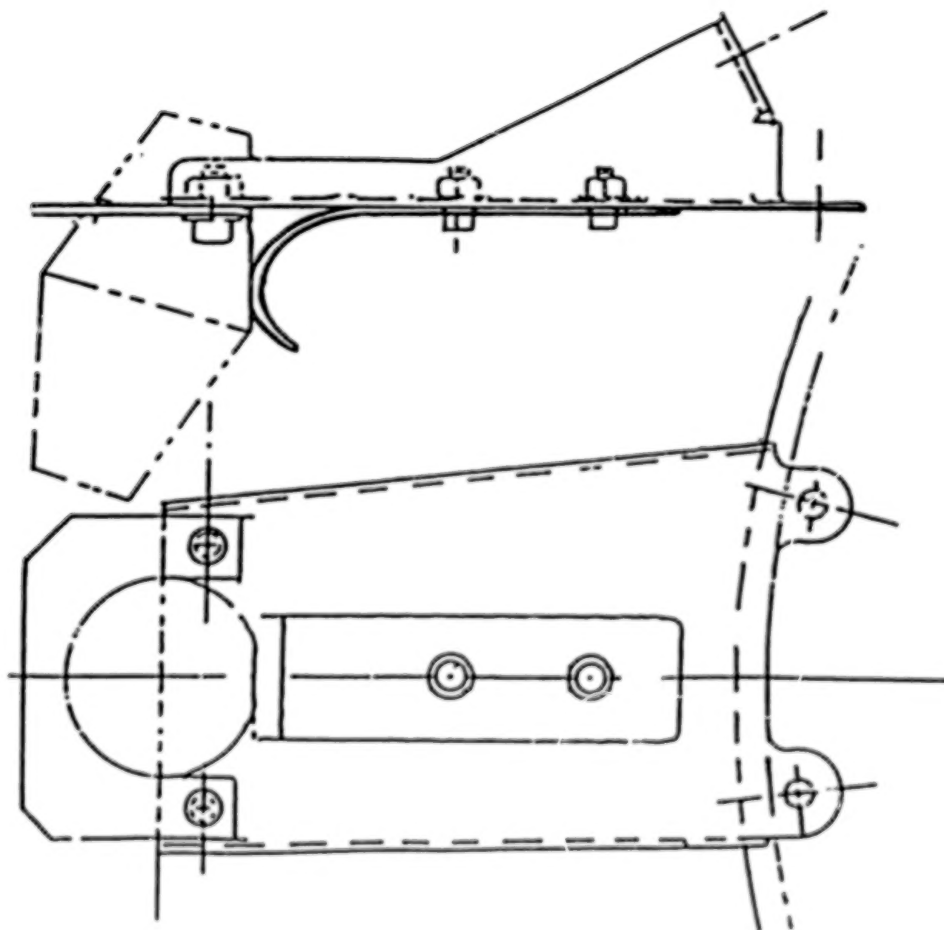


Figure 3. Tip Mass Restraint Bracket

ORIGINAL PAGE 18
OF POOR QUALITY

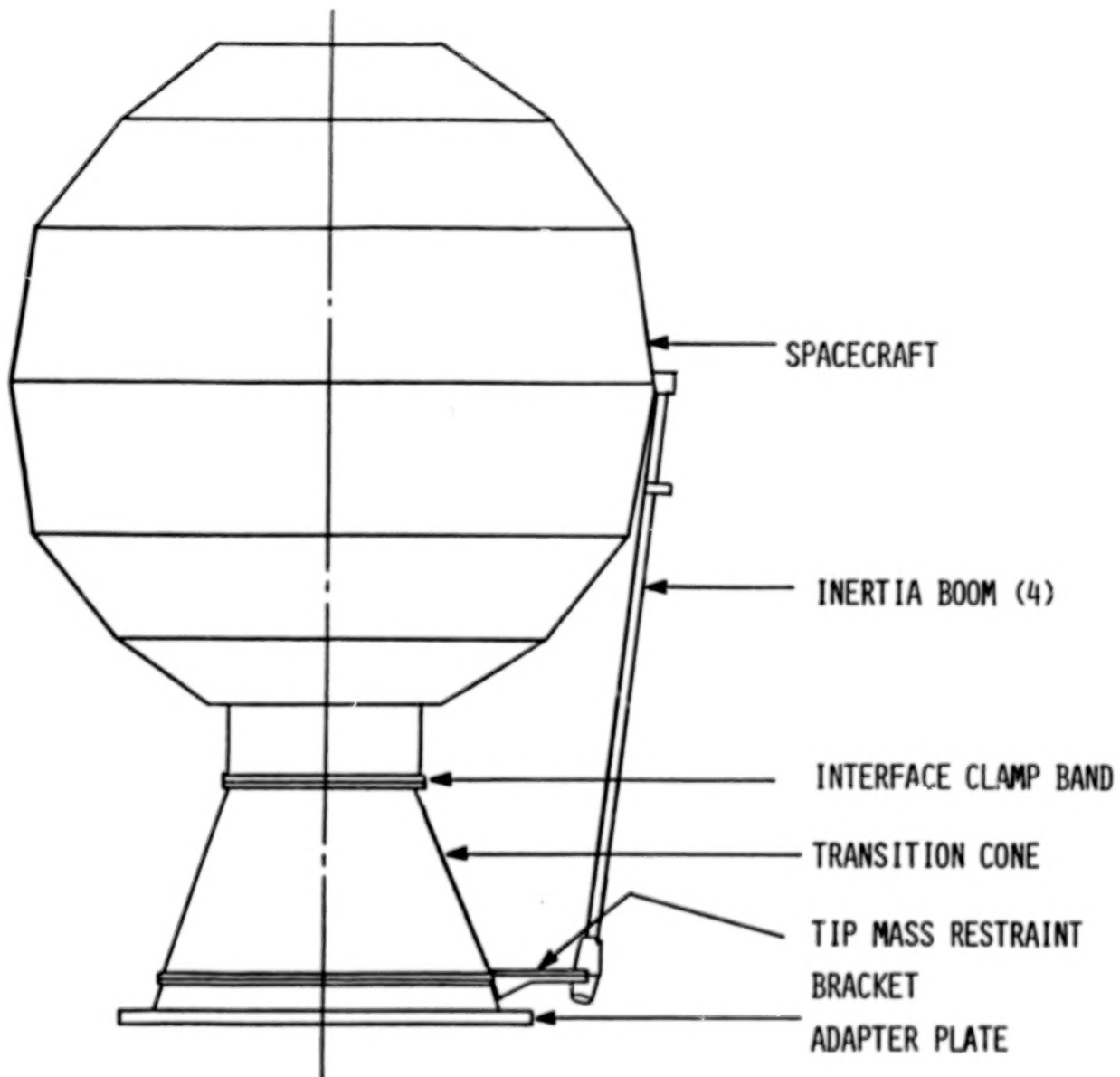


Figure 4. Assembly for Boom Testing

With this second degree of angular freedom, the boom would be free to swing back subject to Coriolis forces as well as outward in response to centrifugal forces. The dynamics of the resulting boom motion during deployment are complex and admit the possibility of absorbing deployment energy in frictional or other damping devices about the axes of both degrees of angular freedom. The second axis, orthogonal to the hinge axis, offered the potential for large amplitude motion with consequent high energy dissipation as well as more available volume for damping devices within the constraints of the design envelope.

Computer Simulation of the 2-Axis Boom Deployment Concept

Computer simulation programs used to study high-speed San Marco boom deployment dynamics have evolved in both fidelity and capability. The understanding of the problem achieved via these simulations has lead to the 2-axis boom deployment concept.

In order to avoid deriving and computer coding equations of motion, the general purpose computer programs N-BOD2 (Reference 2) and DISCOS (Reference 3) were utilized. These programs allow the spacecraft to be modeled as a central rigid body with 4 rigid or flexible appendages. The programs automatically set up the complete set of nonlinear equations of motion taking into account all gyrodynamic interaction effects with no small angle assumptions used. Our task was to define the deployment mechanism in a form compatible with simulation program needs and limitations. Several models for this mechanism were developed. Each new mechanism model added a degree of simulation fidelity and capability not previously present.

The initial 2-axis boom deployment concept investigated consisted of a conical plunger latch with a stiff prestressed spring acting as a boom deployment actuator. It was reasoned that if the prestress level in the spring could be set high enough, adverse Coriolis effects could be overcome and latching would be achieved. The N-BOD2 model for this concept consisted of a central rigid body with 4 identical point connected rigid booms. Each boom had 2 degrees of relative freedom and was symmetrically placed in a plane normal to the spin axis around the spacecraft perimeter. The latching mechanism was modeled as a constant magnitude torque always acting in the direction which aids deployment. The simulation was initialized with a spin rate of 115 rpm and with all 4 booms stowed parallel to the spin axis. These were simultaneously released with zero initial velocity at time zero. The only nongyroscopic load on the system was that associated with the actuator spring in the latching mechanism. Computer simulations revealed that, to overcome Coriolis effects and to insure that the booms would not swing back and strike the spacecraft, spring prestress had to be set at a level beyond that which could be obtained in the space available with obtainable materials. It was further determined that if latching occurred before a significant amount of system energy could be dissipated, the booms had the potential to either break off or be permanently deformed.

In addition to uncovering flaws in initial design concepts, these N-BOD2

simulations provided us with a clearer understanding of boom deployment dynamics. Most importantly, it was noted that the interaction of centrifugal and Coriolis effects tended to produce a resultant boom motion which, to an observer on the spacecraft, appeared as approximate crescent-shaped patterns traced by each boom tip.

Initially, the crescent radius is large while the boom oscillates near the spacecraft, then as the system dissipates energy through various damping mechanisms crescent radius reduces, and the boom approaches the fully deployed state. From this observation, it was reasoned that if the deployment mechanism was free to rotate about the axis defined by the fully deployed boom, the back and forth crescent shaped swinging motion could, so to say, be captured. Then if a braking mechanism could be designed to inhibit this rotational motion, significant amounts of energy could be dissipated through damping prior to latching. The net result would be less violent boom motion with acceptable latching loads. The 2-axis boom deployment concept, discussed herein, is the outgrowth of these initial ideas refined to accommodate system design and scheduling constraints.

The braking mechanism envisioned may be conceptualized as a brake of the friction disc stack type similar to a pedal operated bicycle brake but dimensionally adjusted to fit into available space. By presetting brake pressure before launch, the amount of damping desired could be controlled. Several simulation runs were made to determine at what level the braking pressure should be set at to minimize latching loads, resultant boom elastic deformation, and hinge constraint loads. As a by-product of the numerous runs made, a measure of parameter sensitivity was also determined; crude settings were found to be adequate.

Computer simulation of this mechanism design was achieved via use of the computer program DISCOS. DISCOS provided the ability to extend modeling capability to include the effects of appendage flexibility without introducing any small angle or small displacement assumptions. Boom flexibility was considered to be a parameter which could not be ignored. It was reasoned that the interplay between the tip mass attempting to dominate boom tip deployment dynamics and the mechanism attempting to dominate boom root deployment dynamics would result in significant elastic deformation; it did.

The DISCOS model for this series of simulation programs consisted of a central rigid body with 4 identical elastic beams symmetrically located around the perimeter. Each beam had both distributed mass and a tip mass. Three degrees of elastic freedom were assumed: 2 bending modes, 1 for each orthogonal bending direction, and 1 torsional mode. The DISCOS input specification for the booms consisted of a lumped parameter model. It defined both mass distribution and modal displacement. First clamped-free bending and first torsional modes of oscillation were used. Stiffness was defined by providing modal frequencies. All runs assumed that both bending frequencies were equal, this implied booms with symmetric cross section. The torsional frequency was varied for a few runs to determine if large amplitude bending could induce significant torsional response; it did not. Modal damping could and was also included. It was included primarily to

get rid of the high frequency transient response which masked steady state performance characteristics. The damping values used were consistent with what one would expect to observe for large amplitude oscillations.

The 2-axis deployment mechanism was modeled as a 2-axis gimbal with appropriate damping models specified about each axis. One gimbal axis was defined parallel to the fully deployed boom axis; motion about this axis is intentionally damped by the braking mechanism previously discussed. The other gimbal axis, that is the boom deployment axis, was fixed in the boom normal to its longitudinal axis. Motion about this axis was subject to dry friction taken to be proportional to the constraint torque acting about the axis normal to both gimbal axes. A Dahl friction model was actually used for the description of damping about both axes; that is, below a pre-defined breakaway torque the Dahl friction model is a simple linear spring dashpot. Beyond this point dry friction associated with sliding takes place. This type of friction model is extensively used to model friction associated with systems containing ball or roller bearings. It is also appropriate for the 2-axis boom deployment mechanism.

As in the earlier series of N-BOD2 simulation runs, initial spin rate was set at 115 rpm with booms released from their stowed position with zero initial velocity at time zero. System parameters were varied from run to run in an attempt to find the value of breakaway torque for the braking mechanism which would minimize constraint loads on the gimbal, boom elastic deformation, and the potential of the boom swinging back onto the spacecraft. The net conclusions reached from this series of runs was that it was possible to reduce constraint loads and the potential for boom swing back to acceptable levels; however, elastic deformation could not be reduced to the point where no permanent deformation could be assured.

Further simulation runs revealed that there was another flaw in initial design concepts. The attempt to minimize boom plus tip mass weight lead to the placement of as much extra mass as possible in the tip, thus, weakening the boom. This, so to say, caused a conflict between the tip mass's attempt to dominate boom tip deployment and the mechanism's attempt to dominate boom root deployment. The relatively weak boom effectively allowed both ends to act independently with the boom accommodating via large amplitude deformation. Making use of this new understanding, runs were made with no tip mass and increased boom mass per unit length. The net result was that the mechanism at the boom root dominated total boom deployment and overall performance was acceptable.

Other system parameters were also varied during the course of the study, such as the friction coefficient associated with motion about the deployment axis and initial release position. These runs lead to intuitively obvious conclusions, increased friction in the deployment hinge helps while release from a position other than parallel to the spin axis has no significant effect on overall deployment performance.

Some typical computer output plots are appended as Figures 5, 6, 7, 8, and 9 and are annotated as to significance and interpretation. The end products of a large number of computer runs were some limiting design

criteria and a much better understanding of deployment dynamics.

Limiting cases are of interest and contribute to understanding the situation. With no friction, angular oscillations continue repetitively without damping, and the boom would never latch. On the other hand, if breakaway friction torque exceeds the maximum induced Coriolis torque then there is no sliding about the friction torque axis, and again there is no energy dissipation. This case actually reverts to the simple single hinge boom design—the boom swings out about the hinge axis, and all the deployment energy has to be dissipated at latch-in except for any dissipation due to hinge axis friction.

These considerations led to a design option which is being considered at the time of writing. The booms would be designed to slip about the Coriolis torque axis at a relatively high breakaway torque level, based on an initial spin rate of about 115 rpm. However, the flight system would have a yo-yo designed to reduce spin rate to 38 rpm. If the yo-yo worked, the booms would deploy as a simple single hinge boom, as the Coriolis torque would not be high enough to cause slipping. The booms would be designed to deploy as single hinge booms, at 38 rpm. However, if the yo-yo failed to despin the system, deployment would occur at 115 rpm, Coriolis torques will cause slipping and energy dissipation, and the booms would have at least an enhanced chance of survival for this yo-yo failure mode.

Scale Model Studies

A 1/9 scale dynamic model was built to demonstrate and evaluate the 2-axis boom deployment concept. It had 2 opposed booms with freedom to rotate about the hinge axis and a radial axis, with adjustable torque friction brakes on the radial (Coriolis) axis. There was no deployed position latch, but there was a device to spin up and hold the booms in a folded up position and then release them to deploy.

The model was spun up and deployed at several speeds and torque brake settings, including essentially no friction and friction high enough to stop Coriolis slipping so that the booms deployed as single hinge axis booms. High-speed movies were made of some of these model deployments, and review of them provided an interesting confirmation of the general results of the analytical studies.

With no resistance to Coriolis slipping, the booms perform wild gyrations, including whipping back as far as the hinges allow, confirming that collisions with the spacecraft envelope could occur with inadequate damping. With high friction so that there is no Coriolis slipping, the booms swing out rapidly about a single hinge axis, and flap repetitively, since the model has no latches. With intermediate friction, the booms reach a radially deployed position without excessive gyrations, but the model did not allow accurate frictional matching of the 2 opposed booms so their motions were not in phase. Furthermore, the model had rather stiff booms; and, hence, it was not possible to demonstrate adverse elastic deformation predictions.

Boom Latching Considerations

The inertia booms have to latch into an accurately controlled deployed location because of the spacecraft mass property requirements. However, the latch also has to accommodate high levels of energy at latch in. In other words, the booms latch in fast and hard.

An acute angle conical plunger latch, with a stiff spring actuator, meets the needs for accurate positioning and rapid actuation, though imposed loads are high, on both the latch and the boom.

From the point of view of high-speed deployment capability, the type of detent device which can swing over center and dissipate energy in damped oscillations was attractive. However, it did not seem feasible to design a device of this type with acceptable positioning accuracy or to fit within the available design envelope or to attempt such a design within the developmental time span dictated by the mission schedule.

Current Status of Boom Deployment

The latching consideration and other aspects of the subject system exemplify a dilemma which is common in aerospace mechanism design. We had to come up, very quickly, with a design which could be retrofitted within a mandated schedule and which would do the job acceptably and reliably. We could not afford the luxury of searching for a solution which may have been optimum and perfect, but too late. We also had to start design and make development decisions before all the design parameters were known or understood. The current boom design status is shown in the appended Figures 1 through 4.

Figure 1 shows the angled boom attachment flange with the boom hub inserted into a socket and secured with angled set screws after rotating about the hub axis to align the folded boom tips into the booster cradles. The booms are folded down about 9 degrees past vertical as well as angled back 15 degrees to avoid the spacecraft umbilical tunnel. Thus, the cradles are oriented 15 degrees from the boom flange mounting axes. When the spacecraft separates from the booster, the booms are pulled up out of the cradles and are then free to deploy. The assembly is spinning at separation, at 38 rpm if the yo-yo works, or at 115 rpm if it does not. When the boom reaches a deployed position, a spring-loaded conical plunger is pushed into a socket in the hub, latching the boom into an accurately aligned deployed position. If excessively high Coriolis torques are developed due to high spin rate, the hub is potentially free to slip, depending on the set screw torque, dissipating some energy. This slipping would not affect the deployed boom position but only its angular orientation about the hub axis.

The boom has a tubular inner section, containing the plunger and spring, and an outer section with a wide flat cross section (0.75 inches wide and 0.39 inches deep). The conical tip is to engage and separate from the cradle. The boom is titanium and designed as a distributed mass unit to match the expected nominal inertia control requirements. However, it has a

series of pilot holes in the outer section, to enlarge as lightening holes or to accommodate mounting small slugs of high density tungsten alloy, as may be required for final balance and/or inertia trim.

Update of the Current Status of Boom Development

The foregoing has described the subject ongoing development up to the time of writing. An appropriate updating supplement will be available at the 18th Aerospace Mechanisms Symposium.

References

1. Lang, W. E., "Triaxial Balancing Techniques--a Study of Spacecraft Balance with Respect to Multiple Axes," NASA Technical Note TN D-2144, March 1964.
2. Bodly, C. S., Devers, A. D., Park, A. C., and Frisch, H. P., "A Digital Computer Program for the Dynamic Interaction Simulation of Controls and Structure (DISCOS)," NASA Technical Paper 1219, Vols. 1 and 2, May 1978. (Program code available COSMIC, University of Georgia, Athens, Georgia, Program GSC-12422.)
3. Frisch, H. P., "A Vector-Dyadic Development of the Equations of Motion for n-Coupled Flexible Bodies and Point Masses," NASA Tech. Note TN D-8047, 1975. (Program code available COSMIC, University of Georgia, Athens, Georgia, Program GSC-12846.)

APPENDIX

COMPUTER SIMULATION PLOTS

The following series of figures illustrate system dynamics of the San Marco spacecraft from boom release through latch in.

Figure 5 shows the total energy of the spacecraft system. From 0.0 seconds until 0.47 seconds, energy decrease is attributed to frictional damping in the deployment mechanism. Energy increases between 0.47 and 0.54 seconds when the prestressed spring in the conical plunger snaps the boom into its fully deployed position. After that time, energy loss is from the viscous damping associated with boom bending.

Figure 6 is the spin rate of the main body. It begins at 38 rpm (3.98 rad/sec) and decreases as the booms deploy. At full deployment (0.54 sec), its speed varies between steady state and slightly above steady state, as the booms' motion settles.

In Figure 7, a boom's initial deployment angle is 90 degrees. As the booms are released, the angle reduces to zero degrees which is its fully deployed position.

Figures 8 and 9 show constraint torque at the boom's hinge. In Figure 8, the torque normal to the deployment plane is shown. It is zero until latch in occurs. Thereafter, the deployment mechanism resists motion, and a constraint torque is created.

Coriolis effects cause torques in the deployment plane (Figure 9). Upon boom release, constraint torques are immediately apparent as the deployment mechanism resists motion normal to the deployment plane.

ORIGINAL PAGE IS
OF POOR QUALITY

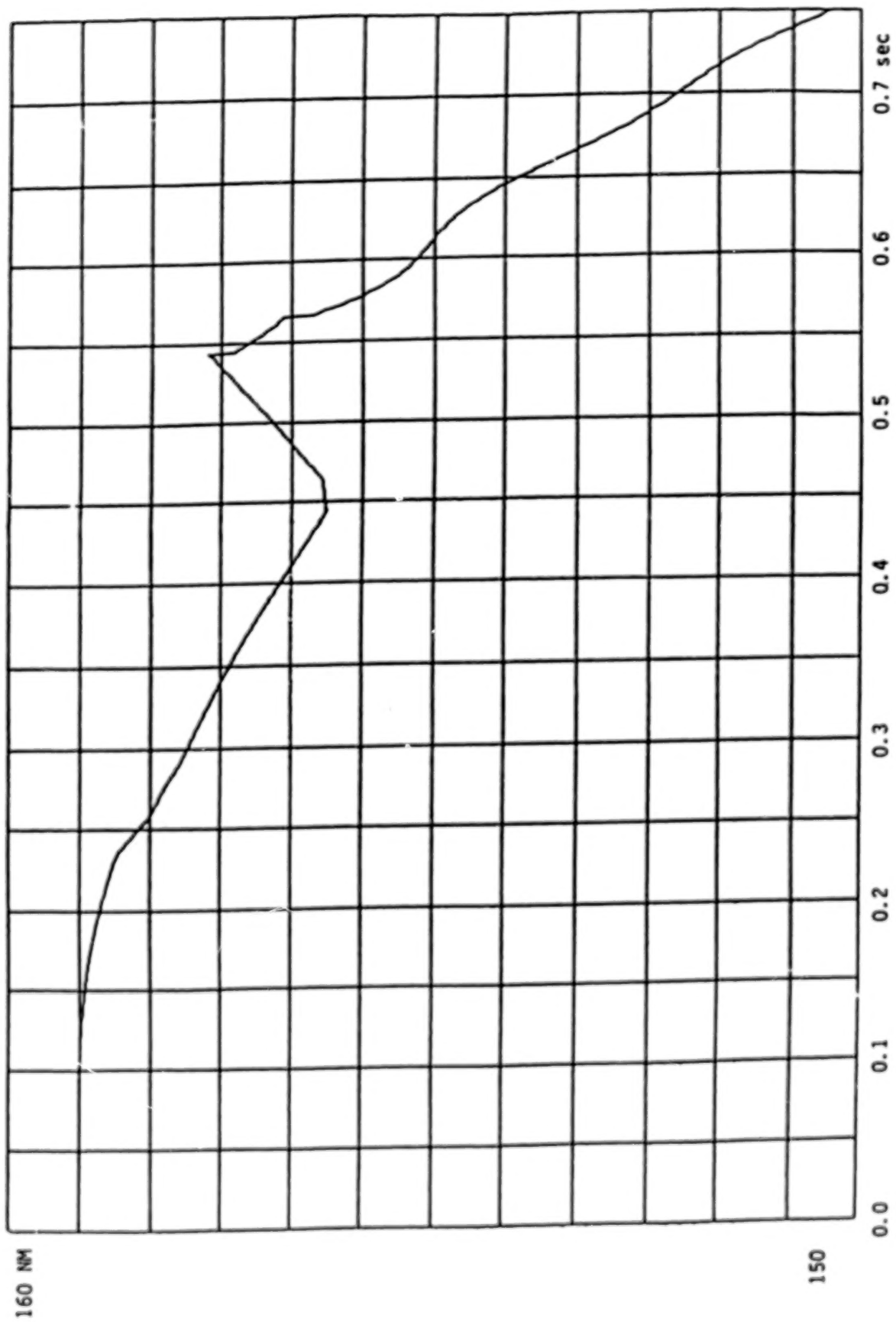


Figure 5. Total System Energy

ORIGINAL PAGE IS
OF POOR QUALITY

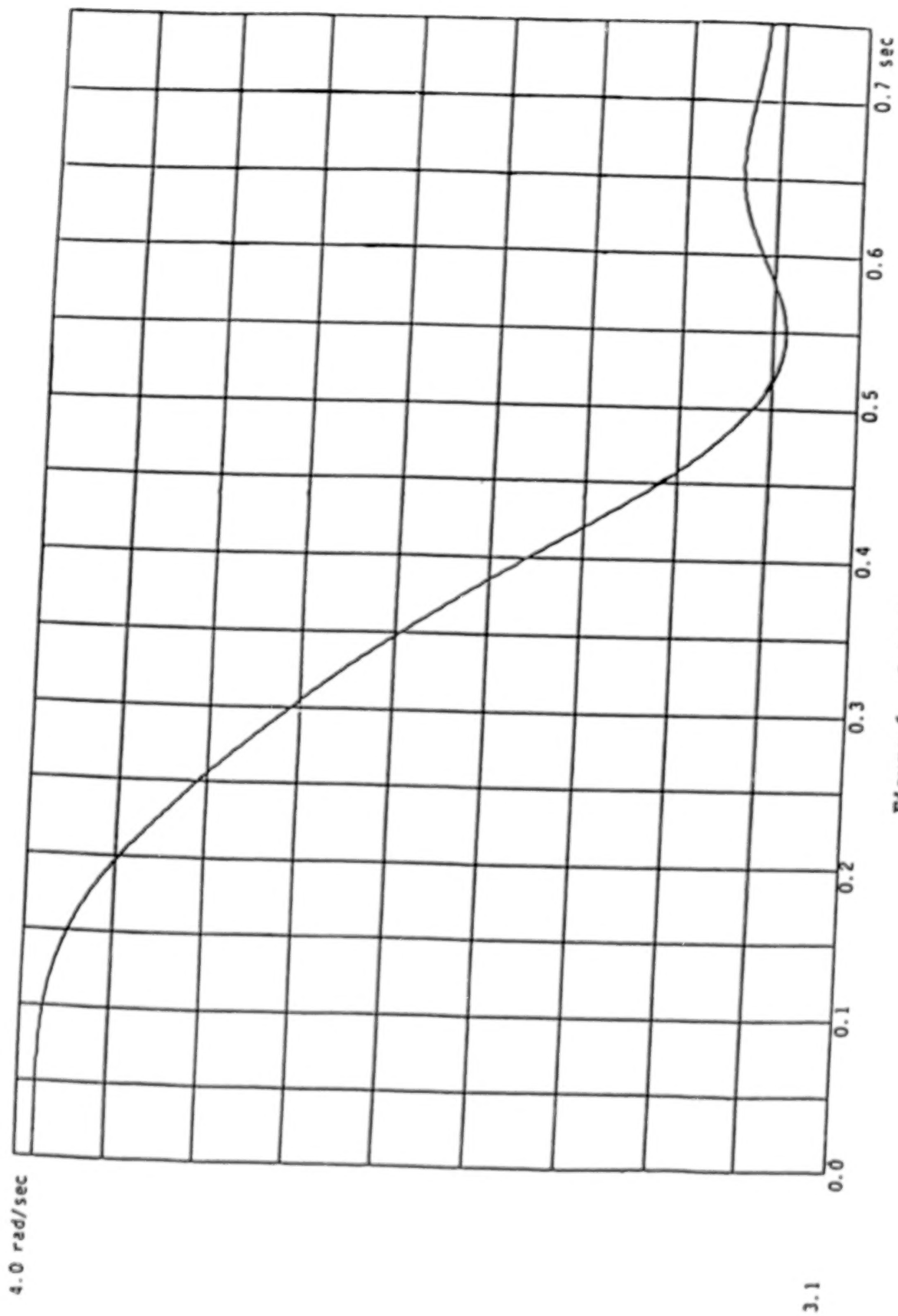


Figure 6. Spin Rate

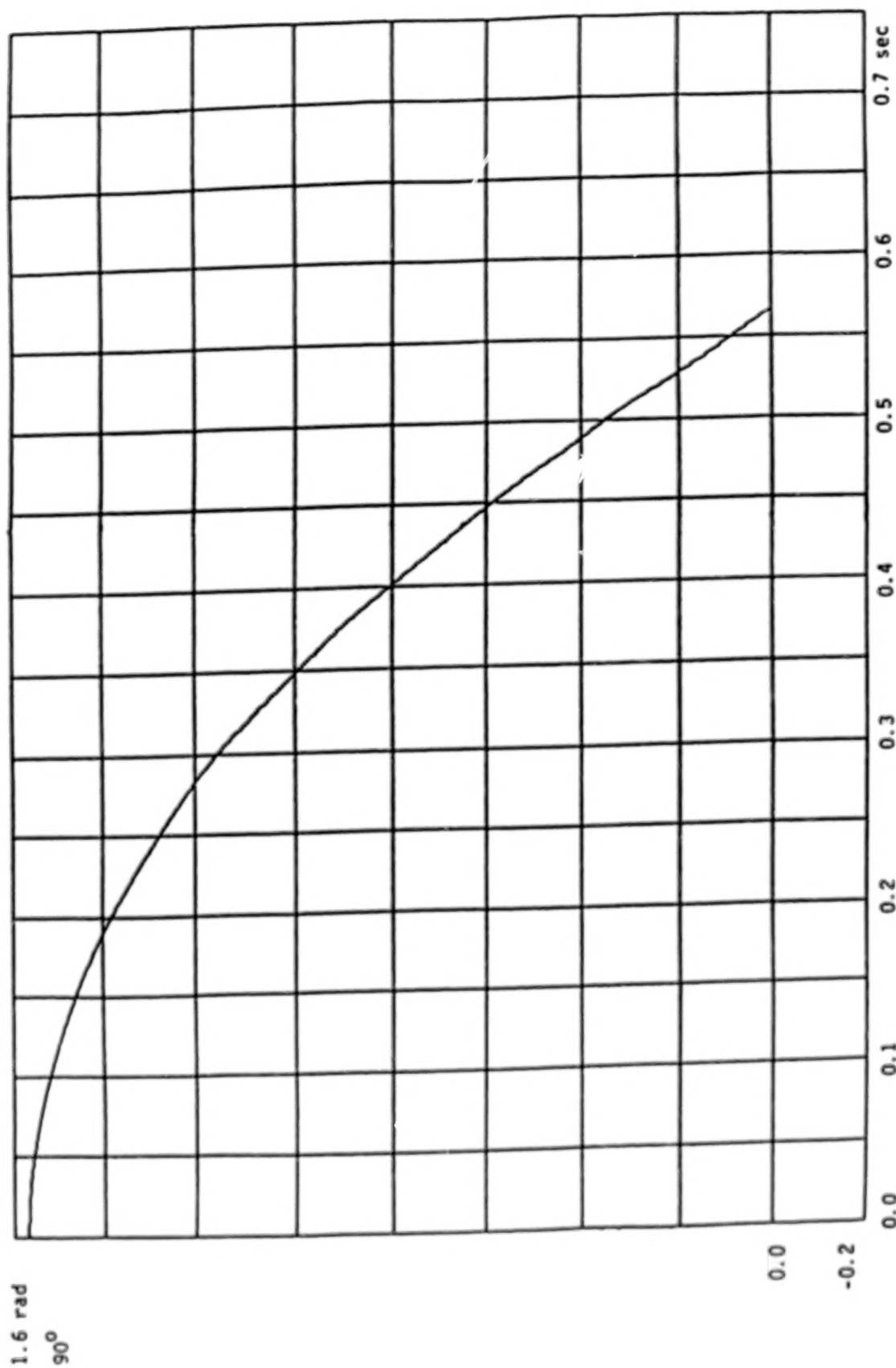


Figure 7. Boom Deployment Angle

ORIGINAL PAGE 19
OF POOR QUALITY

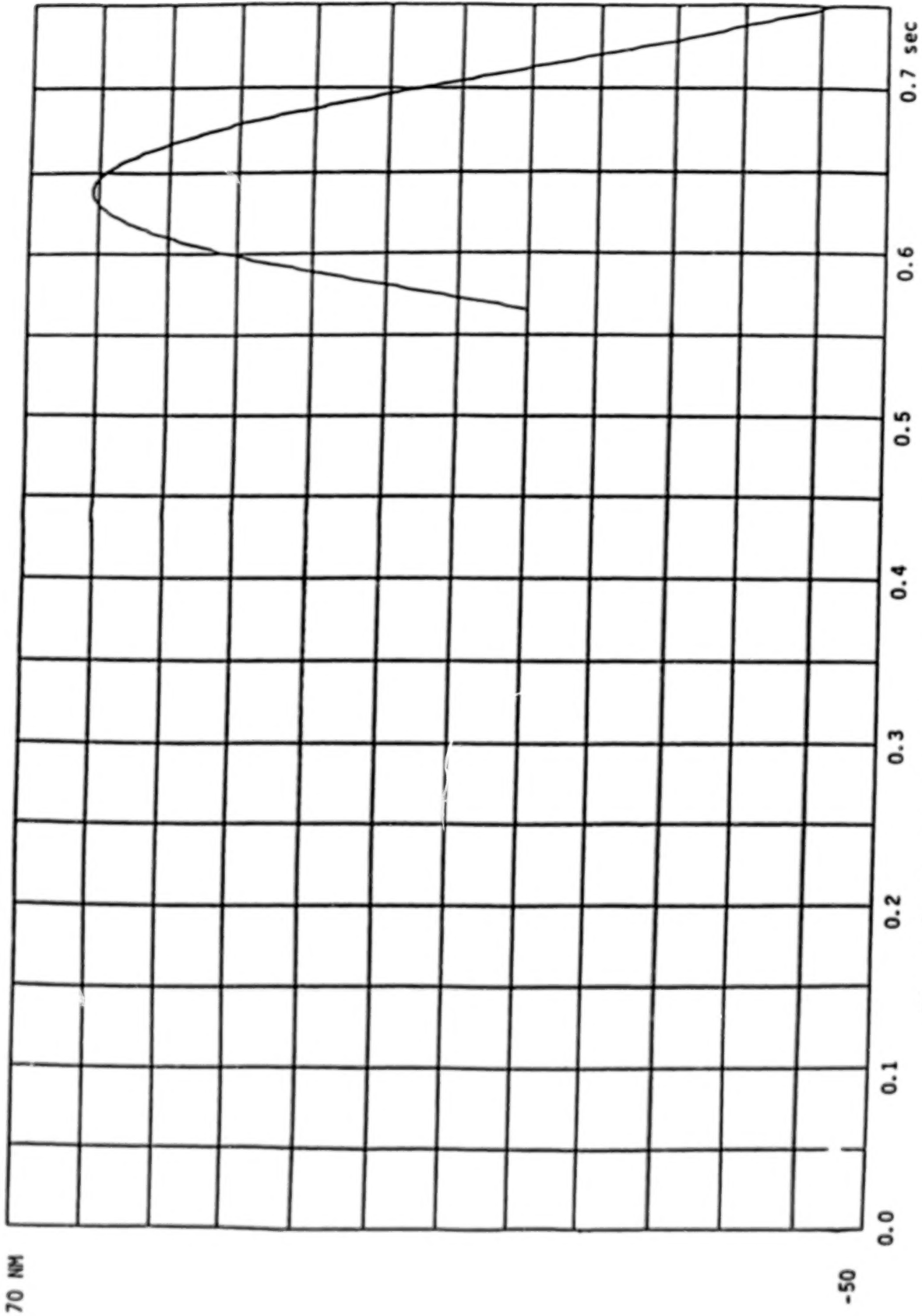


Figure 8. Constraint Torque Normal to Deployment Plane

ORIGINAL PAGE IS
OF POOR QUALITY

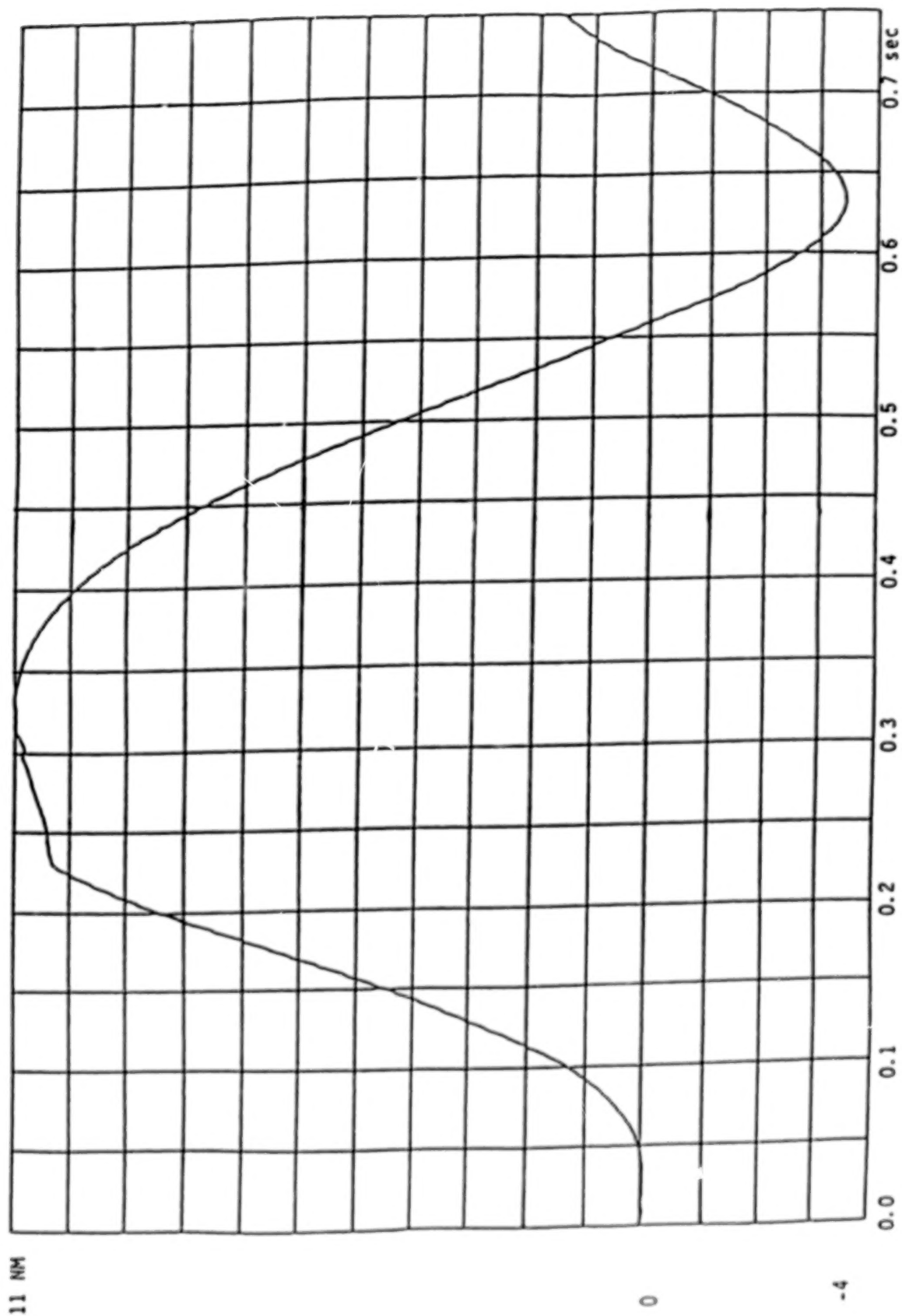


Figure 9. Constraint Torque in Deployment Plane

N84

25082

UNCLAS

DESIGN AND OPERATION OF A DEPLOYABLE TRUSS STRUCTURE

Koryo Miura*

ABSTRACT

A new concept for the one-dimensional deployable truss structure is presented. The deployed configuration of the structure consists of the repetition of an octahedral truss module longitudinally, and thus it is exactly the so-called "geodesic beam" structure. The principal mechanical feature of the truss is that the lateral members comprising the lateral triangular truss are telescoping beams. Contracting of the lateral members results in the deployment of the truss structure. The geometric transformation of this truss of variable geometry is presented. It is shown that both simultaneous and sequential modes of transformation are possible. The validity of the transformation applied to the deployment is verified through design of a conceptual model. This concept of a deployable structure could be a potential candidate for future space applications.

INTRODUCTION

At present, the only established concept for the deployable one-dimensional structure for space applications is the coilable longeron beam. However, a study (reference 1) has shown that the coilable longeron beam (Astromast) is limited to beam dimensions of less than 1 meter because of difficulties in packaging the stowed energy in the beam. For applications that require large beams, deployable beams with hinged longerons or erectable beams must be developed.

Recently, the Rockwell International Corporation and the Vought Corporation studied a number of existing structural concepts for fully deployable beams and platforms (references 2, 3). In spite of these efforts, a satisfactory structural concept which has an advantage over others in every respect has not yet been found. This situation is not changed even if a different set of criteria for selection is used. Under these circumstances, the derivation of new concepts through various possible approaches seems to be beneficial.

The present author has succeeded in devising a new concept for a one-dimensional deployable structure through a unique geometric approach.

*The Institute of Space and Astronautical Science, Neguro, Tokyo, Japan

The concept was verified through a conceptual model. This paper describes briefly the theoretical foundation of the concept, the inherent mechanisms, and the mode of the deployment.

DEPLOYABLE TRUSS CONCEPT

The concept of the deployable truss, which the author proposes herein, is essentially a truss of variable geometry. Figure 1 illustrates a typical example of the proposed concept for the deployable truss structure. The fundamental module of the truss is an octahedral truss composed of a pair of lateral triangular trusses and six diagonal members. The two adjacent modules, which share the lateral truss, compose a repeating unit of the truss. Thus, the repetition of the unit in the longitudinal direction forms the whole structure of the deployable truss.

A part of Figure 1 is enlarged and shown in Figure 2, which illustrates the vicinity around a lateral triangular truss. The details of a lateral member are shown in Figure 3. This member, which is a telescoping beam whose length can vary, contains inside the tubular section an elastic tensile spring that is connected to both ends of the beam. In addition, a latch is installed in the beam to fix its length at the shortest state. Figures 4a and 4b illustrate the purely geometric configuration of the truss in the completely folded and deployed conditions, respectively. Figure 5 shows the almost folded state of the truss.

GEOMETRIC TRANSFORMATION OF THE TRUSS (SIMULTANEOUS MODE)

The outward appearance of the deployable truss shown in the preceding section is known elsewhere if it is a rigid static structure instead of a structure of variable geometry. For instance, in reference 4, that type of truss (geodesic or inverted batten beam) is studied to verify the theory of continuum analogy for large space structures. Actually, this truss is one of the most efficient light-weight structures using the minimum number of component members. In this section, the author shows the geometric transformation by which the truss can be transferred to a compact configuration. With mechanisms installed in the truss as described in the previous section, the truss becomes deployable.

The geometric transformation explained in this section is the mode where the folding/deploying is carried out simultaneously through the whole structure. Let it be called the simultaneous mode transformation.

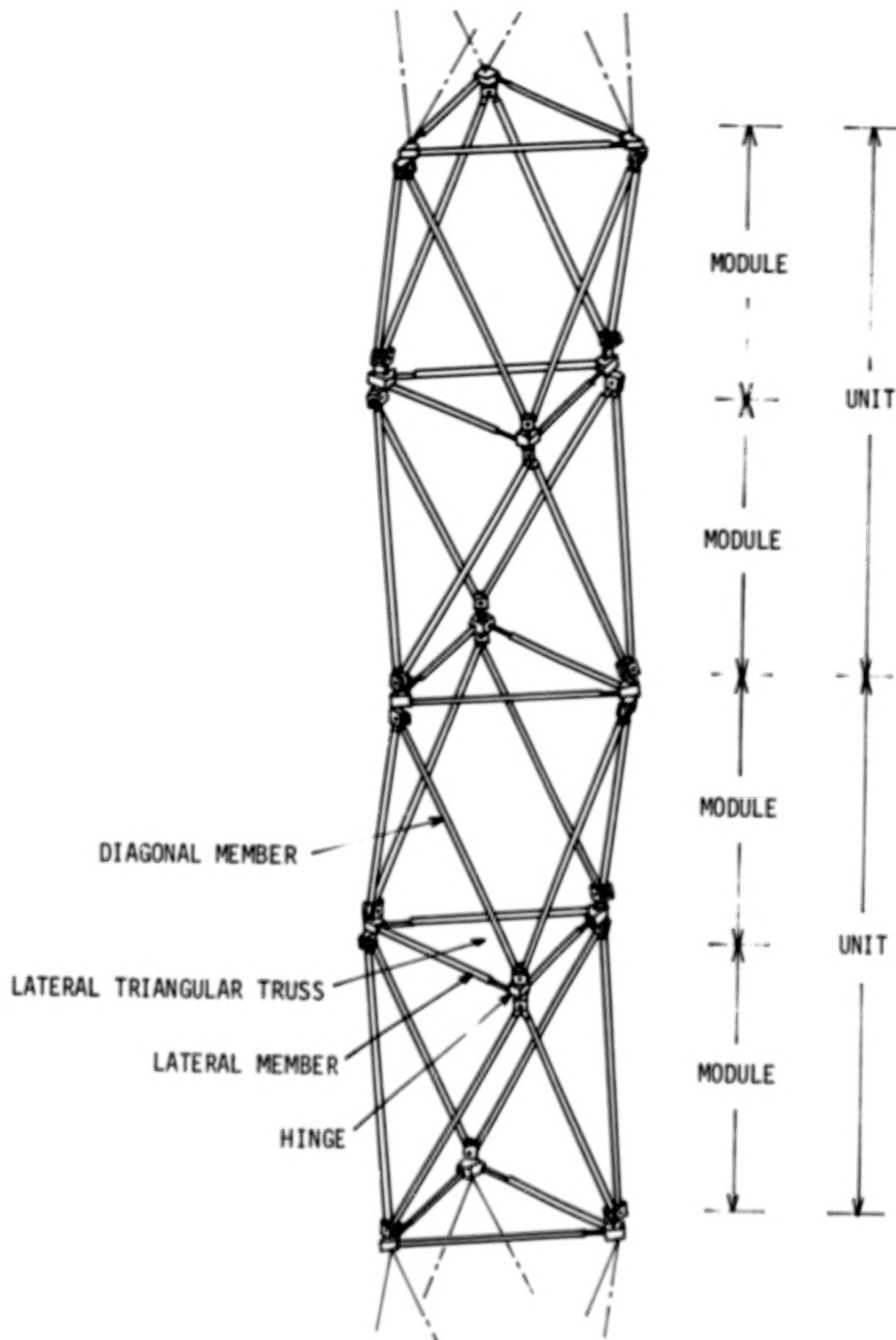


Figure 1. Proposed Concept of Deployable Truss Structure

ORIGINAL PAGE IS
OF POOR QUALITY

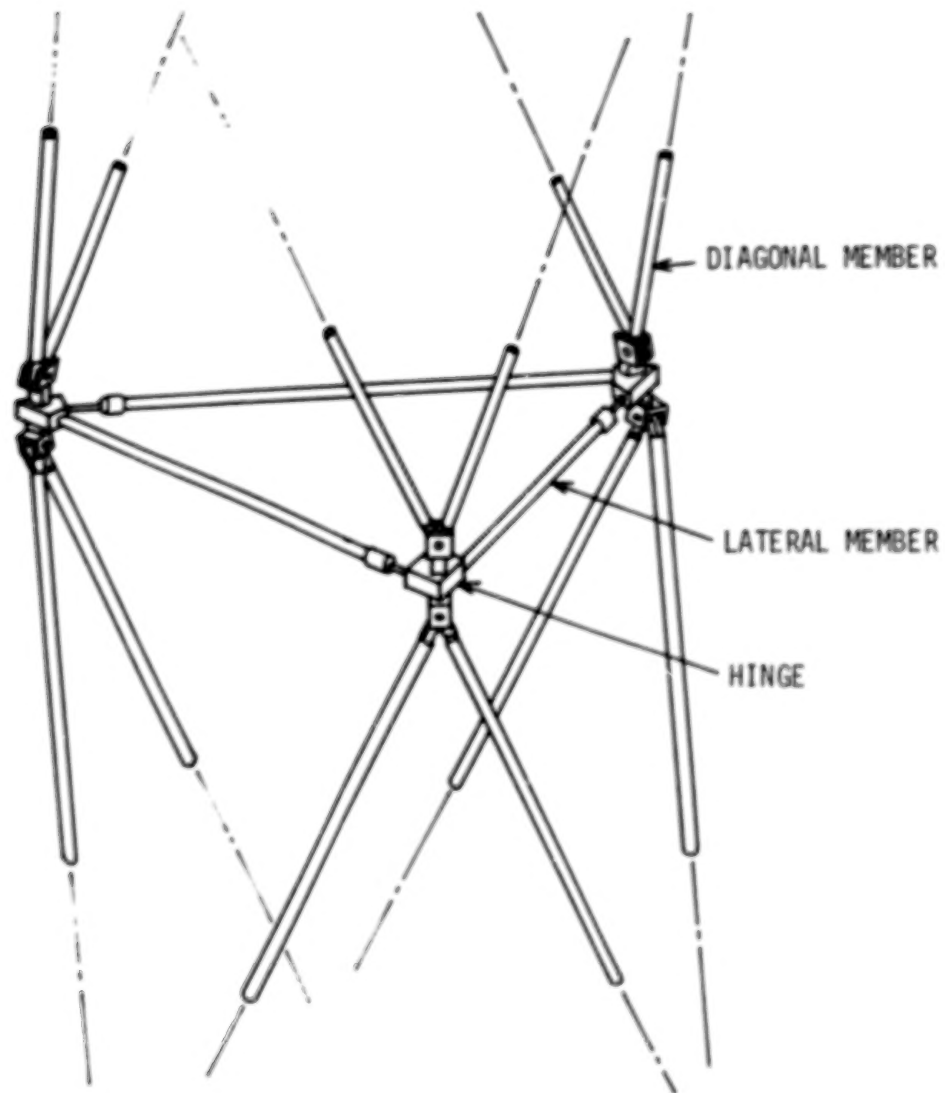


Figure 2. Details of Deployable Truss Structure

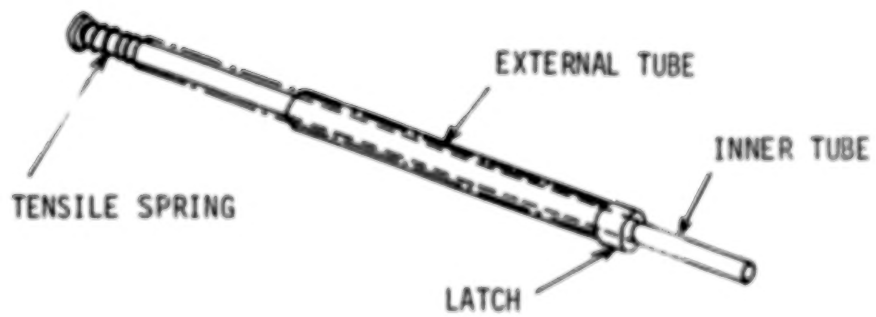
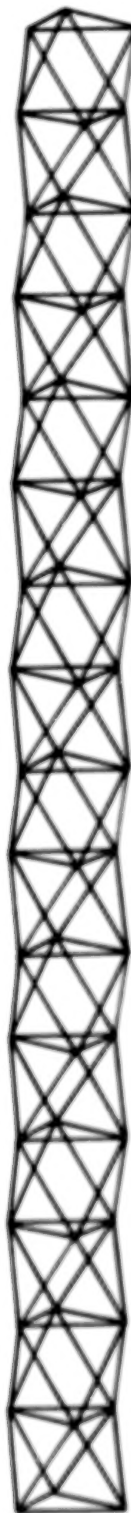


Figure 3. Details of Lateral Member

ORIGINAL PAGE 19
OF POOR QUALITY



(a) Folded



(b) Deployed

Figure 4. Geometric Configurations of Deployable Truss

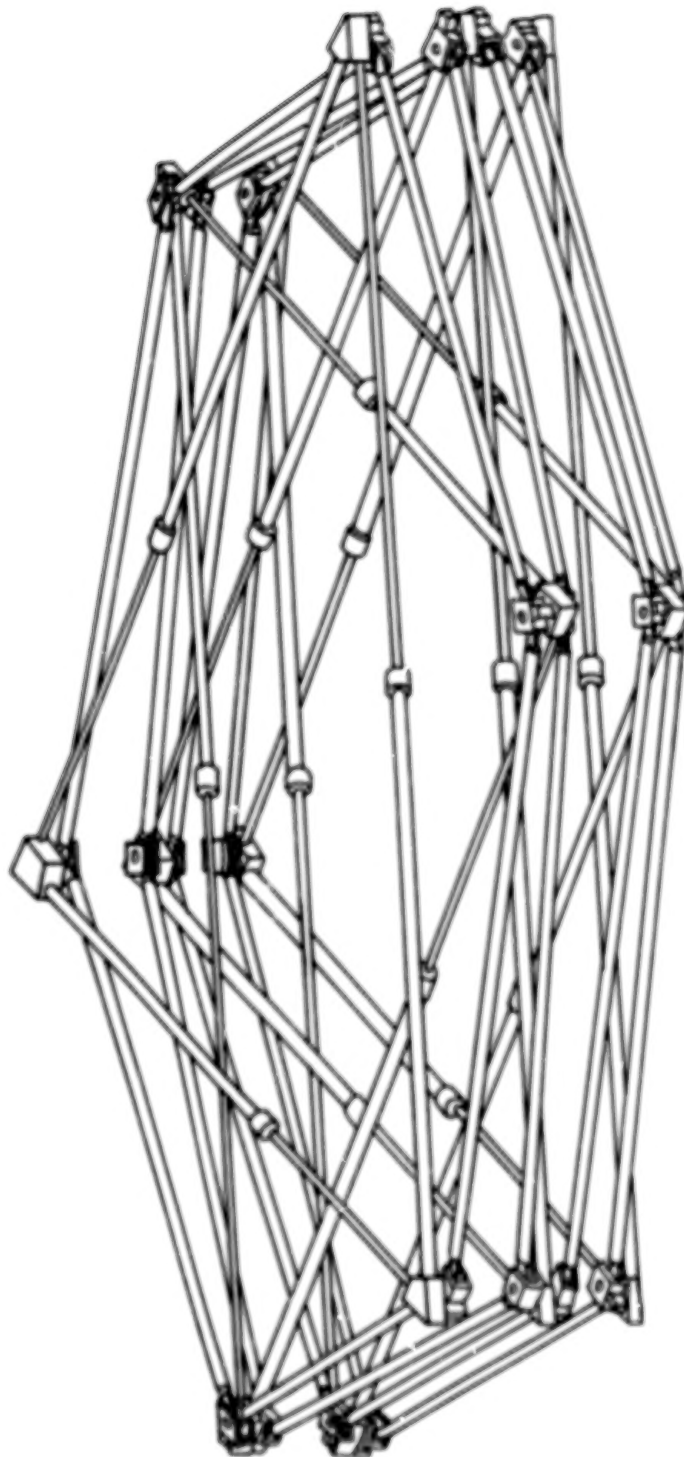


Figure 5. Deployable Truss in Almost Folded State

ORIGINAL PAGE 19
OF POOR QUALITY

Let us consider a single unit that is composed of a pair of octahedral trusses as shown in Figure 6. It is assumed that the lateral triangular truss is regular, the length of a diagonal member is a , and the length of the side of the lateral triangle is b . Then the geometry of the octahedral truss is completely defined by the magnitude of a and b . If a is equal to b , the truss becomes a regular octahedral truss. We shall start with this case and study how the truss is transformed, depending on the relative magnitude of b to a .

As shown in Figure 6a, the face angle between a pair of triangles which compose a concave diamond pattern is taken as 2θ . Then we have

$$\theta = \cos^{-1} (b/2\sqrt{3} \sqrt{a^2 - b^2/4}). \quad (1)$$

For the configuration of Figure 6a, a equals b , and therefore

$$\theta = \cos^{-1} (1/3) = 70.53 \text{ (deg.)}.$$

We are immediately aware that Equation 1 has a nontrivial solution for θ equal to zero. This is the fundamental fact on which the present concept of deployable truss depends. That is

$$\theta = 0, \quad \text{if } b = \sqrt{3} a. \quad (2)$$

The vanishing of the face angle θ means that the height of each octahedral module vanishes, too. In other words, the complete truss is transformed to a flat configuration as shown in Figure 6b.

The proposed concept of deployable truss uses this fact. If we are able to design the lateral member with variable length (i.e., a telescoping beam), we are close to the solution. Let the length of the lateral member vary as follows:

$$a \leq b \leq \sqrt{3} a, \quad (3)$$

then, the height of a module h varies between the limits:

$$\sqrt{a^2 - b^2/3} \geq h \geq 0. \quad (4)$$

ORIGINAL PAGE IS
OF POOR QUALITY

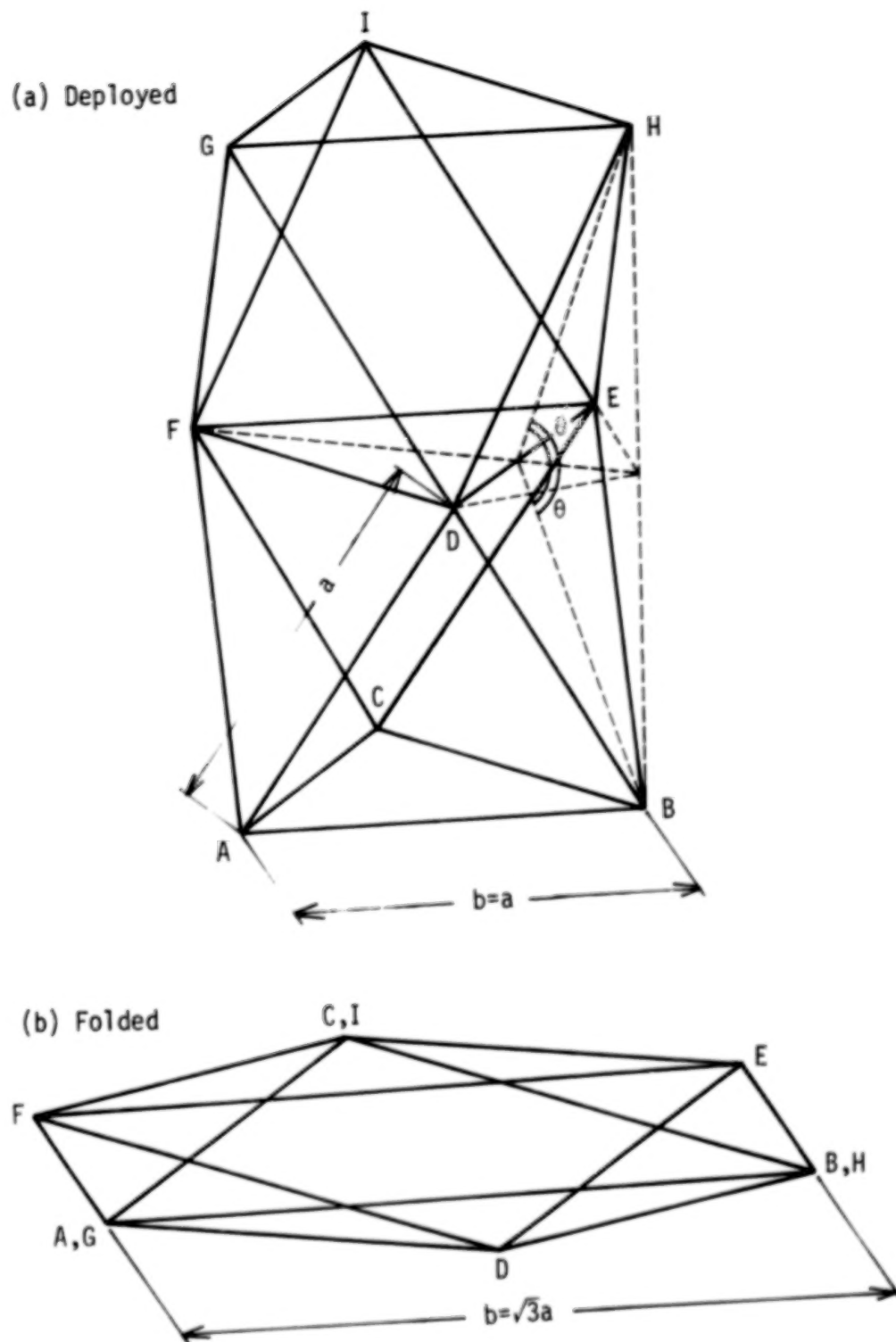


Figure 6. Repeating Unit of Truss

This means that, by extending the lateral members by a factor of $\sqrt{3}$, the height of the truss should vanish.

See Figure 3 for an example of the lateral telescoping member. This member consists of an external tube, an inner tube, a tensile elastic spring inside the tube, and a latch mechanism that is actuated when the member is shortened to a defined length. The diagonal members are fixed length members. Although the hinge mechanism is not shown in detail, it is designed to follow the movement of the truss. Figure 5 shows the shape of the truss at almost fully folded state. This rather strange folding mechanism may be somewhat beyond one's insight. It is easier for one to understand the mechanism through a three-dimensional kinetic model.

GEOMETRIC TRANSFORMATION OF THE TRUSS (SEQUENTIAL MODE)

Theoretically speaking, a geometric transformation in a sequential mode is possible in which each module is deployed successively and other modules remain fixed. Because the sequential mode is important from the point of view of deployment control, we will study that mode in this section.

Figure 7 shows the zone of the truss where the sequential deployment is underway. For clarity of explanation, it is better to divide the whole truss into the following three zones: the deployed zone, the transient zone, and the folded zone. It is assumed that the truss comprises n lateral triangular trusses and $n-1$ modules. The previously mentioned three zones are explained as follows:

	<u>Deployed Zone</u>	<u>Transient Zone</u>	<u>Folded Zone</u>
Lateral truss	1,2,3,.....i-1	i	i+1,.....
Module	1,2,3,.....i-2	i-1, i	i,i+1,...

The important fact is that there exists a geometric transformation which allows the contraction of the i -th lateral triangular truss and the following deployment of the $(i-1)$ -th and i -th modules without interfering with other zones of the truss.

The sequence of motions of the truss, which constitutes the contraction of the i -th lateral truss, is explained as follows: When the i -th triangular truss starts contracting, it is raised from the base and the i -th module starts to deploy. Before that, the $(i-1)$ -th module is partially deployed,

ORIGINAL PAGE 19
OF POOR QUALITY

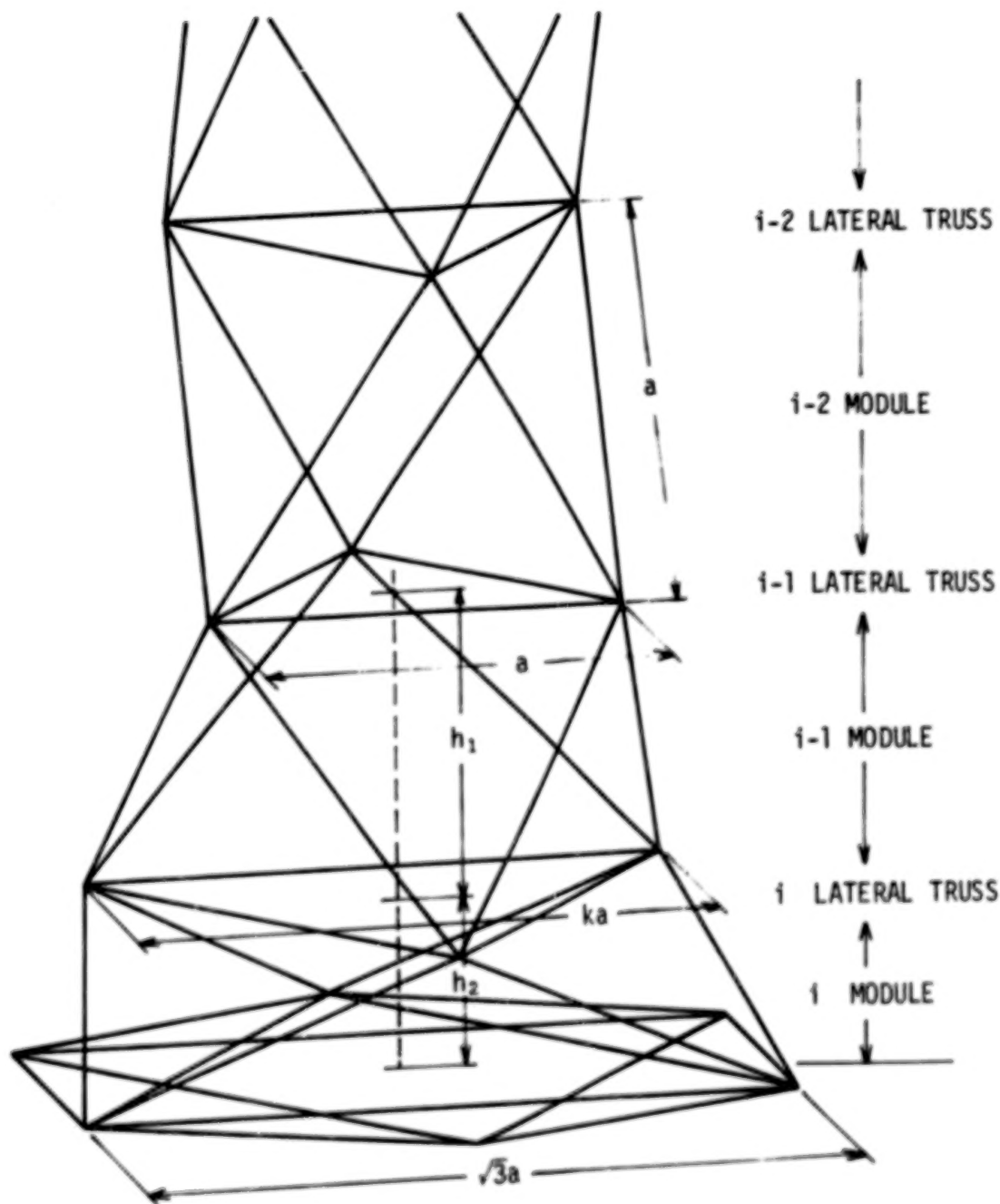


Figure 7. Sequential Mode Deployment

and is continuing to deploy. When the i -th lateral truss finishes its contraction and is latched, the $(i-1)$ -th module completes the deployment. The sequence of this process is illustrated in the series of figures in Figure 8.

The relation between the length of the diagonal member a , the length of the lateral member b , and the height of the module h is obtained easily by using Figure 7. If a and b are connected with the variable parameter k ,

$$b = k \cdot a, \quad \text{where} \quad \sqrt{3} \geq k \geq 1, \quad (5)$$

then, the heights of the modules are

$$h_1 = \sqrt{(2 + k - k^2) / 3} \cdot a, \quad ((i-1)\text{-th module}) \quad (6)$$

$$h_2 = \sqrt{k/\sqrt{3} - k^2/3} \cdot a. \quad (i\text{-th module}) \quad (7)$$

From a practical standpoint, the sequential mode transformation possesses a great advantage over the simultaneous one. This is because in the former case the deploying/folding takes place near the base and thus design of the mechanism is simpler. The outer truss is then always extending from the base as a rigid structure.

CONCEPTUAL MODEL

Although there is no doubt of the validity of the geometric transformations, a model has been constructed to demonstrate the concept. This model, made of acrylic glass tubes and aluminum hinges, is shown in Figure 9. The deployment of the model in a sequential mode is shown in the series of photos in Figure 10. The model works as expected and demonstrates the validity of the geometric transformation.

CONCLUDING REMARKS

A new concept for the one-dimensional deployable truss structure is presented. The deployed configuration of the structure consists of the repetition of an octahedral truss module longitudinally, and thus is exactly the so-called "geodesic beam" structure. The principal mechanical feature

ORIGINAL PAGE IS
OF POOR QUALITY

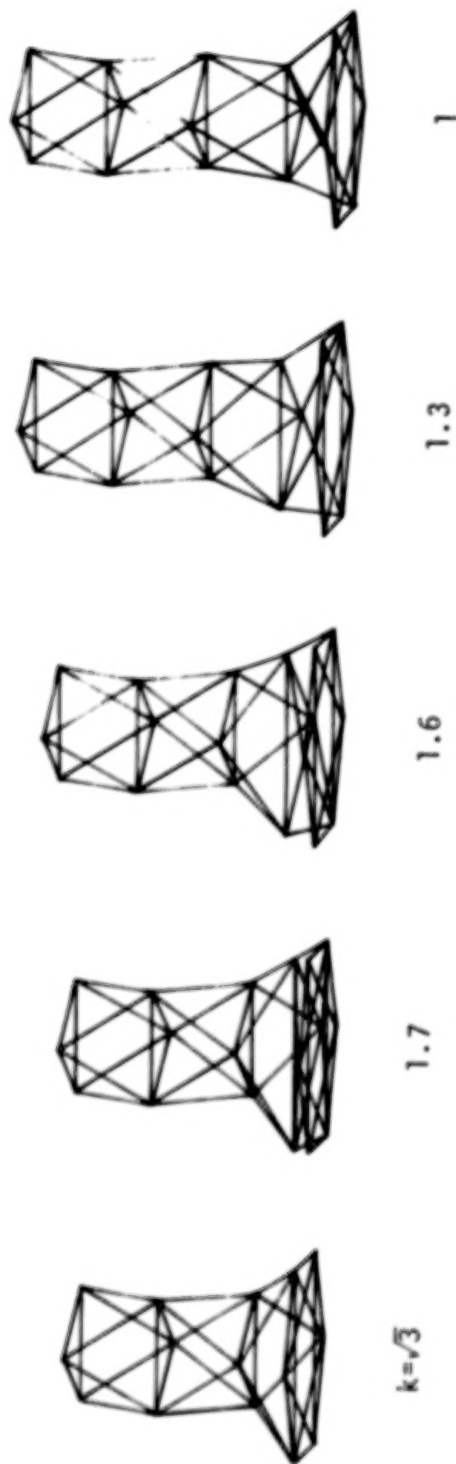


Figure 8. Contracting of Lateral Member and Birth of a Module

ORIGINAL PAGE IS
OF POOR QUALITY

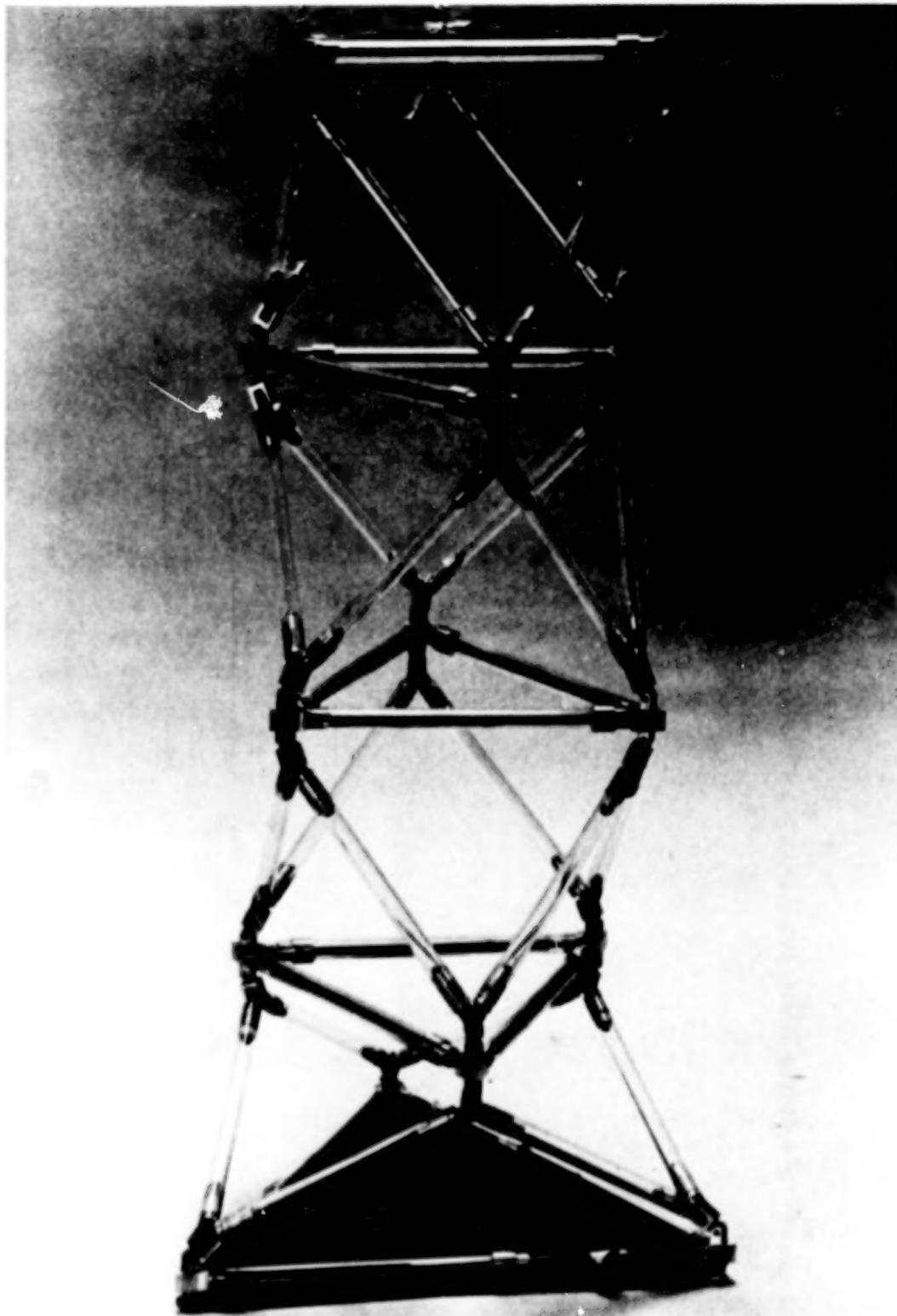


Figure 9. Conceptual Model

ORIGINAL PAGE 18
OF POOR QUALITY

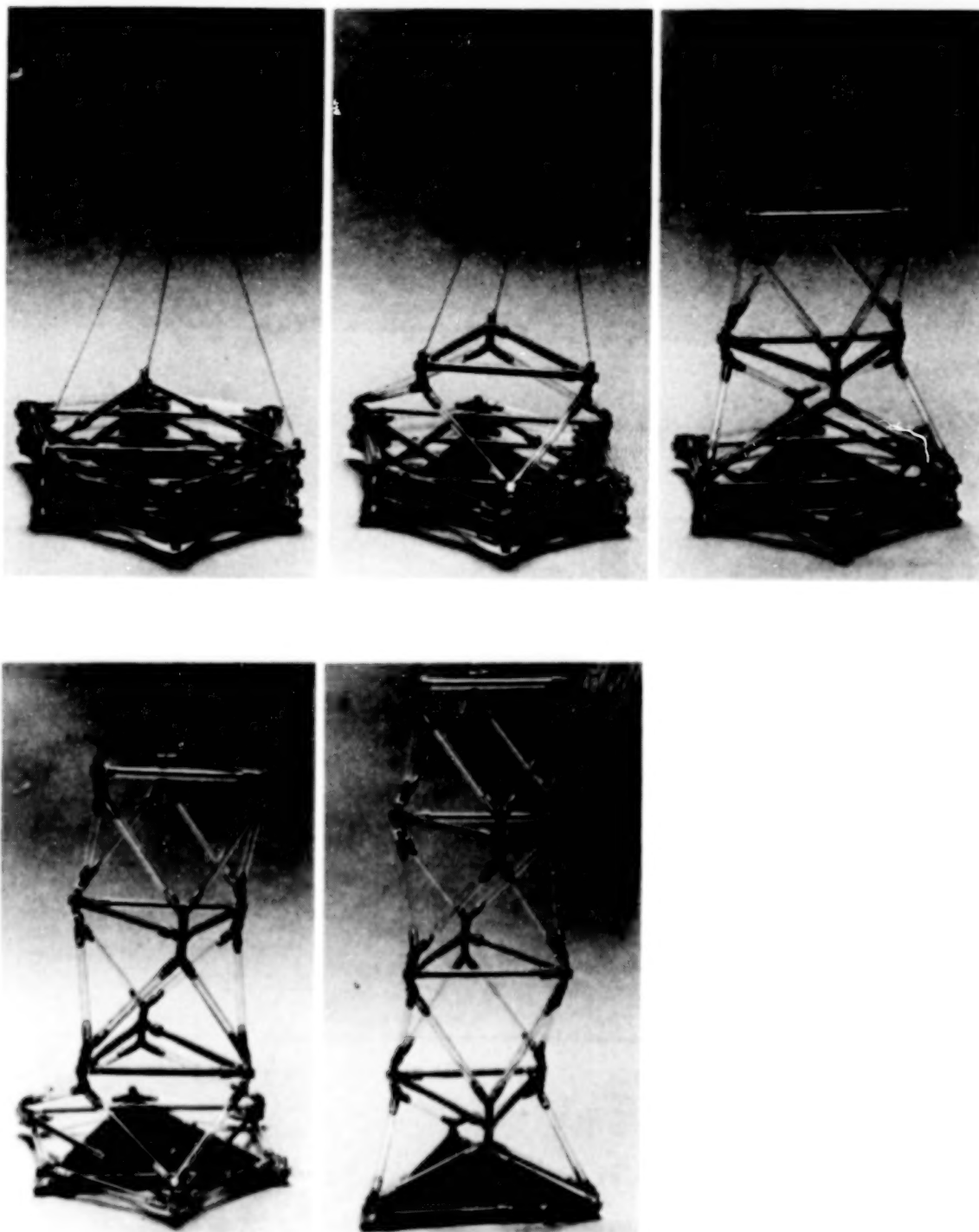


Figure 10. Deployment of Model in a Sequential Mode

of the truss is that the lateral members comprising the lateral triangular truss are telescoping beams. Contraction of the lateral members results in deployment of the truss. The geometric transformation of this truss of variable geometry is presented. It is shown that both simultaneous and sequential modes of deployment are possible. The validity of the concept is verified by means of a conceptual model. Though the study is in its initial phase, this concept for the deployable truss structure seems to have qualities suitable for space applications.

ACKNOWLEDGEMENT

The author wishes to thank to Mr. Kenichi Suzuki of Godo Seisakusho for his contribution in designing the conceptual model.

REFERENCES

1. Mikulas, Martin M., Jr., and Harold G. Bush, "Advances in Structural Concepts, Large Space Antenna Systems Technology - 1982," NASA CP-2269, November 1982, pp. 258-283.
2. Greenberg, H. S., "Development of Deployable Structures for Large Space Platforms," NASA CR-170689, December 1982.
3. Cox, R. L., and R. A. Nelson, "Development of Deployable Structures for Large Space Platforms," NASA CR-170690, December 1982.
4. Noor, A. K., M. S. Anderson and W. H. Greene, "Continuum Models for Beam- and Plate-Like Lattice Structures," AAIA J., 16 (12), December 1978.

N84

25083

UNCLAS

DESIGN AND TEST OF A LOW-TEMPERATURE
LINEAR DRIVER/RATE CONTROLLER

Charles H. Lowry

ABSTRACT

This paper describes the design and testing of a force/rate control device used to deploy an Earth shield on an orbiting satellite/sensor. Test experience, failure modes, and applications are emphasized.

INTRODUCTION

The Teal Ruby Experiment (TRE) involves an Earth-orbiting infrared sensor. The TRE program, which is being carried out by Rockwell International Corporation, Space Transportation and Systems Group, is sponsored by the Defense Advanced Research Projects Agency and managed by the Department of the Air Force, Space Division Headquarters. The P80-1 spacecraft provides a stable orbiting platform for the TRE sensor.

The objectives of the TRE are: (1) to demonstrate that cooperative aircraft can be detected from space with an infrared-type sensor, (2) to establish a global database in several infrared spectral bands that will be useful in defining future space surveillance systems, and (3) to demonstrate mosaic infrared sensor technology in space.

The TRE sensor mosaic focal plane detects infrared energy radiated to space from the Earth in discrete spectral bands. The focal plane and interior optics of the telescope are cooled to cryogenic temperatures by a solid cryogen system that is integral to the sensor assembly. Three electronic boxes mounted on the P80-1 spacecraft functionally support the sensor assembly. Figure 1 shows the TRE mounted on the P80-1 spacecraft.

Figure 1 also shows the Earth shield, which is used to intercept infrared energy and reflected solar radiation from the Earth's surface and to protect the sensor from this heat load. The Earth shield is stowed during launch and until final orbit is achieved. Then, on command from the Earth, a pyro device releases latches and permits the Earth shield to pivot into its deployed position (Figure 1).

This paper describes the mechanical system designed and provided for deployment of the relatively large, lightweight TRE Earth shield; and discusses the advantages of this design and how it could be profitably used in other applications.

ORIGINAL PAGE IS
OF POOR QUALITY

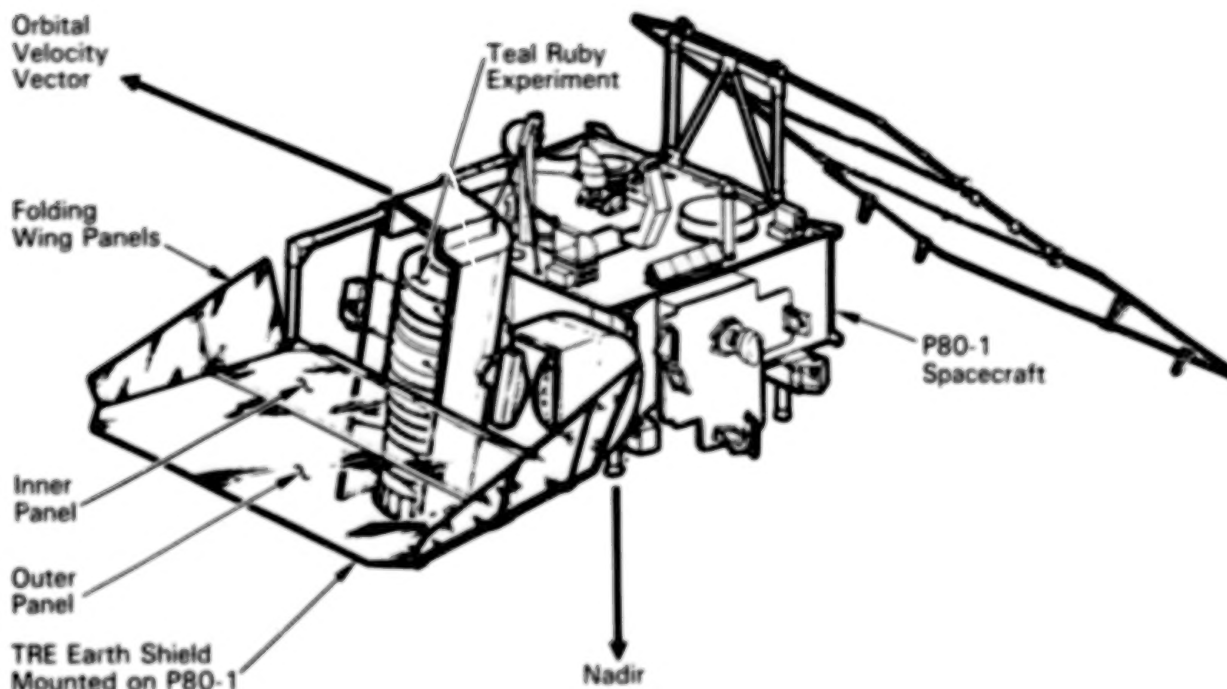


Figure 1. Teal Ruby Experiment with Earth Shield

Single (one-shot) deployment of mechanical and structural devices/members in space often requires a one-way drive mechanism coupled with a rate control device to move deployables into operating position while simultaneously controlling dynamic loads. The drive mechanism must be simple, reliable, and capable of providing the required force with an adequate margin throughout a prescribed temperature range. The rate controller must operate effectively and reliably throughout this temperature range while it limits velocities and loads in the system. Gases or fluids must not leak out, because the device would become ineffective and could contaminate surrounding hardware.

As the United States Space Program moves toward large space platforms, more requirements that involve deployment of basic structural members, antennas, and solar arrays will appear. Therefore, more attention will be focused on driver/rate controller devices. Standardization of concepts, if not standardization of specific designs, could result. To distribute loads and make deployment systems more failure tolerant, several of these devices may be used in parallel in a typical application.

The device described in this paper is a low-temperature, linear driver/rate controller (LDRC) that has been tested and proven effective in controlled deployment applications. The LDRC employs a compression spring for storing energy and a unique welded bellows system to prevent leakage of the low-pressure gas used in the orifice system. Through use of metal bellows and welds in all pressurized joints, it provides a hermetically sealed container

that is without the conventional static or dynamic seals that can become potential leak paths. Further, positive pressurization of the device is verifiable up to the time of launch through use of an external mechanical indicator.

Specific design features in the device, methods of simulating zero-g testing, test results, problems encountered, problem resolutions, and performance data are all topics that are discussed in this paper.

DESIGN REQUIREMENTS

The LDRC was designed to deploy a specific Earth shield from its stowed position to its fully deployed position within a prescribed time period and without inducing excessive loads. Specific design requirements that influenced the chosen concept included the following:

- For redundancy two independent but identical LDRC's will be used.
- The initial deployment force in the stowed position will be 18 kg (40 lb) maximum. Upon release, the LDRC will linearly stroke 11.7 cm (4.62 in.). The final force at the end of a stroke must be at least 3.7 kg (8.2 lb).
- Stroke time will be 3.0 sec minimum and 15 sec maximum. If one LDRC loses its damping capability, the other one will ensure proper system performance.
- Positive prevention of leaks will be emphasized in the design.
- The prescribed volume envelope will be met, and weight will be minimized.
- Dynamic performance will be in accordance with Figure 2.
- A pressure indicator will be provided to verify that no leakage of damping fluid has occurred just before launch.
- A tracer fluid will be used for leak testing on the ground.
- The operating temperature range will be from 380°K to 172°K.
- The device will meet these requirements after exposure to boost dynamics and acoustics.

DESIGN

The design concept chosen involved a basic spring thruster and viscous damping. A gaseous fluid was chosen because of its relative insensitivity to temperature and because of the system elasticity it provides.

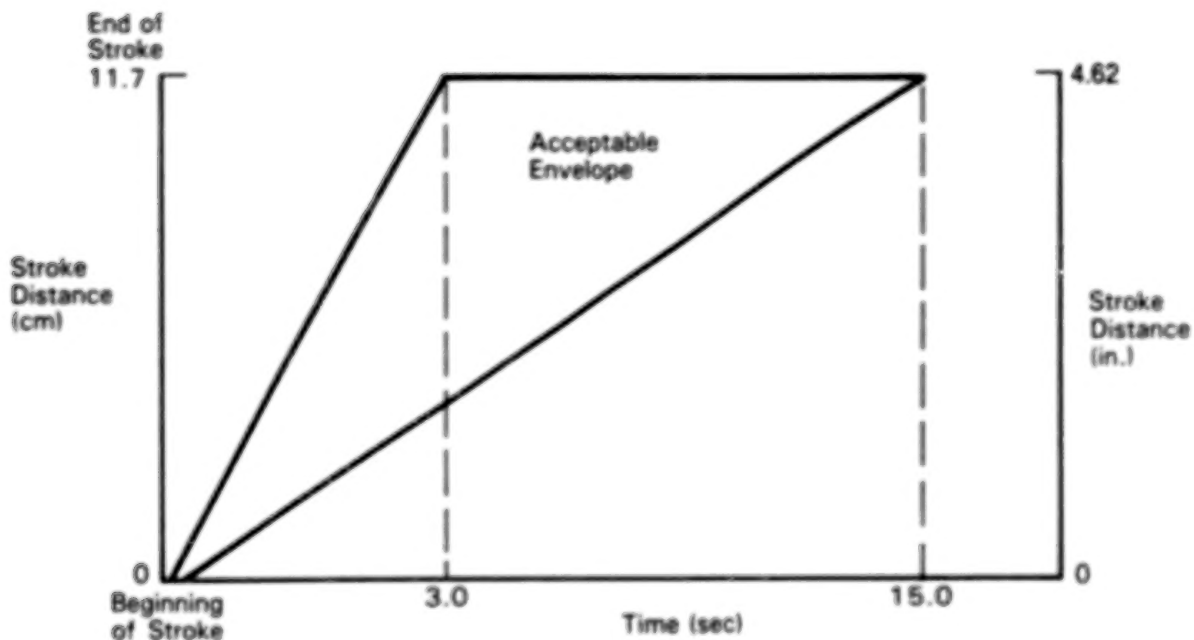


Figure 2. Acceptable LDRC Operating Dynamic Envelope

Leakage of this fluid was a major concern because of possible contamination and also because of changeout and retesting of the actuator, if carried out during critical system environmental testing or late in the sensor check-out and prelaunch phase, would cause schedule delay. Therefore, a totally enclosed, low-pressure gas system, hermetically sealed by welds, was chosen. Conventional static or dynamic seals were not required to maintain the gas in the device. Metal bellows were employed to contain the damping fluid while they allowed the actuator to stroke. The spring thrust system that was chosen is unique because it uses the metal bellows to supplement the force produced by the main thrust compression spring to produce a resultant force versus stroke curve ideal for this application (i.e., high force at the beginning of a stroke, tapering down to the prescribed holding force at the end of a stroke.)

Figure 3 shows the designed of the LDRC device for this application in its relaxed or deployed position. For installation in the stowed Earth shield, the main thrust spring is compressed when the retraction rod is pulled to the left. A latch device is not provided, because the LDRC is held in this position by the stowed Earth shield. A separate pin-puller latch system is provided elsewhere on the Earth shield to initiate deployment and allow the LDRC to stroke.

The LDRC is made up of the following principal parts and constituents:

- Main thrust spring
- Bellows

ORIGINAL PAGE 19
OF POOR QUALITY

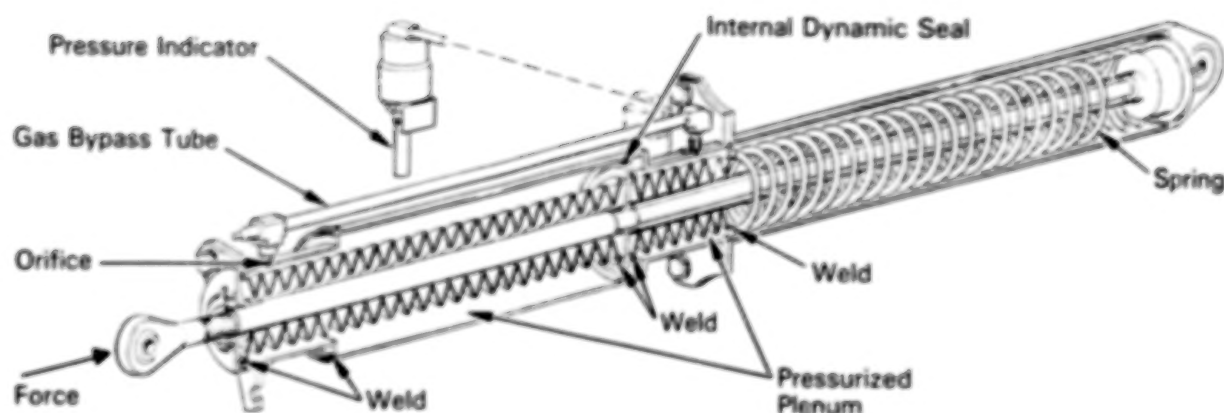


Figure 3. Linear Driver/Rate Controller

- Orifice
- Piston
- Gas
- Pressure indicator
- Housing
- Retraction rod

The main thrust spring is contained in a separate, removable part of the housing to facilitate assembly and to provide access to the spring. This feature allows changeout to a stronger or weaker spring to be carried out as requirements change. Provisions were also made to accommodate dual, nested coil-springs, should they be needed. Tests of the system verified the adequacy of the present spring, whose performance is shown in Figure 4.

The bellows, which were the most challenging aspect of the LDRC design, were the only area in which failures were experienced. The bellows supplier's analytical methods indicated that the critical parameter in this application would be bellows tension loads, and a configuration was established. The bellows were initially made from AMS 350 stainless steel. After several failures, more convolutions were added to both bellows, the heat-treated length was modified, and the material was changed to Inconel 718. These measures were aimed at reducing stress. The heat-treated "free" length is important to the establishment of desired spring force characteristics and to the control of tensile stress in the bellows. The primary failure mode in the bellows involved excessive tension, which is further discussed in a later section.

Installation of the bellows in the LDRC is shown in Figure 3. Each attachment of the bellows is done through tungsten inert gas (TIG) welding.

ORIGINAL PAGE IS
OF POOR QUALITY

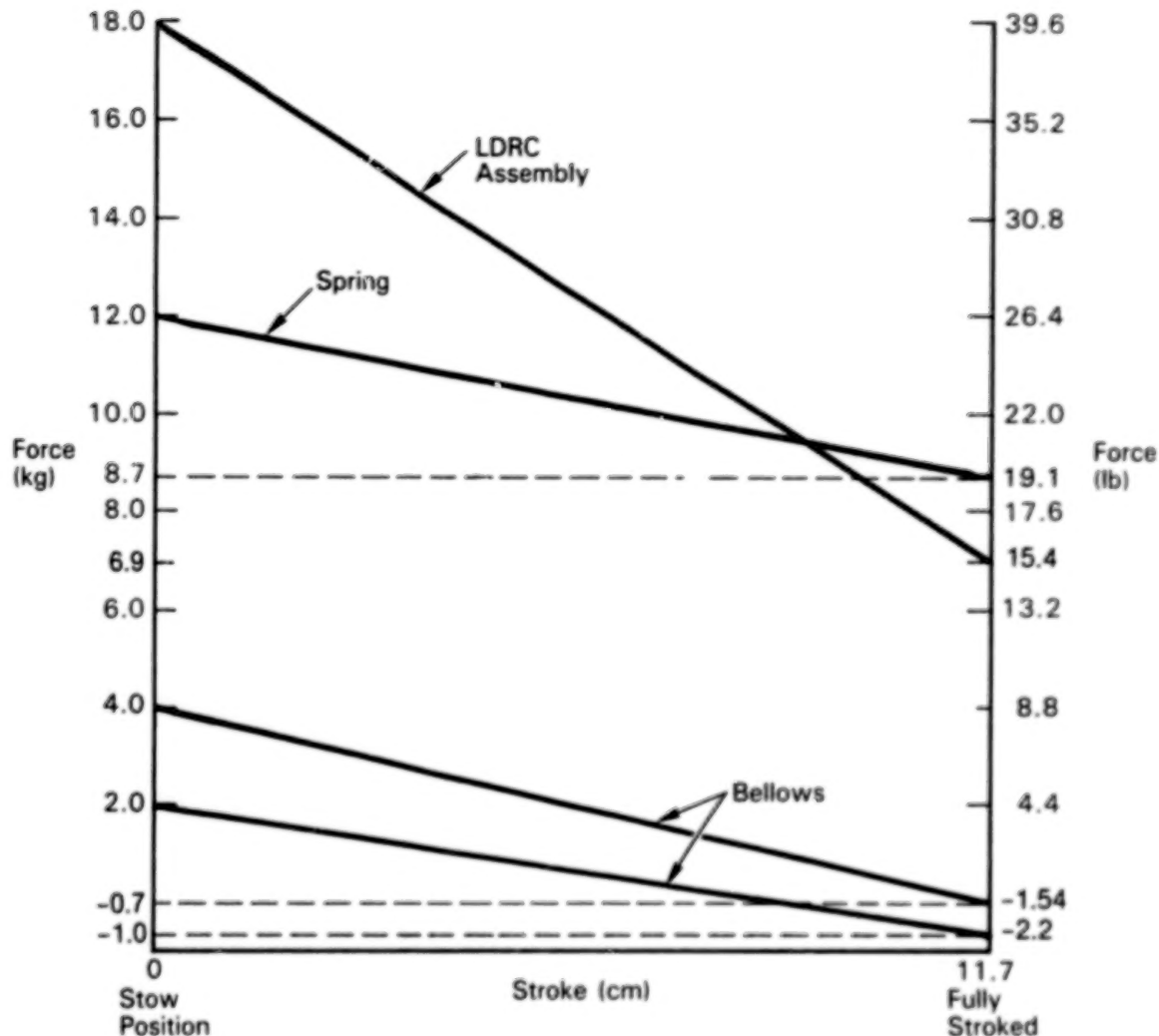


Figure 4. Force Versus Stroke Envelope

All weld joints are identical, so that weld schedules are uniform. Welds are verified by pressure leak testing at subassembly level. No leaks were experienced in this testing by any of the units fabricated.

The thrust contribution of the bellows is shown in Figure 4. Although one of the bellows is compressed and the other bellows are extended through actuation of the LDRC, both have similar force/stroke curves. Both provide opposing forces to the spring system near the end of a stroke. This is governed by the position in which the bellows are held during heat treating, which establishes the "free" length of the bellows.

The size of the orifice controls the damping force. (The orifice is a simple drilled hole in an orifice plate.) Dual orifices could have been provided for redundancy, but this design was not adopted because it would

have resulted in extremely small orifices. The location of the orifice in this application was selected because it was necessary to have changeout capability in the event that performance requirements changed. Thus the orifice is located in an exterior porting system, as shown in Figure 3. Installation of the orifice directly into the piston is desirable because it minimizes the vulnerability of the exterior porting system.

The piston shown in Figure 3 is rather inert; it contains only an omniseal for sealing between bellows chambers that are internal to the hermetically sealed system. Any leakage that occurs at this seal during actuation is considered repeatable and accounted for in performance testing of the LDRC. In other applications, as indicated previously, it may be advantageous to incorporate the orifice in the piston.

The damping gas chosen was 95 percent dry nitrogen and 5 percent helium. Nitrogen was chosen because it is relatively dense, inert, and inexpensive. The helium is used in postmanufacturing checkout and leak check. The system is pressurized at a 2-atmosphere gage reading, which provides a gas density sufficient for efficient damping but at a pressure low enough to avoid stressed joint problems.

A pressure indicator such as that shown in Figure 3 was provided for long-term monitoring. This device is essentially another bellows that can be monitored periodically against a fixed, go/no-go scale just before launch.

The housing is primarily made up of simple, turned parts. Aluminum is used in the spring thruster housing, but steel is used in those areas where welding is necessary.

The retraction rod and the mounting interface on the other end of the LDRC are equipped with spherical bearings to facilitate alignment during actuation.

ANALYSIS

The design and performance capability of the LDRC was largely verified by analysis. In addition to the usual static stress analyses, a versatile dynamic model was constructed to demonstrate the kinematics of the Earth shield panels, the force history of the LDRC, and the time history of deployment. This model can accommodate a family of orifice diameters, spring rates, initial gas pressures, and piston diameters.

From a loads standpoint, the key parameter is the panel deployment velocity at the end of a stroke, which produces impact loads as the panels drive into their stops. By variation of the orifice and spring parameters, a final design configuration was established. The only uncertainty was the precise orifice diameter, and finalization of this parameter was relegated to development testing of the LDRC in a system simulator.

ORIGINAL PAGE IS
OF POOR QUALITY

Figure 5 shows a deployment history of the two main panels of the Earth shield. It can be seen that the outer panel has a major influence on the behavior of the inner panel and the LDRC. The outer panel is released from its stowed position, which allows the LDRC to begin its stroke. The outer panel pivots around the top of the inner panel, driven by spring-driven hinges. As the inner panel is deployed by direct force from the LDRC, the outer panel completes its excursion to its hinge-stop position. This maneuver kicks energy back into the inner panel and thus into the LDRC, driving them temporarily in a reverse direction. This can be seen in Figure 6, which shows the inner panel stroke history. This analysis was useful in varying parameters to ensure that all such perturbations were damped out before the system approached its stops, enabling the system to avoid high-impact loads and rebounds. The LDRC displacement and force history curves shown in Figure 7 reflect this action. As the LDRC is driven backward, damping becomes effective in that direction, also.

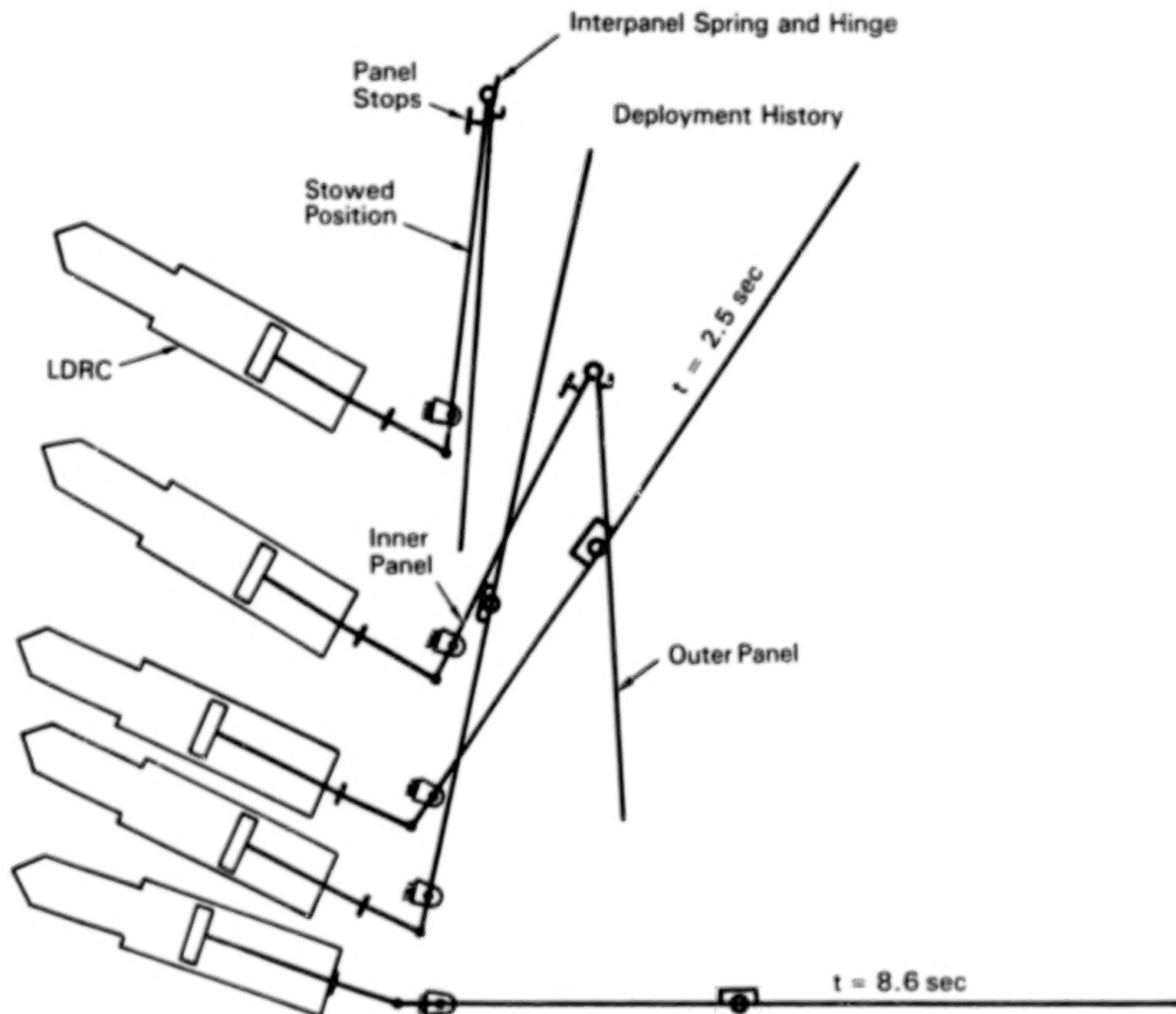


Figure 5. Earth Shield Deployment History

ORIGINAL PAGE 13
OF POOR QUALITY

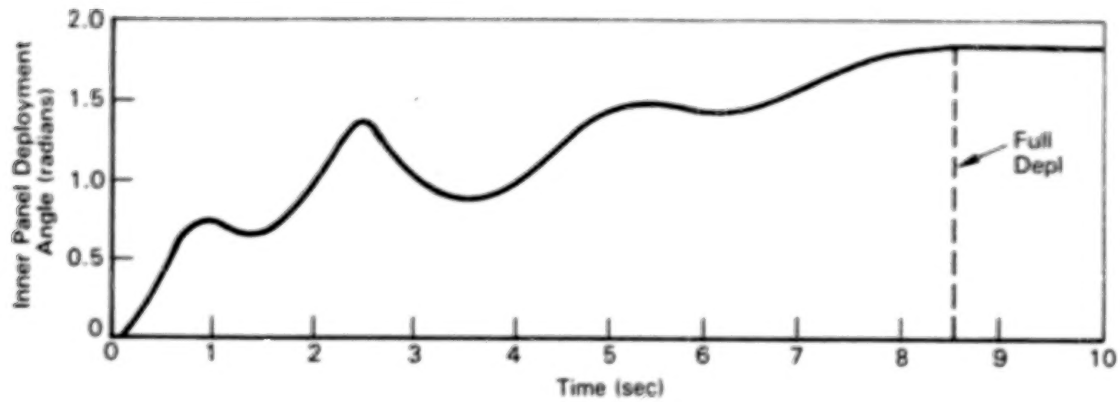


Figure 6. Inner Panel Stroke History

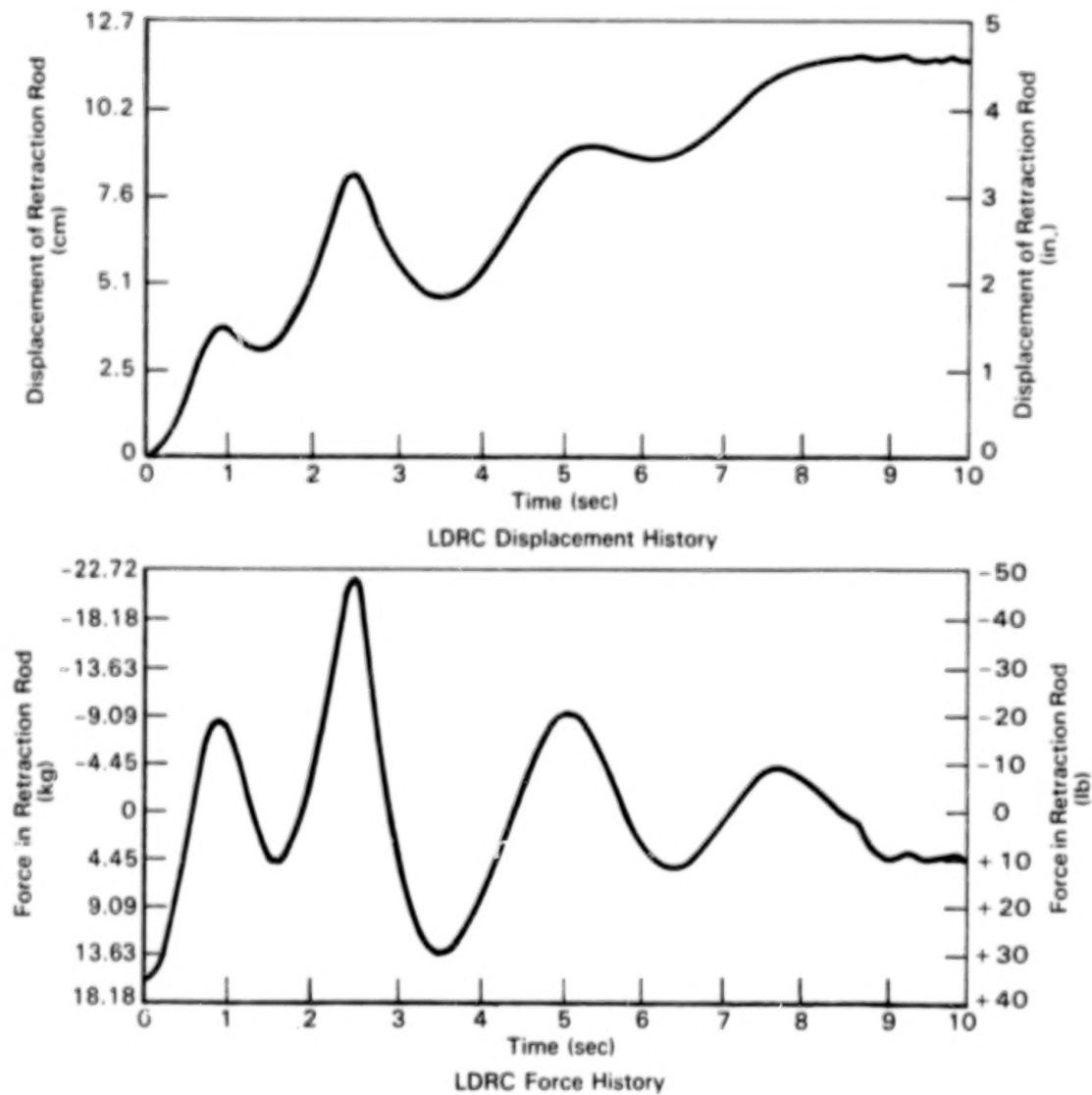


Figure 7. LDRC Displacement and Force History Curves

After system level testing was completed, the analytical model was verified to be representative of actual system behavior. The only variable that changed after the analysis was completed was the orifice diameter.

TESTING

The only development testing carried out involved a series of tests performed with a complete LDRC. No lower level assembly tests were run. The development tests were run with different LDRC orifice diameters at operating temperature extremes. The LDRC was linked to a two-beam panel simulator on an air-bearing table. The beams were mechanized like the main Earth shield panels, with the proper hinges, springs, and stops, and were representative of the mass and moment of inertia of one half of the Earth shield panels. They were supported by the air-bearing table in such a way that they could be deployed in a plane that was parallel to the table top in a relatively frictionless manner. This kind of test was used to minimize the effects of 1-g force. As a result of these tests, the final orifice configuration was established as a 0.5-mm (0.020-inch) diameter drilled hole, and overall LDRC performance with a simulated panel system was verified.

Other testing that was accomplished included acceptance testing of each unit built and qualification testing of two units. Test environments were characterized by random vibration and thermal cycling. Life cycling and extensive leak testing were also carried out.

The only test failure encountered occurred during thermal vacuum testing, when a crack in one of the bellows allowed leakage of the damping gas. A failure analysis was performed, which led to the conclusion that the bellows were structurally inadequate, and the failure mode was low-cycle fatigue. (This failure mode results from continuously cycling the bellows under loads in which the local elastic limit is exceeded.) A crack that starts during this testing will propagate with the number of cycles completed. The bellows tested had undergone approximately 300 cycles.

The bellows, which consist of a series of stamped-out disks with holes in the center, have outside and inside diameter (ID) surfaces that are welded as shown in Figure 8. As the bellows are extended, a load is produced at the weld that tends to pry the weld bead apart or to fail the disk in bending at the edge of the weld. The level of stress produced depends on the materials and the deflection from the heat-treated position. As shown in Figure 8, the pressure on the outside of the bellows aggravates the load condition at the (ID) welds.

The leaking bellows were sectioned and examined. Cracks were observed in numerous locations along the heat-affected zones in the disks. See Figure 9 for a view of the interior of the bellows, where the leak area is identified. Figure 10 shows a view of the heat-affected zone, and multiple cracks that have not yet become leaks are visible there. Figure 11 shows a cross section of the weld area where a crack is located that has progressed through approximately 20 percent of one of the disks.

ORIGINAL PAGE 13
OF POOR QUALITY

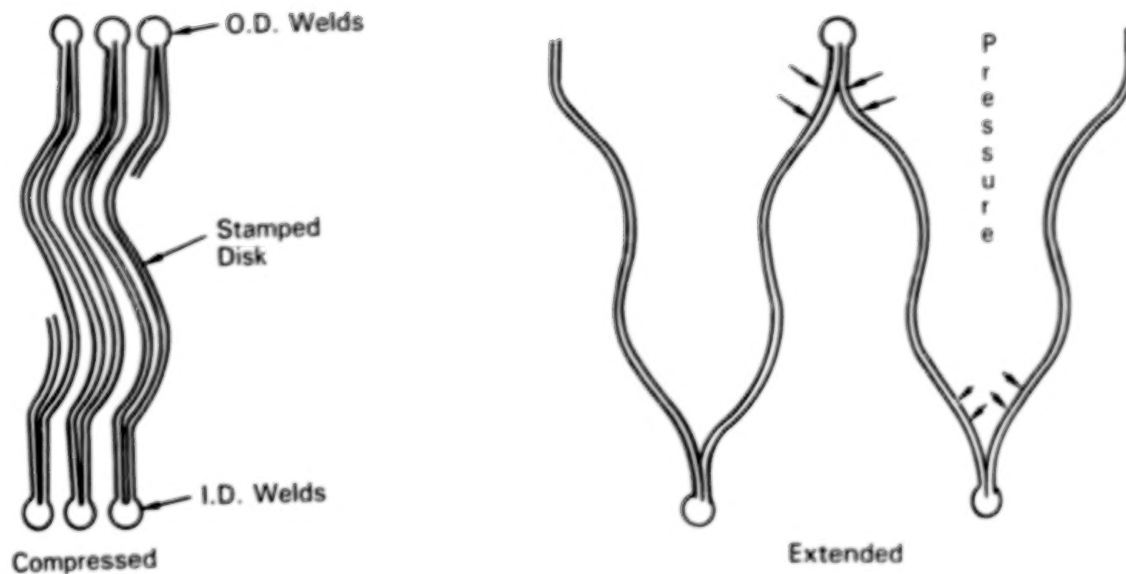


Figure 8. Bellows Cross Section (Not to Scale)

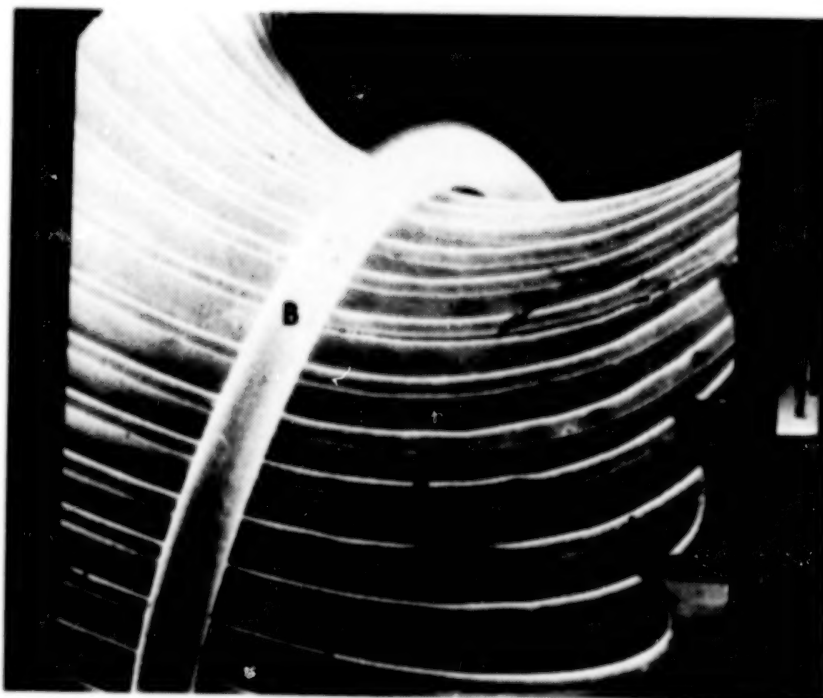


Figure 9. SEM Photomacrograph Showing: A) The Main Leak, B) A Wire Used Only to Hold the Bellows in Place, C) An Artifact

ORIGINAL PAGE IS
OF POOR QUALITY



Figure 10. SEM Picture Showing: A) The Main Crack, B) Secondary Cracks, C) The Weld Bead

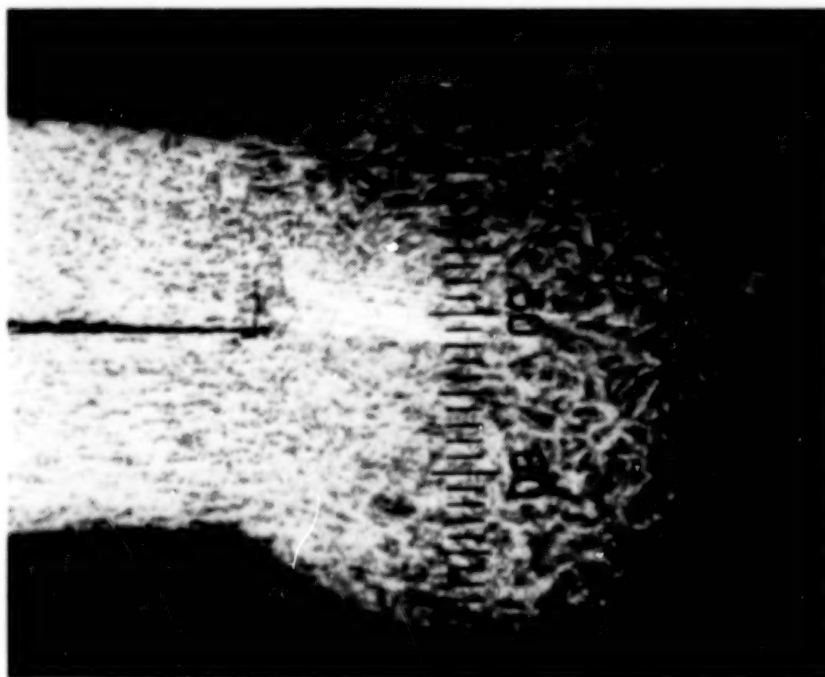


Figure 11. Photomicrograph Showing a Fatigue Crack Starting at the Crotch of the Weld Bead. Note Uniformity in Plate Thickness and Weld Bead (Each Increment Equals 0.00023 Inches)

ORIGINAL PAGE 19
OF POOR QUALITY

As discussed earlier, the solution to this problem involved adding more convolutions to the bellows, heat treating the finished bellows to a prescribed length, and changing the bellows material to Inconel 718. Tests to date have verified this fix.

CONCLUSIONS

The LDRC described in this paper offers a simple solution to a classic mechanical deployment problem. This device, which controls time-to-deployment, end-of-stroke velocities, and end-of-stroke holding force, is relatively insensitive to temperature changes and can function at extremely low or high temperatures. With proper bellows selection, leakage of the damping fluid is not a credible failure mode.

Larger or smaller versions of the LDRC can be used in a number of applications where controlled deployment is a requirement. Through various factors such as gas pressure, orifice size, piston diameter, and springs, the range of application of the basic concept is broadened. In addition, the LDRC design employs components that can be reliably simulated with analytical methods which eliminates the need for extensive and expensive testing, with the possible exception of the bellows. To minimize risks in this area, development tests should be run in which new bellows configurations recycled to verify whether they are working well within their elastic limits.

ACKNOWLEDGMENT

The author wishes to thank the designers of the LDRC, E.M. Altman and A. Holmberg of Rockwell's Shuttle Integration and Satellite Systems Division, for their support in the preparation of this paper.

N84

25084

UNCLAS

EVOLUTION FROM A HINGE ACTUATOR MECHANISM TO AN ANTENNA DEPLOYMENT MECHANISM FOR USE ON THE EUROPEAN LARGE COMMUNICATIONS SATELLITE (L-SAT/OLYMPUS)

Martin D. De'Ath*

ABSTRACT

This paper describes the evolution of an antenna deployment mechanism (ADM) from a hinge actuator mechanism (HAM). The result is a mechanism capable of deploying large satellite appendages in a controlled manner.

The development testing of the HAM identified many improvements to the concept which were incorporated into the ADM. Both of the designs are described in detail and the improvements made to the ADM are highlighted.

INTRODUCTION

The hinge actuator mechanism (HAM) concept was developed by British Aerospace (BAe) in response to an ESTEC development programme.¹ The experience gained in developing the HAM has been applied in the design of the antenna deployment mechanism (ADM), which originally was for the OLYMPUS telecommunications satellite programme but has been further developed for the UNISAT and EUROSTAR satellite programmes.

The HAM was conceived as a device able to deploy large satellite appendages in a controlled manner with a low speed of deployment such that the disturbance impulse to the satellite was minimal. The energy supply to power the HAM was self-contained and required no external actuator to enable operation. The appendage to be deployed would be held down to the satellite by a pyrotechnic release assembly, release of the mechanism would only require power to fire the pyrotechnic and would therefore minimize power requirements for deployment.

The development of the ADM, which required a significant increase in the available deployment torque coupled with a decrease in rotational speed, minimizes any increase in size or mass.

Details of the ADM application within the OLYMPUS antenna deployment subsystem has been included to show a typical application of the ADM and to highlight the operational requirements to be satisfied by the mechanism.

MECHANISM DESCRIPTION

Hinge Actuator Mechanism

Essentially, the HAM is a shaft supported on rolling element bearings that is driven by a large diameter helical torsion spring. The shaft, which in application, would be coupled to a large inertia, has its rate of deployment controlled by an eddy current damper which is driven by a shaft at high speed via a high ratio gearbox (Figure 1).

*Space & Communications Division, British Aerospace, Stevenage, Herts, United Kingdom.

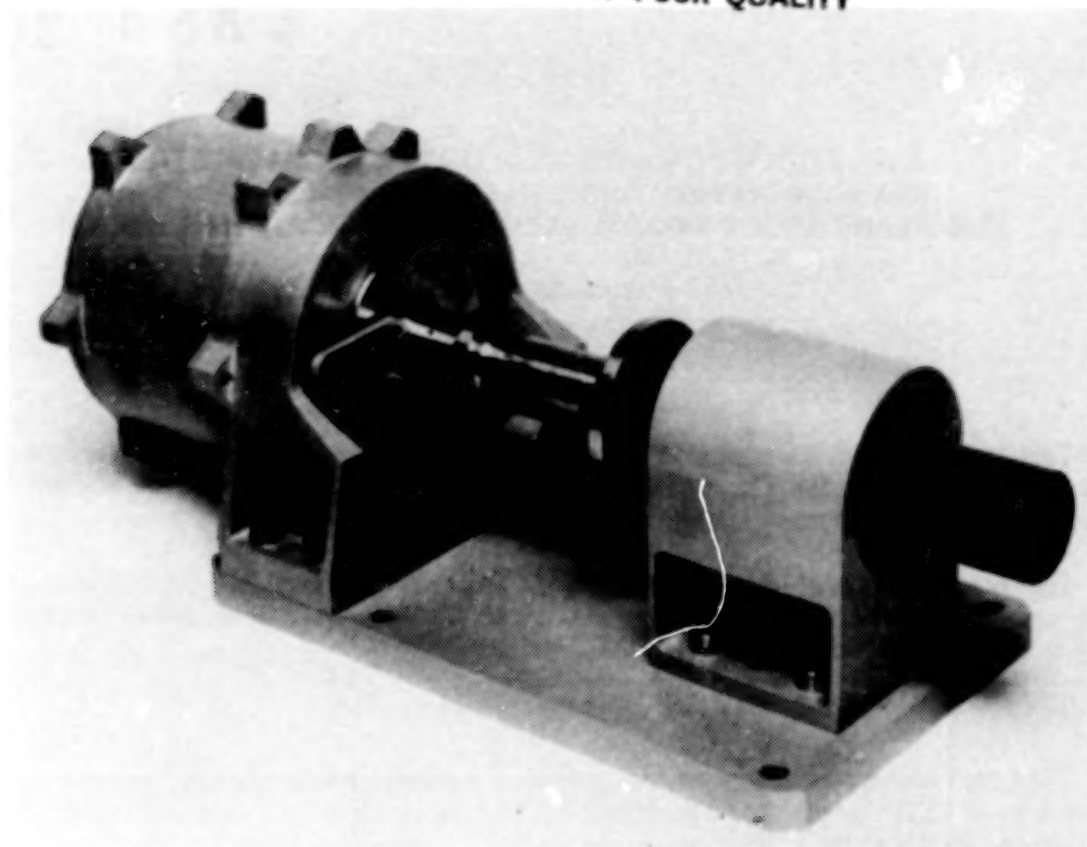


Figure 1. HAM Assembly

The mechanism was designed to give satisfactory performance against the following design requirements:

- a. Hinge load
 - Inertia—Up to 100 kgm^2
 - Mass—Support 12 kg at launch
 - Acceleration—30 g caused by vibration at launch
 - Resistive torque—Up to 0.5 Nm
 - Radial load—1200 N
 - Axial load—120 N
- b. Range of rotation— 90°
- c. Speed of rotation—Between $0.2 \text{ deg. sec}^{-1}$ and $0.5 \text{ deg. sec}^{-1}$
- d. Accuracy of deployment— 0.05° or better after latching
- e. Mass of HAM—1.45 kg

The design, which is to be externally mounted on the satellite sidewall, is capable of successful operation in a thermal environment of -50° to $+70^\circ\text{C}$. The main design features in the HAM are summarized for comparison with the ADM.

Shaft and Main Bearings

The main shaft is supported by a deep groove ball bearing and linear bearing assembly. The deep groove bearing provides the axial location and the in-line linear bearing allows for thermal expansion. The bearings and shaft are sized to accommodate anticipated launch loads of 30 g acceleration acting on the 12 kg mass. Liquid lubricant was used for the main bearing for a low friction torque. The linear bearing was not lubricated but ran on a solid molybdenum disulphide film. Both bearing housings were mounted on a common base to reduce misalignment. In a flight case it was anticipated that any in-line bearings would be separated by about 1 meter and would support an antenna backing structure. As previously stated these bearings would be designed to support only radial loads, the axial movement being unrestrained to accommodate thermal expansions. The shaft in the HAM represents the backing structure, and was manufactured from steel. The bearing housings and base were manufactured from aluminium alloy for lightness.

Spring

The drive spring is a large diameter helical torsion type driving the output shaft directly. The spring is housed within the gearbox and damper subassemblies and attaches to the main shaft adjacent to the main bearing. The housing allows sufficient clearance for the increase in diameter of the spring during deployment and provides adequate support.

The spring has been sized to generate a torque of 1 Nm, providing a comfortable margin over the anticipated resistive torque limit of 0.5 Nm. The steel wire spring was solid lubricated using a molybdenum disulphide film to reduce friction between the coils and housing.

Gears

The output shaft of the HAM drives the damper assembly via a high ratio gearbox. The overall gearbox ratio of 225:1 is obtained using four passes, this is to minimize the size of the gearbox while maintaining adequate tooth strength. During deployment the damper will balance the excess spring torque, the gearbox must therefore be capable of transmitting 1 Nm applied at the drive shaft.

The gears are isolated from the deployable structure launch loads by mounting them out board of the main bearing. The gears and their associated bearings need only be capable of transmitting the torque and containing the gear separation forces during deployment. Because of the high overall ratio the friction torque must be minimized. Therefore, the gears are dry film lubricated using molybdenum disulphide and the bearings are oil lubricated with Fomblin Z25.

An escapement device was incorporated into the design to eliminate any excessive torque being applied to the gearbox when back-driven, thus the design allows simple integration and stowage of the appendage to be deployed.

The escapement device is a one way rolling element clutch that is oil lubricated using Fomblin Z25.

The gears are standard spur gears with the full tooth form and 20° pressure angle. Because of the method of lubrication the gears were manufactured from stainless steel and surface hardened to 60 Rockwell 'C'.

Damper

An eddy current damper is used which utilizes the damping effect of eddy currents induced within a conducting disc rotating in a magnetic field. The induced current, and the energy dissipated, is related to the speed of rotation and the magnetic field strength. The speed necessary to provide damping can be minimized by optimizing the field with respect to the magnetic geometry.

The magnetic circuit was created by 12 magnet pairs (Figure 2), set radially on the damper housing. Simple bar magnets with shaped pole pieces to concentrate the flux between the magnets were used to optimize the magnetic field. Commercially available samarium cobalt magnets and low carbon steel pole pieces were used.

Mass

The total mass of 1.45 kg could be significantly reduced by the adoption of lightweight materials, for example an aluminium shaft and Delrin, an acetal copolymer resin, could be considered for the housing and gear materials.

Performance of the HAM

A test programme designed to fully test the HAM against its design requirements resulted in the following evaluation of the HAM.

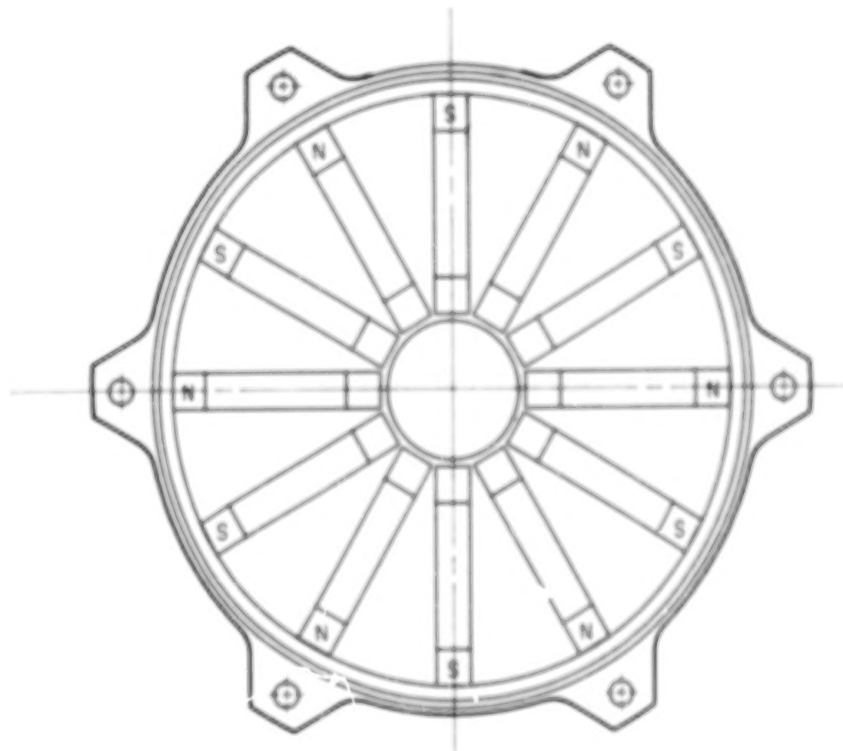


Figure 2. HAM Magnet Layout

The HAM satisfied all the functional tests and operating reliability with the exception of deployment speed. The damper design used a pure aluminium disc and the actual manufactured unit used an aluminium alloy with a higher resistivity. Under test a deployment speed of $1.3 \text{ deg. sec}^{-1}$ was obtained. This speed compared with a calculated figure of $1.2 \text{ deg. sec}^{-1}$ (using the higher resistivity). The accuracy of deployment was well within 0.05° , being 0.01° with a repeatability of deployment better than $\pm 0.004^\circ$.

Conclusions

The HAM programme proved that it was feasible to produce a mechanism capable of accurately deploying an inertia, reliably and at a controlled speed. The error in the deployment speed caused by a change in disc material highlighted the sensitivity of the eddy current damper and magnetic field theory, and the difficulty of reliably predicting the magnetic field strength and the speeds at which the desired damping torques could be achieved.

DEVELOPMENT OF THE ANTENNA DEPLOYMENT MECHANISM

The OLYMPUS telecommunications satellite programme required a multipurpose mechanism capable of a variation in torque output and deployment angle but able to control the rate of deployment for all expected output torques. During development of the ADM, experience that was gained from the HAM programme was extensively applied to the ADM's design. The areas where the most significant improvements were made have been highlighted within this paper.

The ADM concept is fundamentally the same as that of the HAM (i.e., a spring driven shaft mounted in rolling element bearings and controlled by an eddy current damper). The design requirements for the ADM, which have been modified to satisfy the multipurpose roles, are summarized for comparison with those of the HAM as follows:

- Hinge capacity—Up to 27 Nm damping requirement
- Deployment angle—Up to 90°
- Deployment accuracy and repeatability— $\pm 0.01^\circ$
- Resistive torque—0.5 Nm
- Lifetime—5 years storage, 50 'ground' operations, 10 year operational life
- Drive torque—At least 5 times resistive torque
- Impulse shock to spacecraft— $< 1 \text{ Nms}$
- Launch loads—2700 N in any direction

The ADM design improvements in spring motor and damper design are highlighted in the following paragraphs.

Spring Motor

The driving torque capacity for the ADM was increased to 14.85 Nm. As it was not feasible to use a helical torsion spring an alternative spring motor was developed. The motor consists of six constant torque springs each with a torque capacity of 0.1 Nm. The springs are mounted on individual bobbins, and the end of each of the springs is fastened to a common output shaft. To operate the motor, the output shaft is back driven, causing the individual springs to be reverse wound from their bobbins to the common shaft. The shaft is coupled to a two pass reduction gearbox, the ratio of which is 24.5:1. This results in the required output torque at the main shaft. Operation of the motor occurs as the individual springs rewind onto their bobbins.

One advantage of the spring motor is that each of the springs unwinds onto individual bobbins, and because the springs are free to rotate on the bobbins there is no chance of motor seizure, resulting in high reliability. High reliability is achieved by provisions for six individual springs, compared to the single spring of the HAM. Variation in output torque is achieved by varying the number of springs.

The detail design of the spring motor is shown in Figure 3.

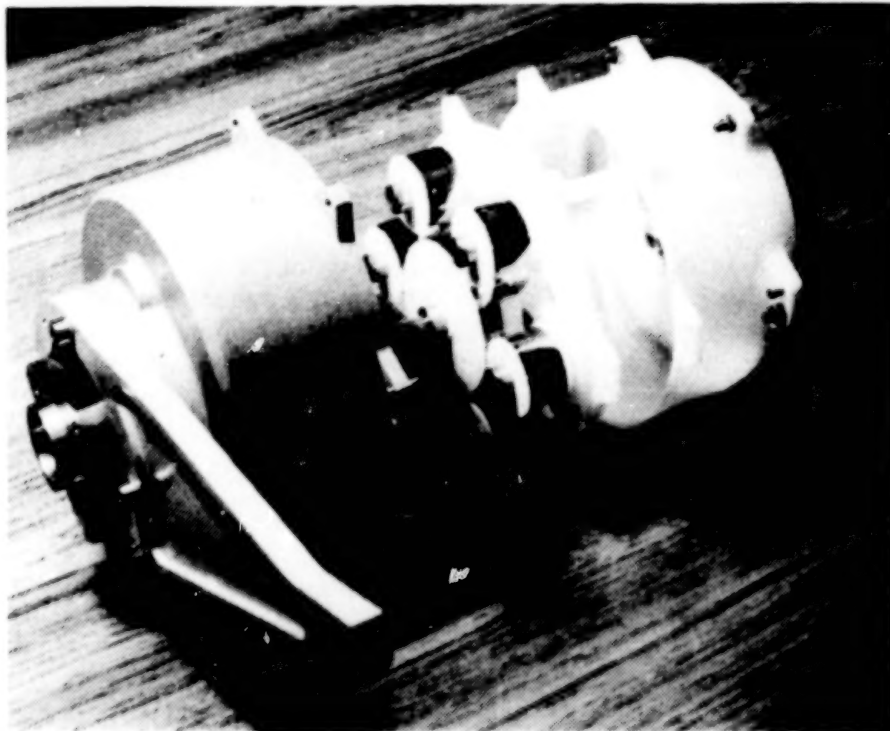


Figure 3. ADM Spring Motor Assembly

Damping

To control the mechanism with the increase in available motor torque, the damping capacity of the ADM was increased accordingly. The HAM programme indicated that the theoretical predictions of deployment speed using the eddy current damper theory were, because of their complexity, difficult to predict. Using the experience gained from the HAM the ADM damper configuration was re-designed. The next section describes the theory used in the predictions of damper performance, and the changes made between the HAM and the ADM.

Eddy Current Damping Theory

Equation 1 has been derived from the theory covered in "Permanent Magnets."² This equation predicts the damping torque that may be expected from a disc rotating within a magnetic field.

$$T_d = \frac{2 B^2 r^2 a b t \omega_d N}{5 \rho} \quad (1)$$

A magnet pole is assumed to generate a rectangular magnetic field. See Figure 4.

Where,

B	=	Magnetic field strength	(Tesla)
a	=	Field or magnetic width	(m)
b	=	Field or magnetic length	(m)
r	=	Mean radius of magnets around disc of rotation	(m)
N	=	Total number of magnets around disc housing	(m)
t	=	Thickness of the conducting disc	(m)
ρ	=	Resistivity of conducting disc	(Ωm)
ω_d	=	Angular velocity of conducting disc	(rad/sec)
T_d	=	Damping torque generated by the disc	(Nm)

The magnetic field strength in the gap between the magnets is estimated from equation 2.

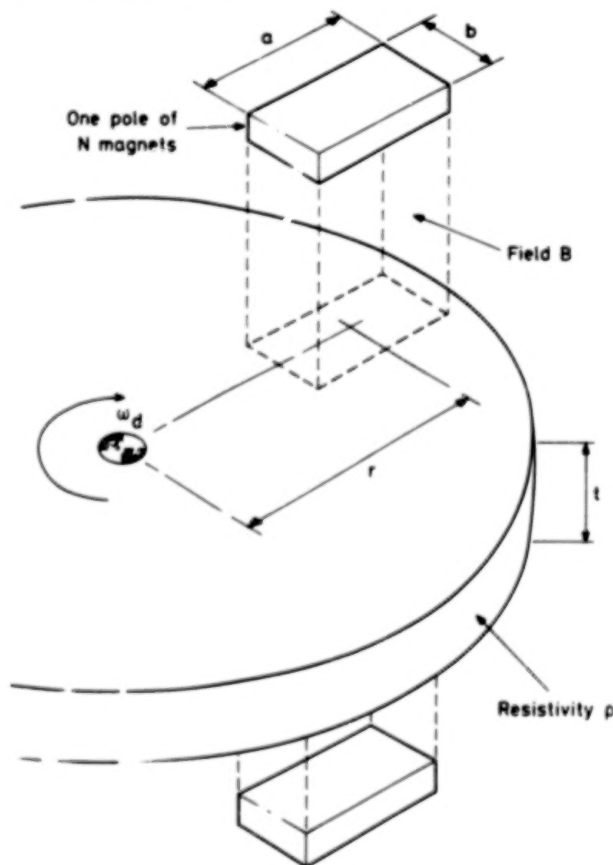


Figure 4. Damper Theory Figure

$$B = \frac{Br}{K_1 \left(\frac{Ag}{Am} \right) + K_2 \left(\frac{Lg}{Lm} \right)} \quad (2)$$

Where,

B	=	Flux density in gap	(Tesla)
Br	=	Remanance of magnet material	(Tesla)
K ₁	=	Leakage factor	
K ₂	=	Magneto motive force factor	
Ag	=	Cross-sectional area of gap	(m ²)
Am	=	Cross-sectional area of magnet	(m ²)
Lg	=	Length of gap	(m)
Lm	=	Effective length of the magnet	(m)

In equation 1, where ω_d and T_d represent the speed and torque in the damper, the output speed and torque may be represented by the expressions,

$$\omega_d = \omega \cdot G \quad \text{and} \quad T_d = \frac{T}{G}$$

where G = gear ratio between the damper disc and output shaft.

By substitution into equation 1 and by rearranging equation 3 is obtained.

$$\omega = \frac{\rho T}{G^2 B^2 a. b. t. N r^2} \cdot \frac{5}{2} \quad (3)$$

In calculating the flux density in the gap, (equation 2), two factors need to be quantified, K_1 and K_2 .

Factor K_1 , the leakage factor, is calculated by relating the useful flux existing between two opposing poles through the disc and that lost between poles parallel to the plane of rotation of the disc. The values of K_1 were quantified during the design stage and are unique to the design of the HAM and ADM.

Factor K_2 , the magneto motive force factor, determines the ability of the circuit to produce a current. This factor, however, is difficult to quantify accurately and has been taken in both cases to be 1.4.

Summary of Damper Calculation for the HAM

The following values have been used in the determination of the flux density from equation 2.

Br	=	0.9 Tesla
K ₁	=	3.32
K ₂	=	1.4
Ag	=	25 x 10 ⁻⁶ m ²
Am	=	25 x 10 ⁻⁶ m ²
Lg	=	4 x 10 ⁻³ m
Lm	=	20 x 10 ⁻³ m

These result in a calculated flux density of 0.250 Tesla.

During deployment, once a constant speed is obtained, the system is in equilibrium and the damping torque is equal to the excess spring torque. The HAM torsion spring sizing was based on the average available torque.

$$\begin{aligned} T &= \text{driving torque to be damped} \\ T_s &= \text{average supply torque} &= 0.9015 \text{ Nm} \\ T_r &= \text{resistive torque} &= 0.50 \text{ Nm} \\ T_d &= \text{bearing frictional torque} &= 0.0005 \text{ Nm} \end{aligned}$$

$$\therefore T = T_s - T_r - T_d$$

$$\text{Driving torque to be damped} = 0.40 \text{ Nm}$$

The radial distribution of the magnets led to two magnetic circuits with a mean effective radii of r_1 and r_2

$$\begin{aligned} r_1 &= 0.002 \text{ m} \\ r_2 &= 0.038 \text{ m} \end{aligned}$$

Also,

$$\begin{aligned} \rho &= 5.7 \times 10^{-8} \Omega\text{m} \\ G &= 225 \\ t &= 0.002 \text{ m} \\ a &= 0.005 \text{ m} \\ b &= 0.005 \text{ m} \\ N &= 12 \end{aligned}$$

Substitution into equation 3 for both circuits and summation of the results reveals the expected deployment speed.

$$\omega = 0.0207 \text{ rad/s}$$

$$\text{or, } 1.19 \text{ deg. sec}^{-1}.$$

This indicates that the mechanism should take 75 seconds to deploy 90° . From testing it was discovered that the mechanism took 68 seconds to deploy.

In comparison the following developments were carried out for the ADM and the results summarized in the following section.

Summary of the ADM Developments

The magnet arrangement was changed from the radial arrangement as shown in Figure 2 to a circumferential layout in Figure 5. This resulted in more magnetic pole pairs at an increased mean effective radius. Additional benefits of this change are that the reduction in the number of magnets has reduced the mass and that the leakage factor has been reduced, resulting in an increase in the flux in the gap and consequently the overall efficiency of the damper.

The gear ratio between the damper and output shaft has been increased from 225 to 1378:1. This increase was achieved by incorporating an additional two pass gearbox between the spring motor drive shaft and the damper shaft with a ratio of 56.25:1. Therefore, the damper may be expected to produce the results that follow.

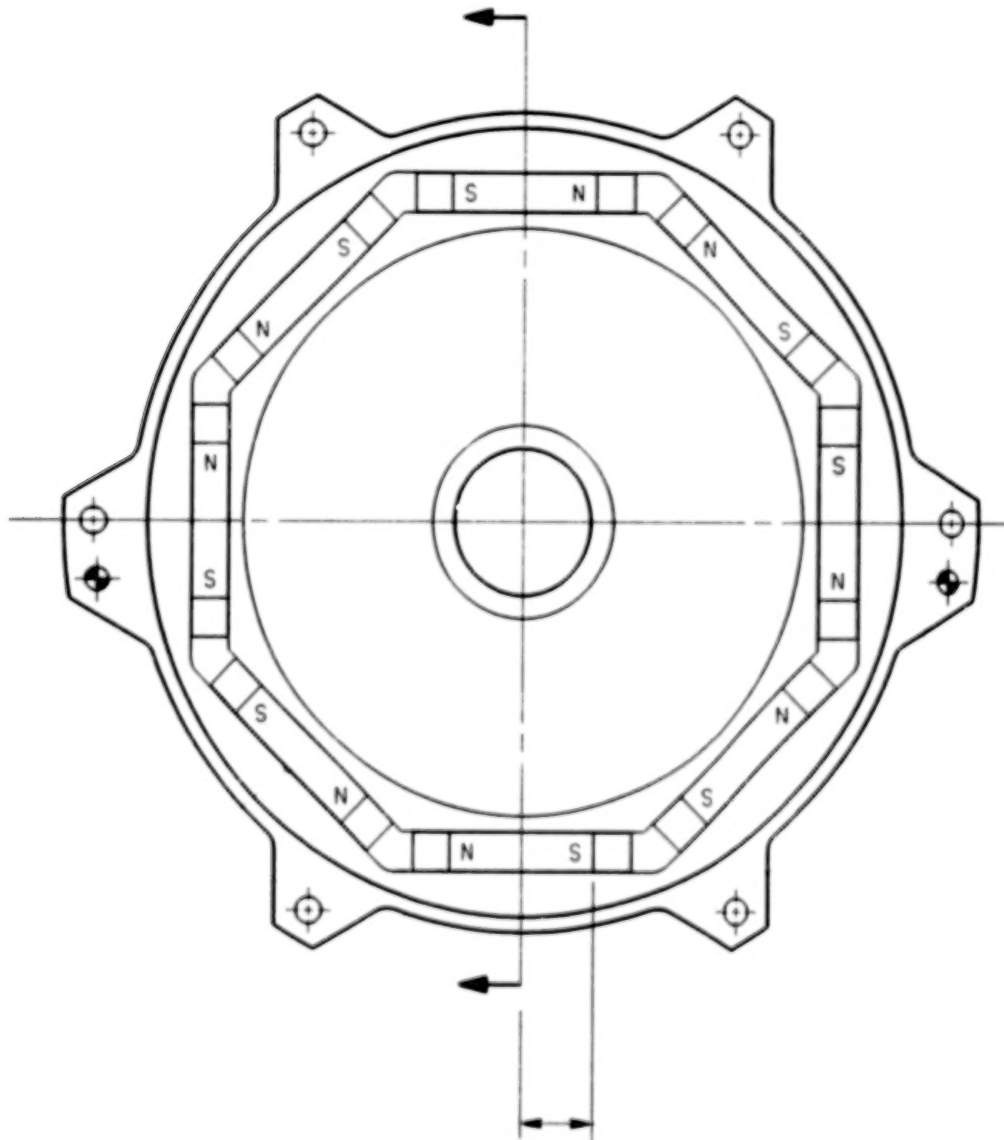


Figure 5. ADM Magnet Configuration

Summary of ADM Damper Calculations

Flux in gap B

For application in equation 2.

$$\begin{aligned} B_r &= 0.85T \\ K_1 &= 1.24 \\ K_2 &= 1.4 \\ A_g &= 25 \times 10^{-6} \text{ m}^2 \\ A_m &= 25 \times 10^{-6} \text{ m}^2 \\ L_g &= 4 \times 10^{-3} \text{ m} \\ L_m &= 20 \times 10^{-3} \text{ m} \end{aligned}$$

$$\therefore B = 0.5592 \text{ Tesla.}$$

This may now be used to predict the deployment speed ω .

Driving torque T.

$$\begin{aligned} T_s &= \text{supply torque} &= 14.85 \text{ Nm} \\ T_r &= \text{resistive torque} &= 0.50 \text{ Nm} \\ T_f &= \text{frictional torque} &= 0.011356 \text{ Nm} \end{aligned}$$

$$\therefore T = 14.33 \text{ Nm}$$

Also,

$$\begin{aligned} \rho &= 5.7 \times 10^{-8} \Omega\text{m} \\ G &= 1378 \\ B &= 0.5592 \text{ Tesla} \\ r &= 0.045 \text{ m} \\ t &= 0.002 \text{ m} \\ a &= 0.005 \text{ m} \\ b &= 0.005 \text{ m} \\ N &= 8 \end{aligned}$$

Resulting on substitution into equation 3 a deployment speed.

$$\omega = 0.0021 \text{ rad/sec}$$

$$\text{or} \quad 0.12 \text{ deg/sec}$$

This indicates a deployment time for a rotation of 90° of 750 seconds.

At present, test results are not available for the mechanism deploying a resistive torque of 0.5 Nm, so the conclusions made are based on the theoretical calculations and the experience gained in eddy current damping.

Conclusions of the ADM Damper Development

The damping capacity of the ADM has been significantly improved by increasing the overall damper gear ratio from 225 to 1378 and by increasing the mean radius while at the same time reducing the number of magnet pairs. The rate of deployment is down by a factor of four and the damping capability has been increased by about 14 times.

The most gains have been achieved theoretically in this area of development and it is expected that these gains will be supported experimentally.

MATERIAL SELECTION

During the design of the ADM, extensive use of lightweight materials for low-stressed components and housings has been incorporated. Delrin, an Acetal copolymer, was used for housings and the damper gears where considerable mass savings were achieved.

Mass

A mass estimate for the ADM includes the additional in-line bearing assembly and results in an overall mass of 2.3 kg. With this slight increase in mass, performance is improved substantially over the HAM.

Conclusion

The ADM is a versatile mechanism capable of deploying large deployable structures on satellites accurately and in a controlled manner such that the disturbance impulse to the satellite is kept to a minimum. A significant increase in drive torque and damping capacity was achieved in the development of the ADM without a significant increase in mass compared to the HAM.

APPLICATION OF THE ADM

The ADM has been used in the OLYMPUS antenna deployment subsystem (ADS). This subsystem supports during launch and deploys after launch the 1.2 m reflectors and antenna pointing mechanisms (APM) that are to be used on the east and west sidewalls of the spacecraft.

The ADS is comprised of three main equipments: the ADM, the deployable arm (ARM), and the pyrotechnic release assembly (PRA) as shown in Figure 6.³ The PRA is used to hold the ADS to the satellite sidewall during launch, and via the pyrotechnics release the ADS after launch. The ARM forms the backing structure onto which the APM and reflector are mounted. The ADS is required during operation to form a thermally stable platform from which the APM/ and reflector may operate without degradation for the satellite lifetime of 10 years.

ORIGINAL PAGE 19
OF POOR QUALITY

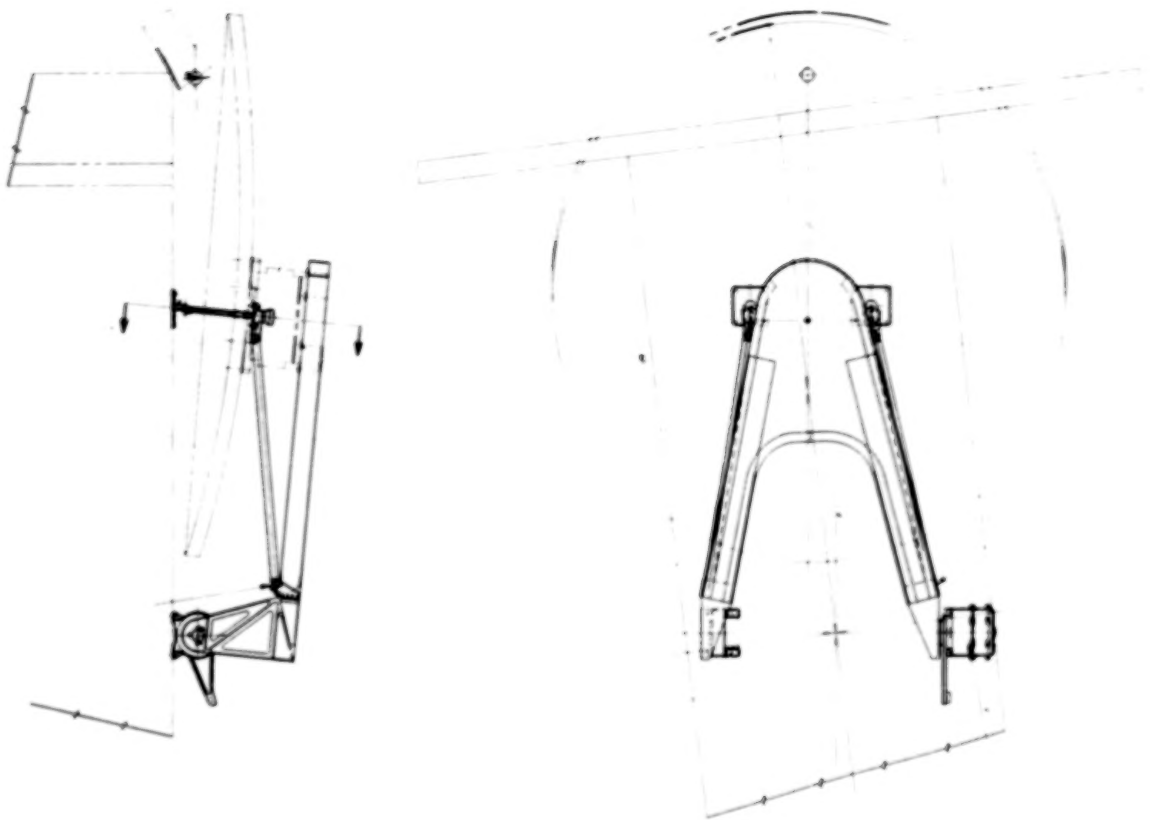


Figure 6. ADS Assembly

REFERENCES

1. Gallagher, K., "Hinge Actuator Mechanism Programme - Final Technical Report," TP7951, British Aerospace, 1982.
2. Hadfield, Iliffe, "Permanent Magnets."
3. Dace, R., "Antenna Deployment Subsystem (ADS) Design Description Report," (RPT/LCS/53636/BAe), British Aerospace, 1983.

N84

25085

UNCLAS

THE IMPORTANCE OF THERMAL-VACUUM TESTING IN ACHIEVING
HIGH RELIABILITY OF SPACECRAFT MECHANISMS

K PARKER*

ABSTRACT

This paper describes the work performed at the European Space Tribology Laboratory (ESTL) on thermal vacuum testing of complex mechanisms for the European Space Agency and several European customers. The objective of these tests is to assess the mechanism reliability by monitoring performance in an environment that closely resembles the environment that will occur during flight. To be both valid and cost effective, these tests must be performed in a detailed, formally controlled manner.

A review of the major test observations at ESTL over 10 years is given, during which time some totally unexpected failure modes have been detected. Full confidence now exists in many mechanism and component designs, and much valuable data have been obtained that are available to mechanism designers for improving reliability.

INTRODUCTION

The European Space Tribology Laboratory (ESTL) is operated by the National Centre of Tribology on behalf of the European Space Agency (ESA). This laboratory is dedicated to the study of all aspects of tribology, lubrication, and wear processes that are applicable to spacecraft technology.

An essential part of the work in ESTL is to carry out carefully controlled thermal vacuum tests on complete mechanisms or individual components, whereby the conditions anticipated to occur in flight are accurately simulated, particularly with regard to the presence of thermal gradients across a mechanism.

A recently available analysis† of 316 spacecraft from 46 United States programmes revealed 1600 separate anomalies of varying degrees of importance as regards their impact on the overall reliability. A significant proportion were attributable to electromechanical devices which had been assumed to be reliable under all possible operating conditions. Could some of these anomalies have been avoided by the application of more testing?

* European Space Tribology Laboratory, Risley, Warrington, United Kingdom

† Briscoe, H.M., (1983), European Space Agency, private communication

ORIGINAL PAGE 18
OF POOR QUALITY

The purpose of this paper is to emphasize the importance of selective thermal-vacuum testing for achieving high reliability and to review the work conducted at ESTL for the past 10 years. During this time period, over 70 thermal vacuum tests were performed for ESA and several European mechanisms manufacturers.

TESTING PHILOSOPHY

In the interest of a cost-effective demonstration of spacecraft mechanism reliability, ESA placed great emphasis on thermal-vacuum testing of complete assemblies, particularly those assemblies required to operate to within close tolerances throughout the lifetime of the satellite. This type of testing is often the most demanding of these tests done on a mechanism, combining the hostile vacuum environment with the subtle stresses produced by adverse temperatures and temperature gradients.

It is not always possible, even with elaborate thermal control systems, for a satellite mechanism to operate in a predictable isothermal environment. For example, a solar array drive mechanism will have its shaft exposed to a different environment than the housing, bearing and slipring unit. With geostationary satellites the system will be exposed to an eclipse cycle during which the shaft temperature is rapidly reduced and then restored to its normal level.

Despite comprehensive thermal analysis it is usually difficult to obtain accurate predictions of the temperature distribution in a mechanism. Also, when several components may be operating to different control sequences, resulting in variable power dissipation from motors, sliprings, and cables, thermal gradients can occur over small areas of a device.

Although the performance of individual components may have been separately assessed before assembly into a complex mechanism, unfortunately it is still the case that unpredictable behaviour and possibly failure of a component can occur in systems subjected to extreme temperatures and temperature gradients. Complete confidence in a particular design is only achieved when every possible failure mode has been identified and either designed out of the system or accepted with adequate demonstration of reliability.

The ESA insists that rigorous thermal-vacuum testing be applied to all critical mechanisms, with emphasis on the application of thermal gradients. The several categories of test are:

- To provide data for assisting in the design of new components or systems (Development Test)
- To verify that a mechanism, when built to a prescribed standard, will fulfill the operational requirements with an adequate safety margin (Qualification Test and Life Test)

ORIGINAL PAGE IS
OF POOR QUALITY

- To confirm that a particular flight unit will conform to the specific mission requirements (Acceptance Test and Refurbishment Test)

During testing of, for example, a solar array drive mechanism usually it is necessary to define two boundary interface temperatures to characterise the thermal environment and to act as control temperatures for the test. These are typically:

- T_1 - shaft/array interface temperature
- T_2 - housing/satellite interface temperature

Figure 1 shows¹ a typical envelope of qualification temperatures and the way in which the test temperatures are derived from the anticipated operational temperatures, which are determined from thermal transfer calculations and data obtained from actual flight experience. Four specific thermal vacuum test conditions are apparent: hot soak, cold soak, positive differential, and negative differential, allowing for a 15°C safety margin.

It has proved to be vital that the tests be formally controlled in accordance with a carefully constructed Test Procedure which is agreed with all interested parties before the start of the test. Formal Product Assurance supervision, applied at a mutually acceptable level, is an essential guarantee of test control. Of fundamental importance is the regulation of the amount of testing to achieve optimum efficiency and cost effectiveness and to avoid unnecessary procedures that could result in wasteful over testing. There must be no possibility of the test system introducing possible failure modes.

TEST EQUIPMENT

Figure 2 shows part of the ESTL. Certified clean-room conditions have proved to be essential in the success of thermal-vacuum testing, particularly with regard to the handling and inspection of mechanisms. Different areas conforming to Federal Standard 209B Class 100, Class 1000, and Class 10,000 cleanliness conditions are maintained.

Several different types of ultrahigh vacuum chambers are shown in Figure 3 and a simplified diagram of the internal components of a 1-meter diameter facility is shown in Figure 4. To conform to the ESA testing philosophy, emphasis is always placed on maintaining very clean test systems and for this reason the only types of pumps used on the vacuum chambers are high-reliability turbo-molecular, titanium sputter ion, and cryogenic pumps. environment is often determined by the amount of vapour outgassing from the mechanism under investigation. It is usually considered that a valid tribological test can be performed below 10^{-7} mbar. Each system is fully instrumented with mass spectrometry facilities for residual gas analysis.

ORIGINAL PAGE 18
OF POOR QUALITY

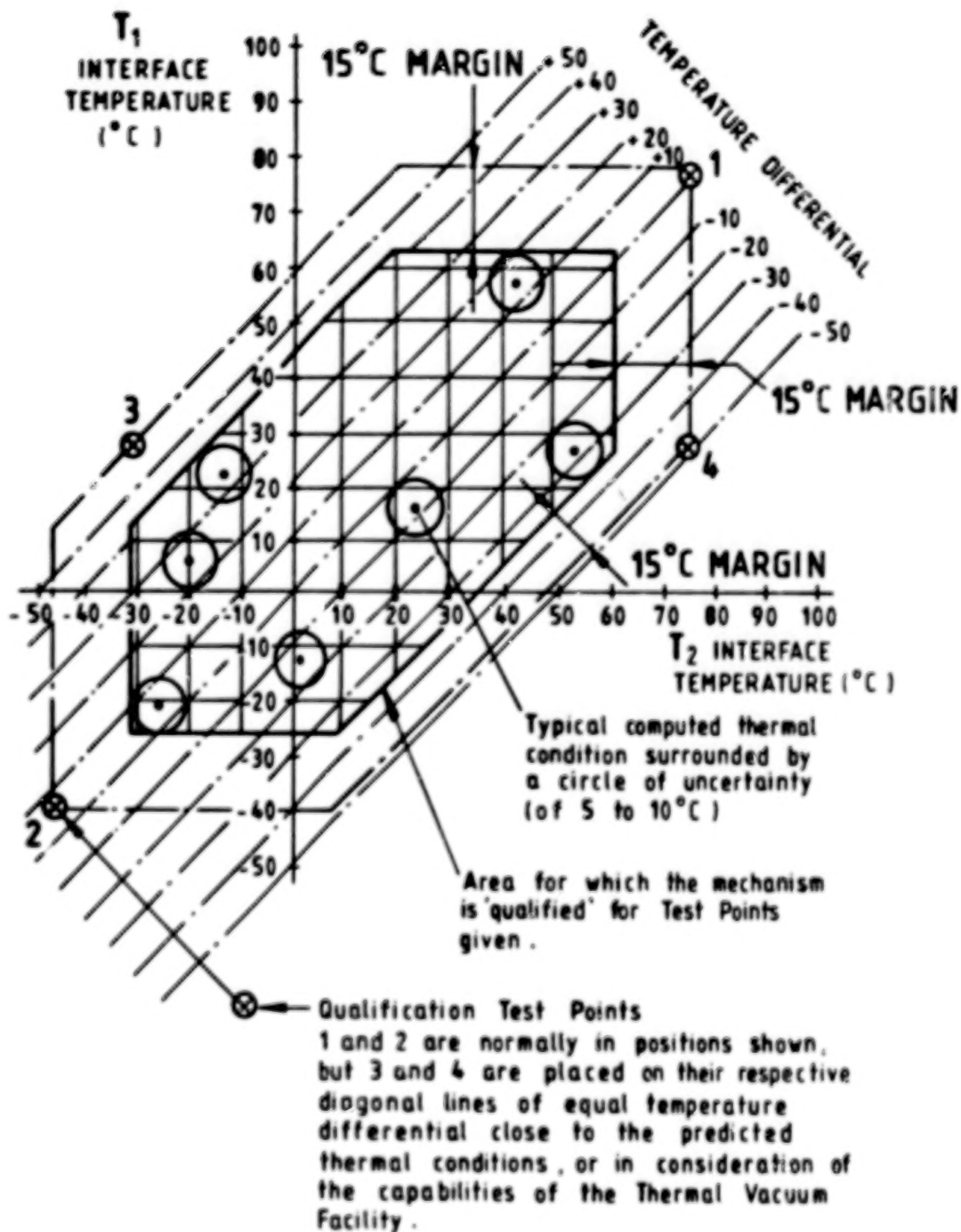


Figure 1. Example of System Used to Derive the Thermal-Gradient Test Temperatures

ORIGINAL PAGE IS
OF POOR QUALITY



Figure 2. Part of the ESTL Clean Room Laboratory

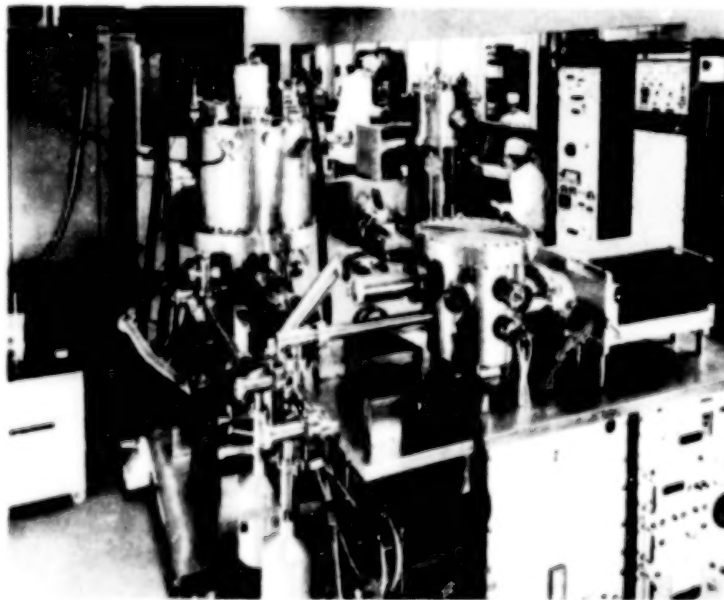


Figure 3. Some of the ESTL Thermal-Vacuum Test Facilities

ORIGINAL PAGE 13
OF POOR QUALITY

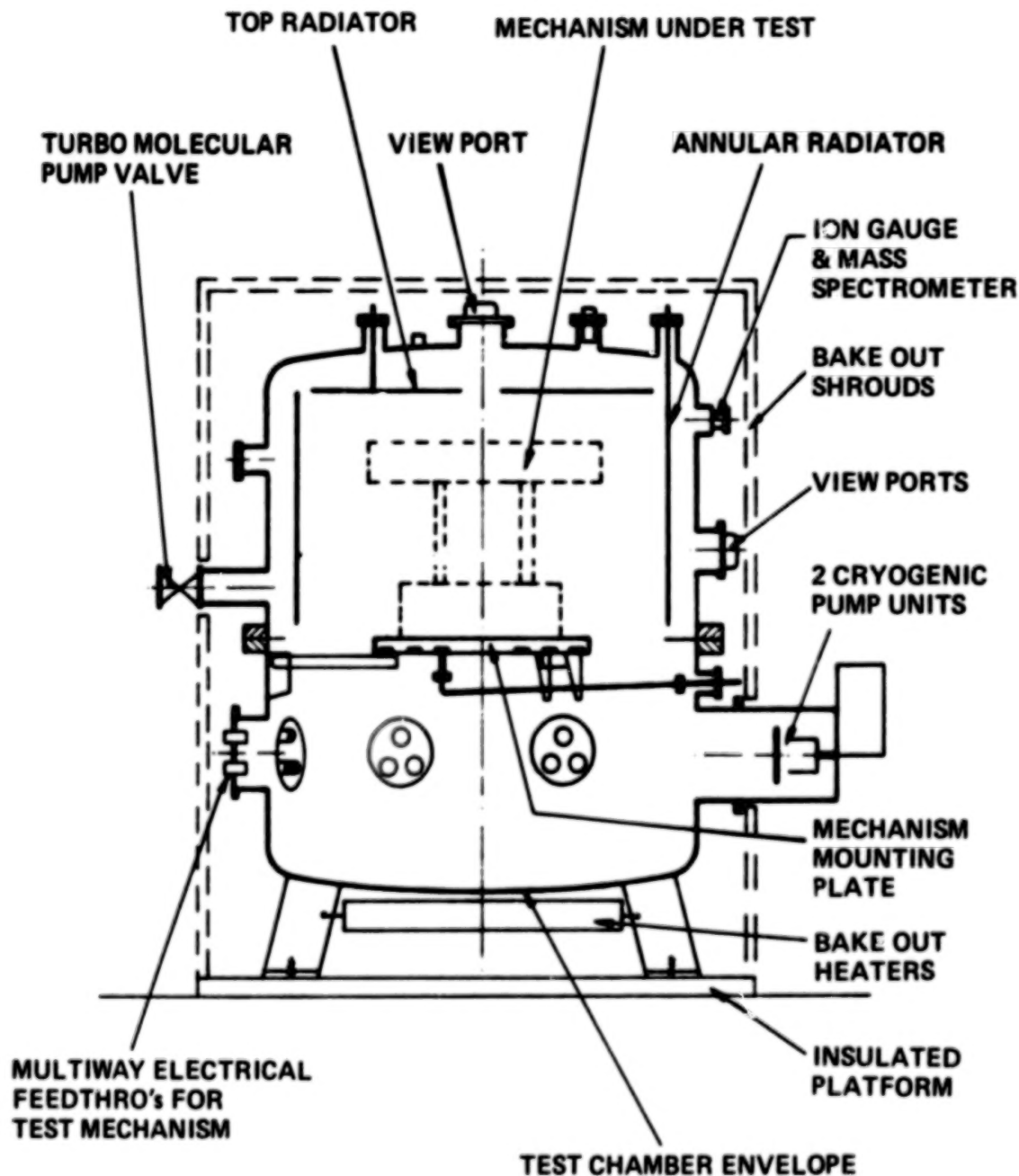


Figure 4. Main Features of a 1-Meter Diameter
Test Chamber

ORIGINAL PAGE 19
OF POOR QUALITY

This is very important as undesirable gas species such as oxygen and other active gases must be identified and, where possible, excluded. Usually, it is necessary to ensure that the partial pressure of oxygen, for example, is well below 10^{-9} mbar.

A thermal interface enclosure is built around the mechanism in such a way that there are two independently controlled boundary interface temperatures. These two temperatures are determined by radiation to and from thermal shrouds whose temperatures are controlled in the range -90° to $+120^{\circ}\text{C}$ by high reliability fluid-circulation systems and electrical heating units. Space-approved materials of certified purity are used throughout the construction of the thermal-test environment.

Instrumentation systems are available to monitor to very fine limits such test parameters as thermal distribution, speed, torque, angular motion stability, and slipping electrical noise, as the thermal tests proceed. Data acquisition systems are of course necessary to deal with the information analysis. Selected parameters of the thermal control system, the pumping units, and the mechanism under test are linked to high-reliability, redundant protection systems so that any deviation from prescribed limits can be sensed and the appropriate corrective action can be automatically taken. This is vital to ensure that there is never any risk of the test itself causing the possibility of additional failure modes.

REVIEW OF TEST OBSERVATIONS

Seventy thermal-vacuum tests have been conducted over the past 10 years. In many of these, of course, the mechanisms operated within specified limits, which allowed confidence to be gained in the particular designs used. In some, valuable data were obtained, during dismantling operations, of the degree of wear and other changes that had occurred in the various components. In about 35 percent of the tests, however, some unacceptable deviation from the desired performance occurred, which enabled possible failure modes to be identified and provided valuable data feedback to manufacturers for making the necessary modifications.

Occasionally, total failure has occurred as a result of seizure of a shaft, bearing or lubrication failure, excessive friction, or excessive temperatures in a motor.

Solar Array Drive Mechanisms

The majority of this class of important mechanisms tested at ESTL have been intended for communications satellites in geostationary orbit where the mechanism is subjected to thermal gradients.

ORIGINAL PAGE IS
OF POOR QUALITY

Typical test temperatures are:

	Shaft Interface	Housing Interface
Hot soak	+90°C	+55°C
Cold soak	-50°C	-25°C
Positive Differential	+50°C	0°C
Negative Differential	-35°C	+15°C

Additional tests may be necessary to simulate the extreme thermal conditions experienced in an eclipse, typically a drop of 60°C in the shaft temperature in 72 minutes followed by an increase of 60°C in 30 minutes. The mechanism must maintain solar alignment after the eclipse simulation.

Of fundamental importance is that the angular motion must be smooth, so as to avoid reaction torque disturbances to other systems. Often a brushed motor is used to give an impulse every 4 seconds or so. Ideally, each impulse should result in 0.0167° of rotation and an important part of the test is to measure any deviation from this value.

Many European solar array drive mechanisms use bearings of the highest available precision which have been lubricated by a thin film of lead deposited by an ESTL plasma ion-plating process.

The solar-generated power, typically 2 Kw, is transmitted by sliprings which are often fabricated from silver or copper with a gold plating. A common brush material is a composite of silver/copper/MoS₂ in volume ratio 82.5/2.5/15, respectively. Assessment of the electrical noise across the interface is necessary as this could result in unacceptable power loss and radiation interference.

Figure 5 shows a solar array drive being loaded into a vacuum chamber. In Figure 6, another type is shown being fitted with a thermal enclosure.

In 1975, ESTL commenced a 7-year real life test on such a mechanism, to fully quantify the time-dependent parameters and to obtain data that would enable us to assess the validity of accelerated life testing on systems using solid lubrication. Many thermal changes were made in this test, including 420 eclipse simulations. The test was very successful, only minor changes occurred in the measured parameters. Of significant interest was that the test chamber pressure took several years to stabilize at about 1×10^{-8} mbar because of continuous outgassing from the mechanism surfaces and cable looms. It is important to note that over a long period of time this outgassing can be a primary cause of failure due to degradation of materials. The rotational stability and motor power requirements were remarkably consistent, showing that the friction in the sliprings and brushes had remained

ORIGINAL PAGE 13
OF POOR QUALITY



Figure 5. A Solar Array Drive Mechanism Being Loaded into a Test Chamber

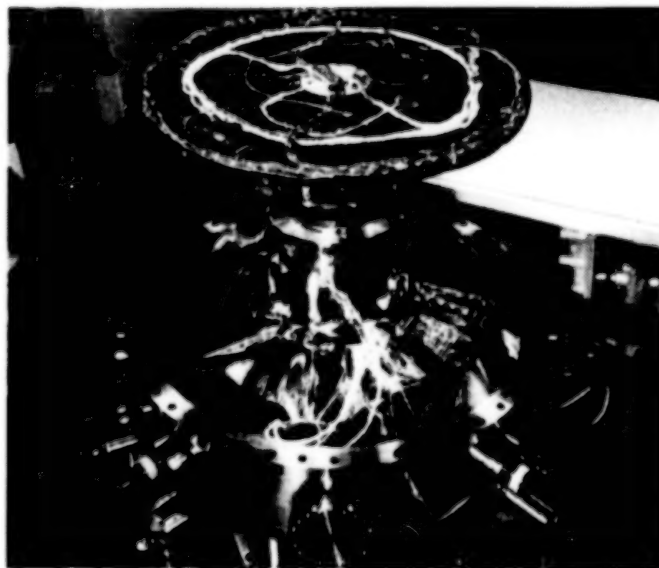


Figure 6. A Solar Array Drive Mechanism Being Fitted into a Thermal-Gradient Enclosure

ORIGINAL PAGE 19
OF POOR QUALITY

substantially constant. The sliprings were tested with various current levels ranging from 100 mA to 7 Amp. Most gave variable amounts of electrical noise, within specification, but two circuits passing 500 mA produced intermittent noise pulses that were equivalent to a resistance change of 2 ohms. The characteristics of these transients were such that they could only have been caused by the presence of variable amounts of brush wear debris, and an inevitable conclusion is that some suspicion must fall on the use of MoS₂ as brush lubricant.

A second 7-year real life test on a different type of mechanism had to be abandoned after 4 years because of excessive deviation from the position control stability criterion. Subsequent examination revealed that time-dependent degradation of the efficiency of an optical encoder had occurred. This failure was completely unexpected.

Some other important observations during tests on various mechanisms were:

- Surprising variation in performance of nominally identical mechanisms, presumably due to minor changes of material specification and variations in fabrication tolerances.
- Seizure of shaft in a housing during a cold test at -50°C.
- In a cold test, a high torque was present over only about 1° of rotation due to unbalanced flexure of a diaphragm used to preload the bearings.
- An unusual thermal distribution was monitored within a mechanism, implying that a serious design fault was present. Subsequent investigation revealed that a thermistor bead had become detached from its cemented mounting.
- A very unusual fault on a thermistor, whereby it operated correctly below 30°C but was apparently open-circuit above 30.5°C.
- Excessive temperature (140°C) in a stepper motor in a hot test with the mechanism shaft controlled at +90°C. This was due to inadequate design of a heat sink.
- Complete failure of an actuator and lever system that was used to one two redundant motors in a gear drive device.
- Unexpected thermal distribution in a mechanism that invalidated previous theoretical analysis. This was due to the power dissipation from motors and slip rings being underestimated.
- Contamination of test environment by silicone compounds following rupturing of an overheated memory alloy element of a bearing off-load assembly. The heater current had been incorrectly specified.
- Unexpected variations in angular motion stability with temperature. This could only have been detected by thermal vacuum testing.
- Permanent set of a release cable of a bearing off-load device after a long period of storage under tension. When released, full retraction did not occur and the cable made contact with nearby components.
- Rubbing of insecure cable on rotating component.

ORIGINAL PAGE IS
OF POOR QUALITY

- Excessive noise and power loss in slipring unit apparently due to changes in the slipring surface properties resulting from degradation of molybdenum disulphide lubricant.
- Microswitch failure at low temperature.
- Excessive outgassing from a mechanism that did not appear to have been manufactured to approved standards of cleanliness.

Despin Mechanisms

In 1975, ESTL commenced a unique real life test on a despin mechanism in which the bearings were lubricated by BP2110 grease with BP110 oil impregnated in the cages and in Nylasint reservoirs. At a speed of 60 rpm these were operating under conditions bordering on those of boundary lubrication. Assessment of the time-dependent properties of this system was necessary, one area of uncertainty being the effectiveness of oil-creep barriers and oil seals. If oil migration did occur it was essential to investigate the effect on the sliprings. Rotation was by means of a two-phase brushless motor with the current being continuously adjusted to maintain a constant speed of 60 ± 1 rpm. Modest thermal conditions were imposed on the device, with the shaft temperature at either -5° or $+45^\circ\text{C}$.

Again, because of continuous outgassing, the test chamber pressure took several years to stabilize at about 1×10^{-8} mbar.

Although there was no significant overall deterioration in the performance of the sliprings, there were large but temporary increases in interface resistance following a change of thermal conditions. This may have been a consequence of the presence of variable amounts of oil, or differential axial expansions causing the brushes to run on a slightly different track, several days of running-in being necessary before the resistance returned to normal.

There was a gradual increase in the motor current probably because of a continuous reduction in the field strength of the permanent magnets in the motor. This aging process is known to occur at about 7 percent per year for the magnetic materials available in 1973 when the mechanism was designed.

This unique and very successful mechanism has recently been dismantled and some very valuable information has been obtained from detailed component inspection. For example, the bearings were in very good condition with adequate reserves of clean oil. Although there was a significant amount of wear debris in the slipring unit this did not effect their operational efficiency.

It is important to note, however, that this device had originally failed quite dramatically when the shaft seized in a cold test due to neglect during manufacture of critical tolerances between stationary and rotating components. The failure was caused by a screw head projecting 1 mm too far above a housing flange.

ORIGINAL PAGE 19
OF POOR QUALITY

Recently an accelerated life test was performed on a despin mechanism for the European Giotto (Halley Comet) mission. Validation of the system torque stability was essential for this very special satellite component which determines the antenna-pointing performance.

Motor Drive Systems

Many different types have been evaluated. Of particular interest are torque stability, power dissipation, bearing performance, brush stability, stability of potting compounds, generation of wear particle contamination, and magnetic circuit stability. Some major observations were:

- Unexpected torque characteristics in high-speed brushless motor at elevated temperatures - our test results did not agree with the manufacturer's predicted performance.
- Overheating due to inadequate thermal coupling between motor and a suitable heat sink. The rate of power dissipation and thermal transfer in vacuum had been underestimated.
- Failure of gold-surface coating on meshing teeth of a high resolution stepper motor, due to the substrate medium not being of sufficiently hard material.
- Inadequate radial stiffness in an experimental stepper motor.
- Degradation in performance of motor and gearbox unit due to inadequate grease lubrication and the effect of cumulative wear debris.
- Dry lubricant in gear systems can sometimes result in compaction in the roots of teeth.
- High temperature in high-speed motor with oil-lubricated bearings. Too much oil resulted in high torque and power loss. To maintain constant speed, more current was demanded in the motor, leading to even higher power dissipation. It is always essential to use the correct amount of the recommended lubricant.

Slipring Assemblies

Slipring assemblies are present in several types of mechanism. See Figure 7 for a typical unit. Much valuable data have been obtained on reliability in terms of contact resistance variation, power loss, stability of materials, friction, wear, and distribution of wear particles. Some problems have been identified in units that have been widely used and assumed to be of high reliability under all conceivable operating conditions:

- Visible ring surface tarnishing does not necessarily indicate performance deterioration, but one such unit, stored for over 18 months after a successful test, was retested and found to have high contact resistances and increased operating temperature. In vacuum, the effect was temperature dependent but the anomaly disappeared completely on exposure to air again. This unit had brushes incorporating molybdenum disulphide as a lubricant. This phenomenon has been observed in other similar systems, and detailed observation reveals that high contact

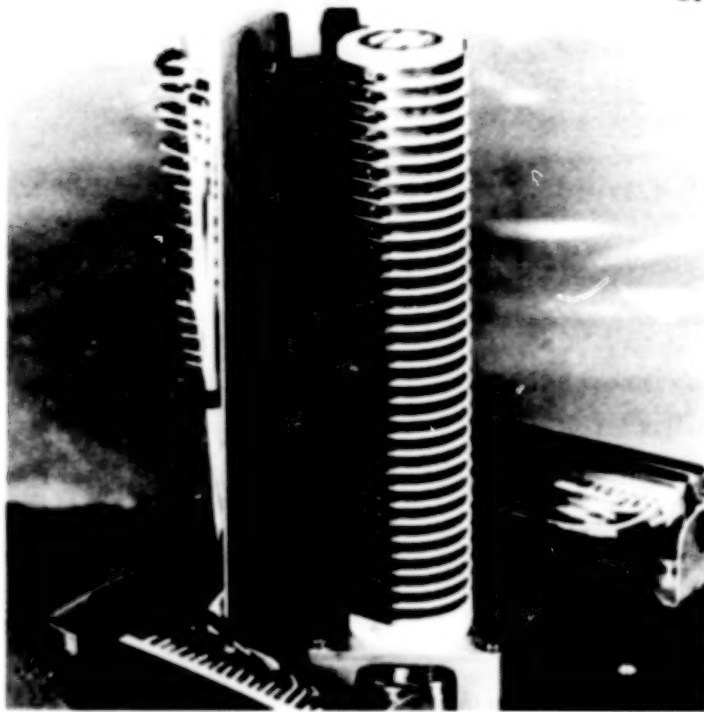


Figure 7. A Typical Slipring Assembly

resistances can be present over very small localized areas. Thus in very low-speed systems there is a very real danger of disturbance to slipring circuit currents.

- High contact resistance in a unit which, prior to delivery to ESTL, had inadvertently been operated for many unscheduled revolutions in air. Black deposits, originating from MoS_2 brush lubricant, were removed from the sliprings before the test could be repeated satisfactorily.
- Thermal changes can provoke a significant, but temporary increase in contact resistance.
- Unexpected differences in performance among nominally identical units due to changes in brush spring pressure, surface condition, brush conformity and alignment, and distribution of wear debris.
- Often the effect of thermal dissipation distributed between the sliprings, brushes, cables and connectors has been underestimated, particularly in dense clusters of cables near anchorage points.

These test observations have resulted in ESTL embarking on a review of current slipring technology, particularly with regard to the reliability of molybdenum disulphide as brush lubricant. The presence of silver sulphide can have a significant effect on surface properties.³

Antenna Pointing Mechanisms

One type of a two-axis controlled platform is shown in Figure 8. Tested over a wide temperature range, it was vital to assess the dimensional stability, the pointing accuracy, and the bearing torque of these complex mechanisms. Very stable pointing accuracies of better than $\pm 0.05^\circ$ were consistently measured but there was some temperature-dependent drift of the null-balance position. In one mechanism, the stability of a stepper motor was disturbed by an incompletely brazed flexure pivot, a device which some design engineers treat with caution as regards their long-term stability.

Gimballed Momentum Wheels

A double-gimballed momentum wheel is shown in Figure 9. The complexity of these mechanisms demanded a test of the wheel motor, operating at 4000 rpm, the gimbal torquer motor, the angular position transducer, and the gimbal bearing which must have a very low, stable friction to avoid orthogonal precession torques affecting the overall stability. The large framework could be sensitive to dimensional change with temperature over the range $+55^\circ$ to -40°C . It is interesting to note that with this particular mechanism, oil-lubrication was preferable to lead lubrication in the gimbal bearings. This could only be found by doing a thermal-vacuum accelerated life test.

Other Mechanisms

Several short but essential tests have been performed on various bearing assemblies, lubrication systems for air-lock cables, and scaled-down models of the Space Telescope roll-out array. Detailed assessment of many components of these items was necessary as the designs were new and very limited knowledge was available of possible failure modes.

Three faint-object-camera mechanisms (filter wheel, refocusing, and shutter mechanisms (Figure 10)) for the Space Telescope were subjected to simultaneous accelerated life tests, each performing in excess of 40,000 actuations. Many measurements have been made on a large number of critical items such as stepper motor, actuator motor, spring assembly, flexure pivots, lead-screw, lead-lubricated bearings, plastic gears, and electromagnetic position sensors. These mechanisms were typical examples of the dilemma often experienced by a mechanism designer, who must guarantee that the complete mechanisms will conform to the required specification but must use components that, although of the highest quality available, are not guaranteed by the various suppliers to fulfill the required specification.

Miscellaneous Observations During Mechanism Inspection

An essential aspect of thermal-vacuum testing is that it demands an additional, independent inspection procedure before and after the test. Occasionally, it may be permissible to dismantle a mechanism for detailed post-test component evaluation.

ORIGINAL PAGE 19
OF POOR QUALITY



Figure 8. One Type of
Antenna-Pointing Mechanism



Figure 9. A Double-Gimballed
Momentum Wheel Assembly

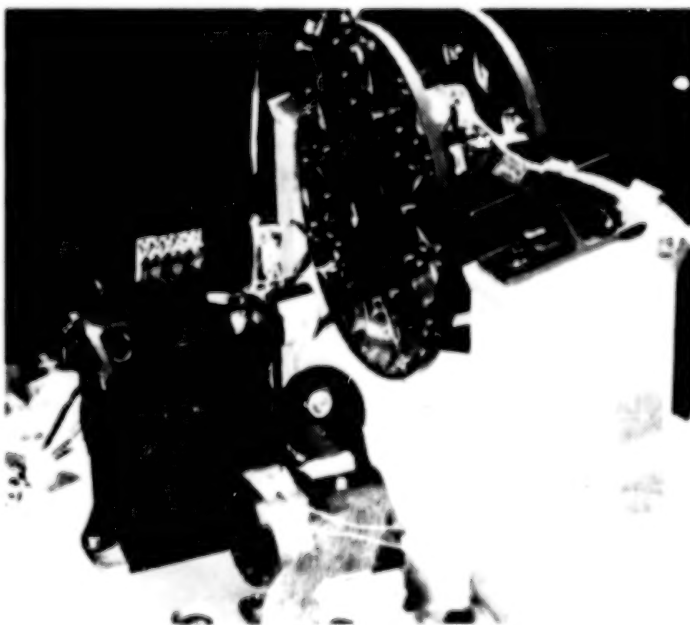


Figure 10. Three Mechanisms
for the Faint-Object Camera
of the Space Telescope

Much valuable data have been obtained on the reliability of many components and lubrication systems. Many minor, but certainly not trivial, problems have been encountered.

A secondary, but very important, advantage is that as a result of the work in ESTL it has been possible to advise manufacturers of improvements that must be made in component design, fabrication techniques, and handling procedures. It has been our experience that, however high are the standards which are achieved in organisations with elaborate inspection procedures, one limiting factor in achieving high reliability will always be the human factor, whereby occasional accidents, errors, poor judgement and lack of consistent attention to detail will inevitably occur, particularly when working within the constraints of tight budgets and time scales. Regrettably, there have been examples of defects which, although almost trivial in themselves, could, given the right set of circumstances, contribute to a failure mode. Some examples include: undesirable blemishes, scratches, poor surface finish, misalignment, and inadequate cleaning of critical components; poor soldering and cable insulation techniques, associated with contamination by splashes of solder, adhesives, and potting compounds; handling of bearings with bare hands can eventually cause small localized areas of corrosion; burrs, swarf, and damaged surface coatings on and near fasteners; particle contamination from many sources; and electrical cable rubbing on sharp edges of rotating components.

CONCLUSIONS

Thermal-vacuum testing has proved to be essential in providing a detailed assessment of the reliability of complex mechanisms by subjecting them to realistic simulations of the anticipated flight conditions, where lifetimes in excess of 10 years are now expected.

Of vital importance is that these tests have been proved to be cost-effective in avoiding delays and disturbances to a number of European projects, as several previously unknown failure modes have been detected. There is now complete confidence in many designs following independent, fully-documented performance assessment.

Much valuable data have been obtained on many mechanisms and components about their operational parameters, power dissipation, and wear processes. There is frequent evidence of how important it is to implement comprehensive inspection and product assurance systems at all stages of mechanism development and construction, to avoid the human factor of accidents, errors, and poor judgement.

ACKNOWLEDGEMENTS

The greatly appreciated help of Mr. Mervyn Briscoe, recently retired from ESA, in the preparation of this paper. This paper is published by permission of Dr. T. N. Marsham, Managing Director of the Northern Division, United Kingdom Atomic Energy Authority.

REFERENCES

1. Briscoe, H. M., A Rationale for the Testing of Space Mechanisms, Proceedings of First European Symposium on "Space Mechanisms and Tribology", ESA SP-196, 1983.
2. Roberts, E. W., Sliding Electrical Contacts in Space: Observations on Existing Technology and New Trends in Low-Speed Applications, Proceedings of First European Symposium on "Space Mechanisms and Tribology", ESA SP-196, 1983.

N84
25086

UNCLAS

IMPROVING SLIPRING PERFORMANCE

DONALD N. MATTEO*

ABSTRACT

The use of dry film lubricated, silver bearing slipring/brush combinations is not new to space applications. General Electric's product line of solar array drive and power transfer assemblies (SADAPTA's), dating back to the mid 1970's, all include slipring assemblies with this material combination. These slipring assemblies (including very similar designs flown by other contractors) have enjoyed considerable on-orbit success, however, recent experiences have indicated the need to improve the dynamic noise performance of the sliprings.

This paper describes the original slipring design for the DSCS III spacecraft, the handling and testing of the slipring assembly before launch, the on-orbit performance indicating the need for improvement in dynamic noise, the subsequently incorporated design improvements, and the results of testing to verify noise performance improvement.

INTRODUCTION

Any Earth orbiting spacecraft that is equipped with a continuously rotating solar array and is attitude controlled in such a way that one axis is continually pointed at the Earth, requires a means of transferring electrical power and signals across the rotating joint (solar array drive) from the solar array to the spacecraft centerbody. This transfer is usually accomplished with a slipring assembly that is integral with the solar array drive assembly.

A typical slipring assembly is shown in Figure 1. This unit is part of the solar array drive and power transfer assembly (SADAPTA) for the DSCS-III spacecraft, a synchronous altitude communications satellite developed by General Electric for the United States Air Force. The unit, shown in a partially assembled state, is built integrally with the solar array drive shaft. (For the purpose of this paper, the array will be considered to be the rotating body and the satellite centerbody stationary.) Wires carrying electrical power and signals from the rotating array are routed down the ID of the shaft (from the right in the figure) and pass through slots in the shaft where they are soldered to the sliprings as part of the slipring rotor assembly. Brushes, fixed to the housing by the brush block assembly (shown as the upper surface of housing in the figure), contact the sliprings and "pick off" the power and the signals from the rotating assembly. The

*General Electric Company, Space Systems Operations, Valley Forge, Pennsylvania

ORIGINAL PAGE IS
OF POOR QUALITY



Figure 1. DSCS III Slipring Assembly

wires, shown protruding through the top surface of the brush block assembly, are soldered to the brush holders and carry the power and the signals to connectors (not shown) which mate with the vehicle harness.

The subject of particular interest in this paper is the variation in sliding contact resistance at the brush/ring interface and the resultant variations in signal strength (noise) for signals carried across this interface. Although variations in contact resistance can also affect the slip-rings carrying power, this paper will concentrate on the signal carrying rings because:

- Power rings operate at higher current densities and are less susceptible to contact resistance effects.
- Power rings on all GE SADAPTA's embody two to three times as much brush redundancy and, therefore, are almost totally unaffected by individual high resistance spots.
- Small variations in current across power rings are less detrimental to system performance than similar variations on signal levels.
- Actual experience on power rings has been very good with respect to current variations.

SLIPRING CONFIGURATION

Figure 2 shows the DSCS III SADAPTA, which contains two slipring assemblies: one to transfer the power and signals from the north solar array and one for the south array. These assemblies are interconnected by a 1.8-meter (six-feet) long Beryllium shaft and are driven at orbit rate by a set of redundant drives located at the south end. Figure 3 shows some of the internal details of one of the slipring assemblies.

Each of the two slipring assemblies consists of a set of conductive rings (the rotor assembly) that rotate with the solar arrays and a set of brushes (mounted to the brush block assemblies) that are fixed to the satellite centerbody. The conductive rings are hard silver, plated over copper which is plated over the epoxy rotor. Epoxy barriers are provided between rings to prevent shorting. The brushes are stackpole SM-476, a silver, MoS₂, and graphite composition, which are soldered to Glidcop AL 20 brush arms. There are two brushes per signal ring which are electrically and mechanically interconnected by the brush arms (Figure 3). Brush force is maintained at 23 grams nominal. The rotor assembly is assembled to the SADAPTA shaft and is supported by the SADAPTA shaft bearings (Figure 4).

ORIGINAL PAGE 13
OF POOR QUALITY

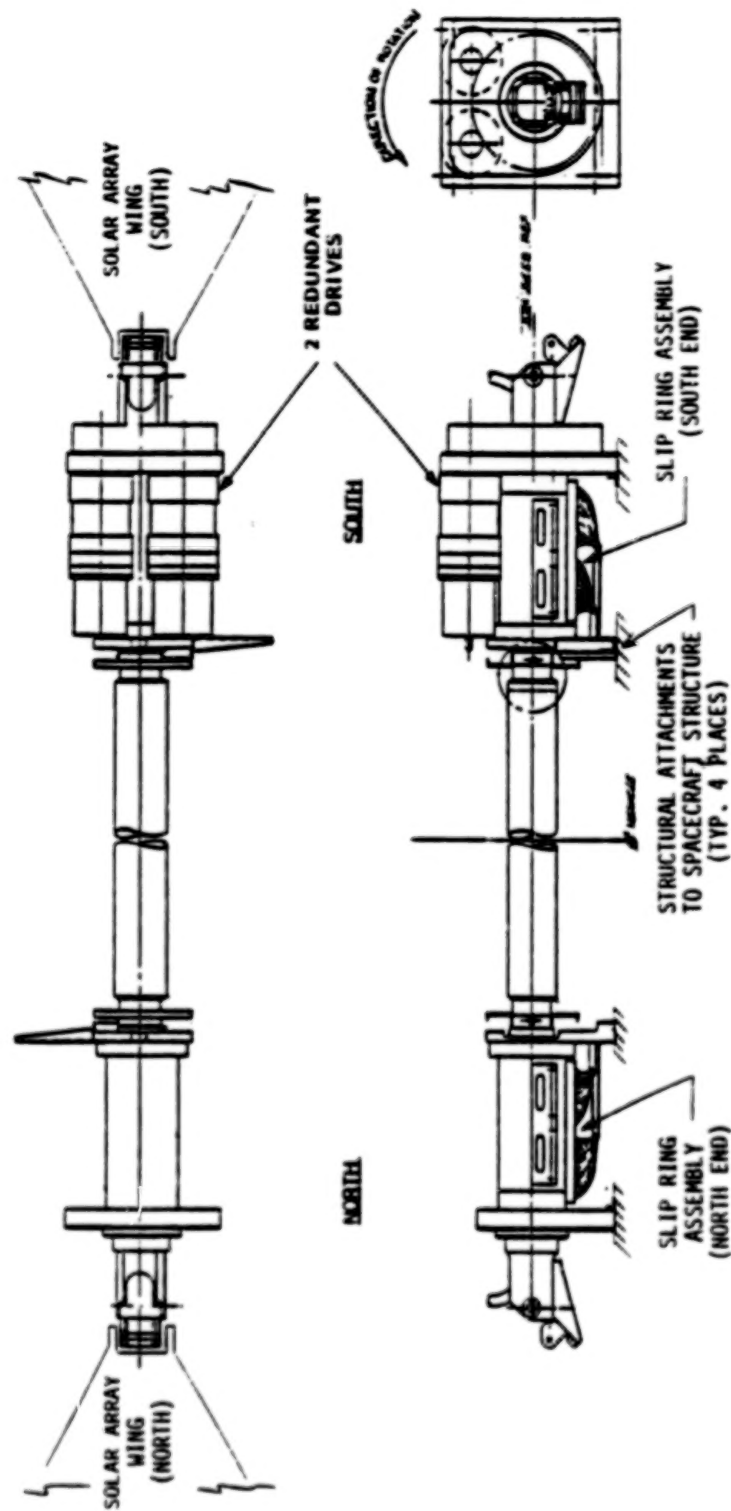


Figure 2. Solar Array Drive and Power Transfer Assembly (SADAPTA)

ORIGINAL PAGE 13
OF POOR QUALITY

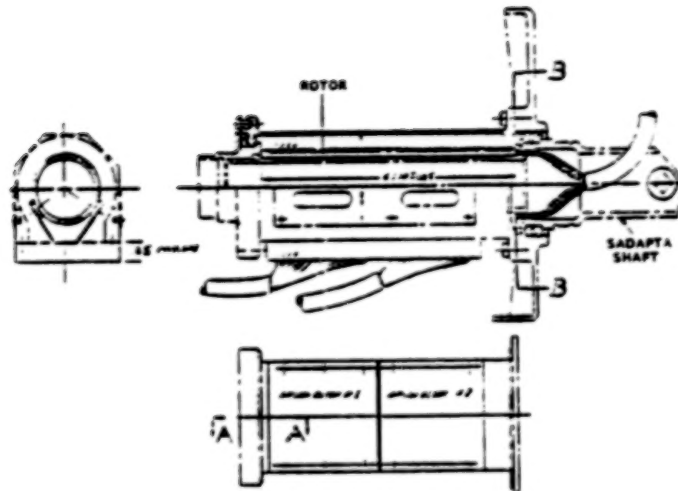


Figure 3. Typical Brush/Brush Spring Assembly

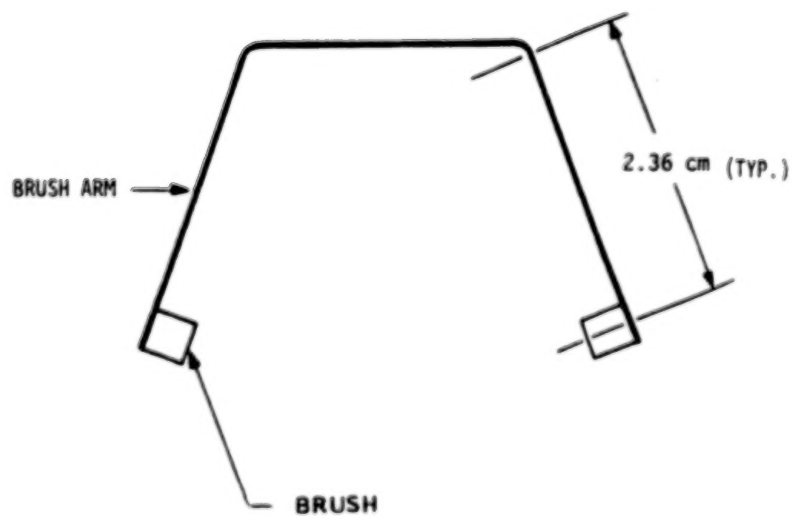


Figure 4. Typical Slipring Assembly

FUNCTIONAL RELATIONSHIP BETWEEN SLIPRINGS AND CRITICAL SIGNALS

Figure 5 is a functional relationship schematic showing how signals from the Sun sensors (mounted on the rotating solar array) pass through the sliprings and into the attitude control electronics (ACE) buffer amplifiers. Several other signals and electrical power pass through other rings, but have been deleted for clarity to concentrate on the more critical Sun sensor signals. Figure 6 is an electrical schematic showing how Sun sensor signals from each of the north and south solar array wings pass through the sliprings, are fed to the ACE buffer amplifiers, and the outputs of the buffer amplifiers are fed to the difference amplifiers (the output of which is a direct measure of spacecraft attitude). This output, in addition to being available to telemetry, is used directly in the yaw attitude control loop.

The control of the spacecraft yaw axis during normal orbital operations is accomplished using Sun sensors mounted on the yokes of the solar array for sensing yaw attitude coupled with Kalman filter type algorithms implemented digitally in the ACE.

The Sun sensors are simple-analog silicon cells mounted in two units: one on the north solar array yoke and one on the south (Figure 7).

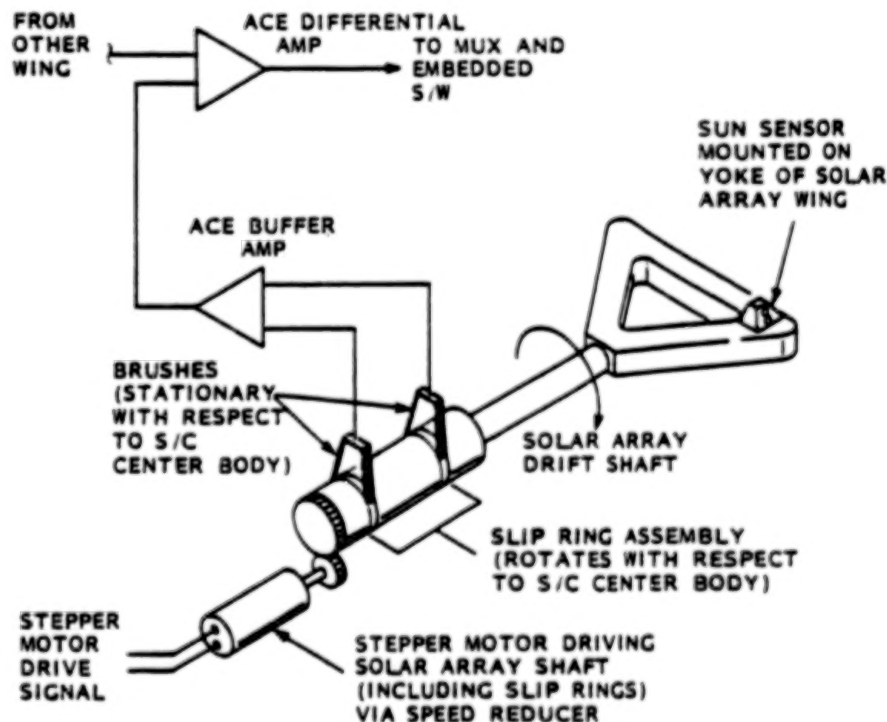


Figure 5. Functional Relationship Schematic

Each unit is comprised of four silicon detectors and a thermal control system to maintain the temperature of the Sun detectors nearly constant ($\pm 0.5^\circ\text{C}$ variation about a nominal 25°C). The north unit is comprised of

ORIGINAL PAGE IS
OF POOR QUALITY

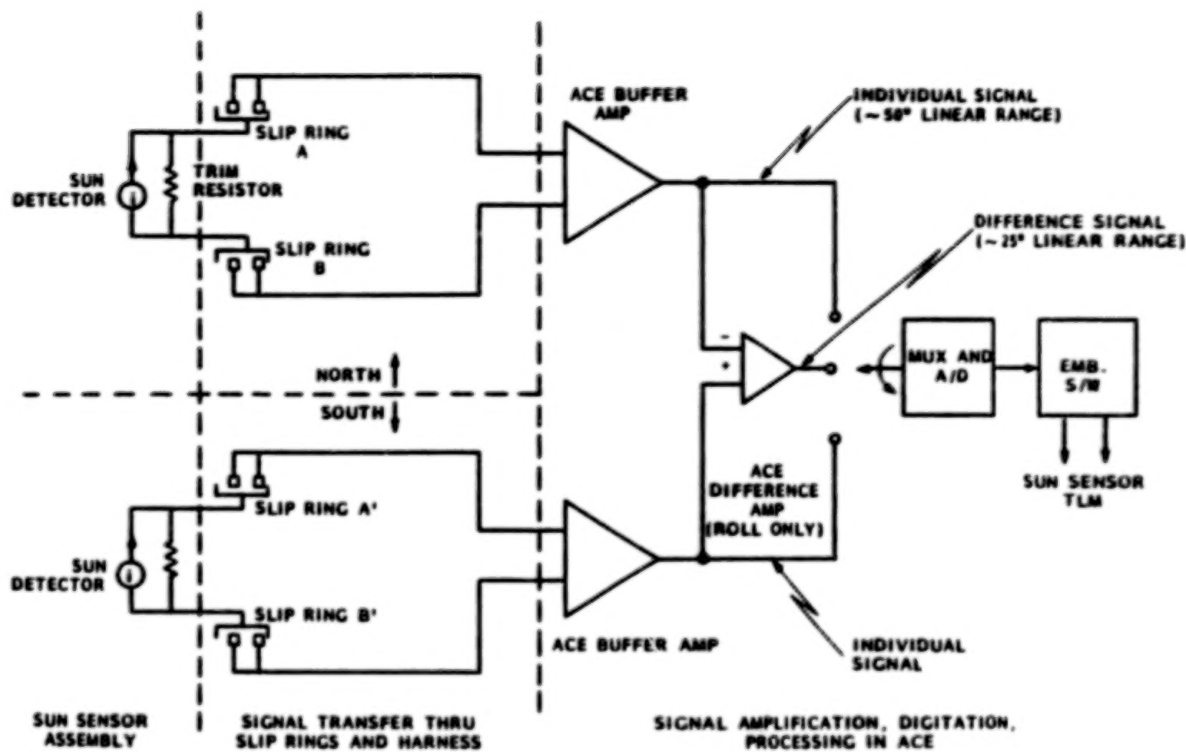


Figure 6. Electrical Schematic of Attitude Control Electronics, Sun Sensors, and Sliprings

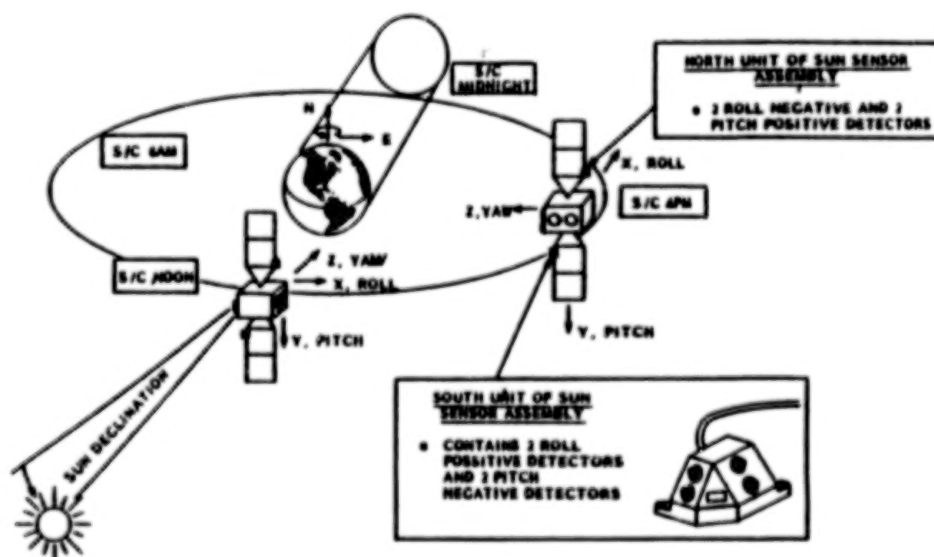


Figure 7. DSCS-III Sun Control Geometry and Sensing

two roll negative and two pitch positive detectors, and the south unit is comprised of two roll positive and two pitch negative.

The detectors that are used for yaw control are the roll Sun sensors. Note that the roll and yaw axes interchange inertial orientation every 90° of spacecraft orbit motion (Figure 7). This results in the roll eyes sensing pure spacecraft roll attitude at noon and midnight and pure spacecraft yaw attitude at 6 am and 6 pm. At intermediate orientations these detectors measure a portion of roll and a portion of yaw, the apportioning factor being a sinusoid of orbit frequency.

Pitch detectors are used to sense spacecraft pitch motion during acquisition maneuvers and to sense solar array position with respect to the sun-line during normal orbit operations. Accordingly, the sliprings are directly in the spacecraft yaw attitude control loop and any degradation of slipring performance can directly affect spacecraft attitude performance.

BACKGROUND OF THE NOISE PROBLEM

Recognizing the sensitivity of the spacecraft performance to slipring induced noise, several precautions were taken (before the first DSCS flight) to control any noise to tolerable levels. These precautions were:

- A specification of $800\text{-m}\Omega$ maximum (at the system level) was established for any variations in signal ring resistance during all ground testing. The level was calculated to be well within the limits which would yield within specification yaw performance. Component level acceptance limits were much lower ($20\text{ m}\Omega$).
- The ACE and its imbedded software converts the analog difference signal between the north and the south Sun sensors into digital words (counts) for use in the attitude control algorithms. It was determined that proper yaw attitude control would result if noise-induced effects represented less than one count. It was calculated that the sensitivity of the system to slipring noise was 0.5 to 0.6 counts/ohm. Accordingly, the $800\text{-m}\Omega$ limit for slipring noise content was well within acceptable limits.
- It was known that motion between the brushes and the rings in a moisture bearing atmosphere would produce a partially insulating film of MoS_2 on the rings. Accordingly, during all periods when the sliprings were rotated or vibrated during ground testing (other than in thermal-vacuum testing), the slipring assembly was purged with filtered, dry gaseous nitrogen.
- End-to-end systems tests were run, stimulating the sensor eyes and monitoring the output of the ACE difference amplifiers, verifying that the output was within tolerance limits.
- The system was designed to sample Sun sensor signals at the time when the contact resistance of the brushes/rings was expected to be most stable, that is when the sliprings/solar array drive shaft were at rest between bursts of motor pulses.

When the DSCS III first flight vehicle's sliprings were last tested for noise (before launch) the resistance variations ranged between 50 and 700 m Ω .

ON-ORBIT OPERATIONS

Shortly after DSCS III orbit injection and approximately 6 hours after three-axis attitude control was established, the solar array drive was commanded to track the Sun, and an oscillation in yaw was detected. The redundant roll Sun sensor loop (there are two complete loops, from Sun sensors through ACE) was selected for control. The oscillations were eliminated. Approximately 1 month later, the original roll Sun sensor loop was again selected for control as a diagnostic measure. Yaw oscillation immediately resulted. The redundant roll Sun sensor loop was again selected for control and the oscillations stopped. The redundant roll Sun sensor loop has successfully controlled the spacecraft ever since. Except for further diagnostics, there were no additional occurrences of yaw oscillation.

POTENTIAL CAUSES OF YAW OSCILLATIONS

All potential causes of the previously mentioned anomaly were investigated. In addition to the sliprings, those included:

- The Sun sensors
- The vehicle and solar array harnesses
- The optical effects
- The ACE

Each of the previously listed potential causes of the problem were the subject of intensive investigations. These investigations, other than the slipring investigations, are outside the scope of this paper. Although a single source of the problem was not pinpointed, the most likely cause was determined to be resistance variation noise introduced into the Sun sensor signal circuits by contact resistance changes at the slipring/brush interface. This conclusion has been determined for the following reasons:

- Measured on-orbit data have indicated variations in the output signals of the individual buffer amplifiers and of the differential amplifier
- Variation in the output of the ACE differential amplifier will directly result in the type of anomalous yaw attitude performance that has been observed.
- The only element in the loop consisting of the Sun detectors, the trim resistors, the harnessing, the sliprings, and the ACE amplifiers that has been measured to have a variable parameter that could account for the anomaly is the slipring assembly, the contact resistance of which has been measured to vary.

- Postlaunch ground tests on deliberately degraded slipring assemblies have resulted in resistance variation noise of the right order of magnitude to have caused the anomaly. (Note that all testing before launch on undegraded slipring assemblies resulted in noise figures well below the level necessary to account for the anomaly.)

CAUSES RELATED TO SLIPRINGS

Several potential causes of the yaw anomaly, which are related to the slipring assembly, were considered. These causes are discussed in the following paragraphs.

Electrostatic Discharge

The spacecraft was launched during a period of high solar-storm activity, so the possibility of build up of high electrostatic discharge (ESD) energy near entrance to the umbra was thought to be possible. Theoretical analyses were performed to predict the magnitude of the ESD discharge currents and subsequently tests were performed to validate the numbers. The tests indicated that this phenomena could result in 0.05 A surging through the sliprings for a period of 1200 ns. Tests using the engineering model SADAPTA were subsequently performed to demonstrate the effects of various ESD discharge current magnitude and duty cycle. The results of the tests indicated that, if anything, ESD discharge currents tended to clean the sliprings and brushes. In addition, no apparent pitting of the brushes or rings occurred. Accordingly, ESD was eliminated as a cause of the problem.

Temperature Gradients

Temperature gradients within the slipring brush block assembly were considered as a possibility. If the sliprings experienced a large temperature gradient, thermally induced stresses could result in failure of the signal leads. Examination of flight and qualification data, however, showed that the SADAPTA temperatures were near normal (approximately 20°C), so this type failure was eliminated as a suspected cause.

Mechanical Shifting

Also considered as potential problems were mechanical shifts within the slipring assembly that would cause the brushes to contact the sides of the track and misalignments of the brushes that would result in the brushes contacting the track in a skewed attitude for a portion of the total 360° of travel. Investigations of the track and brush tolerances indicated that displacement of the brush block sufficient to cause contact with the side of the track could not occur. Tests on the engineering model SADAPTA were subsequently run to test these hypotheses. Because the test results did not produce the noise signatures observed in the flight data, further investigations of brush displacement/misalignment were not considered necessary.

Contamination

Contamination on the surface of the sliprings was considered as a possible cause or contributor to the problem. Investigation of system test data, which indicated that contamination would be cleaned up after several rotations, also indicated that a large amount of noise could appear if the SADAPTA was quiescent for several weeks--even under constant purge. The most striking evidence of this is a 6 hour test which had been performed about 2 weeks after a thermal-vacuum test. During this time, the rings were under continuous purge, but the first orbit of the rings showed large values of Sun sensor noise over a significant portion of the orbit. Noise of amplitude of 20 counts peak-to-peak occurred on the north roll negative Sun sensor signal covering a span of 2.5 hours from near spacecraft night to 3:00 am. Because the flight spacecraft was stationed at NASA/Kennedy Space Center for a long period before launch, it is certainly possible for initial contamination to be present when the rings were first used in space.

Although it was a viable theory, all ground test results indicated that the noise would disappear within several rotations of the SADAPTA shaft. This was not happening on-orbit. Furthermore, the magnitude of slipring resistance variation apparently necessary to produce the on-orbit disturbances (20 to 30 Ω) was several times the magnitude of any theoretical contamination induced contact resistance change or that which had been measured in ground testing.

Other interesting theories considered and discarded were:

- Discontinuities or bumps at the ring/lead wire attachment--CAD generated plots of design attach points (below surface of rings) showed that the locations bore no resemblance to the observed locations (solar array position with respect to time) of on-orbit or ground test noise.
- Vibration of brush/brush springs causing brushes to bounce out of contact with rings--Calculations showed that well over 100 g's would be required to drive a normally preloaded brush out of contact with its ring. Nothing in the system dynamics could cause that level of acceleration on the brushes in orbit.

ENGINEERING SADAPTA TEST RESULTS

A series of tests were run on the engineering south SADAPTA which was the life test unit. This SADAPTA had been stored in the engineering laboratory without nitrogen purging and had been exposed to varying conditions. Furthermore, the brush forces on all rings were well below the specification values of 23 grams.

A number of observations were made concerning this engineering unit:

- a. There was no difference in noise as a result of a change in signal polarity.

- b. There were small differences in noise due to radial and axial forces up to 10 pounds applied to the output shaft.
- c. The noise was significantly lower with two brushes than it was with one brush (likewise four brushes produced better results than two (i.e., two rings in parallel)).
- d. The trailing brush appeared to be quieter than the leading brush.
- e. Increasing brush force above 23 grams did not appear to reduce noise, but decreasing force below 10 to 13 grams did cause an increase in noise.

Test data plotted in Figure 8 were generated by deliberately lifting the brush off of the ring with calibrated forces when the companion brush was out of contact. The following important observations are from these data:

- The 23-gram force appears to have been optimally selected because it lies just beyond the knee of the curve.

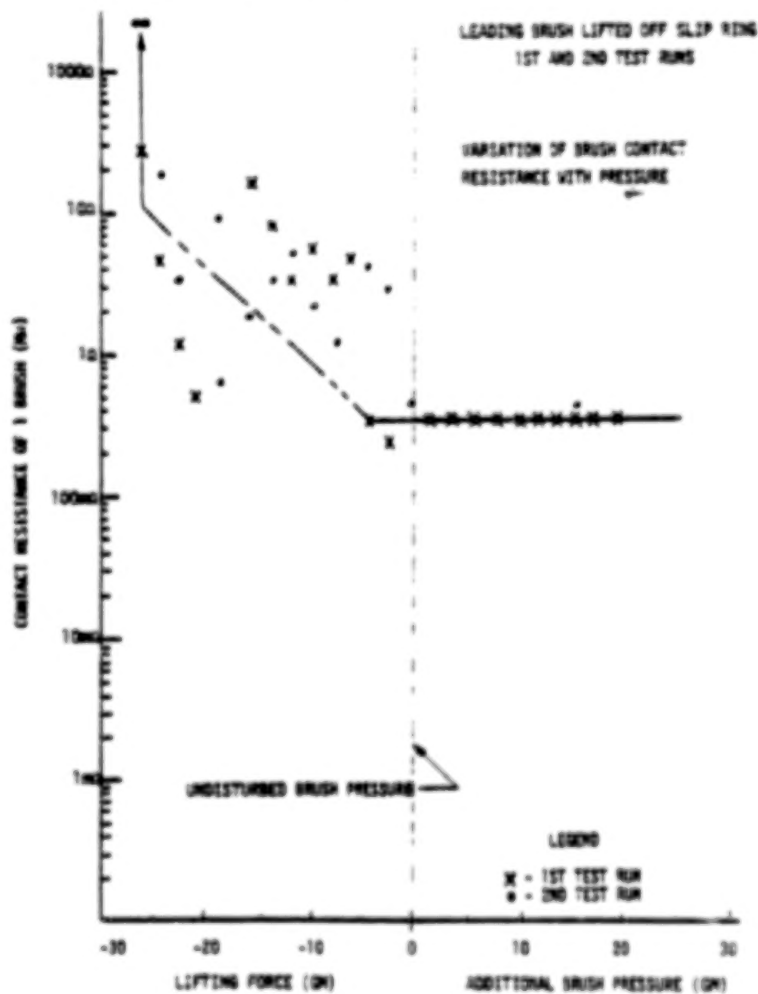


Figure 8.

- Increasing nominal brush force beyond 23 grams does not appear to improve contact, but it can provide margin for brush force variation in production or service without degrading performance.
- Decreasing the brush force below the 23-gram nominal can produce resistance variations of the magnitude necessary to account for orbital performance (particularly when viewed in the light of subsequently discussed system nonlinearities).

With attention focused on low brush force, a series of more controlled brush force versus noise tests were run. A special fixture was designed and built for accurately measuring the undisturbed brush forces of the engineering unit slipring assemblies. As can be seen from Figures 9 and 10, the brushes on this unit (after considerable testing and handling) do not line up well and significant variations in brush forces are to be expected. In fact, on the south unit the forces varied from five to 18 grams, and on the north unit (which had always been a quiet performer) the forces varied from 16 to 22 grams. A series of dynamic noise measurements were then made (including some with deliberately altered brush force).

Figures 11 and 12 are plots of the resulting data. Again, the sensitivity to brush force is obvious, both on magnitude and frequency of noise spikes.

It was concluded that the cause and corrective action for the potential low brush force must be identified.

BRUSH SPRING INVESTIGATIONS

The material used for the slipring brush springs, Glidcop AL20, and the processes used for fabricating the springs were investigated in detail. These investigations are too lengthy to discuss in detail here, but the salient points of the investigations were:

- Soldering the Glidcop with a high temperature silver solder caused a significant drop in elastic modulus (13-percent change).
- Tests of the spring constant of Glidcop springs showed that the calculated values using published data were much lower than the test results (35-percent lower).
- The process used to bend the springs produced nonuniform bends, some of which could result in surface cracking of the springs.

Each of the factors suggested that the force on the brush holding it against the ring may have been inadequate on some brush/ring assemblies. This concern has been removed for future SADAPTA's by changing the brush spring material to beryllium-copper and increasing brush force from 23 to 41 grams per brush to provide margin.

ORIGINAL PAGE 18
OF POOR QUALITY

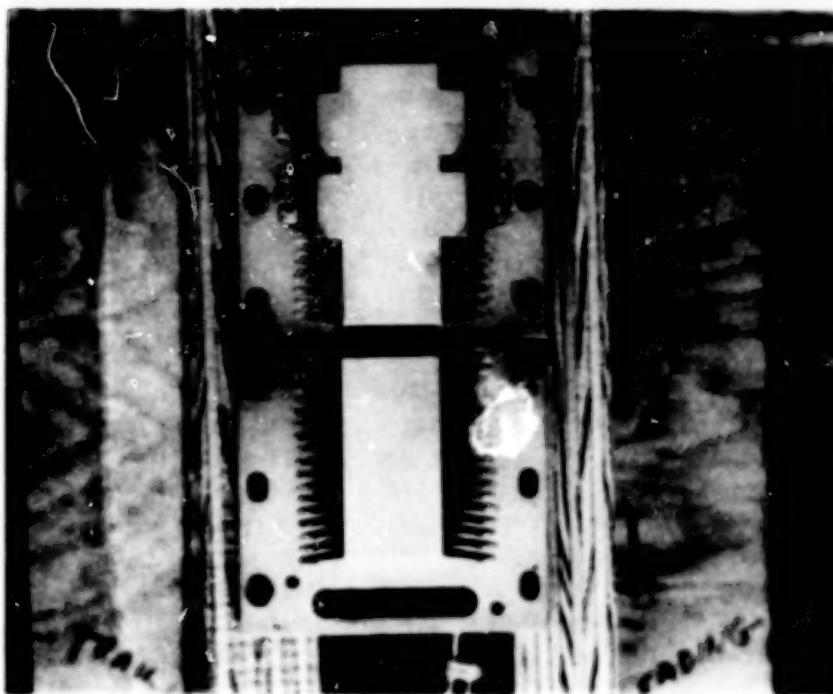


Figure 9. View of the Brush Blocks from Above. (The trailing brushes are on the left and the leading brushes on the right. Note that the brushes are irregularly aligned.)

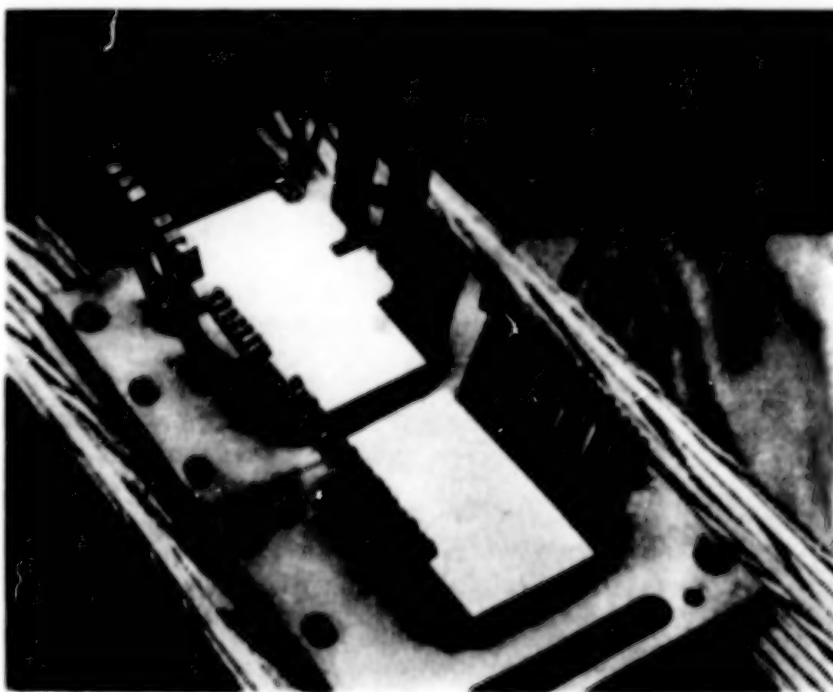


Figure 10. View of the Disassembled Brush Blocks from the Side. (The trailing brushes are on the left and the leading brushes on the right.)

ORIGINAL PAGE 19
OF POOR QUALITY

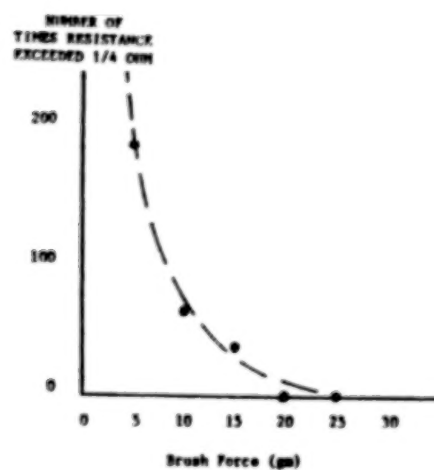


Figure 11.

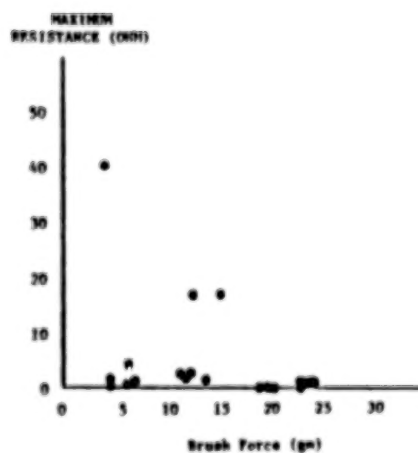


Figure 12.

SYNCRHONIZATION

The effect of synchronization between the Sun sensor signal sampling and solar array drive cycle must be considered in any discussion of the effect of slirping noise on attitude control errors. It has been determined that the lack of such synchronization will introduce errors into the Sun sensor signals (and resultant attitude control errors) which can readily be eliminated by resynchronization.

Figure 13 shows the timing relationship between the periods when the solar array drive is driven by bursts of motor pulses, the rest periods between pulse bursts, and the typical resistance variation as a function of time which results from slirping motion. As shown, the planned data sampling time was designed to occur near the end of the rest periods when resistance is expected to be most stable. Should data sampling occur during motion (or shortly thereafter), considerably larger resistance variations should be expected. In fact, early in the DSCS III mission, this lack of synchronization did occur because of certain commands that reset the relationship between onboard counters. At that time it was believed that the slirping performance was degrading rapidly with time, when in fact what had occurred was the previously mentioned desynchronization. When discovered, this problem was easily corrected by ground command to resynchronize.

NONLINEARITIES

As mentioned before, early mission performance indicated apparent increases in slirping resistance which were very high compared to any reasonable expectation of increased slirping resistance. It was discovered by analyzing and testing the Sun sensor circuitry that increases in total circuit resistance (contributed to by increases in slirping resistance) caused nonlinear effects which made the resistance increase appear higher than it actually was. This was corrected by circuit changes that are outside the scope of this paper.

DESIGN AND PROCESS CHANGES

For subsequent DSCS spacecraft the following changes are being implemented:

a. Paralleling of Rings

All critical Sun sensor signals are now brought across the rotating joint on two parallel slirpings (four brushes for each signal and four brushes for each return). As previously noted, this paralleling drastically reduces slirping noise in the following manner:

- (1) The contact resistance of a set of four brushes is minimized by the law governing resistances in parallel:

$$\frac{1}{R_T} = \frac{1}{R_1} + \frac{1}{R_2} + \frac{1}{R_3} + \frac{1}{R_4}$$

ORIGINAL PAGE 19
OF POOR QUALITY

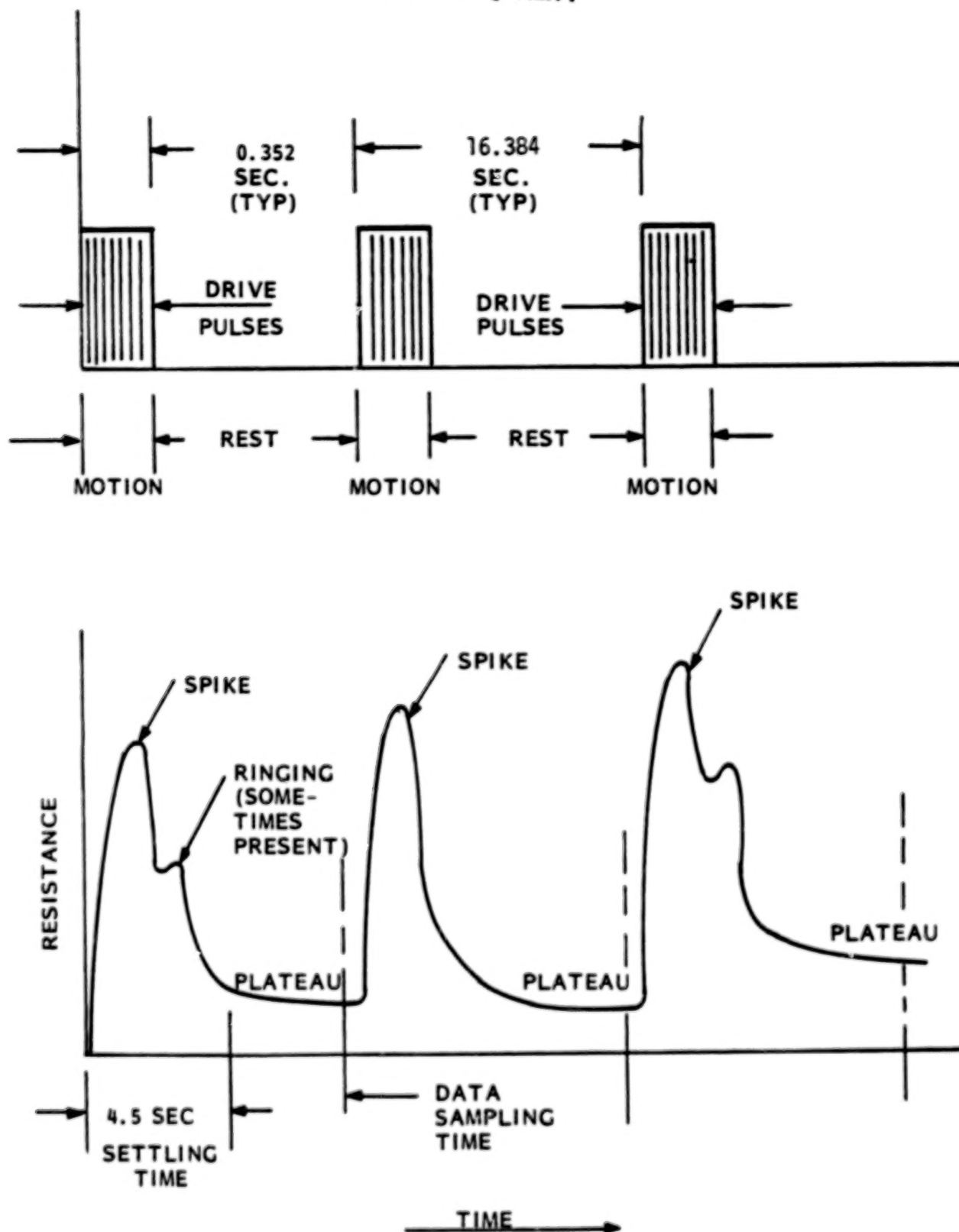


Figure 13. Typical Slipping Resistance Trace

- (2) The statistical probability of having at least one low-resistance path at any instant of time is very high. If such a low-resistance path exists, it will dominate the total resistance (R_T) and maintain a low-noise signal across the slipring set.

(b) Nitrogen Purging

The nitrogen purge has been extended so that it now covers the total vehicle life (with the exception of a few hours). Purging will eliminate the possibility of contamination caused by oxidation.

(c) Brush Configuration

The brush contact force has been increased from 23 grams per brush nominal to 41 grams per brush nominal.

The brush pairs that were mechanically and electrically interconnected have been electrically separated to enable testing of individual brushes for noise during acceptance testing at the vendor.

The brush spring material has been changed from 0.010" Glidcop AL20 to 0.012" beryllium copper, and the brush attachment has been changed from silver solder to soft solder.

(d) Relocation of Buffer Amplifiers

The ACE buffer amplifiers have been relocated to the rotating array. This has the effect of transmitting amplified signals across the sliprings and reducing the system's sensitivity to slipring noise from 0.5 ohms per count to 42 ohms per count.

The changes have been tested on both engineering and prime hardware and have shown that:

- Significantly less noise is produced by the sliprings.
- The system is considerably less sensitive to any noise that is produced.

A life test to evaluate the effects of increased brush force on brush life is currently underway.

CONCLUSIONS

The following general conclusions can be reached about the management of slipring noise in a spacecraft control system.

- To initiate the noise, some form of dielectric contamination must exist at the slipring/brush interface.
- A reduction in brush spring force to significantly less than the design minimum force must occur to render the slipring assembly susceptible to the previously mentioned contamination.

- The fewer the number of brush/ring sets in contact with each signal circuit, the more statistically susceptible the circuit is to contamination induced resistance variations.
- Critical sensor signals should be carried by two parallel sliprings, thus placing four brushes in parallel.
- Synchronization of sensor sampling times and drive pulses must be maintained at all times.
- Slipring assemblies of this type must be purged with clean, dry nitrogen at all times (except when specifically precluded by test operations underway at the time such as leak testing) up to as close to launch time as possible.
- Margin above nominal brush force should be provided to account for in-process or in-service degradation (this was changed from 23 to 41 grams per brush for DSCS-III).
- The individual brushes of a brush pair should be electrically separated to enable in-process measurement of individual brush/ring contact resistances during testing.
- Whenever possible, critical signals should be amplified before passing across the sliprings.

REFERENCES

(All GE Documents)

Haltner, A. J., "Rate of Insulating Film Growth on Silver Slip Rings," PIR-U-1R30-DSCS-1077, October 14, 1981.

Haltner, A. J., "Static Discharges of Slip Ring Noise," PIR-U-1R30-DSCS-1199/B-0780, February 7, 1983.

Haltner, A. J., "Potential for Ice Formation on Slip Rings During Launch Phase (Response to Action Item 26)," PIR-U-1R30-DSCS-1212-B-0903, April 12, 1982.

Haltner, A. J., and D. Matteo, "Tear-Down Observations on Engineering Life Test SADAPTA Unit on March 19, 1983," PIR-U-1R30-DSCS-1209/B-0899, April 7, 1983.

Haltner, A. J., and R. Ross, "Examination of Engineering Life Test SADAPTA Brushes by Scanning Electron Microscopy," PIR-U-1R30-DSCS-1210/B-0900, April 8, 1983.

Haltner, A. J., "Observations on III-A2 SADAPTA," PIR-U-1R30-DSCS-1223/B-0955, May 4, 1983.

Koller, R., "Minimum Flow of Dry Nitrogen Gas, to Preclude Diffusion of Building Air into the DSCS SADAPTA," PIR-DSCS-7201, October 26, 1981.

Matteo, D., and A. J. Haltner, "Response to Action Item 64, DSCS Yaw Anomaly," PIR-U-1R21-DSCS-B-0917, April 18, 1983.

Stockoff, E., and A. Schneider, "Effects of Brush Pressure on Slip Ring Electrical Noise," PIR-U-1R21-DSCS-7630, August 26, 1983.

"Process Specification for Requirements and Procedures for SADAPTA Nitrogen Purging and Contamination Control," 171A4899.

N84

25087

UNCLAS

THE DESIGN AND DEVELOPMENT OF TWO-FAILURE TOLERANT MECHANISMS FOR THE
SPACEBORNE IMAGING RADAR (SIR-B) ANTENNA

S. J. Presas*

ABSTRACT

This paper describes the performance requirements, design constraints, and design qualification status of the mechanisms necessary to restrain, deploy, and stow the SIR-B antenna experiment on the Shuttle Orbiter.

INTRODUCTION

The SIR-B antenna is a flat array that must mount stowed into a standard European Space Agency Shuttle pallet within a small envelope so that the pallet may be shared with other experiment(s). For this purpose, the antenna array was divided into three sections: center, aft, and forward. The center section remains attached to a pallet mounting truss, the fore and aft sections rotate on hinges perpendicular to the Shuttle centerline to nest atop the center section. The forward is the inner leaf and the aft is the outer leaf. Upon command, the mechanism must remove the Launch and Landing Restraint System (L/LRS), deploy the antenna leaves to a flat position, and initiate antenna tilt on an axis parallel to the centerline of the Shuttle to any command position between 15° and 60° elevation. After experiment conclusion, or at any time during the mission, the mechanism must stow the antenna and latch it ready for re-entry. (See Figure 1 and Figure 2.)

DESIGN CONSTRAINTS

Safety Considerations

Because the antenna protrudes beyond the Shuttle payload bay door envelope after it is deployed and tilted to the maximum angle of travel, safety requirements may be met only by jettisoning the antenna array or by using two failure tolerant mechanisms to ensure safe stowage and latching into landing configuration. We have selected the latter approach. See Figure 3.

Loads

The stowed antenna is exposed to the launch and landing loads encountered in the Shuttle cargo bay.

Performance

The deployed antenna array must deploy and remain flat within 6.35 mm (0.25 inch).

*Ball Aerospace, High Technology Products, Boulder, Colorado

Schedule

Existing mechanisms were to be used where possible to reduce design and development time.

Power

28 Vdc power available.

115 Vac 400-Hz power available (manual controlled console only).

Sixteen pyro-initiator circuits available (eight pyro devices possible; manual console only.) Restricted to NASA Standard Initiators (NSI-1) only.

Environment

The antenna mechanism must be capable of operation in hard vacuum at -34.4° to $+71.1^{\circ}\text{C}$ (-30° to $+160^{\circ}\text{F}$.) Multilayer insulation may be used as required to maintain the mechanism temperature within those limits.

DESIGN SUMMARY

The basic antenna array is made of eight subarrays or panels arranged into three sections. All panels are supported by tubular aluminum structure. The center section is backed by a rigid triangular truss and the aft and forward sections are supported by a flat frame. The antenna array is stowed into approximately one third of its deployed length (from 10.74 to 3.99 m) (423 to 157 inches). The center section remains stationary, the forward (inner) section folds into it, and the aft (outer) section folds over the other two. A locking latch between the center and outer leaves is provided to obtain a solid package. See Figures 1 and 2.

To mount the antenna array into the Shuttle accommodation pallet, a rigid tubular frame (pallet truss) is used that also serves to support the two redundant electrical control boxes.

The antenna pointing requirement is accomplished through a tilt hinge, located between the pallet truss and the antenna array, the axis of which is parallel to the antenna array longitudinal axis. The hinge moves between solid stops and is stowed solid to the pallet truss and locked by a latch for launch and landing. See Figure 3.

The antenna panels are bolted onto the tubular structure by a system of flat fittings with holes to fit the various tube diameters. The fittings have either round or elliptical holes to accommodate panel differential expansion relative to the structure.

From Mission Profile

- The antenna must be stowed and latched during Shuttle launch.
- The latches are retracted and held.
- The antenna array to be deployed flat within 6.35 mm (0.25 in).
- The antenna is pointed (tilted) to a (commanded) angle and must hold within 0.5°.

From Safety (Constraints)

- Double failure tolerant mechanisms to stow antenna within Shuttle door envelope.
- Double failure tolerant mechanisms to latch for landing.
- Single failure tolerant bearings throughout the system.

From Ground Testing

- Actuator torque 11.30 Nm (100 in-lb) minimum.
- Structural rigidity required at 1 g for ground functional tests.

MECHANISM DESCRIPTION

Drives

The aft and forward folding hinges are driven by dc rotary dual drive actuators (DDA) in both deploy and stow directions. In the event of total dc actuator failure (double failure), or two dc power failures, the DDA is a pyro pin puller, and a preloaded viscous dampened actuator (VDA) is released by another pin puller. The VDA will rotate to contact a leaf hinge cross pin and mechanically power the leaf back to stowed position. This third redundant option is manually controlled from the Shuttle cabin through a separate pyro firing console. See Figures 4 and 5.

The tilt hinge is similar to the folding hinges except that there is a negator spring, constantly engaged in the stow direction, which provides a backlash cancelling preload to achieve accurate antenna pointing. There is also a rotary potentiometer for tilt position feedback. See Figure 6.

Launch/Landing Restraint System (L/LRS)

The fore and aft leaves are firmly held to the center leaf by stops reacting against the hinges, and latched by a mechanical claw mounted at the center leaf structure which captures a roller at the forward leaf, thus trapping both leaves against the center leaf.

The entire antenna array is also held to the pallet truss by a similar mechanical claw and roller combination

MECHANISM DETAILS

- Dual Drive Actuator (DDA)--Originally developed by the Jet Propulsion Laboratory (JPL) for their Galileo Antenna Deployment. [Ref: 16th Aerospace Mechanisms Symposium, NASA Conference Publication 2221, May 13-14, 1984.] The DDA basically consists of two dc motors driving independently through redundant differential harmonic drives.

Because of inertial loading of the antenna structure, the DDA output rpm needed to be reduced 10:1 by modifying the harmonic drive gear ratio which increased the output torque. An output torque limiting clutch has been added to the DDA.

- Viscous Dampened Actuator (VDA)--A rotary vane within a matching cylinder for a 186° minimum rotation is dampened by 100,000 centistokes silicone fluid. Rotary power is provided by two constant torque (negator) spring packs on two cylindrical guides at each end of the rotor. There is a thermal compensator/reservoir device Belleville spring loaded and positioned at approximately midstroke during room temperature filling of the VDA chamber.

All three VDA's are preloaded before flight and retained by independent pyrotechnically initiated pin pullers.

A cross pin, which is located at the hinge pin end and closest to the VDA, rotates within a scroll chamber formed by one of the VDA spring guides. As the pyro pin is retracted and the VDA spring guide rotates, the flat at the scroll end contacts the cross pin and transmits torque to the hinge pin. There is never contact between the VDA and the antenna drive mechanism until the pyro pin is pulled.

- Launch/Landing Restraint System (L/LRS)--This consists of a roller and an electric motor actuated claw that engages the roller. The roller is supported by a pin through a bracket bolted to either the aft leaf or antenna truss frame. This claw is part of a latch mechanism in a housing bolted to either the antenna center truss or the pallet truss frame.

The claw pivots through an arc of 42° pushed by a carriage driven by a ball screw nut. The ball screw is rotated by an actuator with two motors on the same shaft. See Figure 7.

Because of the two fault tolerant requirements, as a backup to this main claw for the (landing) stow function only, there is a secondary claw deployed by a pyro pin puller. After deployment the secondary claw is held in place by a ratchet and pawl device. The secondary roller is located by the same pin and bracket arrangement used for the primary claw. See Figure 8.

• Bearings--All critical bearings are single failure tolerant.

- The main hinge bearings are aluminum cylinders with a solid lubricant at the I.D. and O.D. The lubricant is a polyester resin interdispersed with polytetrafluoroethylene (PTFE) in flock or powder form. (Figure 9).
- The latch assembly ball screw end bearings also have polyester/PTFE lube and run inside beryllium metal sleeves.
- The main hinge thrust bearings are large outer diameter, aluminum washers lubricated on both sides with polyester/PTFE lube.
- The latch rollers are coated, outer diameter and inner diameter, with molybdenum disulfide solid film lubricant.
- The latch main claw actuator has leaded bronze dual rotating surface sleeve bearings at the output shaft.

DEVELOPMENT PROBLEMS AND SOLUTIONS

Ball Screw

The latch assembly ball screw mechanism was originally designed to contain Nomex felt wipers bonded to the ice scraper. The wiper method of retention was found unsatisfactory because during engineering verification tests, a wiper came off and was trapped in the ball nut. The wiper was eliminated and the ball screws were lubricated and assembled minus the wipers. The latch assembly contamination barrier surrounding the mechanism was improved to minimize the risk of contaminants entering the area. There were no difficulties with an open (no barrier) latch assembly used during the hinge assembly specimen vibration and thermal vacuum tests.

Hinges

Initially all antenna trusses were to be assembled and riveted, then the hinge press fit, matched drilled, and held with bolts. Because of tolerance requirements, the hinges needed to be mated with an assembly tool (continuous bar), the truss corner fittings matched to the hinges and then the truss work connected and riveted. This method of assembly resulted in satisfactory alignment.

Lubrication

Tight fits between fittings and outer diameter tubing caused surface scratches in some tubes. This problem disappeared when the tubes were lubricated with a film of BASD grease 37951M. All excess grease was wiped off after assembly.

Thrust Washers/Shims

To compensate for thermal expansion/contraction, the fold leaf hinges on the VDA side require a gap of 0.61 ± 0.05 mm (0.024 ± 0.002 in) which is controlled with solid aluminum shims. During assembly with the antenna array in the vertical position (hinge centerline perpendicular to floor), this structure deflected to the point that the shims were in bearing (thrust loads) and some wear and metal shavings appeared. The problem was solved by measuring the gap to be compensated and machining custom spacers (to obtain the desired 0.61 ± 0.05 -mm gap) from spare thrust washers. There was no difficulty in machining polyester/PTFE material to obtain a load sharing thrust bearing system for 1 g assembly.

QUALIFICATION STATUS

The dual drive actuators have been designed, manufactured, and tested. Engineering verification testing and qualification included vibration tests. All flight hardware is now installed.

The viscous dampened actuators have been designed, manufactured, and filled with silicone fluid. Acceptance and engineering verification tests at minimum and maximum temperature in vacuum have been completed.

Performance simulation tests were conducted with a test specimen of a latched tilt hinge in the vertical position in a thermal vacuum chamber. These tests were followed by random vibration tests.

CONCLUSIONS

A different approach to two failure tolerant mechanisms has resulted in an experiment that does not require jettison capabilities to comply with the NASA safety requirements applicable to "Payloads using the Space Transportation System." [Ref: NASA HNB 1700.7A.]

All development problems encountered so far have been corrected. The hinge assembly specimen tests verified the bearings and latch assembly performance at extreme temperature in vacuum and at random vibration.

ACKNOWLEDGEMENT

The author wishes to thank the National Aeronautics and Space Administration, Lyndon B. Johnson Space Center for their permission to publish this paper and to acknowledge the contributions of the engineering staff at Ball Aerospace, High Technology Division, the Jet Propulsion Laboratory Pasadena, California, and the Rockwell Corporation, Downey and Seal Beach, California.

Table 1
Limit Loads and Motion Requirements

Component	Limit Load or Torque	Motion Requirements	Actuator/Output
Tilt hinge	Calculated mission max torque 3.96 N.m (35 in.-lbs.)	Max. rotation 15° to 60° antenna pos. at 2°/sec max from 60° max, return to 15° position back-up mode	DDA (loc. cit.)/ output 14.71 N.m (130 in.-lbs.) 0.15 rpm (0.9°/sec) VDA (loc. cit.)/ output 10.73 N.m (95 in.-lbs.) 0.0095 rpm (0.57°/sec at -34.4°C at -30°F)
Fold hinge	Calculated mission max torque 2.396 N.m (21.2 in.-lbs.) Actual test at vert. position 3.390 N.m (30 in.-lbs.)	Normal max rotation 180° Back-up max rotation 180°	DDA/see above VDA/see above
Latch (main claw)	Separation load 6547.4N (1472 Lbf) Torque at actuator 2.877 N.m (25.47 in.-lbs.) Running Loads 0.565 N.m (5 in.-lbs. max)	Hold at limit claw motion	General Design Inc. actuator model 9280/ Actuator holding torque de-energized 5.649 N.m (50 in.- lbs.) Actuator running torque 2.25 N.m (20 in.- lbs.) actuator max torque 5.649-7.910 N.m (50-70 in.-lbs.)
Latch Secondary claw pyro initiated	Inertial load of 0.457 Kg (1.03 lbs) Ratchet load of 51.15N (11.5 Lbf) Remaining load of 444.8N (100Lbf) after initial 0.013m (0.50 inch) stroke	17.8mm (0.70 inch) linear motion for a 42° claw rotation	ASD Spec 74232-501 (linear) pin puller/ Engineering unit successfully tested at required condi- tions

ORIGINAL PAGE IS
OF POOR QUALITY

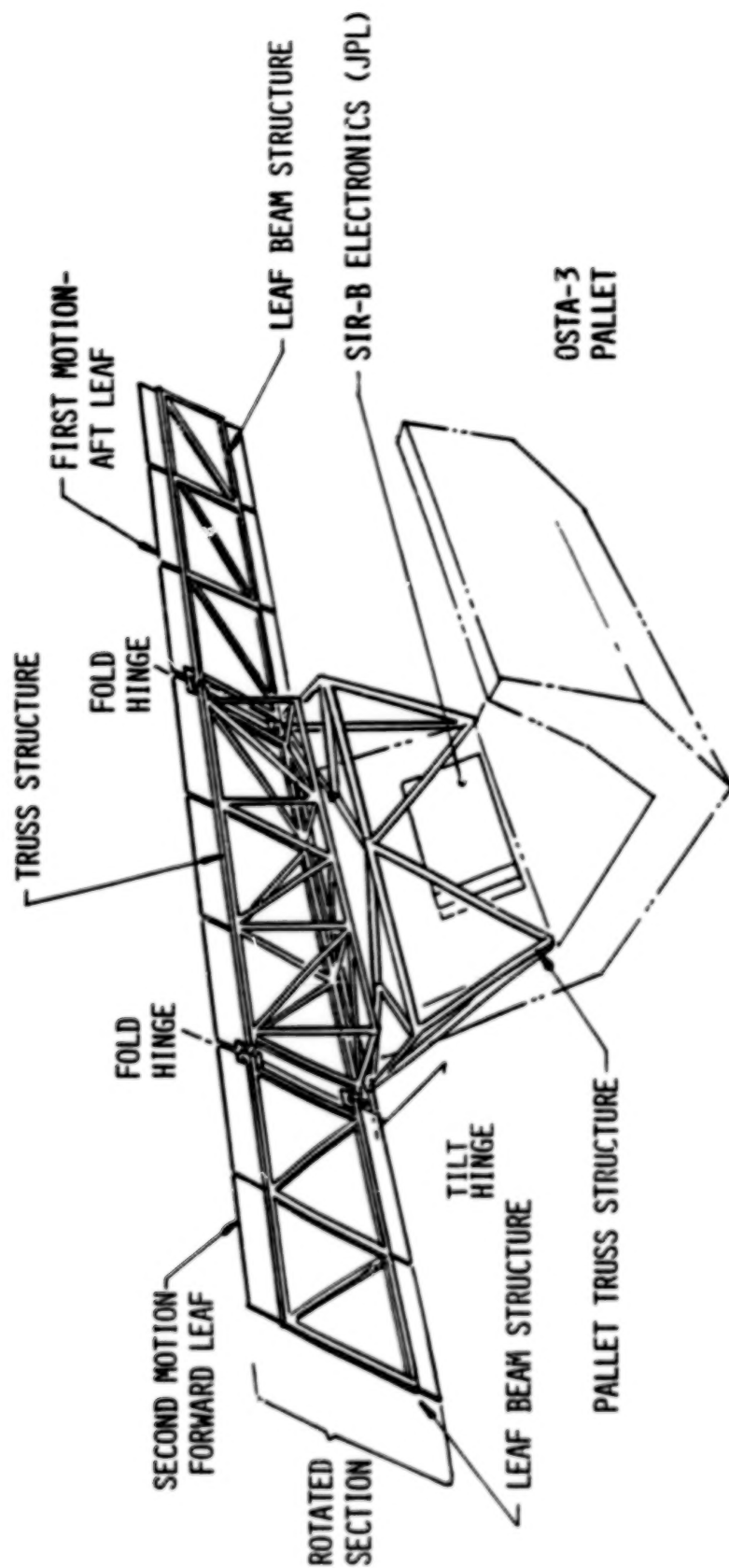


Figure 1. SIR-B On-Orbit Configuration

ORIGINAL PAGE 19
OF POOR QUALITY

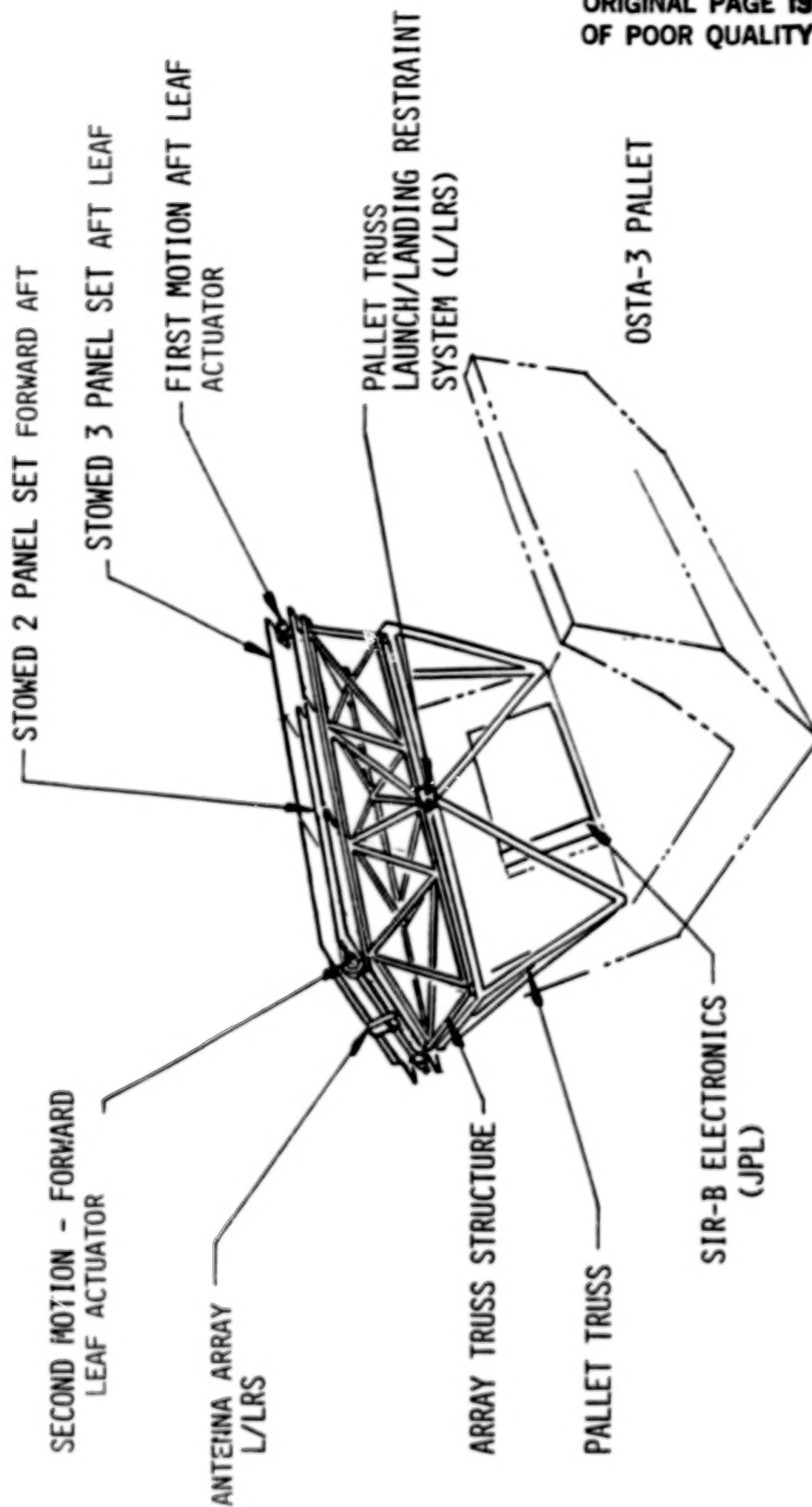


Figure 2. SIR-B Launch/Landing Configuration

ORIGINAL PAGE 19
OF POOR QUALITY

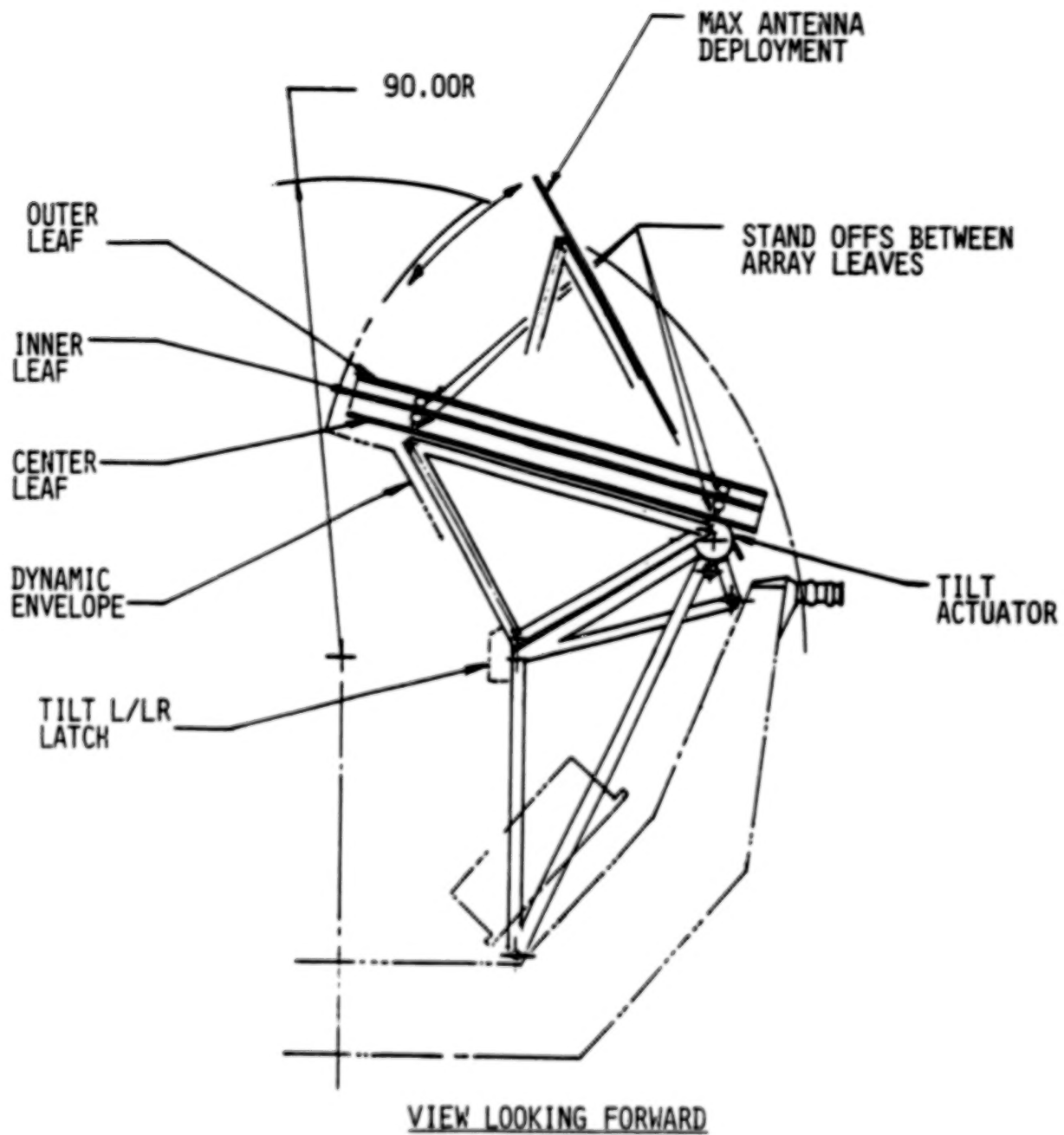


Figure 3. SIR-B Launch/Landing Configuration

ORIGINAL PAGE 13
OF POOR QUALITY

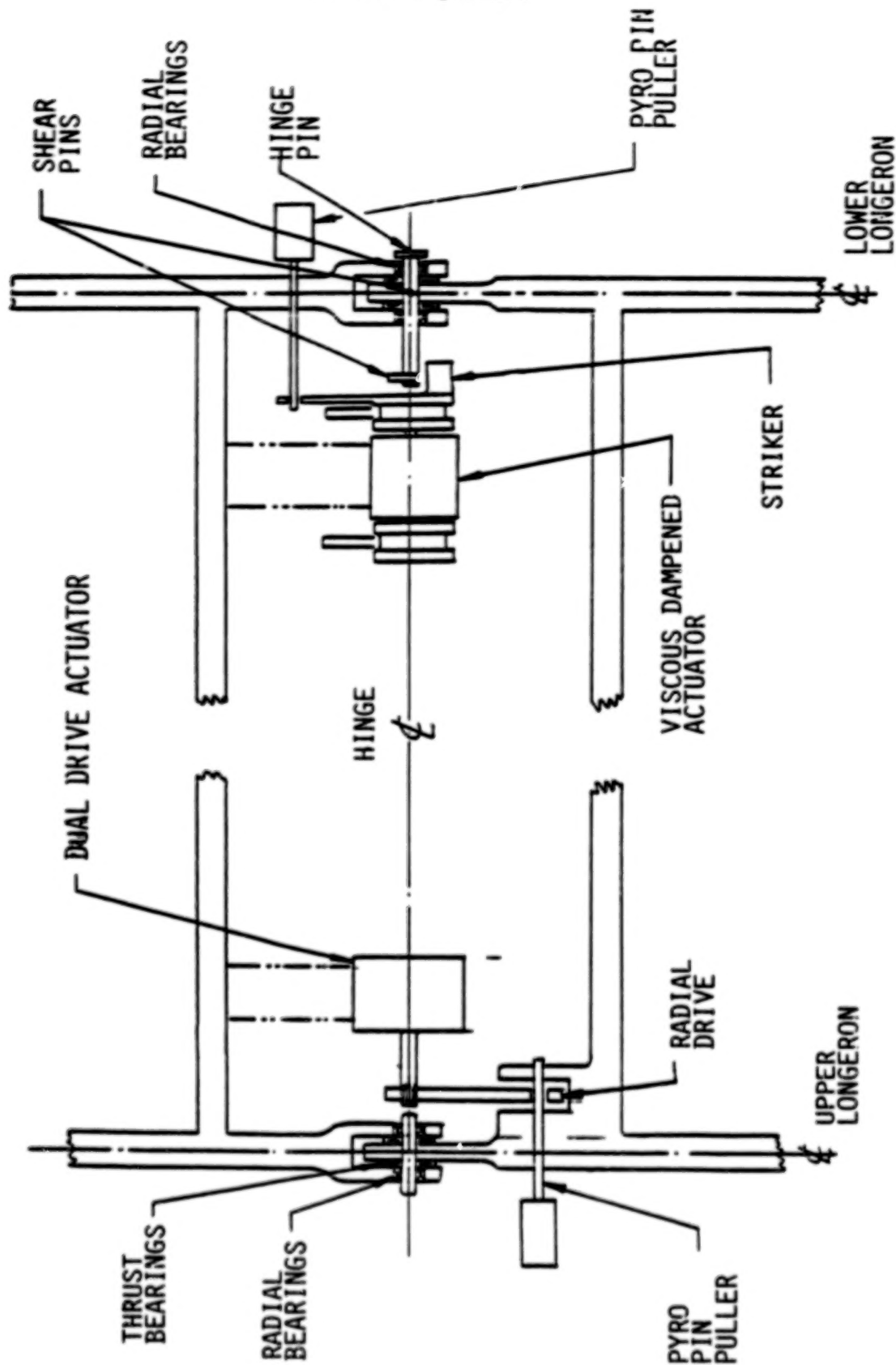


Figure 4. System Functional Diagram (Leaves)

ORIGINAL PAGE 19
OF POOR QUALITY

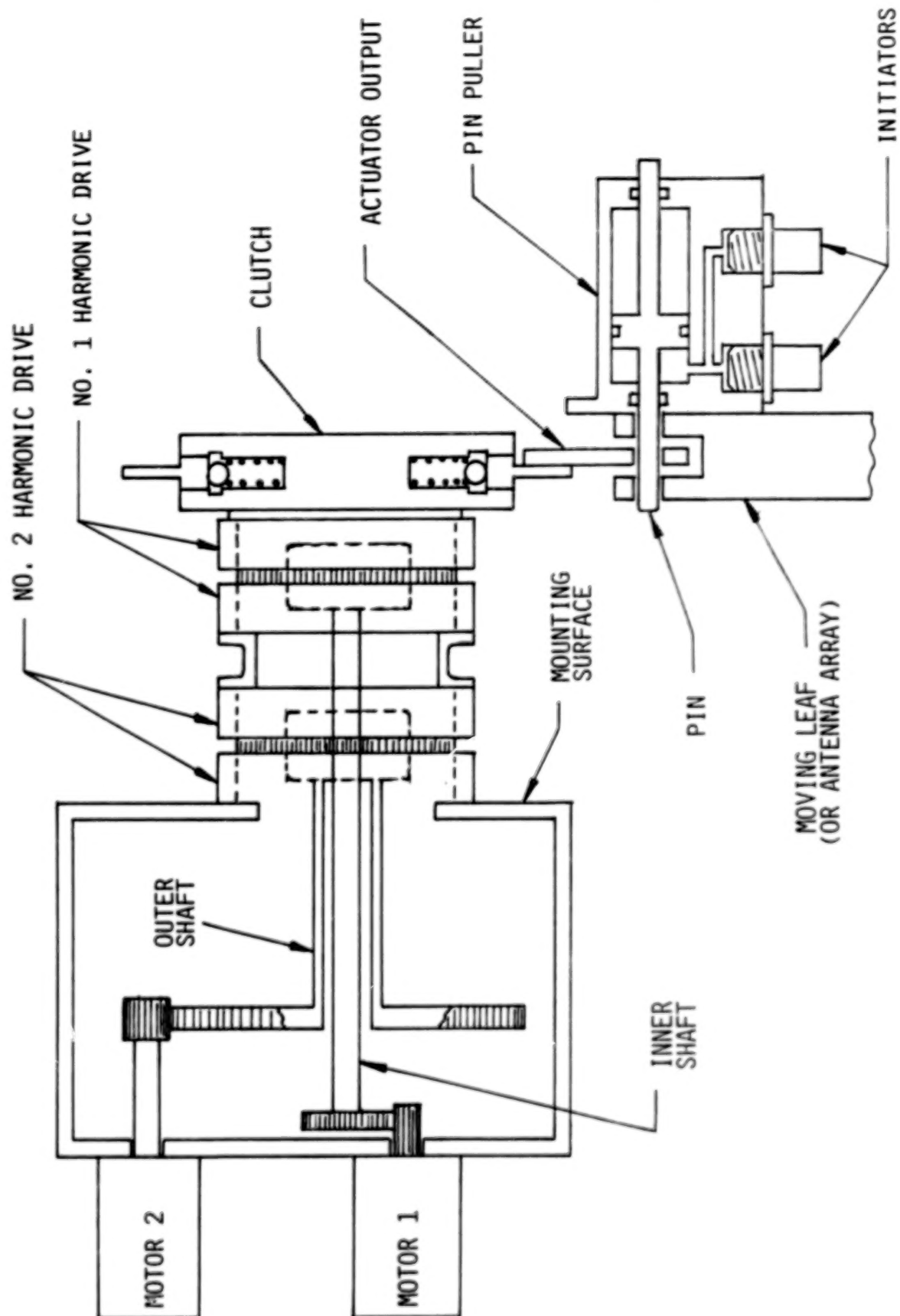


Figure 5. Dual Drive Actuator and Pyro Disconnect
Schematic Diagram

ORIGINAL PAGE IS
OF POOR QUALITY

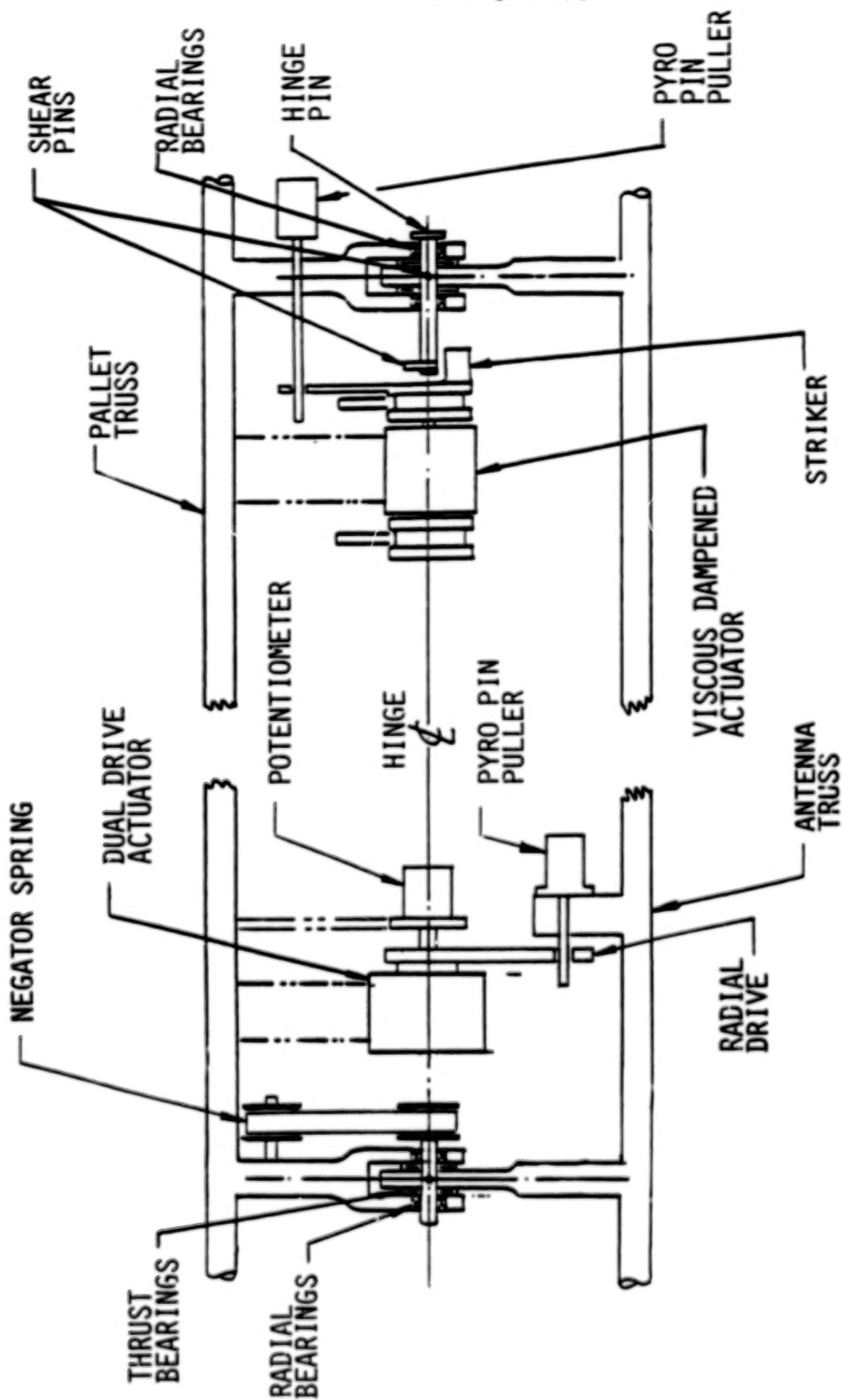


Figure 6. System Functional Diagram (Tilt Hinge)

ORIGINAL PAGE 19
OF POOR QUALITY

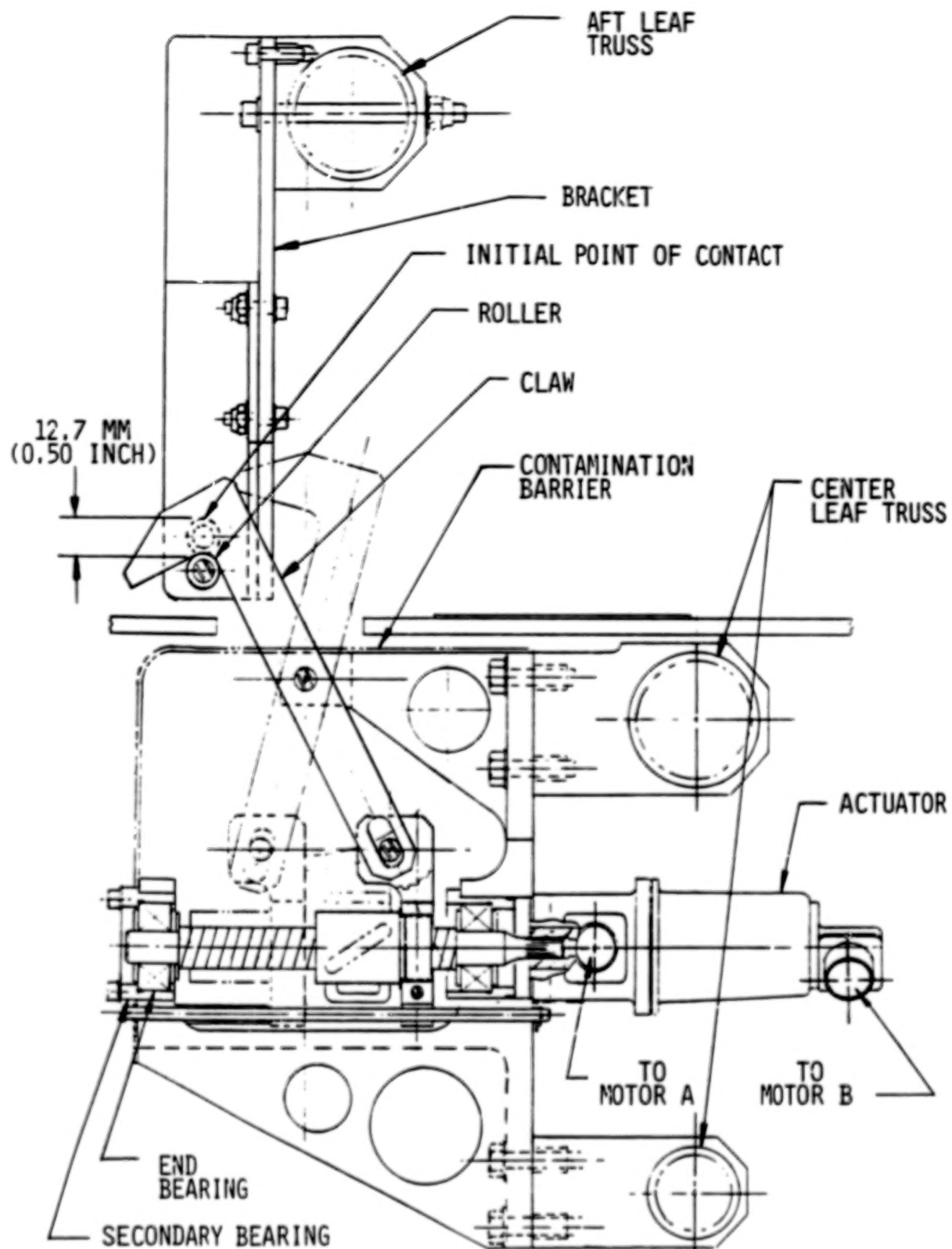


Figure 7. Launch/Landing Restraint System

ORIGINAL PAGE 13
OF POOR QUALITY

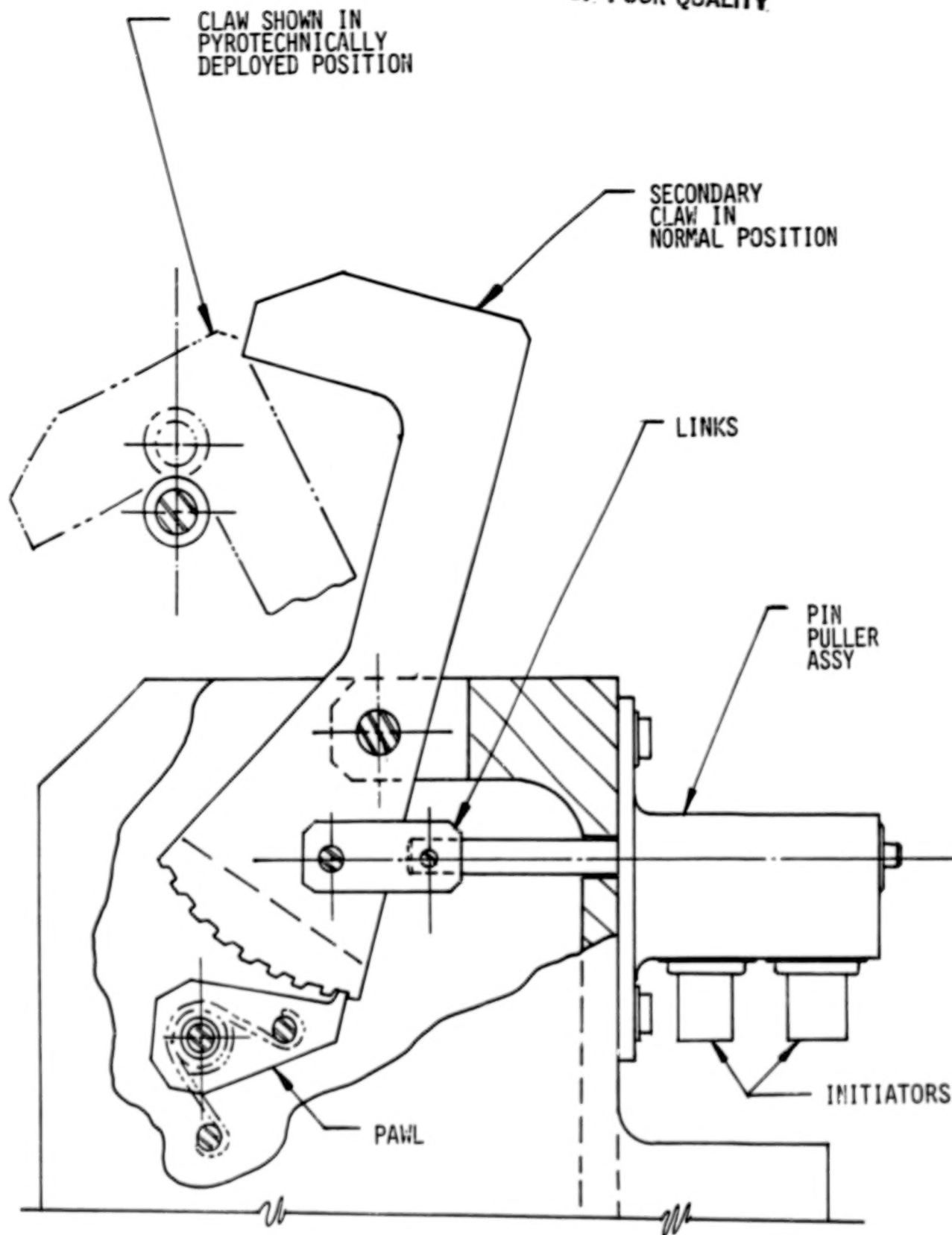


Figure 8. Secondary/L/LR Latch

ORIGINAL PAGE 19
OF POOR QUALITY

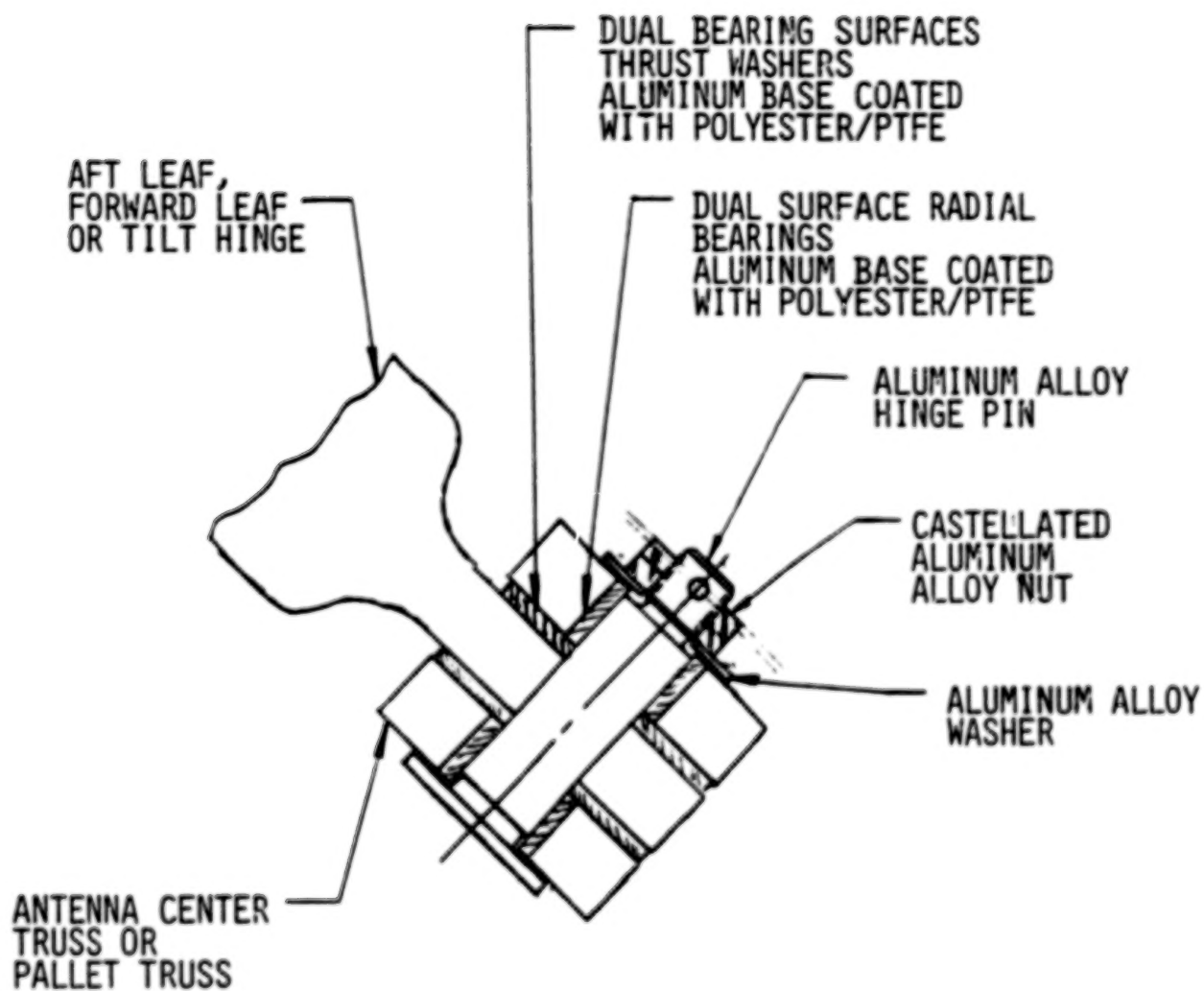
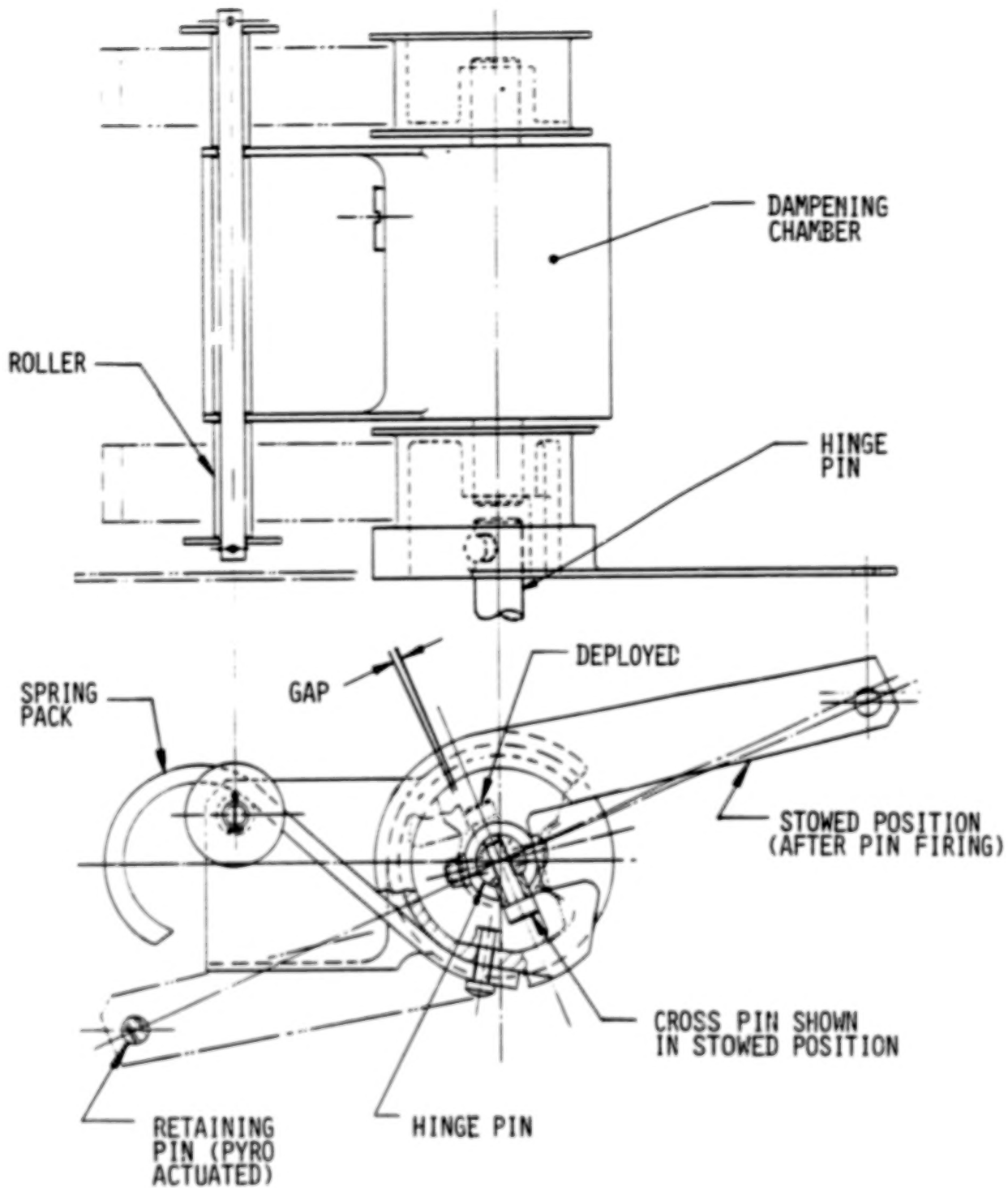


Figure 9. Typical Thrust/Radial Load Carrying Hinge



TYPICAL VISCOUS DAMPENED ACTUATOR INSTALLATION

Figure 10. Typical Viscous Dampened Actuator Installation

ORIGINAL PAGE 19
OF POOR QUALITY



Figure 11. Antenna Truss in Deployed Position

ORIGINAL PAGE 13
OF POOR QUALITY

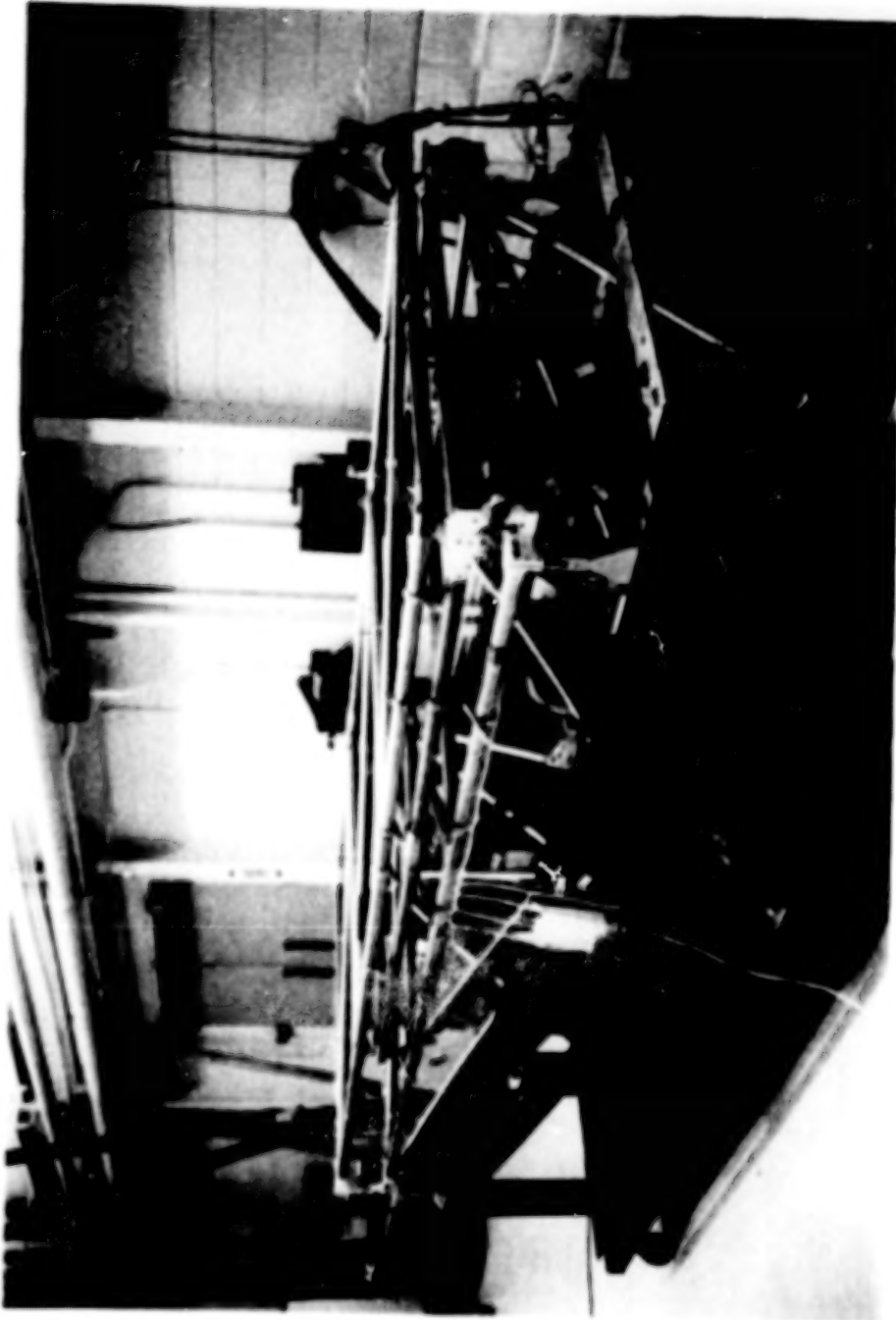


Figure 12. Antenna Truss in Stowed Position

ORIGINAL PAGE 18
OF POOR QUALITY

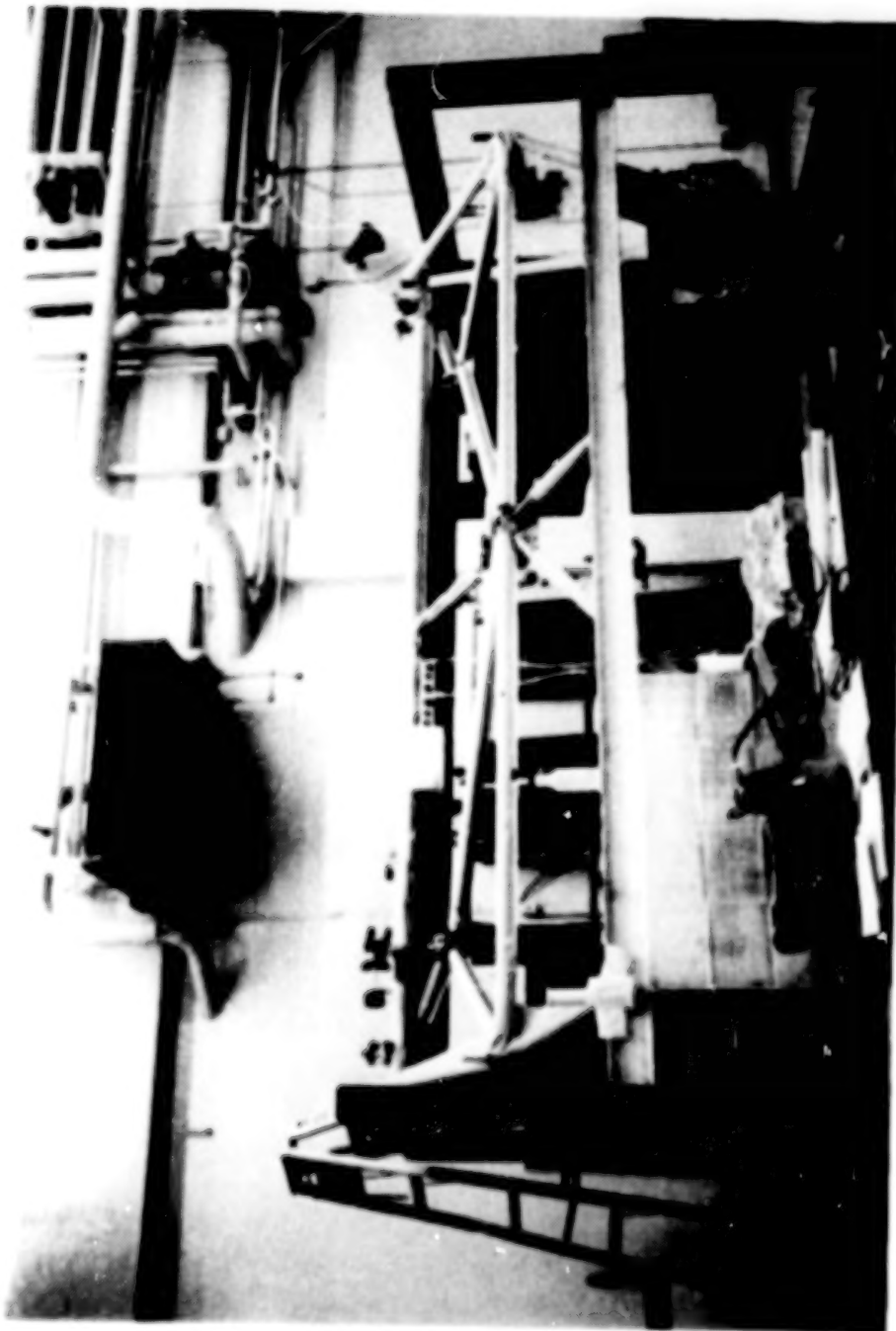


Figure 13. Pallet Truss

ORIGINAL PAGE 18
OF POOR QUALITY

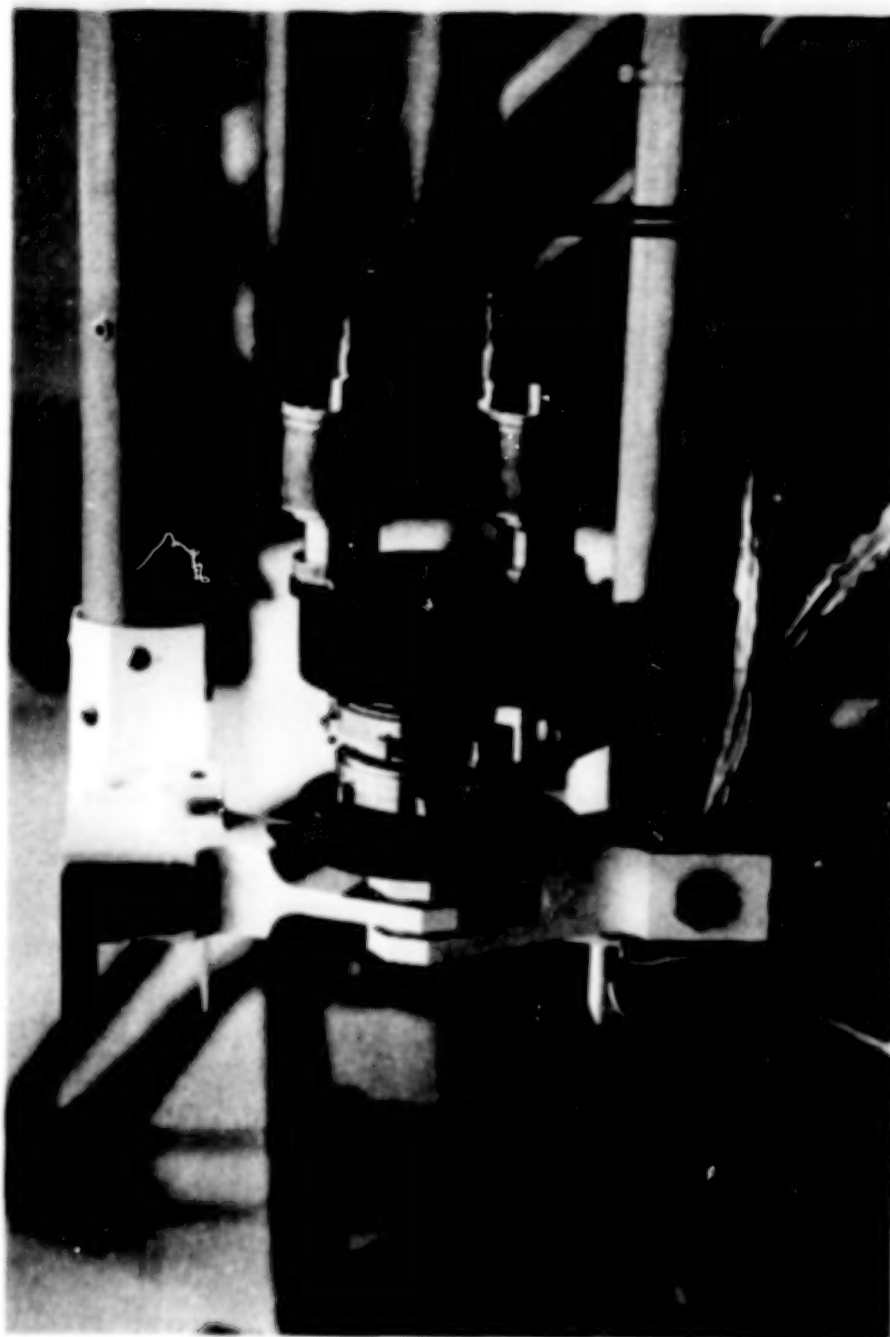


Figure 14. Typical Dual Drive Assembly Installation

ORIGINAL PAGE 18
OF POOR QUALITY

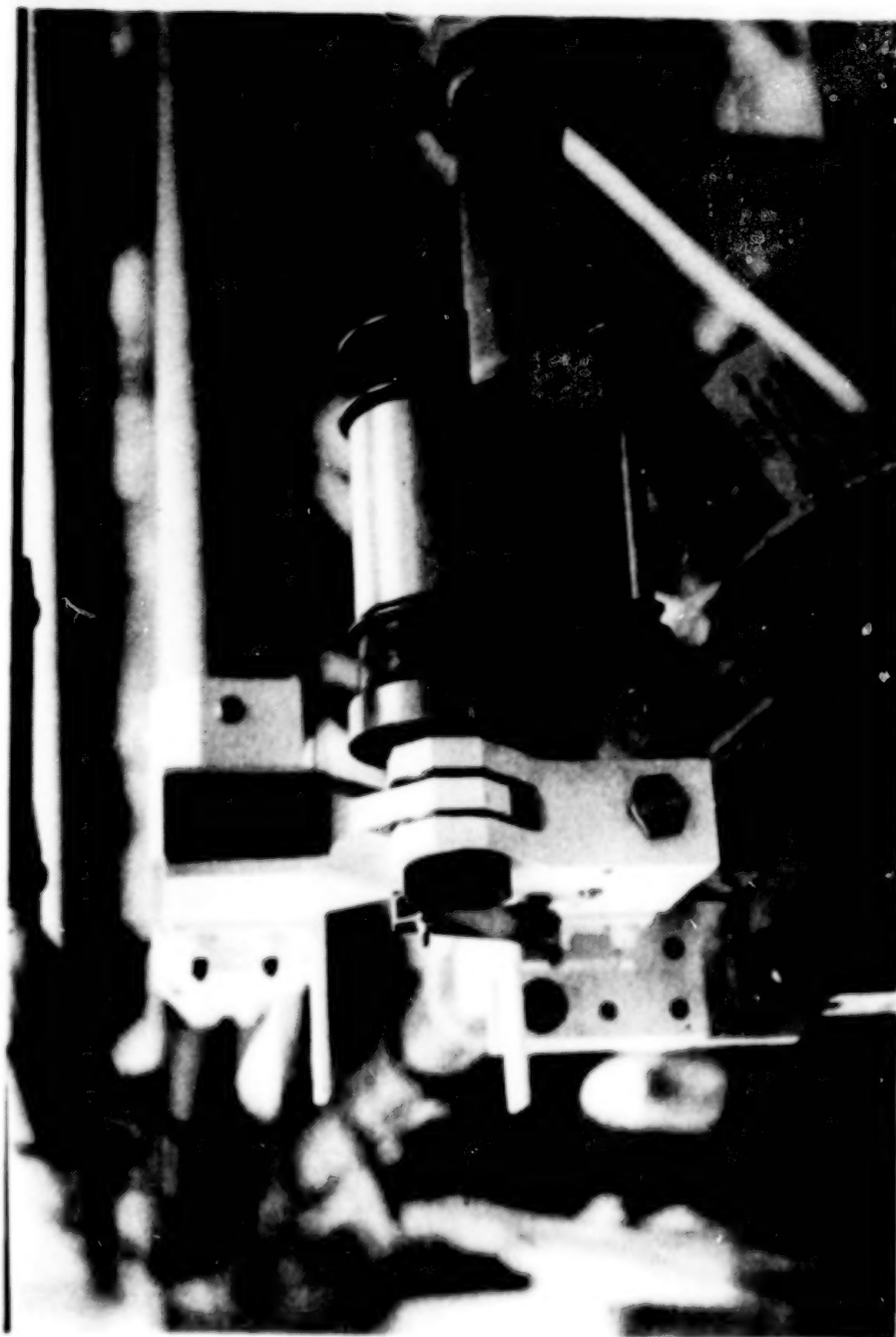


Figure 15. Typical Viscous Dampened Actuator Installation
(Shown in Preloaded Position Retained by Tooling Pin)

ORIGINAL PAGE 13
OF POOR QUALITY



Figure 16. Viscous Dampened Actuator in Unloaded Position

ORIGINAL PAGE 19
OF POOR QUALITY

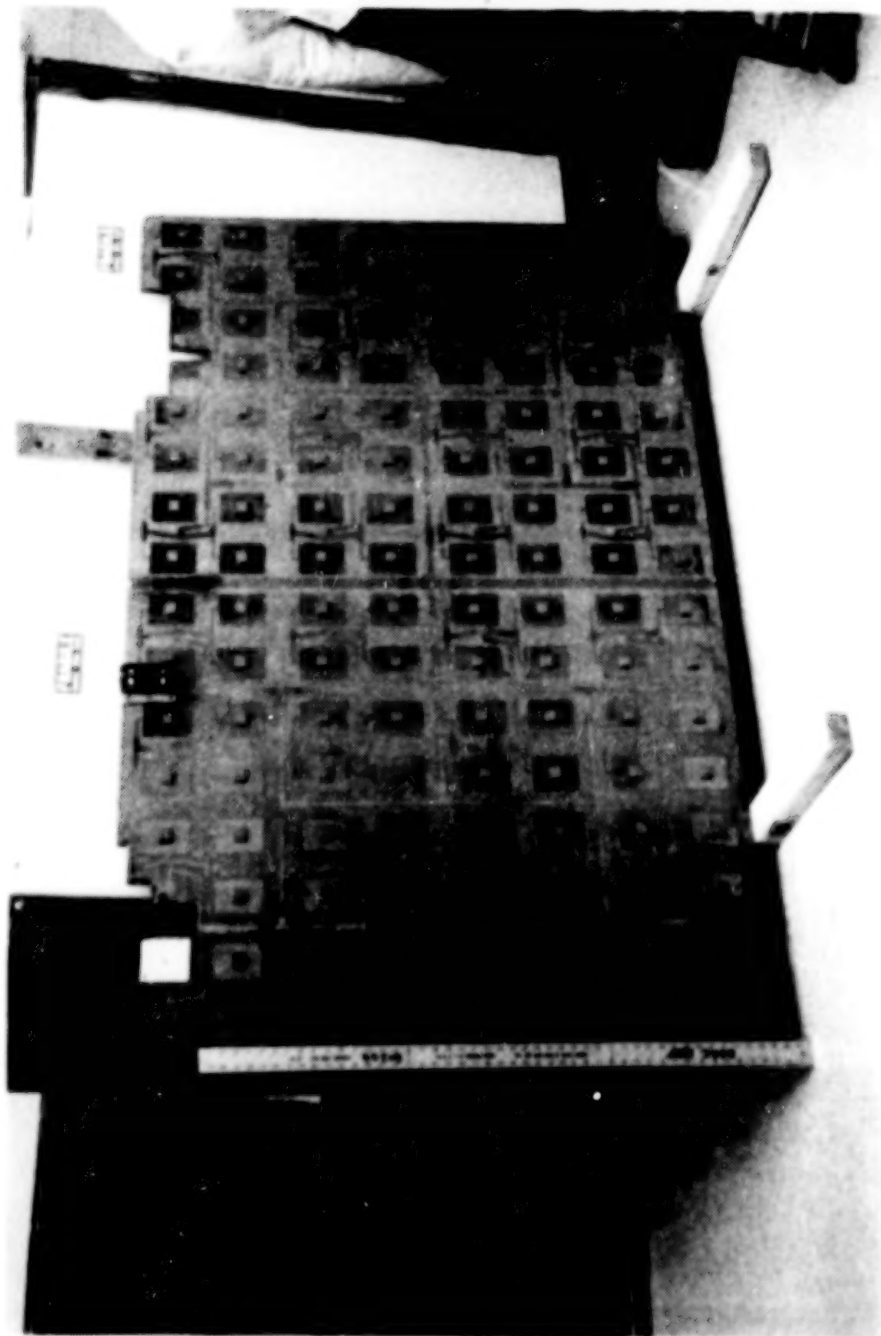


Figure 17. One of Eight RF Panels
(Ruler is 1.8 m (4-ft) long)

N84
250888

UNCLAS

INHERENT PROBLEMS IN DESIGNING TWO-FAILURE TOLERANT ELECTROMECHANICAL ACTUATORS

Stephen Hornyak*

ABSTRACT

An electromechanical ac-powered rotary actuated four-bar linkage system for rotating the Shuttle/Centaur deployment adapter is described. The essential features of the deployment adapter rotation system (DARS) are increased reliability for mission success and maximum practical hazard control for safety. This paper highlights the requirements, concept development, hardware configuration, quality assurance provisions, and techniques used to meet two-fault tolerance requirements. It presents the rationale used to achieve a degree of safety equivalent of that of two-failure tolerance. Conditions that make this approach acceptable, including single failure point components with regard to redundancy versus credibility of failure modes, are also discussed.

INTRODUCTION

During the last 3 years, a NASA/DOD agreement led to the design, development, and procurement of the Centaur G-prime and Centaur G high performance upper stages. The configuration is derived from the flight-proven Atlas/Centaur and Titan/Centaur vehicles. The Centaur G-prime is a NASA-unique version of the configuration that will launch the Galileo and International Solar Polar (ISPM) spacecraft. The Centaur G will carry and eject DOD-unique satellites into geostationary or 12-hour orbits. The Centaur spacecraft will fly as a dedicated Shuttle payload. Integration of the Centaur upper stage into the Orbiter is accomplished by using the Centaur integrated support system (CISS), consisting of the Centaur support structure (CSS); deployment adapter (DA); and the associated CISS electronics, fluid, and mechanical systems. An overview of the Shuttle/Centaur configuration is illustrated in Figure 1.

The DARS is part of the CISS mechanical systems and performs the DA rotation function for both Centaur G-prime and Centaur G upper stages. This paper describes the rotation system designed for G-prime and discusses possible changes for the G version.

The DARS is required to provide reliable DA positioning for Centaur separation and deployment, to react primary reaction control system (PRCS) jet moments during the erected position without latches, and to return the Centaur safely back to the stowed position in case of an aborted mission. Following a successful Centaur ejection from the Orbiter cargo bay, the function of the DARS is to rotate the empty DA back to the stowed position and restrain it for Orbiter landing. Independent single-failure tolerant primary and backup rotators are used in combination to guarantee the effect of two-failure tolerance. The rotation system is fail-safe in that two failures will not lead

* General Dynamics Convair Division, San Diego, California

ORIGINAL PAGE 19
OF POOR QUALITY

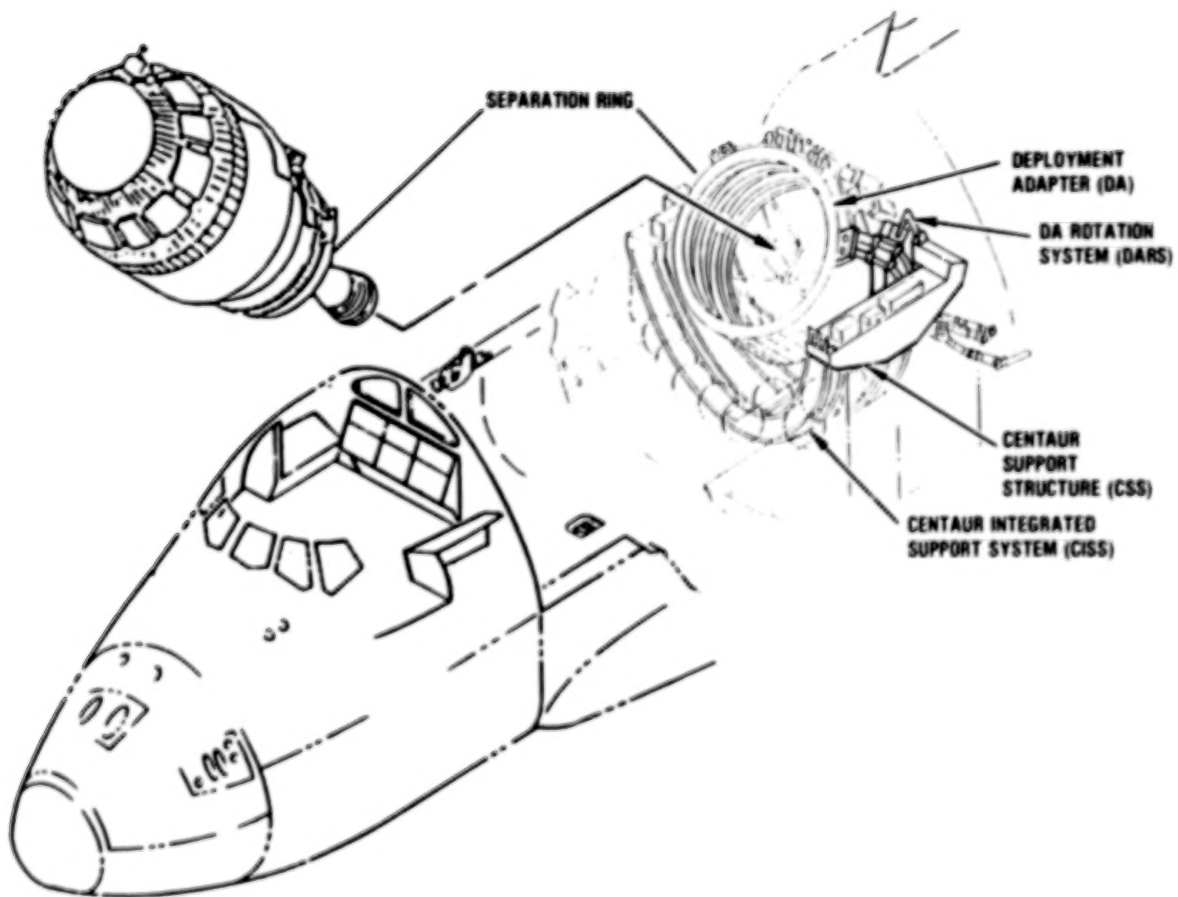


Figure 1. Shuttle/Centaur Configuration.

to catastrophic hazard. Manual disengagement capability of the link, for contingency only, is provided with the use of crew trained EVA (extra vehicular activity) to free a jammed rotator in orbit.

The Centaur spacecraft can be then returned to the stowed position using the contingency EVA winch (designed to restow the IUS manually) which is a slightly modified version of the contingency payload bay door winch mounted on the Orbiter forward bulkhead.

The relationship between DARS and CISS is shown in Figures 2 and 3. The DARS and the systems interfacing with DARS are shown in block diagram form in Figure 4.

The concept, the requirements, and the procurement specification of the mechanisms described in this paper were developed by General Dynamics, which subcontracted the electromechanical rotator unit design, manufacturing, and testing to the Hoover Electric Company.

REQUIREMENTS

The requirements imposed on the rotator to perform several functions within severe constraints are summarized as follows:

Safety Requirements (in accordance with NHB 1700.7A)

- Independent primary and backup rotation methods are required.
- Combination of primary and backup methods must be two-failure tolerant.

Operational Requirements (in accordance with JSC-07700 Volume X, Appendix 10.16, September 30, 1983)

- Erect Centaur to 36° minimum, 45° maximum rotation angle for Centaur separation.
- Erection capability required under active vernier reaction control system (VRCS) or free drift conditions (PRCS and Orbiter maneuvering system (OMS) translation modes inhibited during rotation).
- Capability required to react VRCS and PRCS loads while Centaur is in the erected position.
- Orbiter/CCE (Centaur cargo element) dynamic interactions shall be minimized.
- Multiple (up to six) erection/restow cycles anticipated for each mission; restow capability for abortive missions is required.
- Performance is required through 10 Orbiter missions over 10 years.
- Fatigue life must be designed to four times the expected number of mission cycles.
- Redundancy verification is required during turnaround.

System Requirements (derived, assumed, or self imposed)

- Rotate DA to 45° in 4 to 5 minutes.
- Operation is required in both one g and zero g conditions.
- Disengage the crank clutches of both primary and backup rotators during ascent and reentry (in case of an aborted mission).

ORIGINAL PAGE 19
OF POOR QUALITY

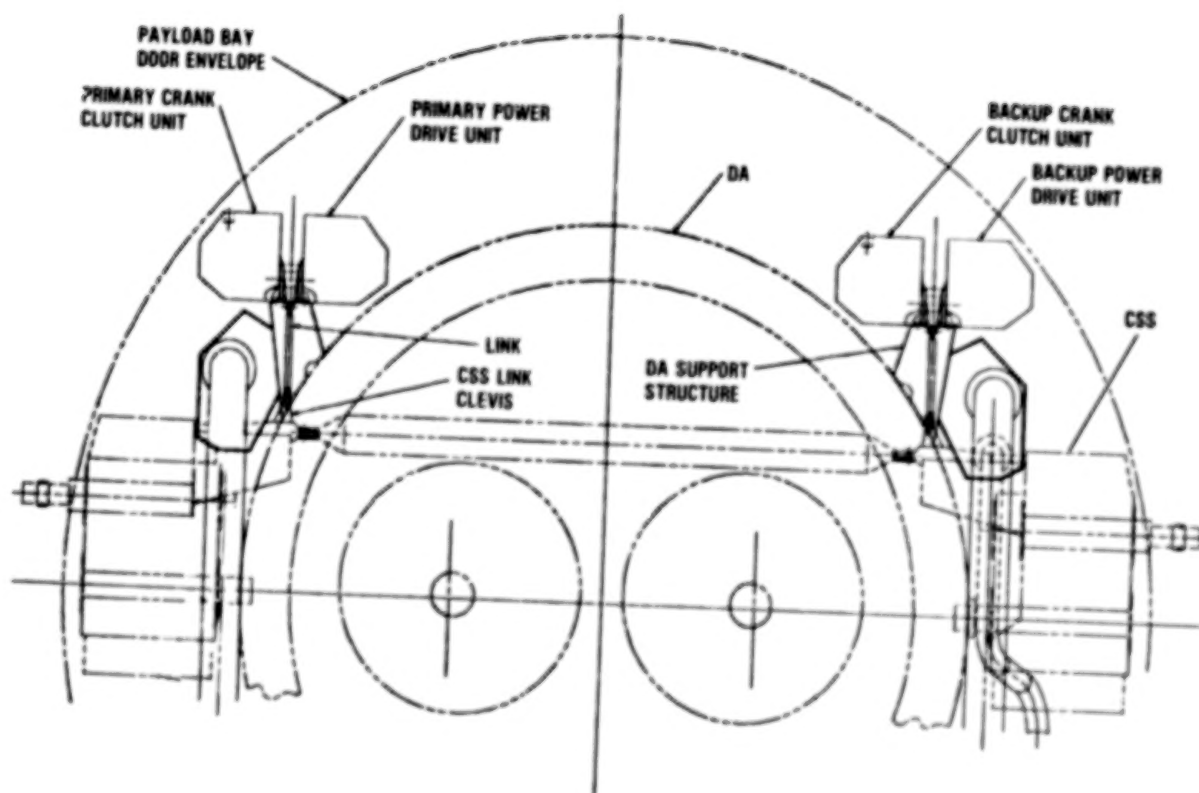


Figure 2. DA Rotation System Configuration (Rear View).

ORIGINAL PAGE 12
OF POOR QUALITY

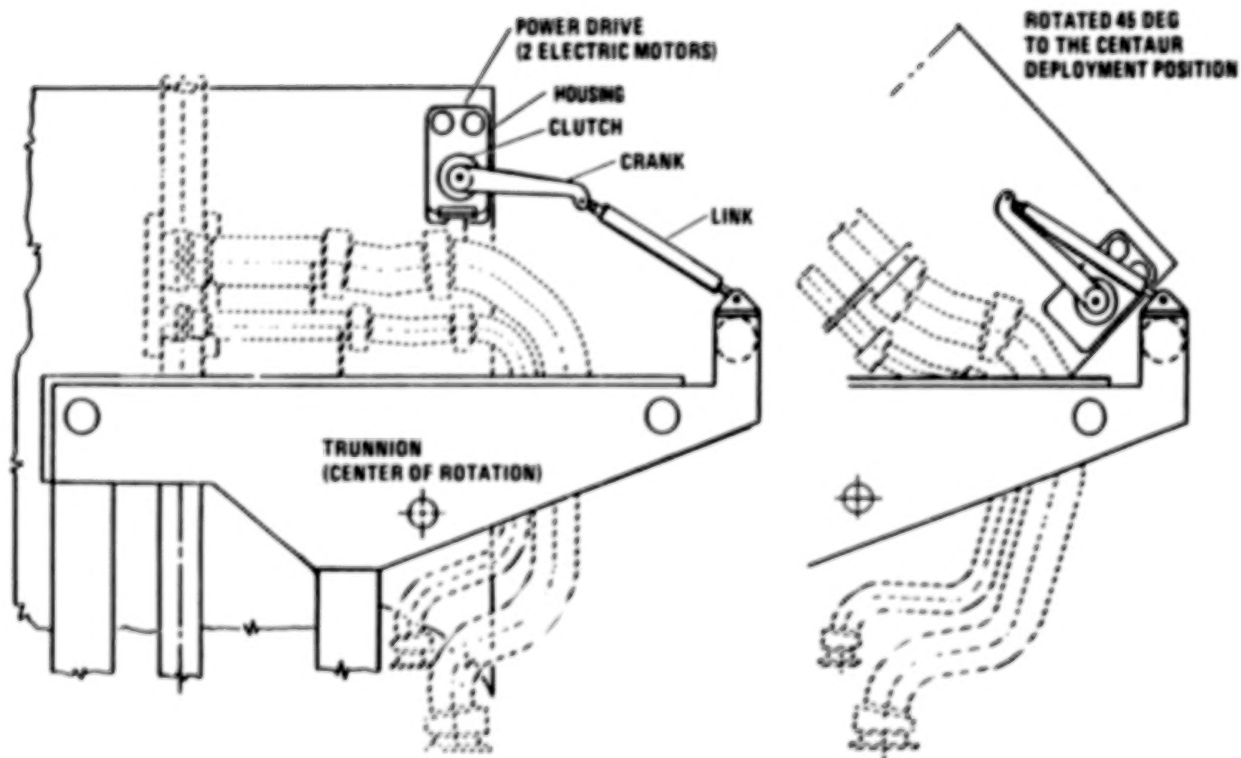


Figure 3. DA Rotation System Configuration (Left-Hand Side View).

ORIGINAL PAGE 19
OF POOR QUALITY

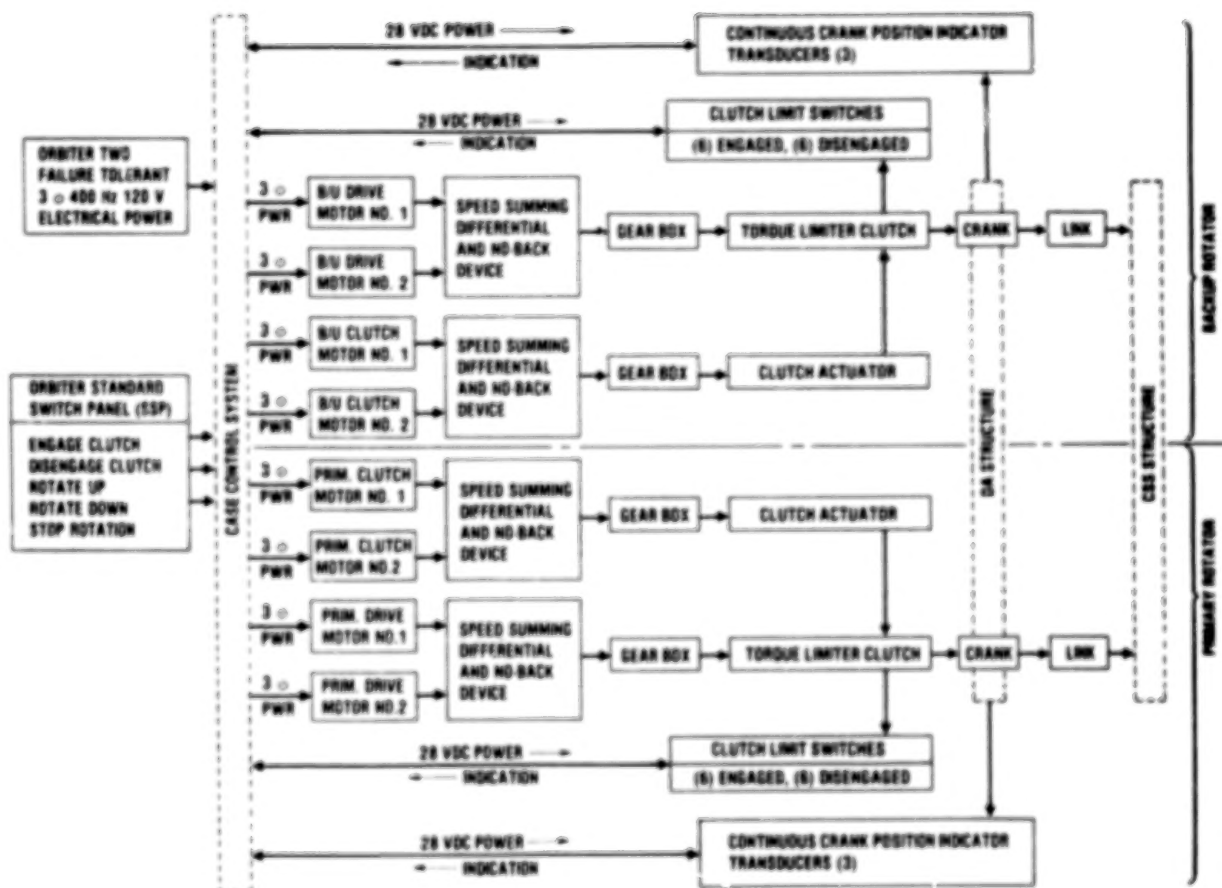


Figure 4. DA Rotation System (Functional Block Diagram).

- Only one of the clutch or rotation motors shall operate at a time.
- Weight shall not exceed 310N (70 lb) per rotator.
- Operation is required at temperature extremes from -73° to 121°C (-100 F to 250 F).
- The rotator must perform after exposure to severe vibroacoustic environments during Shuttle ascent to orbit, with special consideration for its installed position on the structural support extending from the aft ring of the DA.
- After a successful Centaur separation, the DA shall be returned to the reentry position 0.5° beyond the nominal stowed position of Centaur and preloaded against a stop using both rotators to react Orbiter landing loads safely.
- DA in any position must not violate the payload bay door envelope.
- Limit switches, crank position transducers, ac power, and avionics shall be two-failure tolerant.
- Software/Control requirements are:
 - a. Automatic rotation operation after crew initiation.
 - b. Automatic failure detection and reconfiguration.
 - c. Orbiter signals are not required for operation.
- Ground checkout requirements are:
 - a. One rotator to cycle DA with CSS in horizontal position.
 - b. One rotator to cycle counterweighted DA with CSS in vertical position.
- Existing space technology (manufacturing and testing) developed for electromechanical rotary actuators employed in the Orbiter and other similar space applications shall be used as applicable in the rotation system design.

CONCEPT DEVELOPMENT

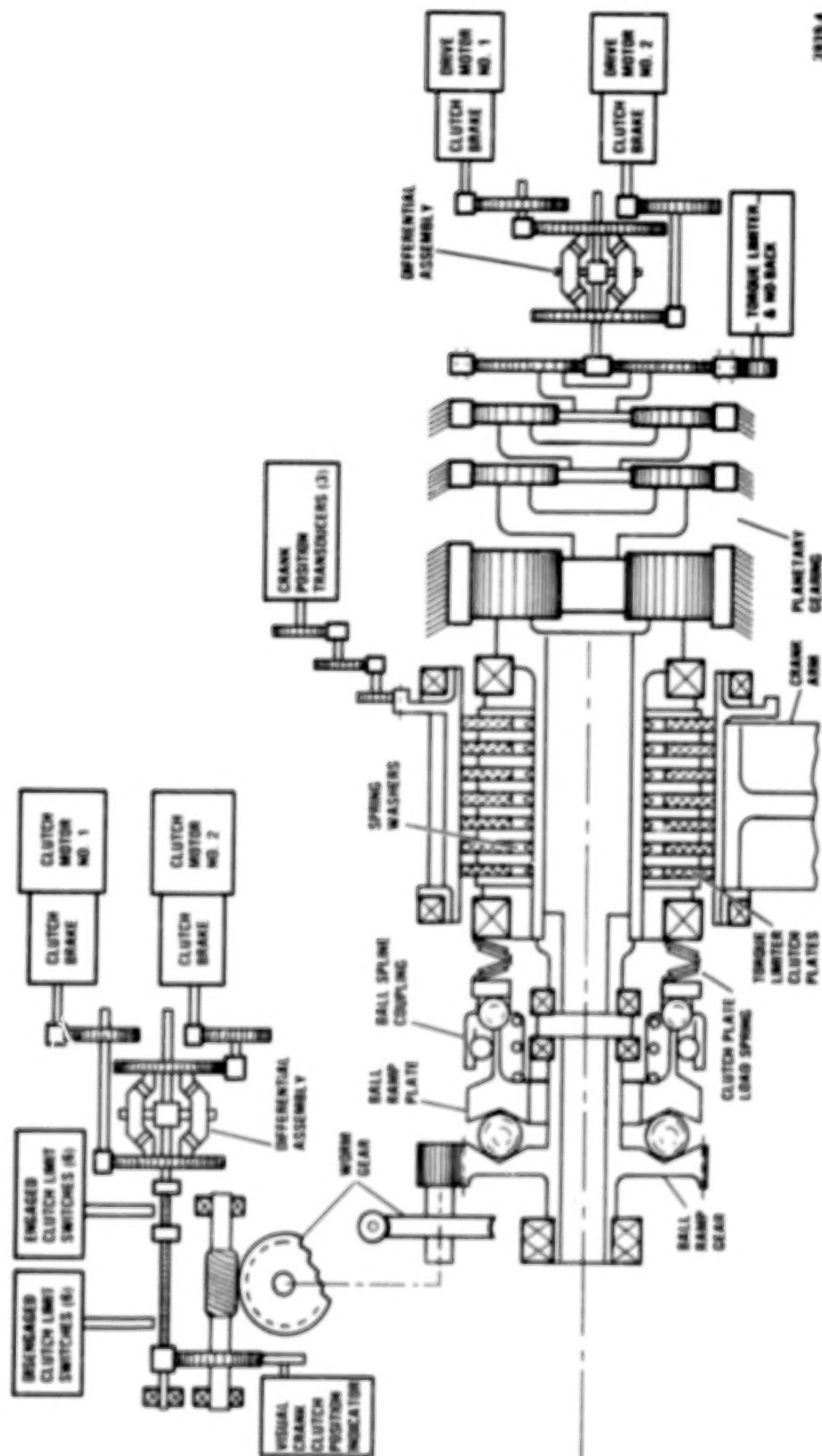
During the design selection phase, most of the problems centered around the two-failure tolerance requirement. Many different designs were conceived and eliminated in tradeoffs. Rack and pinion, ballscrew, chain, cable, and steel-belt drives — employing one or a combination of hydraulic, pneumatic, electrical, and pyrotechnically powered actuators — were evaluated against linkage drives. The linkage drive was selected for this application based on its excellent kinematic behavior. This electromechanical quadric crank mechanism concept, which uses reliable technology already developed and tested for similar applications in the Orbiter, ensures trouble-free performance and avoids the costly development usually associated with an innovative design and the inherent risks associated with meeting tight schedules.

HARDWARE CONFIGURATION

One DA rotator, illustrated in Figure 5, consists of the following major components.

- A. Rotary actuator, including the following subassemblies:
 - (1) Power drive unit — a rotary electromechanical device consisting of two input channels driving a rotary output shaft through a reduction gearing arrangement that provides for independent operation of each input channel. The two input channels will not be operated

ORIGINAL PAGE IS
OF POOR QUALITY



3939-4

Figure 5. DA Rotator Component Arrangement (Schematic).

concurrently. Failure of any one channel will not affect operation of the remaining channel. The power drive unit output torque will meet the requirements with either channel operating.

- (2) Crank clutch unit — actuated by an electromechanical device similar to the power drive unit. The clutch will transmit the output shaft torque of the power drive unit into the crank shaft. The power drive clutch is located between the output shaft of the unit and the crank shaft. Limit switches are used to indicate engaged and disengaged clutch positions. The clutch also serves as a torque limiter, protecting the rotator and the interfacing structure from overloads.
 - (3) Crank — transforms crank shaft torque into force in the link. Electrical rotary position transducers are used to indicate continuous crank position.
 - (4) Housing — supports the crank shaft, power drive unit, and crank clutch unit. It is capable of withstanding the full crank load and maximum vibration loads while bolted rigidly to the housing support structure on the DA.
- B. Link — The link is pushed/pulled by the crank arm and transfers crank output into deployment adapter position. The link has two self-aligning rod end bearings and is pinned to the CSS-mounted clevis.

The rotator is designed to perform the required functions under the following conditions:

- The available power is two-failure tolerant Orbiter 400 Hz 115/200 vac, three-phase, four-wire for motors and 28 Vdc for limit switches and transducers.
- The two drive motors and the two clutch motors are identical, and each motor operates independently. Failure of a motor or a power failure to that motor will be followed by switching off the disabled motor and switching on the second motor to complete the function. The de-energized motor does not interfere with the performance of its twin motor. Each is rated to perform under the worst-case combination of temperature, altitude, voltage, frequency, and loads.
- Operating time is 45° rotation in 4 to 5 minutes.
- Loads are divided into four categories. The crank torque limit values are as follows:
 - (1) Operating in orbit—520 Nm (4,600 in-lb)
 - (2) PRCS jet moments—2,940 to 4,070 Nm (26,000 to 36,000 in-lb)
 - (3) Landing—2,920 Nm (25,800 in-lb) reacted by two rotators
 - (4) Ground checkout—570 Nm (5,000 in-lb)
- Maximum slip torque at crank shaft—4,070 Nm (36,000 in-lb).
Minimum transmission torque at crank shaft—2,940 Nm (26,000 in-lb).
- Rotator overall stiffness—113,000 Nm (1.0×10^6 in-lb) per radian minimum spring rate in the direction of crank rotation, measured at the center of the rotator mounting plate.
- Position transducers: Crank rotation between mechanical stops is monitored by three position transducers per rotator. A group of five transducers will be used simultaneously, combining the primary and backup rotator transducers, to meet two-failure tolerant signal control criteria for Centaur positions, ensuring a three-versus-two vote by avionics in the worst-case condition. The sixth transducer is reserved for instrumentation.
- Limit switches: The crank clutch unit has 12 single pole double throw limit switches. Six nor-

mally open contacts of six independent switches will close simultaneously to signal engaged clutch position and another group of six switches will signal disengaged clutch position. Five "engaged" and five "disengaged" limit switches out of each group of six switches will be used to meet two-failure tolerant crank clutch position signal criteria. One engaged and one disengaged switch will be used for instrumentation.

QUALITY ASSURANCE PROVISIONS

Verification of the requirements is accomplished by one or a combination of the following methods: analysis, similarity, test, and inspection. The test program associated with the DA rotation is shown in Table 1 and summarized as follows.

- Individual Acceptance Tests (Hoover Electric Company)
- Qualification Tests (Hoover Electric Company)
- Design Evaluation Tests (General Dynamics)
- Factory Acceptance Tests (General Dynamics)
- Eastern Launch Site (FLS) Ground Checkout Tests (NASA/General Dynamics)

The purpose of this extensive test program is to demonstrate adequacy of the design for the intended use and support two-failure tolerant capability. Qualification test durations are four times the duration of the anticipated number of mission duty cycles. Qualification testing will begin in August 1984 in parallel with the Design Evaluation Test.

TWO-FAILURE TOLERANCE RATIONALE

Interpretation of redundancy, associated with static and dynamic component design, serves to determine two-failure tolerant characteristics.

There are inherent problems in the practical application of a two-failure tolerant electromechanical system that can be effectively studied in parallel with manned Orbiter missions. With the presently available technology and many different interpretations of redundancy, it is extremely difficult to design a truly two-failure tolerant transmission arrangement that transmits motive force from the electric motor to the link by gears, through a crank, while the crank is engaged by a clutch. This arrangement must also be simple, lightweight, inexpensive, and most of all reliable.

Employing multiple levels of redundancy in electrical or fluid power transmission is relatively trouble free. Electricity or fluid media can be switched readily to maintain a continuous power supply, and a jammed relay or valve does not hinder the course of action. Jamming of a mechanism, however, can stop an operation which can lead to hazardous situations.

A two-failure tolerant electromechanical design becomes complicated, especially in cases where more than one component can jam. Jam removal capability must be provided to allow continuation of the function in case the primary system stops functioning (first failure) and switching to the backup system is impossible for any reason (second failure).

Assume that a two-failure tolerant remotely controlled mechanism has three independent means of accomplishing the assigned task or function. To switch from the first to the second

ORIGINAL PAGE IS
OF POOR QUALITY

Table 1
DA Rotator Test Program

Qualification	Acceptance	Design Evaluation (CISS horizontal)	Factory Acceptance (CISS vertical)	Ground Checkout at ELS (CISS horizontal and/or vertical)
Acceptance Humidity Explosive atmosphere Vibration Endurance vibration Pyrotechnic shock Thermal vacuum Thermal cycle Crank oscillation Cycling Mechanical limits Stiffness Motor Bonding EMC Electrical stress Performance Post test disassembly & examination	Examination of product Performance Functional Vibration Thermal cycle Power consumption Cycling Performance	DA rotation Primary & backup modes verification Electrical parameters Landing loads Rotational spring rates Torque limiter External failure modes Clearances	Counterweight installation/removal verification DA rotation Primary & backup modes verification Electrical parameters Torque requirements Clearance verification	DA rotation Primary & backup modes verification Electrical parameters Power requirements verification DA 0 and 45 degree position verification Visual clutch position indication verification

means and from the second to the third means, remotely controlled jam removal methods are required for the engaging, disengaging mechanism of the first and second means. The combination of the first and second jam removal methods must be two-failure tolerant. If pin pullers are used for jam removal, link capturing devices must be provided for the first and second means. The combination of the first and second link capturing devices must be two-failure tolerant. This system is complicated, heavy, expensive, and requires complex avionic and software systems. Reliability may be degraded because of the complexity.

Ideally, there should be only one super-reliable means of performing the function, with a sufficient degree of built-in redundancy. If external jamming of the system is credible, a backup means is required and the primary means must be provided with redundant jam removal capability to allow the backup to function.

The DA rotation system design follows the definitions, ground rules, and reliability techniques of Reliability Desk Instruction DI No. 100-2F, Failure Mode Effect Analysis (FMEA), established for the Space Shuttle Orbiter subsystems to verify design adequacy with respect to inherent reliability. Some definitions and ground rules from this document follow.

Definitions

- Failure — Inability of a system, subsystem, component, or part to perform its required function within specified limits under specified conditions for a specified duration.
- Failure Mode — A description of the manner in which an item can fail.
- Hazard — The presence of a potential risk situation caused by an unsafe act or condition.
- Redundancy (depth of) — The available (number of) ways of performing a function*.

*NASA SP-7, Dictionary of Technical Terms for Aerospace Use, defines redundancy as "the existence of more than one means for accomplishing a given task, where all means must fail before there is an overall failure to the system."

"Parallel redundancy applies to systems where both means are working at the same time to accomplish the task, and either of the systems is capable of handling the job itself in case of failure of the other system. Standby redundancy applies to a system where there is an alternative means of accomplishing the task that is switched in by a malfunction sensing device when the primary system fails."

Per Webster, the definition is "more than enough" or "superfluous." This interpretation may be the key to achieving equivalent safety by overdesigning the appropriate mechanical components instead of reaching for alternate means.

- Backup Mode of Operation — The available way(s) of performing a function using "like" (identical) hardware.
- Alternate Mode of Operation — Any additional ways of performing a function using "unlike" hardware.
- Criticality — The categorization of a hardware item by the worst-case potential direct effect of failure of that item. In assigning hardware criticality, the availability of redundancy is considered. Assignment of functional criticality, however, assumes the loss of all redundant (backup or alternate) hardware elements.
- Single Failure Point — A single item of hardware, the failure of which would lead directly to loss

*NASA SP-7, Dictionary of Technical Terms for Aerospace Use—Definition of redundancy

of life, vehicle, or mission. Where safety considerations dictate that abort be initiated when a redundant item fails, that item is also considered a single failure point.

- Critical Item — A single failure point or a redundant element in a life or mission-essential application where:
 - a. Redundant elements are not capable of checkout during the normal ground turnaround sequence.
 - b. Loss of a redundant element is not readily detectable in flight.
 - c. All redundant elements can be lost by a single credible cause or event such as contamination or explosion.

Ground Rules

- Dual redundancy:
 - a. The first failure would result in loss of mission.
 - b. The next related failure would result in loss of life or vehicle.
- The loss of all redundant elements by a single credible cause or event is considered unlikely.
- Where redundancy exists in the subsystem, the redundancy is considered during failure analysis.
- "Alternate means of operation" refers to accomplishment of a function and not necessarily to redundancy or restoration of a failed function.
- Failure of structural items (primary or secondary) will not be considered in this analysis. (Structural items are assumed to be designed to preclude failure by use of adequate design safety factors.)

The FMEA for the rotator has been prepared and submitted by Hoover Electric as part of the vendor critical design review.

WAIVER

A waiver request was submitted to the customer specifically to exclude clutches and gear trains inside sealed gear boxes, as well as linkages from multiple level redundancy requirements. This approach is similar to the rationale employed in the Orbiter electromechanical technology, waiving gearing, linkage, and structural component failures as being unlikely (noncredible).

There are indications, however, that this waiver may not be approved for the full-length payloads, which block EVA egress. Suggested solutions are:

- a. Addition of a remotely actuated pin puller and capture device to the primary rotator link. This would allow the primary rotator link to be "broken" if the primary drive and clutch disengagement mechanisms both failed. Rotation could continue using the secondary rotator system.
- b. Use of an energy storage device (e.g., a spring) to hold the stack in a normally-stowed position with remote pin-pullers at the drive links in case of multiple mechanism failure. Actuation of the pin pullers would result in automatic return of Centaur/payload stack to its stowed configuration.
- c. Design of the clutches so that if the primary clutch fails to disengage, the backup rotator

can produce sufficient torque to cause the primary rotator clutch to slip, thus permitting rotation to continue.

Other suitable methods may be studied to develop acceptable design modifications to meet the two-failure tolerance requirement or achieve equivalent safety. In view of the criticality of the G-prime schedule, it would be impractical to impose any unique payload requirements on the G-prime rotation system at this time.

RATIONALE FOR ACCEPTANCE

Summary — Two-failure tolerance is provided to the maximum extent practical. Two independent rotator systems are provided. Each system includes a power drive unit that contains two independent drive motors. Each of the two motors in each power drive unit is capable of rotating the Centaur up for launch (separation) and down to stow for landing. Each power drive unit engages its rotation linkage through a clutch that is actuated by one of two independent motors. Such engagement does not occur until just before rotation in orbit. Three independent ac power sources are switched through the two-failure tolerant avionics system to provide two-failure tolerant power to each power drive and clutch motor. Each motor is controlled by an ac source, in which three independent series inhibits are placed. If any two ac sources, inhibits, or control units fail, the system will not rotate inadvertently and will still permit up or down rotation. The system meets the two-failure requirements in all components except the power drive unit clutches, geartrains, and structural linkage. An engaged clutch that fails to disengage, in conjunction with a jammed geartrain in the same power drive unit, would prevent rotation of the Centaur, as would failure of both clutches or geartrains. However, the combination of the drive and clutch motors of the primary and backup rotators are quad redundant, while each rotator is responding to triple redundant avionic command inputs. It should be noted that the DA rotation system has a higher level of failure tolerance than any Orbiter electromechanical system. For instance, any of the three active payload holddown latches jammed in the latched position will prevent rotation of the Centaur and block EVA.

Discussion — The sequence used to rotate the Centaur after the cargo bay doors are opened is as follows:

- The Orbiter turns on ac1 and ac2 (ac3 is always present at the Orbiter interface).
- Commands from the standard switch panel (SSP) will start Centaur airborne support equipment (CASE) controlled operations by engaging the primary clutch with motor 1. If this motor fails, motor 2 will automatically be activated. When the clutch is fully engaged, the motor (1 or 2) is turned off.
- The Orbiter commands the release of its Centaur holddown latches.
- Commands from the SSP will then activate the primary drive motor 1 and automatically rotate the Centaur out of the cargo bay. If this motor fails, primary drive motor 2 will automatically be activated to rotate the Centaur.
- At the erected position, the drive motor (1 or 2) is turned off automatically. The Orbiter may then secure power sources ac 1 and ac 2.

If a failure(s) occurs that prevents or halts Centaur rotation, the CASE control system will automatically switch over to the completely separate and redundant backup rotator system. Rota-

tion may then be continued by reinitiating commands from the SSP to erect or stow the Centaur. The CASE control system will then activate the components of the backup system in the same manner and sequence as previously mentioned to continue engagement or rotation.

The Orbiter crew can use the SSP to override or back out of the primary or backup operational sequence at any point. This includes returning the Centaur to the completely stowed position for a mission abort.

The DA rotation system is safe as designed and analyzed and may be classified as a cargo element/payload of the Orbiter for the following reasons:

- Each rotator is capable of performing a minimum of 1,000 duty cycles during its operating life, which is far in excess of the 10-mission requirement. The structural ultimate factor of safety is 1.4 (minimum). The components of the system have adequate strength and stiffness. Gear stress levels are one-fourth of the material ultimate stresses.
- Clutches are designed with separation springs between the clutch plates to prevent binding after the clutch is disengaged.
- Bearings, such as those used for the links, incorporate multiple rotating surfaces to ensure that rotational capability exists following surface-to-surface binding of one rotating surface. The life of each rotational surface is adequate to meet the full operating life of the item. If multiple rotational surfaces are not provided, the L10 life of each bearing or rolling element will exceed the required life by a minimum factor of 17.
- In case multiple sliding surfaces are not provided, the normally lubricated surfaces will slide without lubrication, thus providing one-failure tolerance. Also, test and design data obtained from the manufacturer show that the minimum power available to restow the Centaur is 3.2 times the worst-case restow forces.
- To prevent a single-point structural failure, the single structural component and the clutch components have built-in redundancy by oversizing the component for strength. In this case, the limit load is modified to include a suitable safety factor, and the maximum anticipated load is multiplied by that chosen safety factor. Selection of the redundancy safety factor depends on individual credible failure modes related to the function of the single component and analyzed on a case-by-case basis.
- The crank remains in its last actuated position until powered to a new position. Neither an out-of-tolerance condition nor a single component failure affects holding of position or moving to a new position.
- Threaded parts and fasteners are positively locked to prevent loosening during service. Single-fastener attachments have dual-locking features.
- Gearboxes are designed to preclude entry of foreign materials, loss of lubricants, and jamming of gears. No threaded fasteners are used inside the gearbox. Internal volume is kept to a practical minimum.
- Qualification tests will be performed to prove functional capability under extreme environmental conditions. Ground checkout tests before launch and ELS quality control operations will be performed.
- The manufacturer, Hoover Electric, has demonstrated the capability for designing and building similar devices, as exhibited by various electromechanical actuators provided for the Space

Shuttle vehicle (e.g., external tank umbilical door drive actuator, external tank umbilical door centerline latch actuator, external tank umbilical door latch drive actuator, payload bay door bulkhead latch actuator, payload bay door centerline latch actuator, radiator panel latch actuator, radiator panel drive actuator, and manipulator positioning mechanism actuator). The DA rotator employs the same concepts and some identical hardware used in these flight-qualified actuators.

CONCLUSION

The DA rotator design has required state-of-the-art space technology to produce a very reliable rotation system for the Centaur G-prime and G vehicles. Proper interpretation of redundancy is essential for hardware acceptance. This can be demonstrated by using proven electromechanical design methods, careful selection of materials, and with full understanding of hardware and functional criticalities. Simplicity and commonality can greatly improve reliability and safety while achieving mission objectives. Interpretation of redundancy is necessary to facilitate the method of attaining equivalent safety that matches the effect of two-failure tolerance by overdesigning the single critical components. Gears, clutches, and linkage are not two-failure tolerant; however, they are considered acceptable because of ultra-conservative wear, stress, and life factors. The author's observation is that a more explicit definition and guidance tailored for electromechanical designs for space application would be instrumental in equating redundancy to equivalent safety based on credible failure modes of individual components and would help eliminate doubt during the design phase. Differing definitions of redundancy can lead to disagreements resulting in possible design changes impacting schedule and cost.

N84
25089

UNCLAS

PASSIVE SUN SEEKER/TRACKER
AND A
THERMALLY ACTIVATED POWER MODULE

Clete J. Siebert* and Fred A. Morris*

ABSTRACT

This paper describes the development and testing of two mechanisms using a shape memory alloy metal (NITINOL) as the power source. The two mechanisms developed are a passive Sun Seeker/Tracker and a generic type power module. These mechanisms use NITINOL wire initially strained in pure torsion which provides the greatest mechanical work capacity upon recovery, as compared to other deformation modes (i.e., tension, helical springs, and bending). (See Figure 1.)

INTRODUCTION

The term Shape Memory Effect (SME) is used to describe a group of alloys, that upon heating, exhibit a new mechanical property known as shape memory or shape recovery (Figure 2). These alloys possess the ability to remember a shape imparted to them while in the high temperature or austenitic phase. At lower temperatures they are in the martensitic phase and may be strained or deformed to some intermediate shape. All or some of that plastic strain may be recovered by subsequent heating through the transition temperature from martensitic to austenitic states. The transition temperature is quite low (i.e., 80°C (176°F), and the recovery force is approximately 758 MPa (110 KSI).

SUN SEEKER/TRACKER

The Sun seeker/tracker senses any misalignment of the impinging solar radiation and uses this radiation energy to drive the mechanism until it is centered on the Sun. Neither external energy nor signals are required to drive and position the unit.

Present state-of-the-art trackers use optical detectors to first seek the Sun and then preprogrammed algorithms are used to determine and follow the position of the Sun. The drive mechanisms consist of primary and back-up motors, gear trains, and complex feedback control systems.

* Martin Marietta Denver Aerospace, Denver, Colorado

ORIGINAL PAGE 19
OF POOR QUALITY

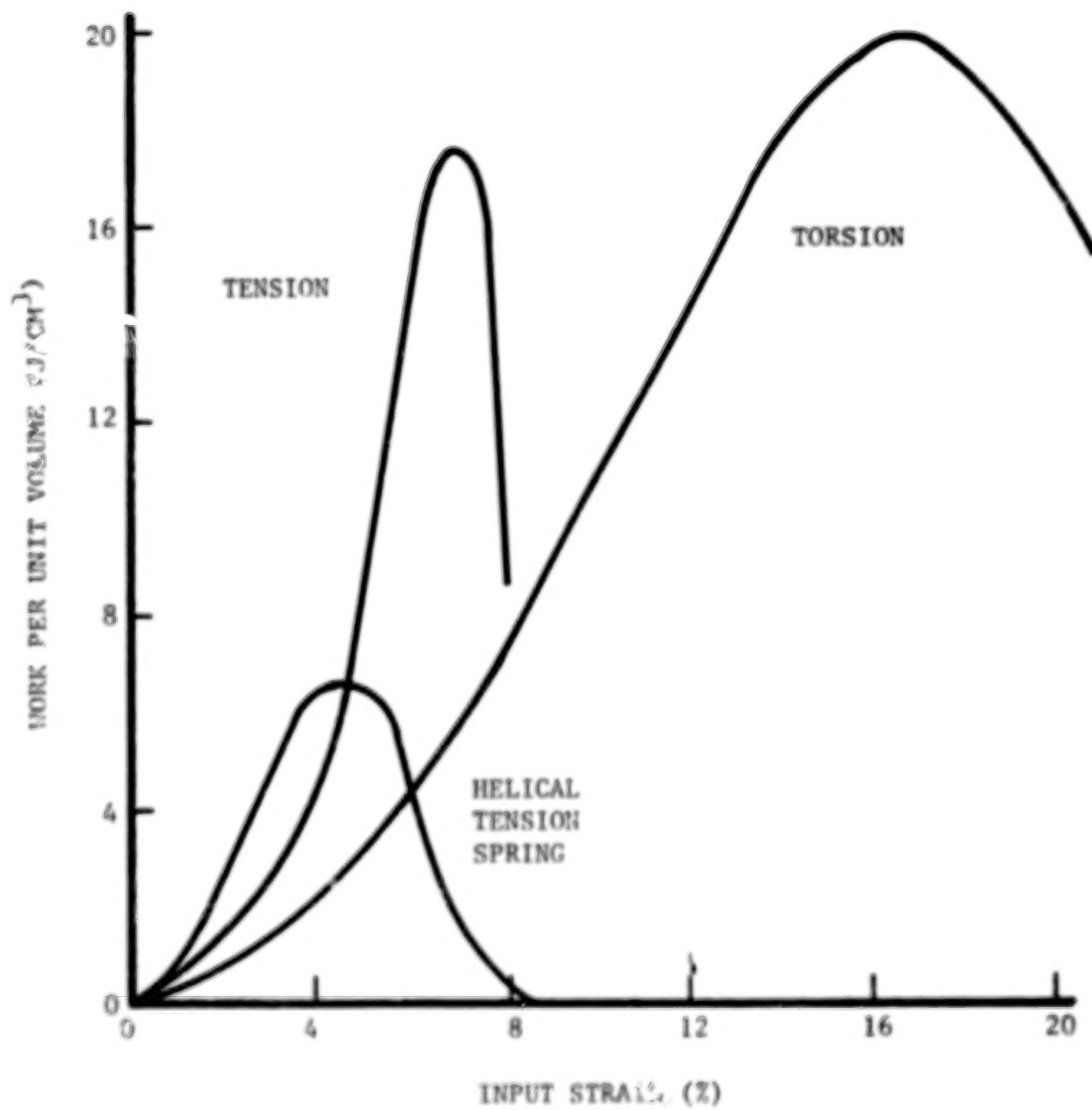


Figure 1. Performance for Three Different Configurations Using
0.14 cm Diameter Wire

ORIGINAL PAGE 19
OF POOR QUALITY

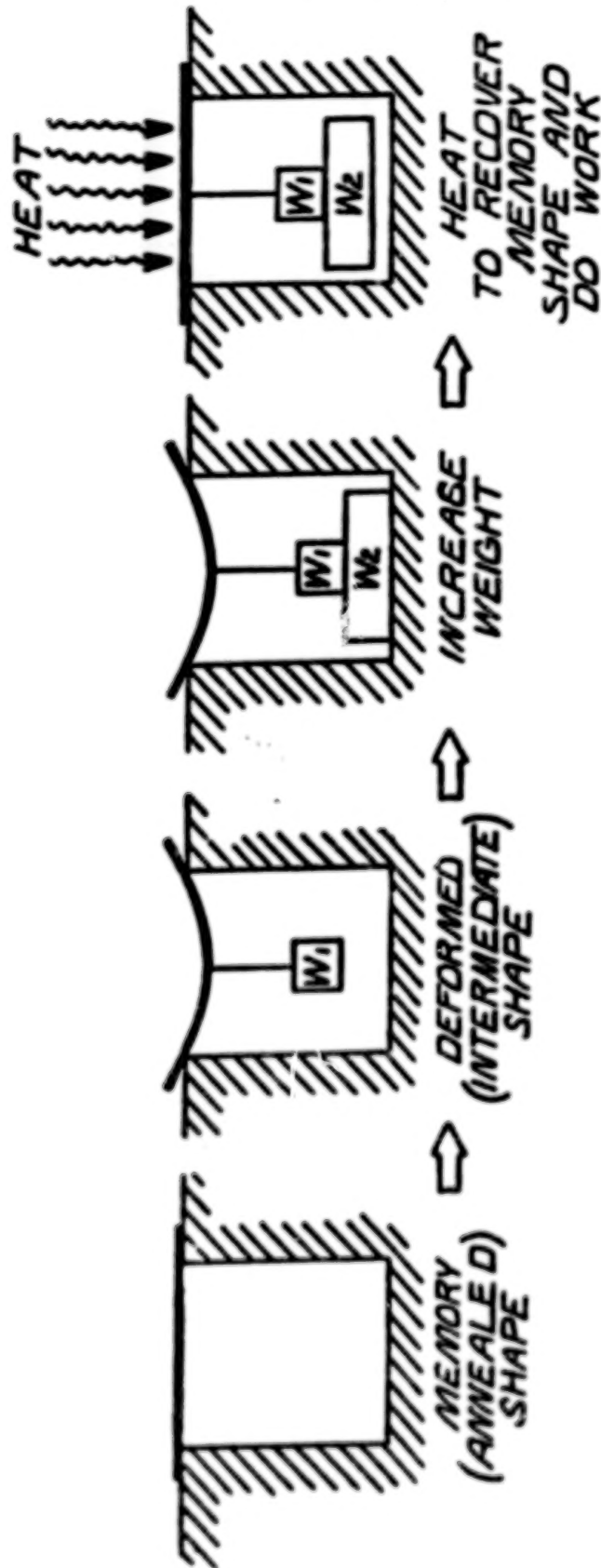


Figure 2. Principle of Shape Memory Recovery and Work

The Sun seeker/tracker (Figures 3 and 4) consists of two major sections: the outer drum and the inner drum, which houses the 33 drive units. These sections are mounted on concentric shafts that rotate independently. The inner drum is divided into 10° sections around the periphery, in which indexing Nitinol drive units are housed (Figures 5 and 6).

The purpose of the drive units is to sequentially index the inner drum around the fixed outer drum until a neutral point is reached; at this time the unit is centered on the Sun. A locking mechanism may be activated to hold the unit in place until the Sun moves far enough to activate one of the positioning Nitinol drives.

Each of the 33 drive units are identical, consisting of only three parts: a lever arm, a torsion bias spring, and a twisted Nitinol wire (Figure 7). The only moving parts are the lever arm and its pivoting head, both of which have bias springs to stow the mechanism after activation. The Nitinol wire is fixed into the rotating lever arm and clamped to the inner drum on the other end. Overall, the whole assembly is very simple and reliable, and its cost could be reduced by investment casting the lever arms and heads since all 33 drive units are identical.

For several reasons the 0.14 cm (0.055 in) wire diameter was selected over the available 0.08 cm (0.031 in) and 0.25 cm (0.098 in) wire diameters to drive the unit. First the work per unit volume ratio was higher for this wire than the others tested in torsion as (Figure 8) and the calculated output torque and overall mechanism size was well suited for a prototype model using the 0.14 cm diameter wire.

When the drive unit is in the stowed position, the cool martensite Nitinol wire, initially twisted approximately 500° , is restrained in a twisted configuration by a torsion bias spring. The overall angular movement is 50° upon heating and is limited in either direction by roll pin stops. Activation occurs when the Sun rays heat the Nitinol wire above transformation temperature and elastic austenitic recovery tends to untwist the wire to the untwisted memory annealed configuration. In the process, the torsion bias spring is wound and the lever arm drives the inner drum with respect to the outer drum 10° , (Figure 3). Now the adjacent wire is exposed and heated, this sequence continues until the mechanism is centered on the Sun and locked into position. As the Nitinol cools, the modulus of elasticity of the wire decreases allowing the torsion bias spring to wind the Nitinol wire and stow the drive unit, totally disengaging it from the outer drum. As it is stowed, the lever arm must clear the next indexing peg on the outer drum. As shown in Figure 9, the spring loaded head of the lever arm pivots to clear the indexing pin of the outer drum.

ORIGINAL PAGE 19
OF POOR QUALITY

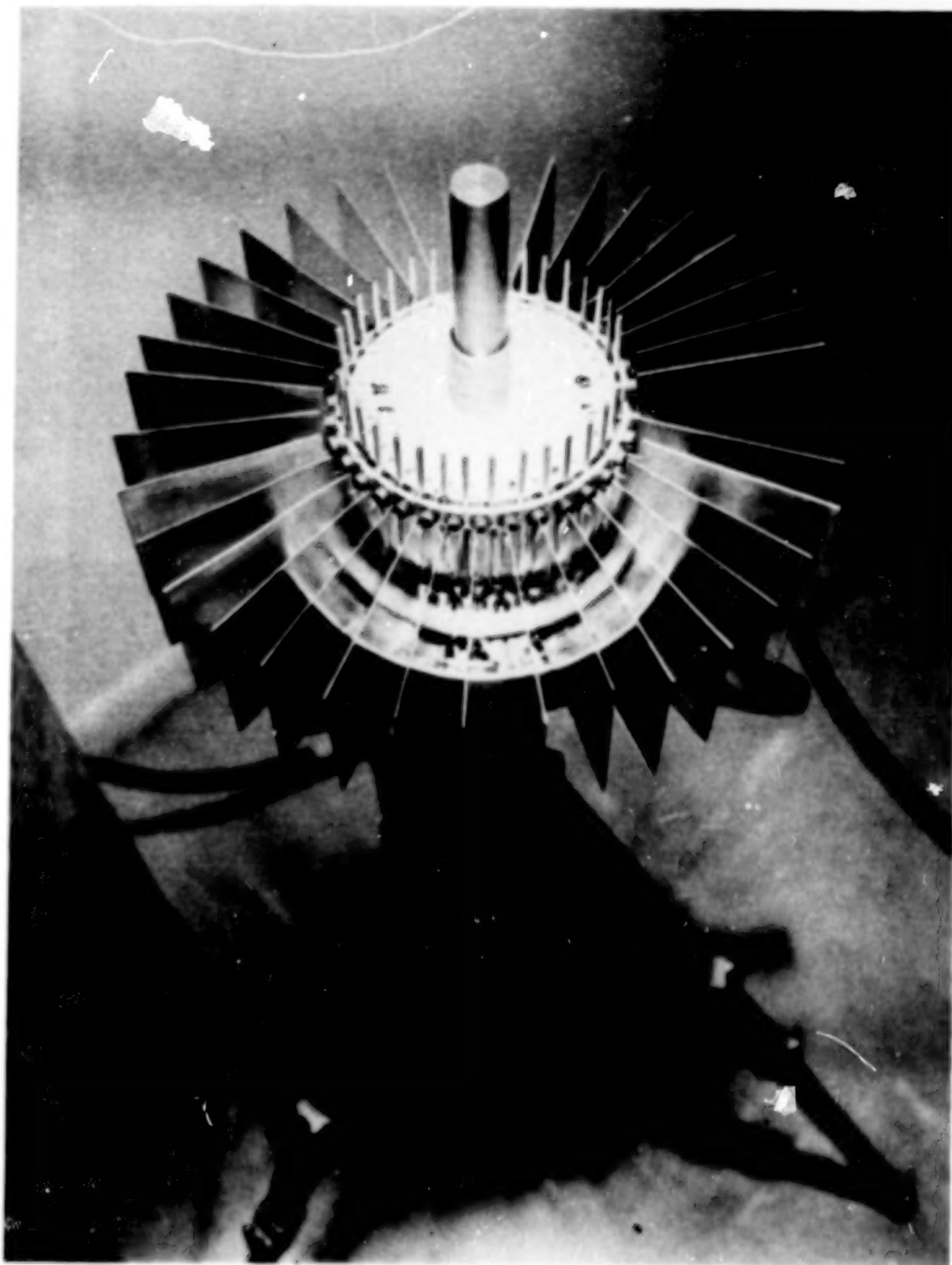


Figure 3. Plan View of Sun Seeker/Tracker

ORIGINAL PAGE IS
OF POOR QUALITY

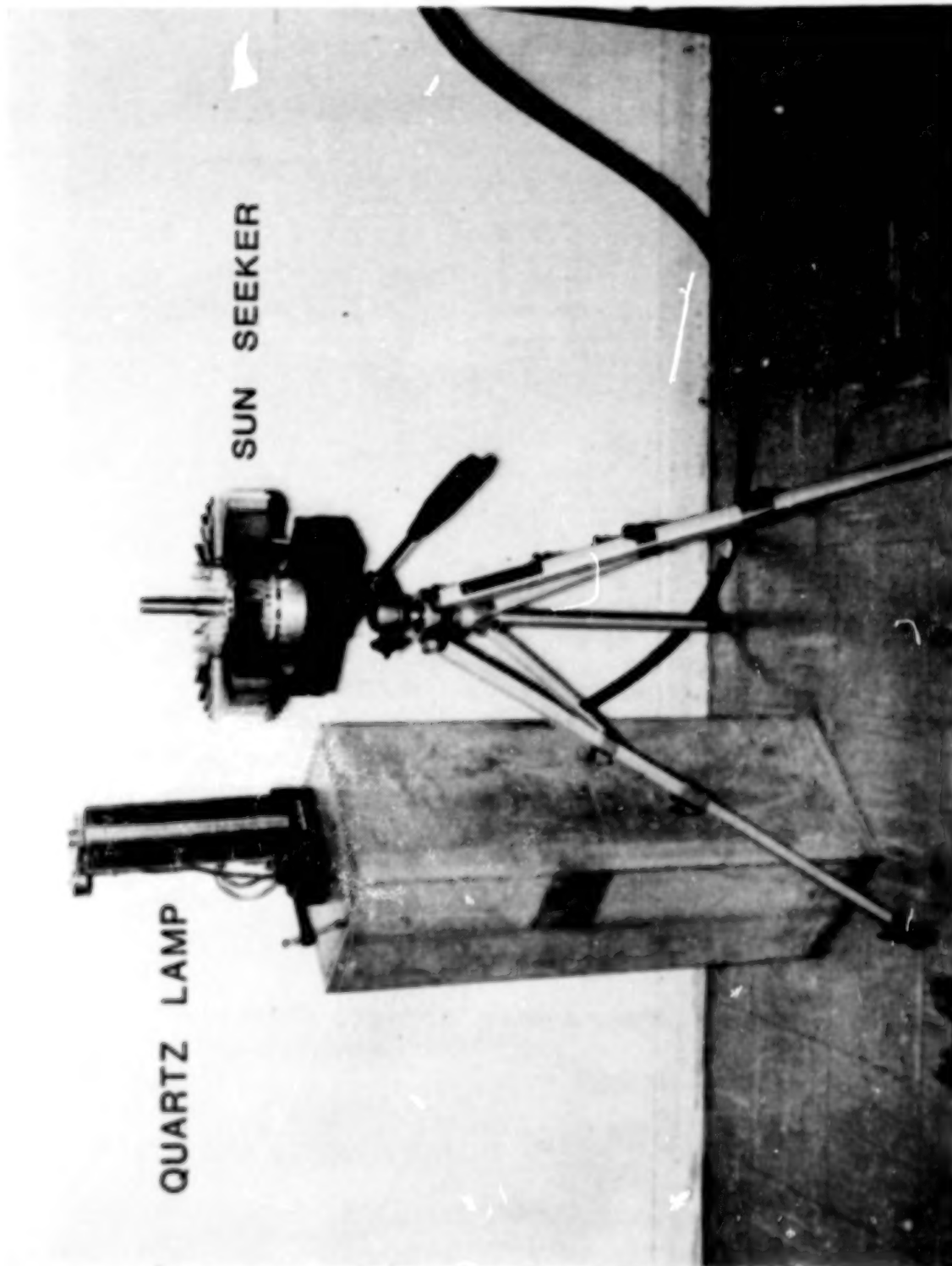


Figure 4. Testing Sun Seeker/Tracker Using a Quartz Lamp

ORIGINAL PAGE 19
OF POOR QUALITY

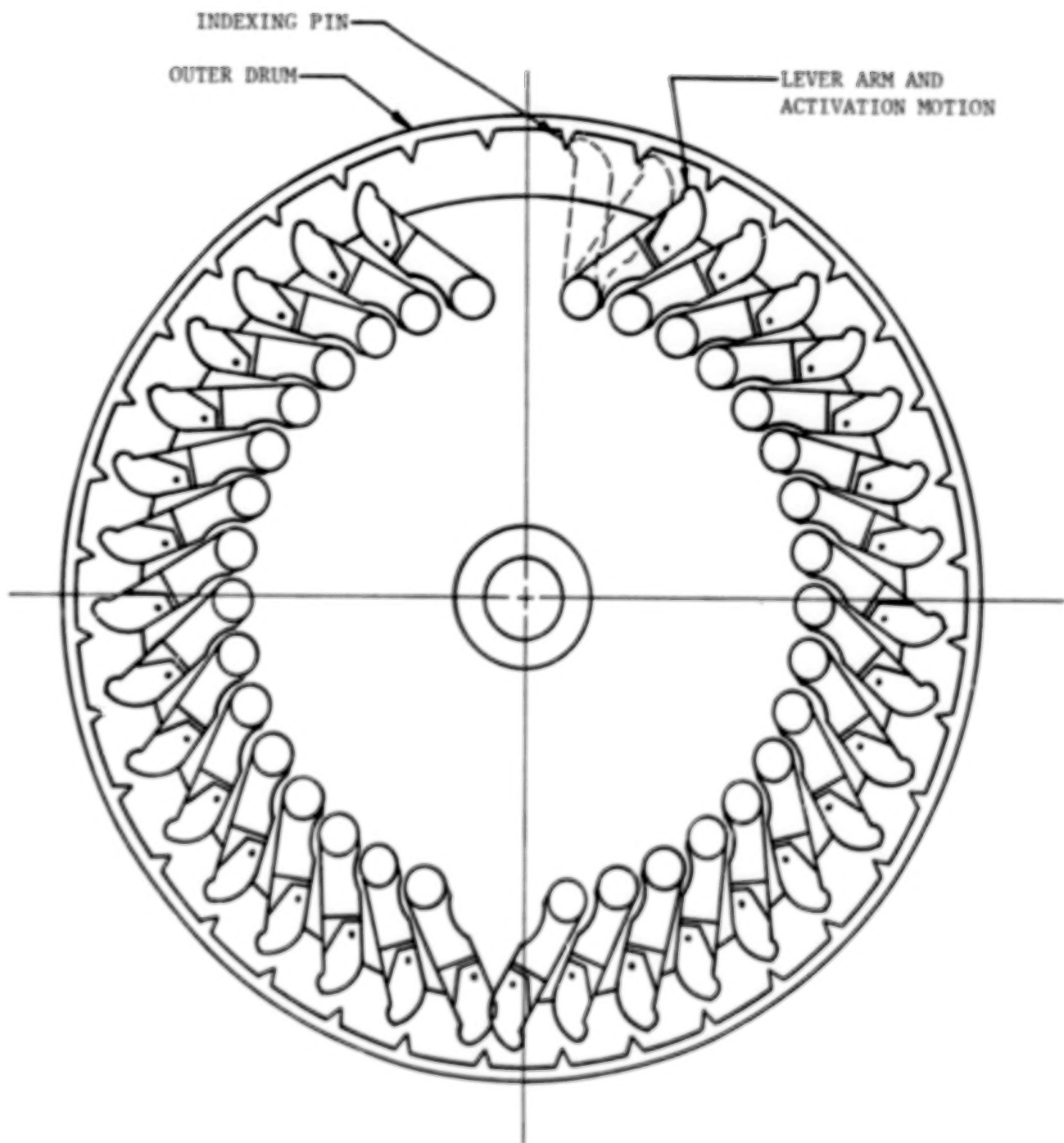


Figure 5. View of Lever Arm Arrangement

ORIGINAL PAGE 19
OF POOR QUALITY

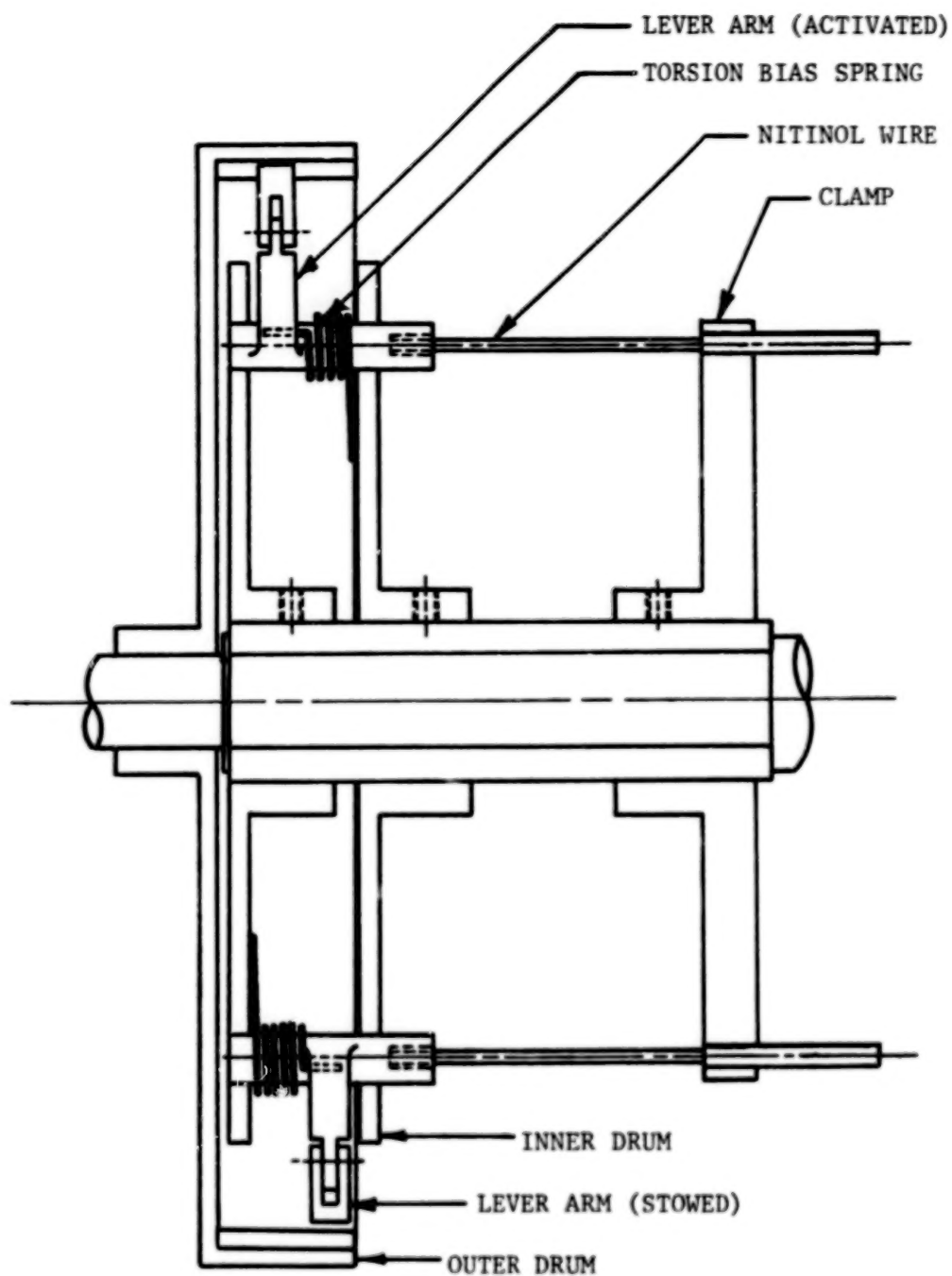


Figure 6. Cross-section of Sun Seeker/Tracker

ORIGINAL PAGE 19
OF POOR QUALITY

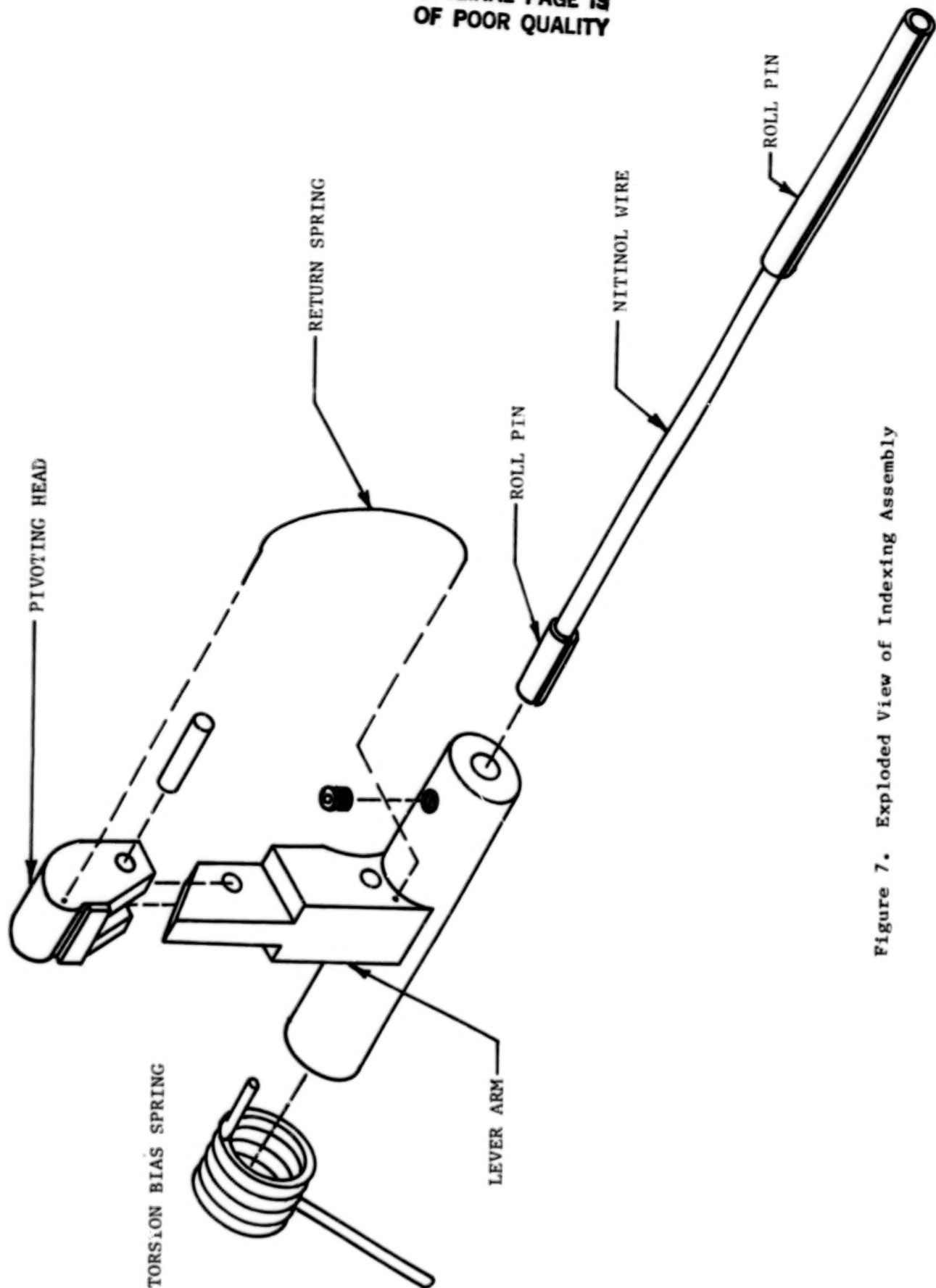


Figure 7. Exploded View of Indexing Assembly

ORIGINAL PAGE 19
OF POOR QUALITY

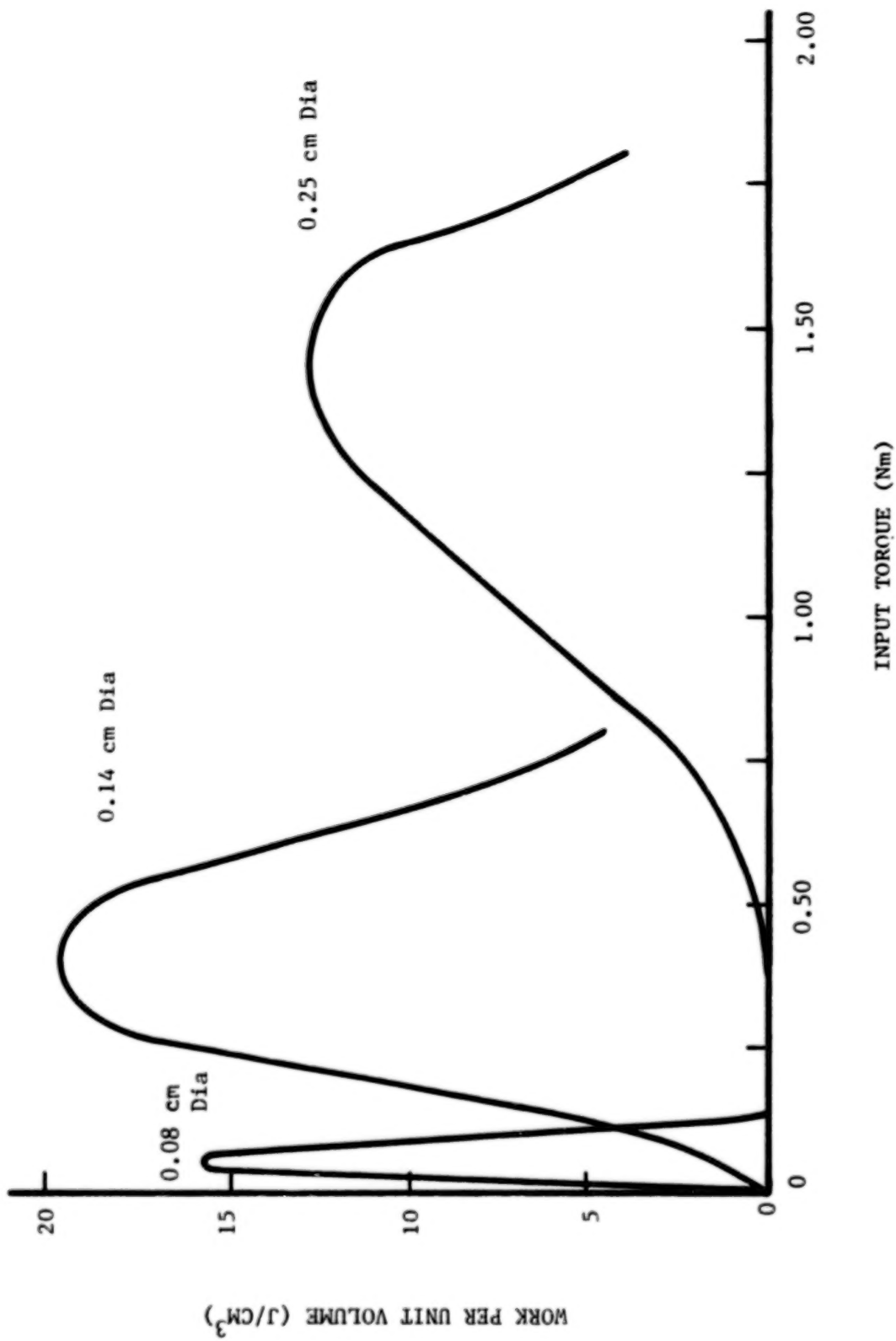
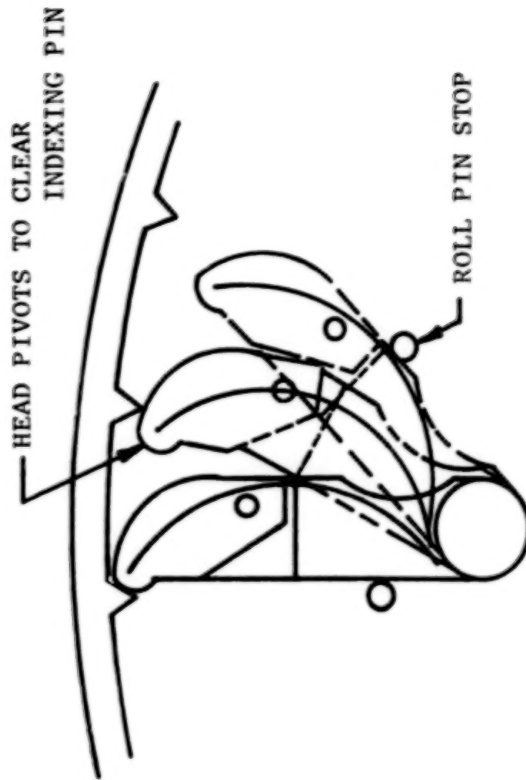
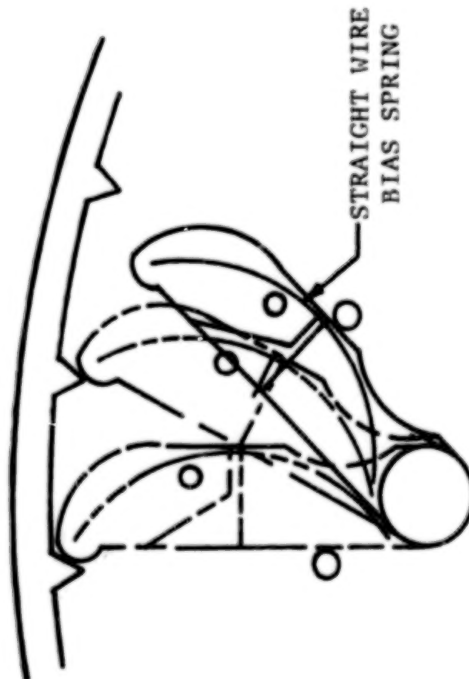


Figure 8. Performance of Three Diameter Nitinol Wires in Torsion



STOWAGE:

OUTER DRUM STATIONARY
AS DRIVE UNIT IS STOWED.
DRIVE UNIT'S HEAD PIVOTS
TO CLEAR INDEXING PINS



ACTIVATION:

INNER DRUM DRIVEN 10°
BY DRIVE UNIT. OUTER
DRUM FIXED

Figure 9. Kinematics of an Indexing Drive Unit

ORIGINAL PAGE IS
OF POOR QUALITY

Baffles are used to allow the sunlight to heat only one of the Nitinol drives at a time. Each drive unit is totally independent from the others. If a unit fails, operation of any other unit is not affected, as the other units will continue to operate accurately. If two of the drive units are actuated, one on the heating cycle and one cooling, the driving unit will still properly function because the lever arms act as a pawl and will not catch on the indexing pins unless they are driving. The lever arms are staggered in two levels to eliminate any possible interference.

To increase the radiation absorption of the wire, a parabolic reflector was placed directly behind the Nitinol with the wire at the parabolic focus point. The wire was also painted black to increase the amount of absorbed radiation; because bare metal reflects a large portion of the impinging radiation.

The number of drive units determines the accuracy of the tracker. This tracker is accurate to $\pm 5^\circ$ of centering on the Sun with 10° indexing steps. Drive units on either side of the center position are arranged to drive towards the centered position, thus the maximum angle the unit will have to rotate when seeking the Sun is 180° . See Figure 5.

The assembled unit is 15.25 cm (6 in) in diameter by 8.9-cm (3.5-in) long and is capable of operating with a restraining torque of 0.36 Nm (52 in-oz) and a stall torque of 0.65 Nm (92 in-oz). The output torque is a function of the size of Nitinol wire driving the unit; larger Nitinol wires could be used to greatly increase output torque.

The unit will track and seek in one axis. If two units were used, the Sun could be sought and tracked in two-axis or in three-dimensional space. At the present time, this prototype unit is undergoing cyclic life tests. To date the unit has been operating daily for 26 weeks using solar energy concentrated by fresnel lenses.

No mechanical problems have been experienced and no Nitinol fatigue or creep has been noted. The only adjustment required has been to manually correct for the ecliptic plane angle every few days.

TORSION DRIVE MODULE

The torsion drive module is a unit containing four Nitinol wires coupled with spur gears producing cyclic rotary motion of the output shaft when activated. This unit can be used in such applications as opening and closing valves and latches, rotating lenses and filter caps into position, window blind controls, or any application that needs a cyclic drive unit with restow capabilities.

The module is a 74 gram compact unit (2.5 cm by 2.5 cm by 8.3 cm) capable of producing output torque of 0.58 Nm (5.1 in lbs) in either direction with up to 200° of rotation. In specific situations where the output characteristics of the module are desired, the SME module would be superior to any conventional drive since because output torque to volume and weight ratios are several times higher.

The module uses four 0.14-cm diameters, 5-cm long Nitinol wires clamped down on one end and coupled with wind-up gears on the other. See Figure 10. Initially, two of the wires were twisted 400° and the others were free from strain. The annealed shape was a straight wire. Therefore, when the twisted wires are heated to transformation temperature, they will recover to their memory (i.e., untwisted configuration). Upon recovery they in turn will wind the two cool martensitic wires while producing an output torque on the shaft clamped to one of the wires. Now the other two wires are twisted and once heated above transformation temperature they will recover, twisting the two cool wires and driving the output shaft with a torque of 0.58 Nm. In this manner, repeatable power is produced in both directions. Output torque is a function of wire diameter, and the angle of twist is a function of wire length. The module could have been made shorter with the same output torque but reduced output angular rotation.

For demonstration purposed, the wires were heated electrically using a 2V rechargeable, wet cell, but any energy source could power the module if it could heat the wire above 80°C.

CONCLUSIONS

A wide range of applications for Nitinol materials appears to exist in a variety of structural and mechanical devices (Figure 11). For space systems applications, the potential of directly using environmental thermal energy to actuate required mechanical motions is attractive.

The material is basically metallic and should exhibit excellent resistance to hard vacuum, temperatures extremes, and radiation.

Further experimental work in characterizing and controlling the thermomechanical properties of Nitinol is required to permit the design and construction of reliable space hardware.

ORIGINAL PAGE 19
OF POOR QUALITY

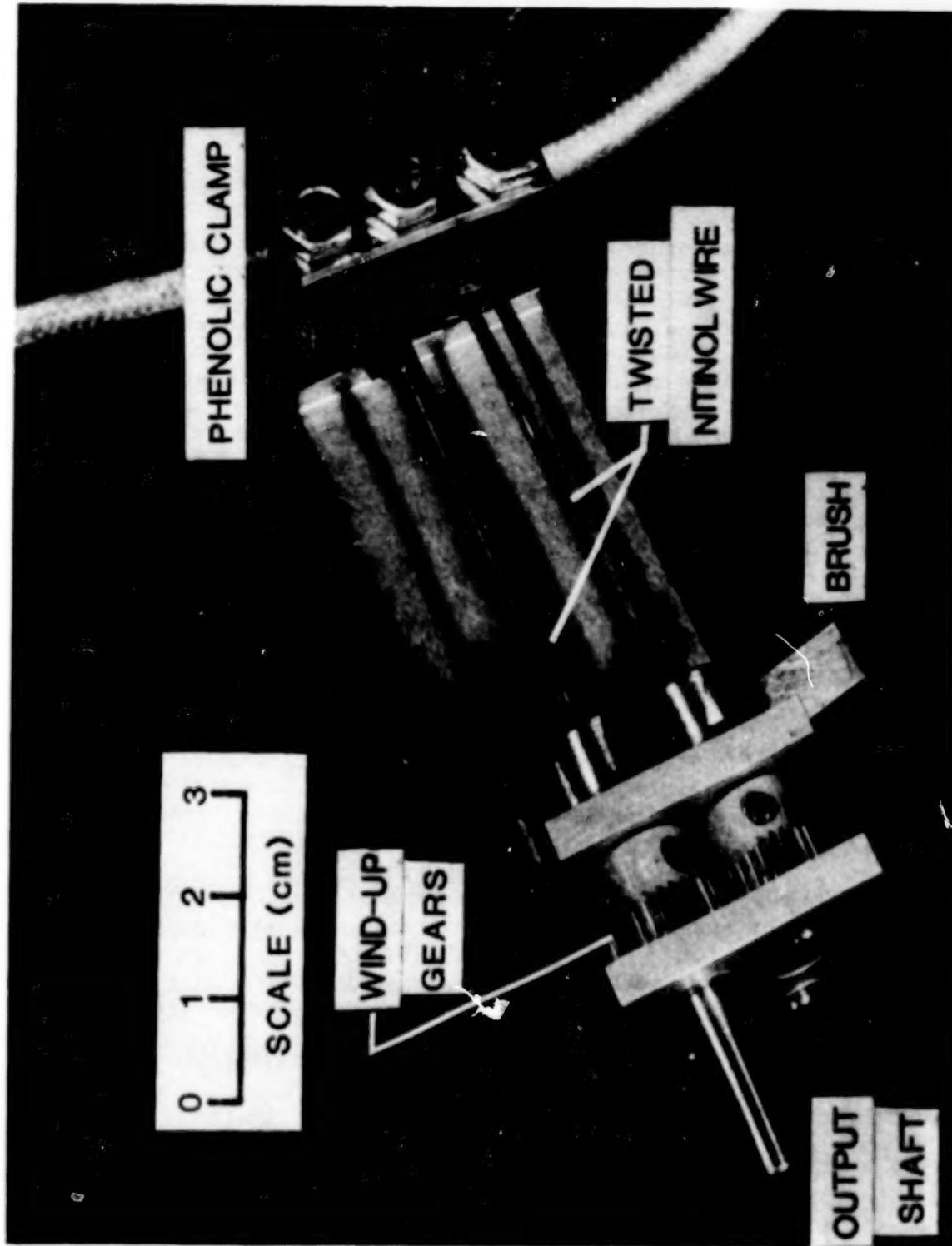


Figure 10. Thermally Activated Power Module

ORIGINAL PAGE IS
OF POOR QUALITY

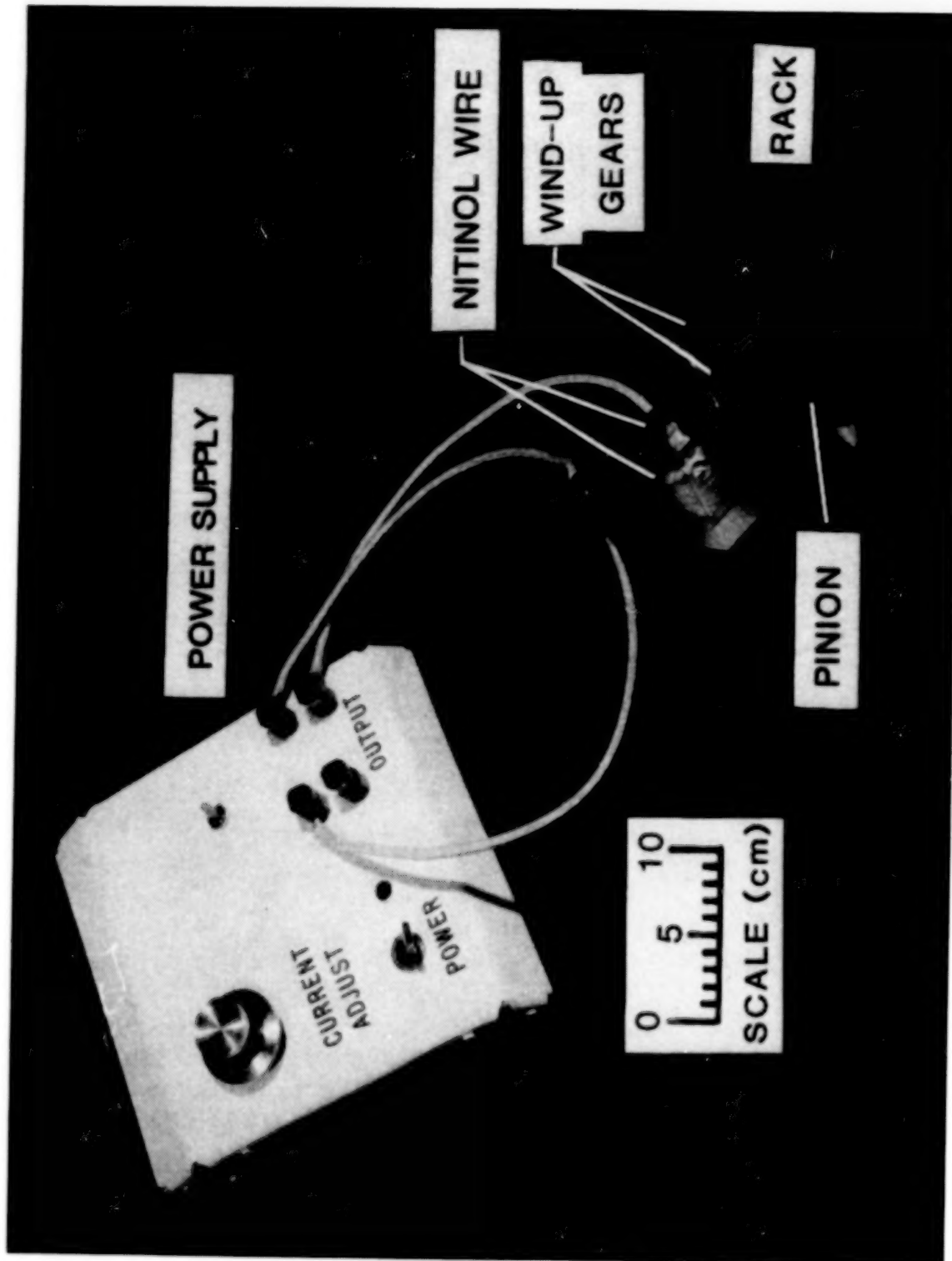


Figure 11. Linear Output Power Module

N84
25090

UNCLAS

D12

N84 25090

THE DESIGN AND DEVELOPMENT OF A SOLAR TRACKING UNIT

Irby W. Jones and James B. Miller*

ABSTRACT

The solar tracking unit was developed to support the Laser Heterodyne Spectrometer (LHS) airborne instrument, but has application to a general class of airborne solar occultation research instruments. The unit consists of a mirror mounted on two gimbals, one of which is hollow. The mirror reflects a 7.6 cm (3.0 in) diameter beam of sunlight through the hollow gimbal into the research instrument optical axis. A portion of the reflected sunlight is directed into a tracking telescope which uses a four-quadrant silicon detector to produce the servo error signals. The colinearity of the tracker output beam and the research instrument optical axis is maintained to better than ± 1 arc-minute. The unit is microcomputer controlled and is capable of stand alone operation, including automatic Sun acquisition or operation under the control of the research instrument.

INTRODUCTION

The solar tracking unit was developed to support the Laser Heterodyne Spectrometer (LHS) instrument. This instrument is intended to fly on the NASA CV-990 aircraft to gather atmospheric spectroscopy data during a sunrise or a sunset. The instrument is shock mounted to the aircraft floor and must track the Sun through a window in the side of the aircraft. The alignment of the LHS instrument optical axis and the output beam from the tracking system is critical and requires the tracker to be mounted on the instrument. The solar tracker unit provides a stable 7.6 cm (3.0 in) diameter beam of sunlight to the instrument, compensating for both aircraft and instrument motion. The unit is microcomputer controlled and is capable of stand alone operation, including automatic Sun acquisition or operation under the control of the research instrument.

SPECIFICATION REQUIREMENTS

The following basic requirements are defined by the instrument science requirements or as a result of the overall instrument and aircraft interface design evolution.

- The unit must be mounted directly to the instrument optical table to eliminate relative motion between the tracker and the instrument.
- Weight must not exceed 18.1 kg (40 lbs).
- Mirror height above mounting surface must be 38.1 ± 2.54 cm (15.0 ± 1.0 in).

* NASA Langley Research Center, Hampton, Virginia

PAGE 186 INTENTIONALLY BLANK

- A 7.62 cm (3.0 in) diameter sunbeam should be delivered to the instrument.
- Tracking stability and repeatability for each axis must be ± 4 arc-minutes, with a goal of ± 1 arc-minute.
- The tracking mirror reflecting surface must be optically flat to one-fifth wavelength at 0.63 microns.
- The optical line of sight (LOS) of the unit should be capable of being positioned to a local coordinate system with an accuracy and repeatability of ± 1.0 arc-minute. Position control range should be $+15^\circ$ to -90° in elevation and $\pm 180^\circ$ in azimuth.
- The unit must be capable of tracking the Sun over an elevation range of $+30^\circ$ to -15° with no obscuration in the output beam.
- Frequency response must accommodate the expected range of aircraft disturbance. Frequency response goal for elevation axis is 100 Hz, and for azimuth axis is 25 Hz.
- A lockable stow position must be provided to protect the mirror optical surface and prevent motion in either axis.
- The system design should be as modular as possible to simplify testing and repair of the instrument in the field.
- The system must be simple to operate, test, and troubleshoot. It should be capable of monitoring its own operation, diagnosing system faults, correcting the faults if possible, and notifying the system/operator in the event of a failure.

MECHANICAL DESIGN

The tracking unit design, which satisfies the requirements outlined above, is shown in Figure 1. A photograph of the completed unit and the control electronics is shown in Figure 2. The unit uses a mirror mounted on a horizontal elevation gimbal to reflect a sunbeam down through a hollow, vertical azimuth gimbal to a turning mirror, and onto the research instrument optical axis. A portion of the sunbeam is also reflected to a telescope which forms an image of the Sun on a photodiode detector. The detector produces error signals that cause the elevation and azimuth gimbals to move in a manner that keeps the Sun image on the detector.

The unit was built, assembled, and tested as three independent subsystems: an elevation gimbal, an azimuth gimbal, and a tracking sensor telescope. After subsystem testing, the three subsystems were integrated to form the complete solar tracking unit and system tests were performed. Figure 3(a) is a front view of the unit. Figure 3(b) shows the same view of the unit with the azimuth gimbal rotated approximately 180° .

ORIGINAL PAGE 03
OF POOR QUALITY

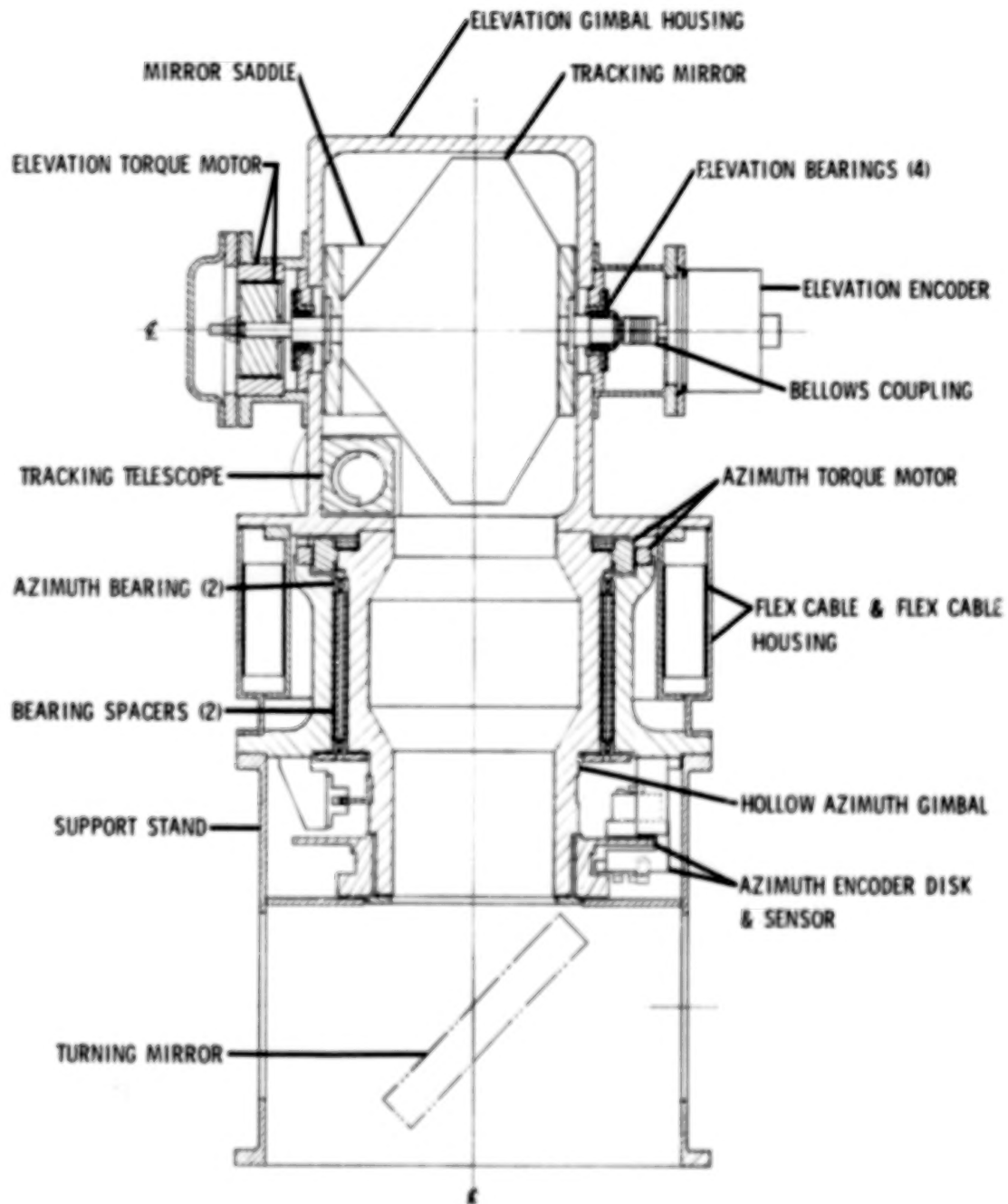


Figure 1. Solar Tracking Unit Assembly

ORIGINAL PAGE 19
OF POOR QUALITY

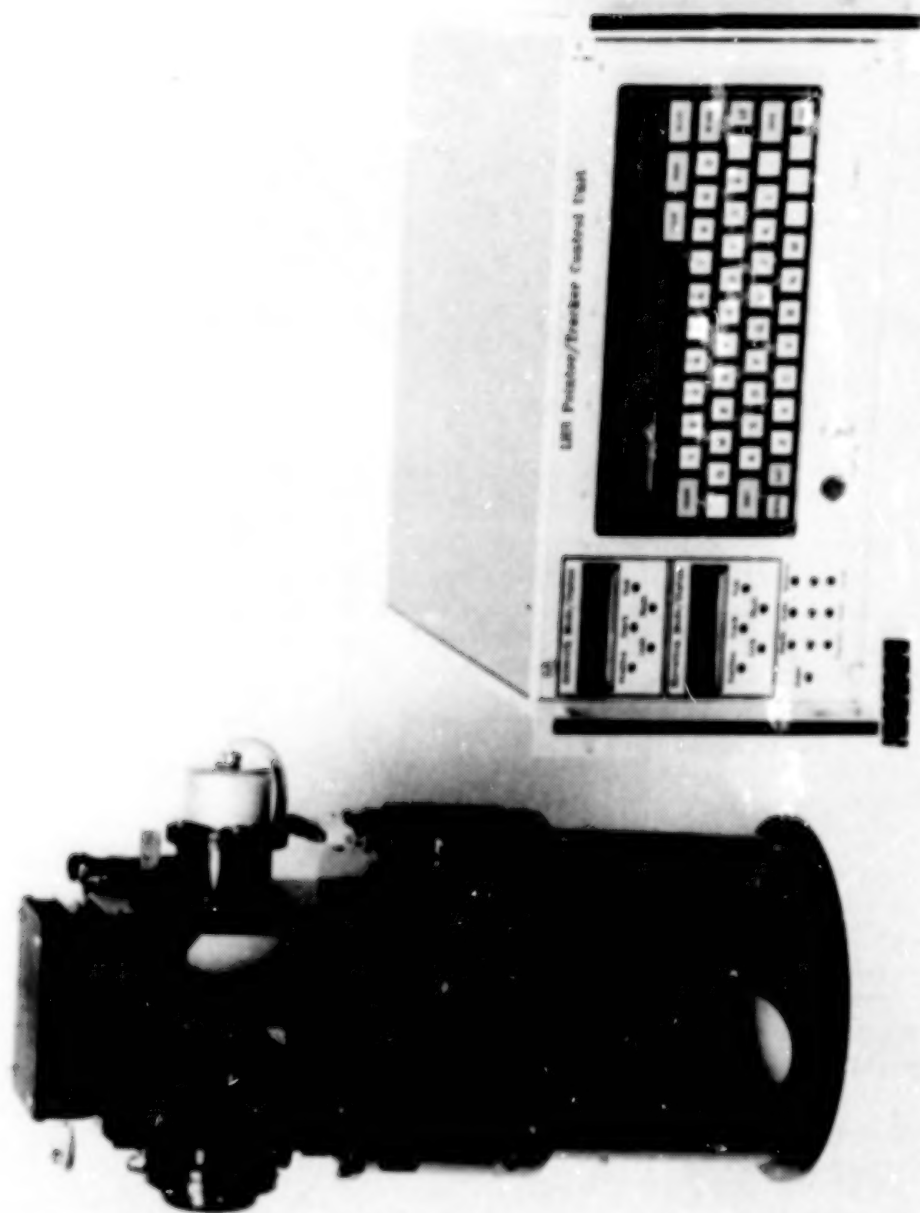
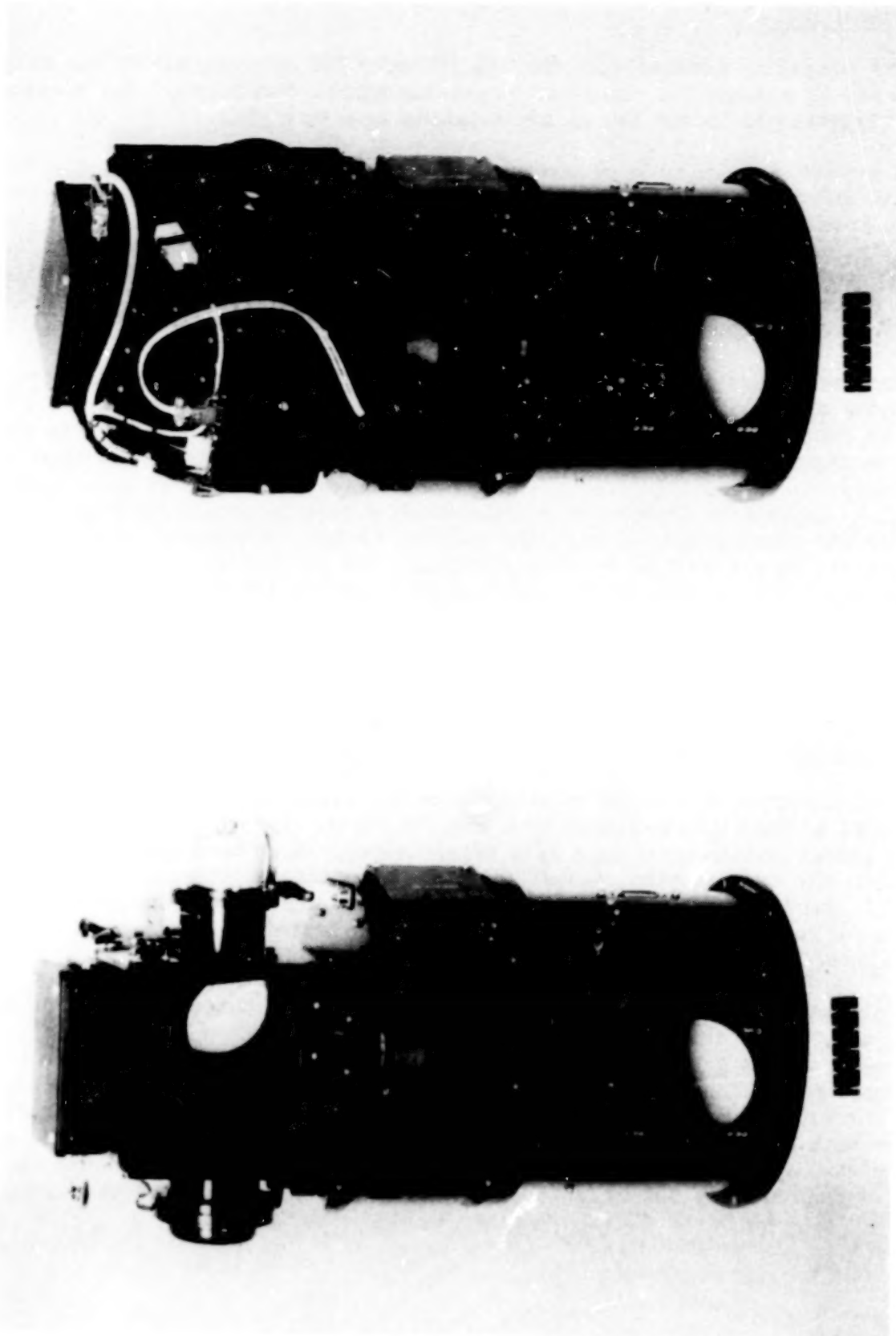


Figure 2. Solar Tracking Unit and Control Electronics

ORIGINAL PAGE 19
OF POOR QUALITY



(a) Figure 3. Solar Tracking Unit (b)

Elevation Gimbal

The elevation housing supports and protects the rotating mirror assembly and serves as a mount for the other elevation gimbal components. The housing itself is attached to the top of the rotating azimuth gimbal.

A saddle assembly, with removable shafts on each side, supports the Sun tracking mirror. The mirror consists of a nickel-plated aluminum body, coated on the front surface with enhanced aluminum for high reflectivity into the near-infrared spectrum. The elliptically shaped mirror is thick enough to be self supporting and mounts to the saddle with three thin legs to minimize mirror distortion induced by the saddle. The shafts are supported by a pair of preloaded bearings mounted to the elevation housing.

The saddle and mirror are driven directly by a brushless dc torque motor. The stator of the component motor is mounted to the elevation housing and the rotor is mounted on one saddle shaft. A direct drive approach was chosen for its advantages over the use of gears. Direct drive gives a greater torque to inertia ratio, thus a higher acceleration capability. The lack of gear backlash gives maximum stiffness for a high-resonant frequency, and for high accuracy and resolution. An absolute angular encoder is attached to the other saddle shaft by a flexible bellows coupling. The encoder has a resolution of 0.33 arc-min, and is used as the position feedback for the control system.

The rotating components are balanced to better than the bearing friction torque: 0.00565 Nm (0.8 oz-in). The gimbal has an operating range of +25 degrees to -90 degrees with a manually lockable stow position at -90 degrees.

Azimuth Gimbal

The azimuth gimbal supports and rotates the elevation gimbal assembly and is mounted to the LHS instrument by a support stand. The hollow rotating part of the gimbal is supported by a pair of preloaded, large bore angular contact bearings. The thin-section, class 7 bearings have teflon separators for a low ratio of starting to running torque. The bearings are factory duplexed back-to-back for maximum structural stiffness, and are separated by a pair of equal length spacers.

The azimuth gimbal is driven directly by a commutated hollow bore dc torque motor. The armature of the component motor is mounted to the rotating, inner part of the gimbal and the field and brush assembly is mounted to the stationary part of the gimbal. The direct drive technique has the same advantages described for the elevation gimbal. A hollow bore incremental angular encoder with a resolution of 3.6 arc-seconds is used for position feedback to the control system. The rotating and stationary parts of the component encoder are carried by the azimuth gimbal in a manner similar to the torque motor.

The rotating components are balanced to better than the bearing friction torque: 0.0318 Nm (4.5 oz-in). The gimbal has an operating range of $\pm 182^\circ$, with stops at each extreme and a manually lockable stow position at the nominal zero position.

Electrical power and signals are transferred through the azimuth gimbal to the elevation assembly by a flex-cable assembly. The flex-cable assembly consists of a loop of laminated flat conductor cable with one end attached to the inner housing and the other end attached to the outer housing (Figure 1). The outer cable housing is attached to the stationary part of the azimuth gimbal, and the inner cable housing is attached to the base of the elevation housing and rotates with the azimuth gimbal. The flat cable loop "walks" along the walls of the inner and outer housings as the azimuth gimbal rotates.

Tracking Sensor Telescope

The tracking sensor telescope, which is mounted in the elevation housing, contains the optics that form the Sun image on the tracking detector and an adjustable mounting system for the detector and preamp electronics. Figure 4 shows the telescope design. A diagonal mirror intercepts a portion of the sunbeam reflected down by the tracking mirror and directs it along the telescope axis. The beam energy is attenuated by a bandpass filter and neutral density filters to produce the desired level of energy on the detector. The filters are mounted in a removable holder which allows them to be changed without removing the telescope assembly from the elevation housing. An 80 mm (3.15 in) focal length lens forms an image of the Sun on the detector. The image size that is chosen provides a 2.0° telescope field of view.

When the telescope line of sight (LOS) is pointed directly at the Sun the image is centered on the four quadrants (active areas) of the detector as shown in Figure 5. If the image is not centered, there are differences between the detector quadrant outputs. These differences are combined to produce the error signals (Figure 6) that cause the tracking mirror gimbals to move and recenter the image on the detector.

The alignment of the tracking unit output beam to the LHS instrument optical axis depends upon the alignment of the telescope LOS to the true azimuth gimbal rotation axis. Any error in the parallelism of the telescope LOS with the azimuth gimbal axis results in a corresponding systematic tracking error as the azimuth gimbal rotates to follow the Sun. To accommodate manufacturing tolerances in the unit, an adjustment is provided to move the telescope LOS. The telescope is fixed to the elevation housing and the LOS is moved by translating the detector assembly in the focal plane of the lens. A compact mechanism in the telescope end produces a $\pm 1.8^\circ$ movement in LOS by translating the detector/preamp assembly in the two orthogonal directions corresponding to the directions the Sun image moves when the elevation and azimuth gimbals are rotated. In addition to the translation adjustments, a rotation adjustment for the detector/preamp assembly of $\pm 2.5^\circ$ is included to null the interaction between elevation and azimuth error signals.

ORIGINAL PAGE IS
OF POOR QUALITY

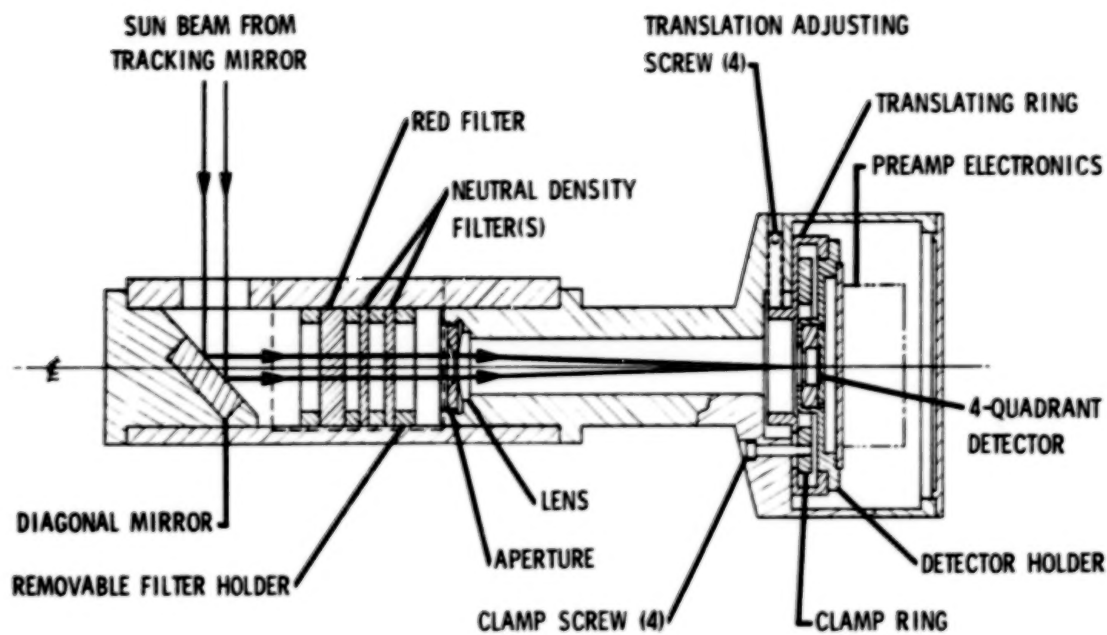


Figure 4. Tracking Sensor Telescope Assembly

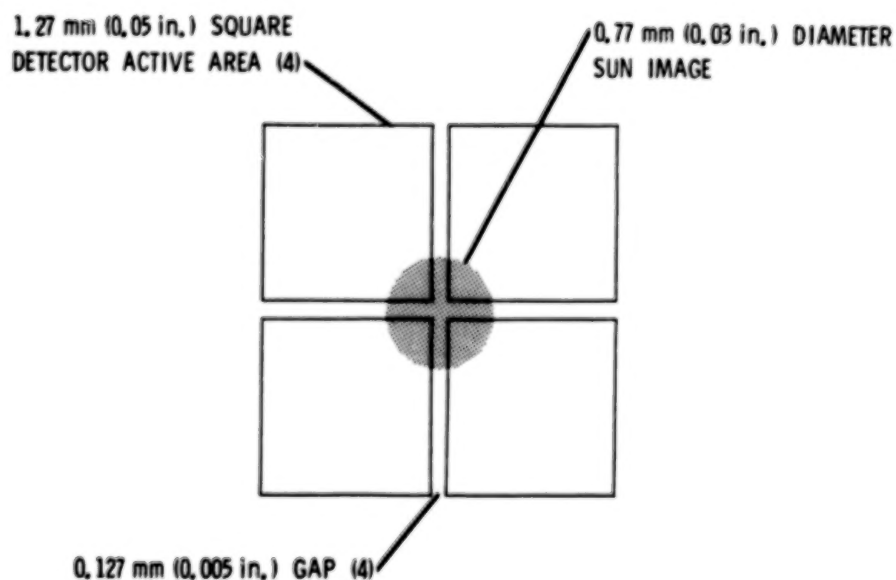


Figure 5. Sun Image on Detector

ORIGINAL PAGE IS
OF POOR QUALITY

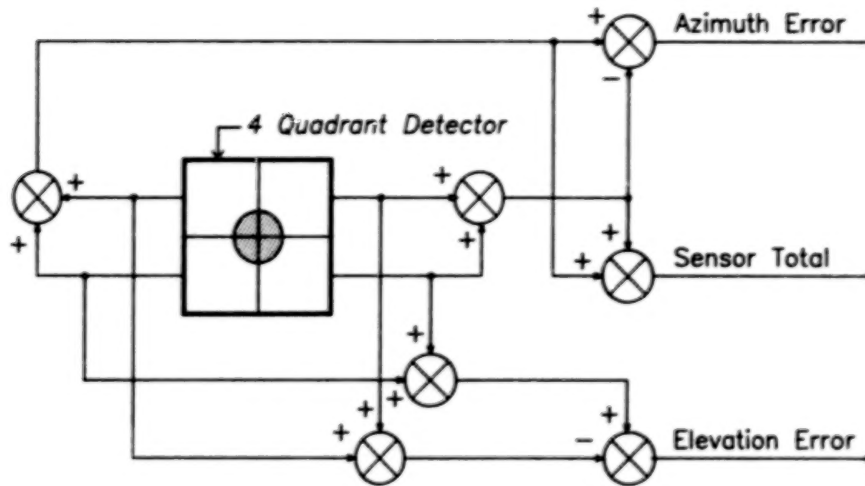


Figure 6. Sensor Error Signal Processing

CONTROL SYSTEM DESIGN

Control of Sun tracker gimbal motions is achieved by the azimuth and elevation servos operating under the control of the system microcomputer. The azimuth and elevation drive mechanisms are similar closed loop servos consisting of the gimbals, motors, encoders, tracking sensor, and the control unit. The control system electronics are composed of modular subassemblies which can be replaced with minimum impact on the system (Figure 7). The control unit contains the microcomputer, servo electronics, interfaces, controls, indicators and power supplies required for system operation. The remaining modular electronic assemblies are mounted on the gimbal assembly.

The servos operate in two basic modes: position and track. In Position Mode the gimbals are controlled relative to the internal coordinate axes of the unit by error signals generated from encoder outputs. In Track Mode the servos respond to error signals from the Sun sensor. Mode selection is achieved by analog switch closures under the control of the microcomputer. All operations of the Sun tracker consist of a sequence of these modes, commanded by the microcomputer.

The design of the control electronics and microprocessor software simplifies normal operation by providing preprogrammed, complex operational and self test features which can be activated by simple commands or switch closures. An extended command set provides access to lower levels of system operation to permit testing, fault isolation, normal operating mode modification, or alternate operating modes.

ORIGINAL PAGE IS
OF POOR QUALITY

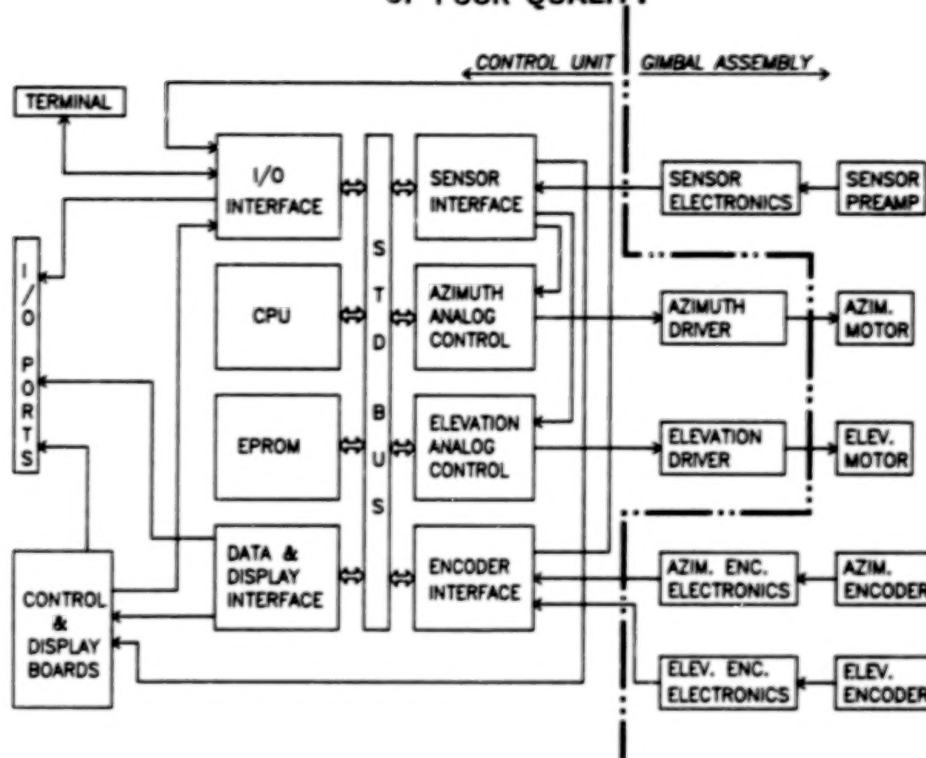


Figure 7. Control System Electronics Modular Interface Design

Servo Design

The elevation and azimuth servos (Figure 8) are similar in design and function so only the azimuth loop will be discussed; however, the differences between the servos will be noted.

Because the azimuth encoder is an incremental type, it requires initialization and a counter to accumulate the angular position information. Initialization of the azimuth encoder/counter occurs during system initialization and is updated (if necessary) every time the gimbal passes through the "zero" degree position. The angular position of the gimbal is provided to the microcomputer at a 1.5-kHz rate by the encoder interface module. In Position Mode the microcomputer uses the accumulated angular position in conjunction with a stored value, representing the desired position, to create position error. Position error is summed with velocity feedback derived by calculating the angular change occurring between the regularly sampled gimbal positions. The resulting error value is converted to an analog voltage by the D/A converter on the analog control module, amplified, and fed through the closed position mode switch. The amplified position error voltage is fed to the analog lead-lag compensation/switched integrator network which was designed to provide the desired closed loop response of the gimbal. The compensated error voltage is converted to a proportional motor current in the current driver module. The motor drives the gimbal to the desired position.

ORIGINAL PAGE IS
OF POOR QUALITY

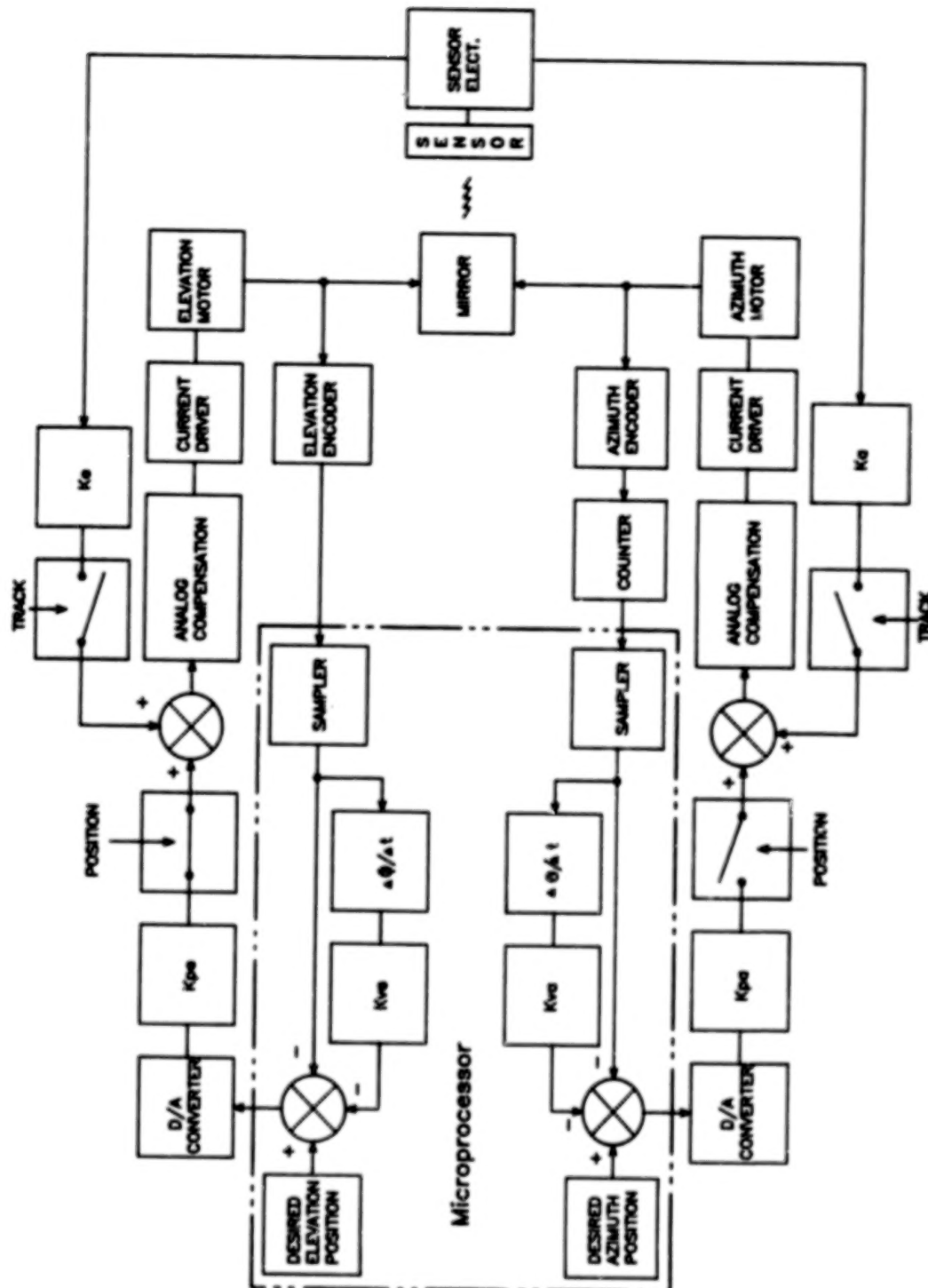


Figure 8. Servo Block Diagram

Because the elevation gimbal has an absolute encoder, the angular position is available from the time power is applied; no counter or initialization is required. The compensation and current drivers have the same form in elevation and azimuth, except for the selection of components and jumpers. The elevation motor is a wide angle brushless dc torquer. This device has a very flat torque response over an angle of approximately 60° , however, its operation is restricted to 120° . This motor is ideal for the elevation gimbal as the angle doubling effect of the elevation mirror makes smooth, ripple free motor operation essential, and only limited angular motion is required.

Although position information is available to the microcomputer in Track Mode, it is not processed to produce error signals, but is used in the fault mode detection logic. The track error signals are produced in the sensor electronics by combining the preamplified four quadrant outputs of the Sun sensor. The elevation and azimuth track error signals are then fed through the closed track mode switch on the appropriate analog control module. These error signals are processed the same as in Position Mode by the analog compensation, current driver, and motor except that they drive the gimbal to maintain the Sun image at the center of the four-quadrant detector.

Sensor Signal Processing

Three signals are produced by the sensor electronics module: elevation error, azimuth error, and sensor total (Figure 6). These signals are fed to the sensor interface module in the control unit where they are amplified by three ganged programmable gain amplifiers. The sensor total signal is converted to a digital value by the A/D converter on the sensor interface module by command of the microcomputer. The system has two uses for the value of the sensor total signal. During Sun acquisition, the programmable gain amplifiers are set to a fixed gain and the sensor total value is compared with a nominal one-half Sun value to determine if the Sun is located within the sensor field of view. The angular response of the four-quadrant sensor is dependent upon the intensity of incident energy. During track, when the automatic gain control (AGC) is enabled, the sensor total value is compared to a design value (representing a nominal one Sun intensity) and the gain of the programmable gain amplifiers is adjusted to maintain the sensor total at the design value. This is required to maintain nominal performance of the servos as the solar energy passes through greater or lesser depth of atmosphere and for ground operation where significant variations of solar energy occur with season, weather, and time of day.

DEVELOPMENT PROBLEMS

Tracking mirror balance

The location of the tracking mirror reflecting surface relative to the elevation gimbal axis had to be changed from the original design to bring the rotating mirror assembly into static balance. The original design, which placed the reflecting surface at the intersection of the elevation gimbal axis and the azimuth gimbal axis, with the mirror body and saddle

located on one side of the axis, required a counterweight to balance the assembly. When the mirror design was completed, the rotary inertia of the mirror/counterweight combination was unacceptably large. The mirror position relative to the elevation gimbal axis was shifted forward to produce a balanced, minimum inertia, rotating assembly which required no counterweight. The final mirror position results in a loss of 17° in elevation LOS capability in the tracking unit, but the remaining range of $+13^\circ$ to -15° is adequate for the LHS instrument.

Azimuth bearing preload

The minimum design value of azimuth bearing preload was one-third the load supported by the bearings: 31 N (7 lb). The installed preload was to be set as closely as possible to this value to minimize starting friction torque. The bearings have a nominal, factory-set preload of 67 N (15 lb) when clamped together, but in the tracker they are separated by a pair of equal length spacers. Spacer fabrication was complicated by the fact that a spacer length mismatch of 0.0011 mm (0.000045 in) could result in a preload variation of 89 N (20 lb). The spacers were fabricated to a length mismatch of 0.0127 mm (0.0005 in). The bearing friction torque corresponding to the design preload was calculated from starting friction versus bearing preload data supplied by the manufacturer. During assembly, the load applied by the inner and outer bearing retaining rings was adjusted to compress the spacers differentially, until the desired starting friction was obtained.

Azimuth axis balance

The azimuth rotating assembly, which includes the complete elevation assembly, was not computer modeled and last minute design changes made the preliminary balance estimations inaccurate. Final balance could only be achieved by removing weight from the elevation housing and using a counterweight mounted to the inner flex cable housing. Space in the housing was critical, so a computer program was employed to calculate the counterweight shape and its location.

Removable neutral density filters

During testing of the tracking unit, conducted after the final alignment of the output beam to the azimuth gimbal axis, an increase in misalignment of almost one arc-minute was sometimes noticed if the filters were changed. The filters may have been refracting the sunlight, and this beam deflection changed the telescope LOS, and thereby, the output beam alignment with the azimuth gimbal axis. The substitution of an iris diaphragm, a nonrefractive element, for the filters would probably have eliminated this misalignment problem. The tracking unit telescope design was not changed, however, because the alignment shift did not affect the operation.

Soft stops to limit gimbal travel

The gimbal soft stops that were incorporated into the design did not pose a problem; however these stops are discussed because they eased the control system development task. Hard stops in the form of an arm contacting a pin were first considered, but soft stops were chosen to limit the structural and bearing loads during the gimbal deceleration. The stops consist of an arm that contacts and compresses a spring loaded plunger. The azimuth stop has a four degree deadband to permit a gimbal travel of $\pm 182^\circ$.

The soft stops proved valuable during the initial control system checkout and testing. Software or hardware errors which caused the gimbal to be driven into the stops caused no damage, and checkout and testing were not restricted by such concerns.

Gimbal Servo Bandwidth

The design objectives included a 100 Hz bandwidth goal for the elevation gimbal control system, which would place it well above the 25 Hz bandwidth goal of the azimuth gimbal. Mechanical design considerations forced the mirror rotary inertia to increase substantially over the original design projections, precluding the possibility of achieving the desired goal. The reduced elevation bandwidth is approximately 50 Hz, which is satisfactory to achieve the tracking requirements. Testing has not shown any significant cross-coupling of motion between the azimuth and elevation gimbals.

TESTING

Because only one solar tracking unit was to be fabricated, all mechanical and electrical subsystems and modules were tested at the lowest possible level. This testing plan served three purposes: established baseline operation of each subsystem, improved the control system modeling, and provided early detection of anomalies. The major subassembly integration and test plan is outlined in Figure 9.

CONCLUSIONS

A solar tracking unit was developed which met or exceeded the LHS research instrument requirements. The unit has demonstrated a tracking stability and repeatability better than ± 1 arc-minute. This unit, designed for use with the LHS instrument in an aircraft environment, could be adapted for use with other similar instruments or applications.

ACKNOWLEDGMENT

The authors wish to acknowledge the work done by Carroll W. Rowland in developing the basic four-quadrant sensor design, and the work done by Ruben G. Remus in converting the system software concepts and philosophies into functional software.

ORIGINAL PAGE 19
OF POOR QUALITY

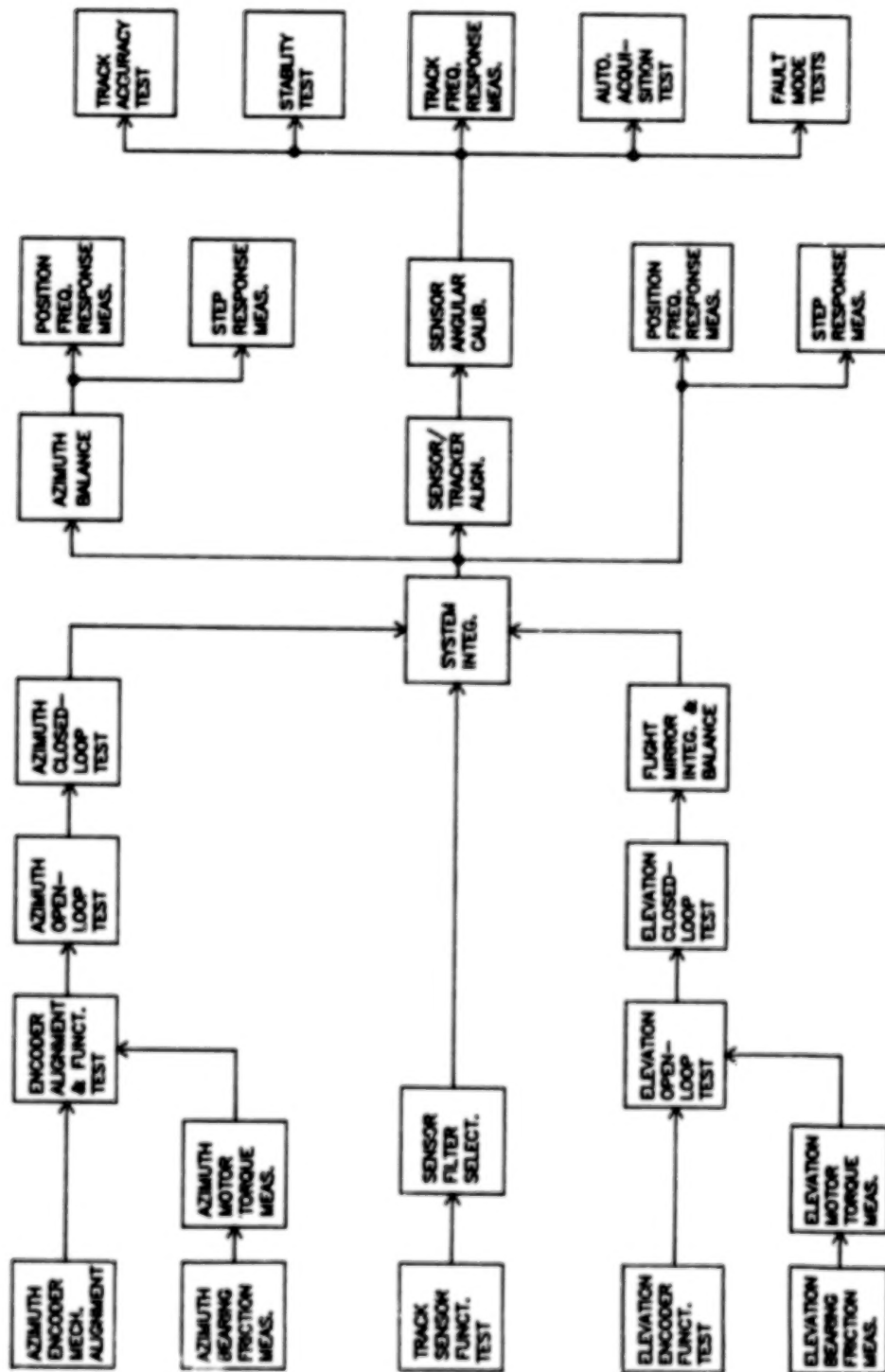


Figure 9. Major Subassembly Integration and Test Plan

N84
25091

UNCLAS

N84 25091

ANTENNA TRACKING MECHANISM FOR GEOSTATIONARY SATELLITES

Colin M. Francis*

ABSTRACT

This paper describes the design and development of a continuous duty cycle antenna tracking mechanism (ATM) for geostationary communications satellites. This paper presents the FACC requirements for an ATM and describes the development mechanism designed and built for the program. The mechanism mechanical configuration and component performance is documented along with its launch and operational constraints. The proposed development tests and the results of computer simulations are discussed. The advantages of this mechanism are its simplicity with inherent reliability, low mass, high stiffness, and ability to accurately point a wide range of antenna sizes.

INTRODUCTION

Communications satellites are tending to use higher frequencies and narrower shaped antenna beams. For these beams to be practical, the antennae have to be oriented accurately at their ground targets. Typically, the allowable pointing error is 10 percent of the beam width, although this depends largely on the gain slope at the edge of the coverage area.

FACC has identified a future requirement for an ATM to compensate for body motions, thermal distortions, and alignment errors of its three-axis communications satellites. The mechanism is to operate continuously using a RF sensor for control loop position feedback.

The critical performance requirements for the mechanism are as follows. The required level of reliability has not been identified, although it should be as high as possible to prevent a mission failure.

Reflector diameters--1.0 to 4.0
Boresight tracking range-- $\pm 2.0^\circ$
Maximum beam-pointing error-- 0.02°
Maximum tracking rate-- $0.1^\circ/\text{sec}$
Control loop--RF sensor
Duty cycle--Continuous
Lifetime--10 years

Mass, height, and power consumption to be a minimum.

*Ford Aerospace and Communications Corporation, Palo Alto, California

PRECEDING PAGE BLANK NOT FILMED.

MECHANISM DESIGN

The development model mechanism is shown in Figure 1. The design consists of three basic units: linear motor, position sensor, and gimbal assembly. The gimbal assembly connects the antenna interface plate to the base plate and permits small angles of rotation about two orthogonal axes. Linear motors and linear position sensors in each axis provide the torque to rotate the reflector and sense its angular position.

There are no wearing surfaces or sources of friction in the design and the gimbal pivots act like torsion springs and do not require lubrication. This ensures high reliability and long operational life. As the design does not contain wet lubricants, and because the moving components enjoy substantial clearances the mechanism can operate in relatively severe thermal environments.

Because of the high axial and radial stiffness of the flexural pivots the gimbal is very stiff axially and in torsion about the unused axis. Each pivot is rated at 2000 N (450 lbs) radial load capability, and even though the full capacity is not intended to be used, it allows simple caging systems to be used for protection during launch.

MECHANISM OPERATION

When a constant voltage is applied to a motor the gimbal deflects a proportional angle and stays there. When the voltage is removed the restoring pivot torque returns the gimbal to its datum position.

The control system is designed to reduce the existing pointing error between the target and the antenna boresight. Dedicated electronics have not been built for the development model mechanism, but real-time computer control is to be used to test the mechanism and its control techniques. For a flight mechanism the control system is provided with RF sensor data and LVDT data (reflector to spacecraft position) in each axis. Only RF data are required to maintain a stable control system, but further development tests may show a system improvement should LVDT data also be used.

Usually, LVDT position data are only required for telemetry purposes and as a back-up control loop for periods when RF data are not available (i.e., preRF acquisition, beacon failure, and excessive body motion).

LAUNCH CONFIGURATION

The ATM may be used for body mounted or deployable reflectors. Figure 2 shows both launch configurations and their caging systems.

ORIGINAL PAGE IS
OF POOR QUALITY

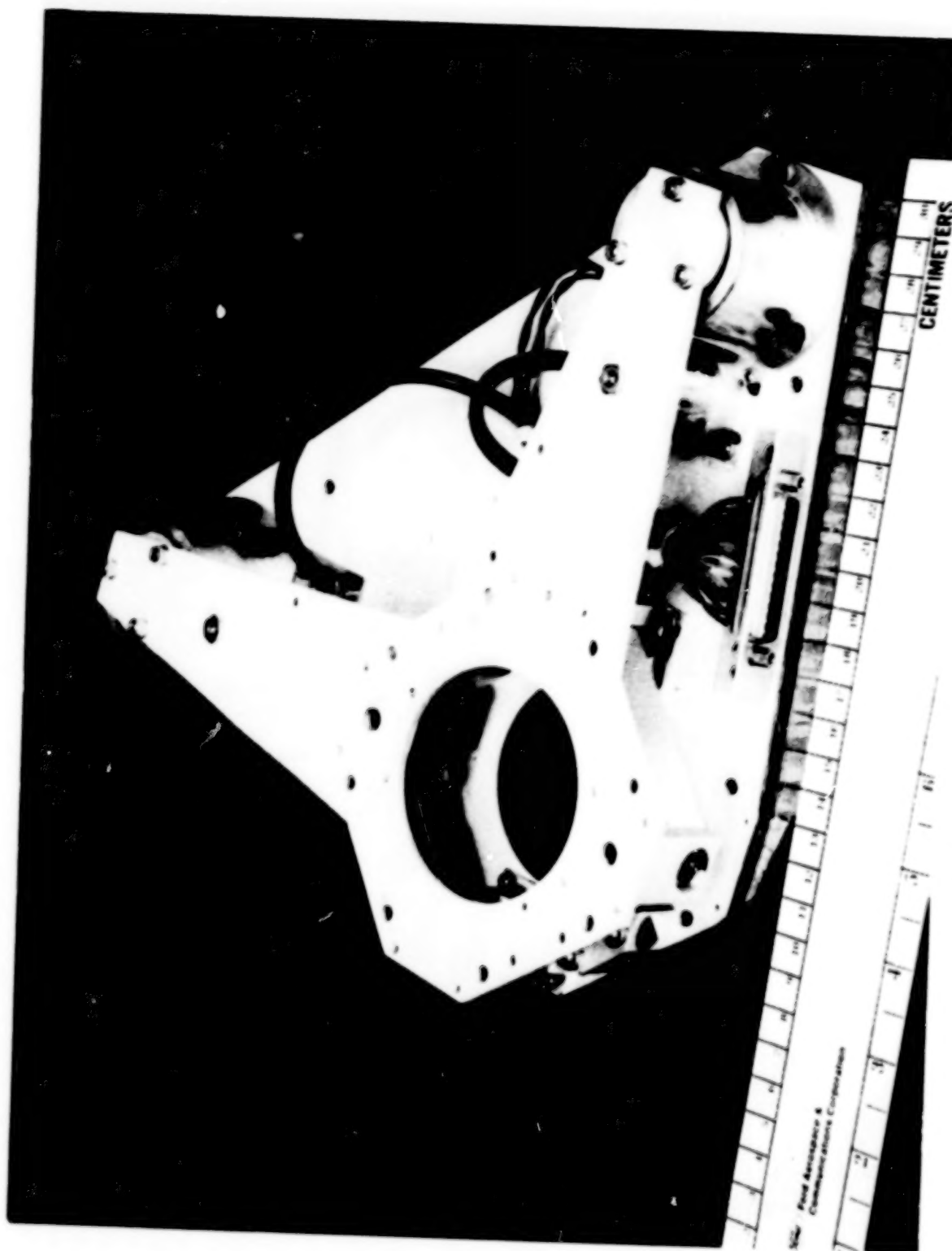


Figure 1. Development Model Mechanism

ORIGINAL PAGE 19
OF POOR QUALITY

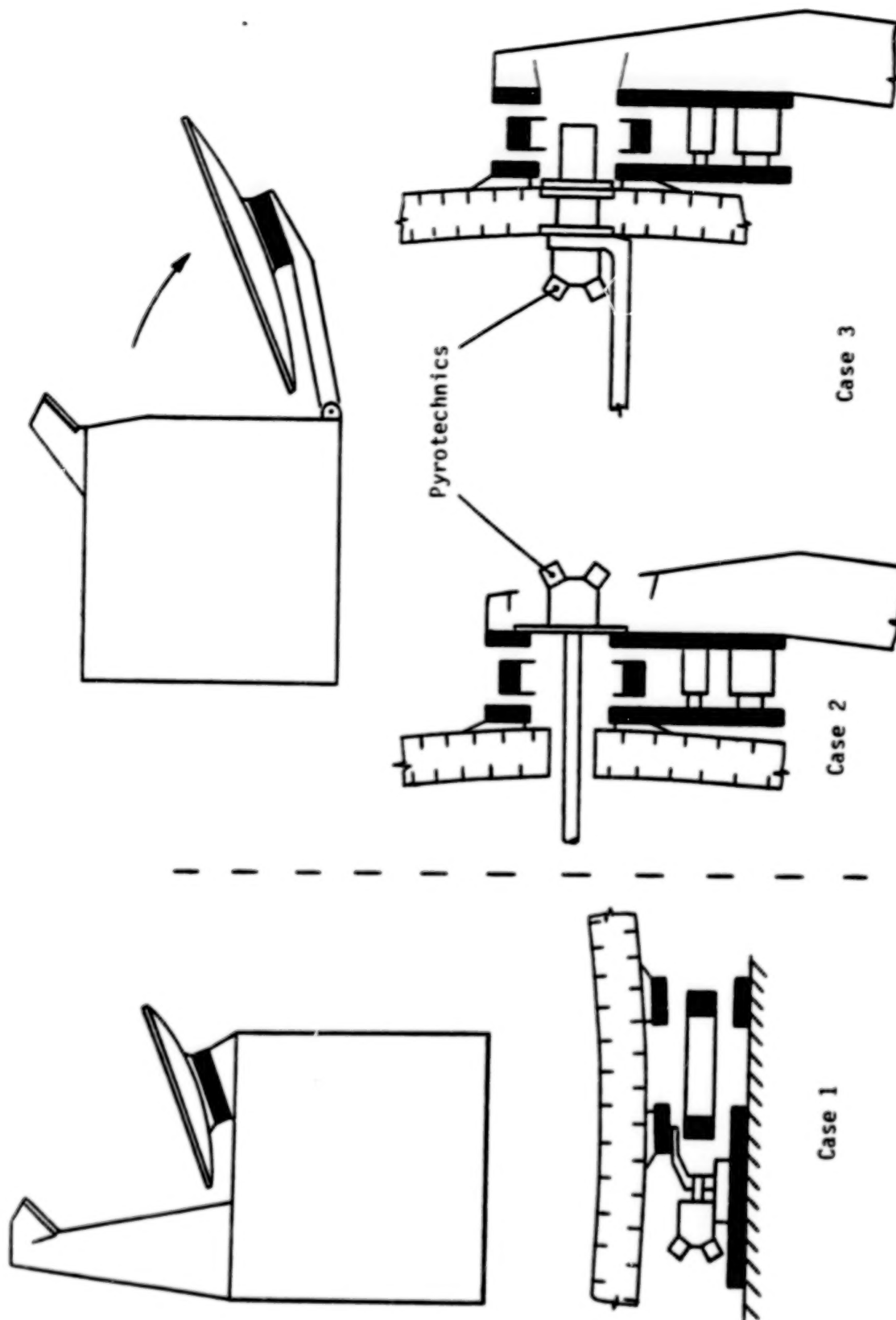


Figure 2. Launch Caging Configuration

Body mounted reflectors are generally of small diameter (1.0 to 2.0 m), and so a pyrotechnic caging device mounted between the antenna interface and the base plate (Case 1) would be sufficient to restrain the reflector. Larger reflectors may require a restraint at a greater radius, with the attachment on the reflector.

Most large reflectors (>2.0 m) will be deployed on a boom from the side of the spacecraft body. Several hold-down configurations are possible with this. The mechanism can be caged to the spacecraft and the reflector snubbed against the body sidewall (Case 2). Or the reflector can be caged and the mechanism either caged or free to rotate (Case 3). The central hole (6.25 cm diameter) can be used for access to the mechanism base plate through the reflector.

It is desirable for both launch and operation that the reflector is mounted centrally on the mechanism with its c.g. directly over the axes of rotation.

GIMBAL ASSEMBLY

The gimbal assembly is constructed around four double-ended flexural pivots. The center section of each pivot is clamped into the gimbal frame and the pivot ends are clamped into supports. Two supports connect the gimbal to the base plate to allow one axis of motion, and the other supports connect it to the antenna interface to create the orthogonal axis.

The pivots are designed to flex through an angle of $\pm 15^\circ$, although interference between the motor components occurs at approximately $\pm 2.5^\circ$. The designed ATM operating range is $\pm 1.5^\circ$.

LINEAR MOTOR CONSTRUCTION

Each axis is driven by a dc linear motor, which is sectioned in Figure 3. Over the mechanism operating range the motor components are noncontacting. Within each motor housing there are redundant windings, effectively giving two motors in each axis. It is intended that only one winding be energized at any instant. The motor core contains two rings of radially oriented permanent magnets, with each ring positioned to be axially coincident with its respective stator winding. Although there are two magnet rings there is only one magnetic circuit, which uses the inner stationary iron piece and the outer stator housing as the return paths.

position. This allows a maximum force of 9.0 N for a 15 Watt input at 20 Vdc.

As the gimbal and motor core are deflected from their datum position the force produced for a given power input decreases. Over the motor operating

ORIGINAL PAGE IS
OF POOR QUALITY

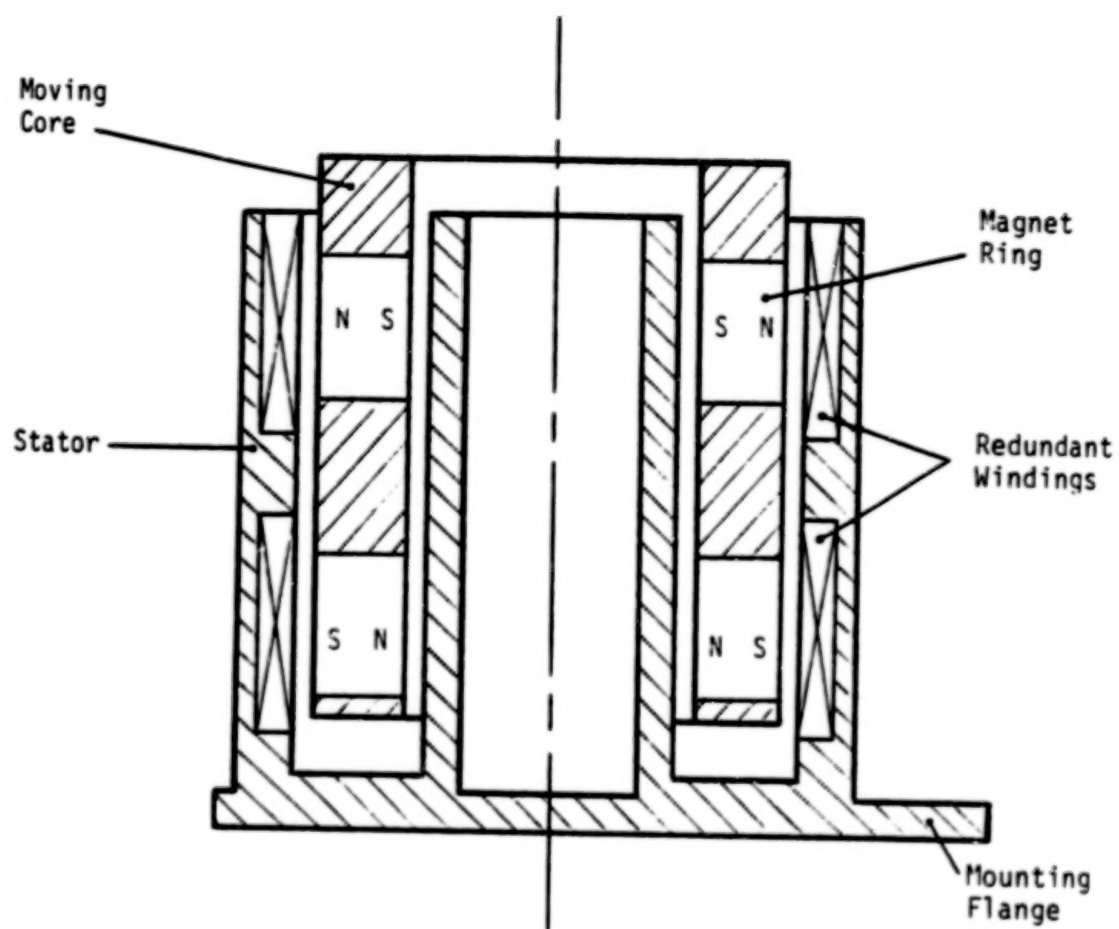


Figure 3. DC Linear Motor

range of ± 3.8 mm the nonlinearity should not be significant to the control system. The slightly angular motion of the core within the stator housing does not appear to cause significant performance degradation.

POSITION SENSOR

The attitude of the antenna relative to the datum position (or spacecraft) is measured by a linear variable differential transformer (LVDT) in each axis. Each LVDT is powered by a signal processing unit, which drives the primary winding with a 2.5 KHz sine wave. An induced current is created in the secondary coils by the high permeability core. From the difference in magnitude of the secondary currents a linear position output (± 10 Vdc) is derived. The stator and core are noncontacting and do not cause friction.

CALIBRATION OF MECHANISM

The computer program which controls the motion of the mechanism requires the input of certain performance parameters. To determine these values, the mechanism is to be calibrated under steady-state conditions.

The power off datum position (with a 1-g counterbalance) is measured optically for each axis. By applying known torques in each axis and measuring the deflection, the gimbal spring constant will be determined. It is predicted to be 0.10 Nm/° , with a linearity better than 5 percent over the operating range. Measuring the deflection against applied motor current will provide the effective motor constant, which will be slightly less than $2.2 \text{ N}/\sqrt{\text{Watt}}$, with a linearity better than 5 percent over the operating range.

Because of end-effect losses and relative rotation of the motor components, the mechanism deflection is not entirely linear with applied current. However, it should be quite sufficient for the control system to achieve the required pointing accuracy. If desired, the effects of nonlinearities can be eliminated by programming the control law with a variable motor constant dependent upon the LVDT position data.

TEST MODE AND CONTROL SYSTEM

To perform a fully representative series of performance tests the mechanism would have to be mounted on a three-axis table (preferably six-axis) and an RF (or laser) beam generated at infinity to simulate the ground beacon. However, at this phase of development the much simpler test setup detailed below is adequate. A version of the "back-up" control mode (LVDT data only) is used to test mechanism performance.

The satellite interface is held stationary and the inertia is commanded to follow a moving target. The target is an imaginary point in space, the

locus of which is generated by the computer. The angular range and rates are generated such that the mechanism experiences loads equivalent to predicted mission conditions. In reality, the target locus is represented by sine curves and step inputs of varying periods and magnitudes.

To determine the existing pointing error, the LVDT output is compared with the target location. The target track and pointing error in each axis and the time are printed every second to provide a hard-copy record of a test run.

The test computer is loaded with a program to control the mechanism (a flow diagram of the control loop is shown in Figure 4). A line in the program samples LVDT position data every 100 mS, converting it from analog dc voltage to a numerical value. The target position (generated by a line in the program) is compared with the LVDT data and an error value is calculated for each axis.

Using the calibrated mechanism performance parameters, the known inertia and the error values, the control program determines the motor voltages required to correct the existing errors during the next sample period. The computer takes a finite time to perform its task and so a time lag develops in the control loop. If the LVDT's are sampled at $T=0$ and the control algorithm takes 100 mS to process, then a new motor voltage will be output at $T=100$ mS in order to eliminate the initial error by $T=200$ mS. With a 0.2 second time lag it is desirable to predict the motion of the target to improve pointing accuracy. This prediction is performed by the algorithm, as the program stores previous position data for comparison.

It is expected that a realistic spacecraft control system would sample and respond every 60 mS, rather than the 100 mS capable by the current configuration.

Once the new motor voltages have been determined the computer outputs them as ± 20 Vdc analog signals. These are amplified to provide adequate current and then passed to their respective motors. The voltage applied to each motor remains constant during the next 100 mS.

The result is that the mechanism drives the inertia back and forth across its range as it tries to follow the demanded locus as closely as possible.

COMPUTER SIMULATIONS

A computer simulation of the mechanism, the spacecraft, and the reflector interaction has been performed. In this, the mechanism base is given angular and linear disturbances representing thruster firings and this causes the feed/reflector combination to misalign the antenna beam. The error angles

ORIGINAL PAGE 19
OF POOR QUALITY

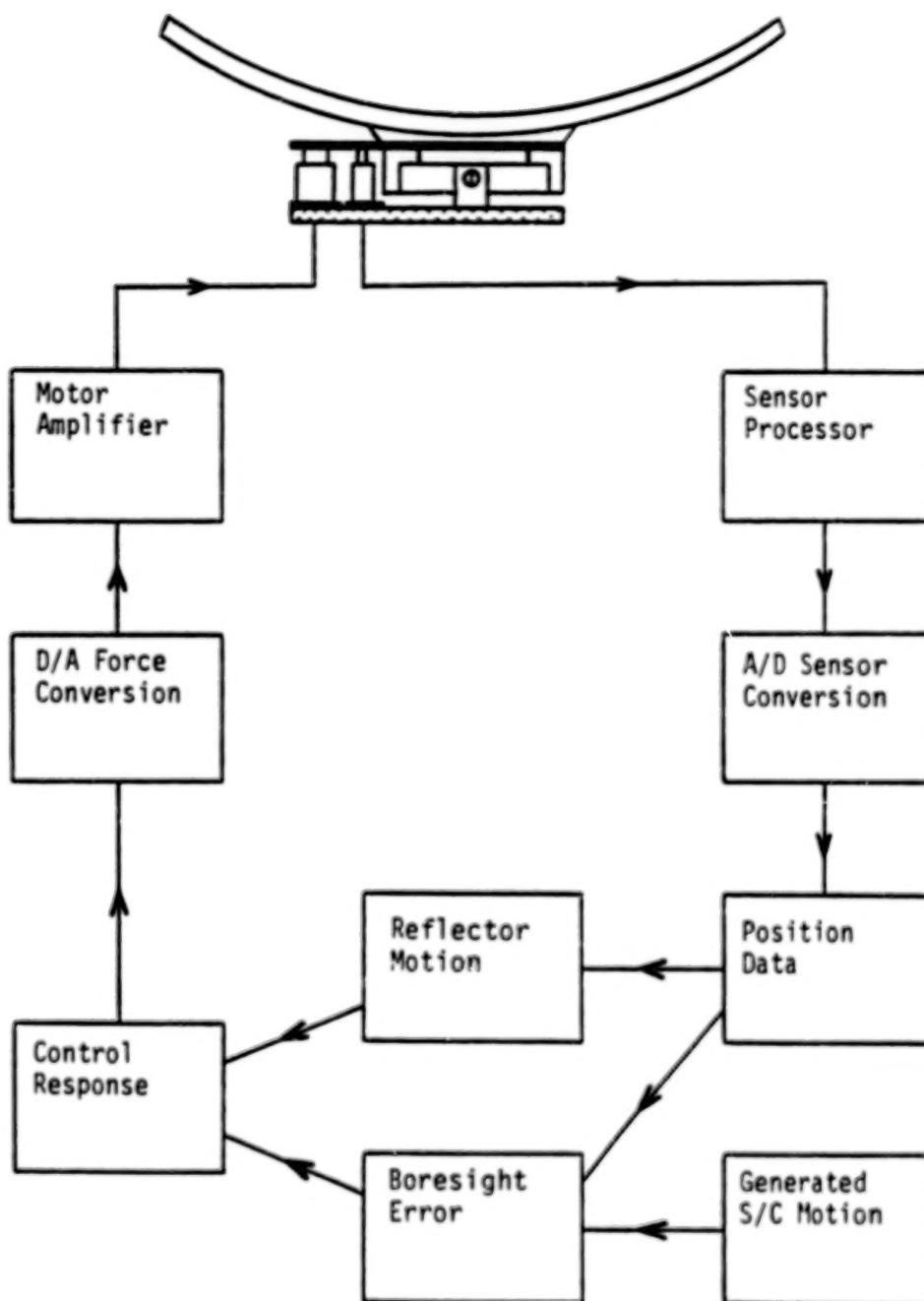


Figure 4. Dynamic Test Control Loop

(representing the RF sensor output) are sampled and a corrective motor force determined. The new force is applied after a suitable time lag and the system dynamics are continuously monitored. Figure 5 shows a typical system response. In this simulation an Intelsat V size spacecraft with a deployed 2-m diameter reflector experiences a 20 N thruster firing. The maximum beam error is 0.02° and the motors draw 0.1 Watts each. After 1.5 seconds the system settles down to an error of 0.001° and total power consumption much less than 1 Watt.

Simulations have been performed for reflectors of 1- to 4-m diameter with inertias of 0.15 to 20 Kgm^2 . By varying the control loop gain for specific reflector sizes this large range of antennae can be successfully tracked. Larger reflectors require greater motor forces, while very small inertias allow high natural frequencies about the pivots, and the lag time causes instability.

FURTHER DEVELOPMENT AND TESTING

The tests performed to date have been limited in their scope. The tests that have been performed have been used to confirm the test setup as much as the mechanism. The initial calibration measurements are very encouraging; however, and indicate that the mechanism performance will be as predicted.

Further tests are due to be performed, which will allow the full capability of the mechanism to be realized. These tests, which will include the extremes of inertia and rates of motion, will explore the interactions between the axes and the effects of motor failures and motor/sensor interference.

CONCLUSIONS

Sizing of the mechanism components appears to be excellent. The power, force, stiffness, and sensitivity relationships between the various components are well matched to produce an optimized tracking mechanism. The mechanism promises excellent performance in a remarkably compact and light-weight package.

The use of the computer allows great flexibility in modifying control techniques, although its operating speed needs to be higher.

Recommended design changes for a flight mechanism are to:

- Incorporate redundant LVDT sensor windings; the failure modes of these need to be investigated
- Increase the radial clearances in the motors to allow greater range and easier assembly

ORIGINAL PAGE 18
OF POOR QUALITY

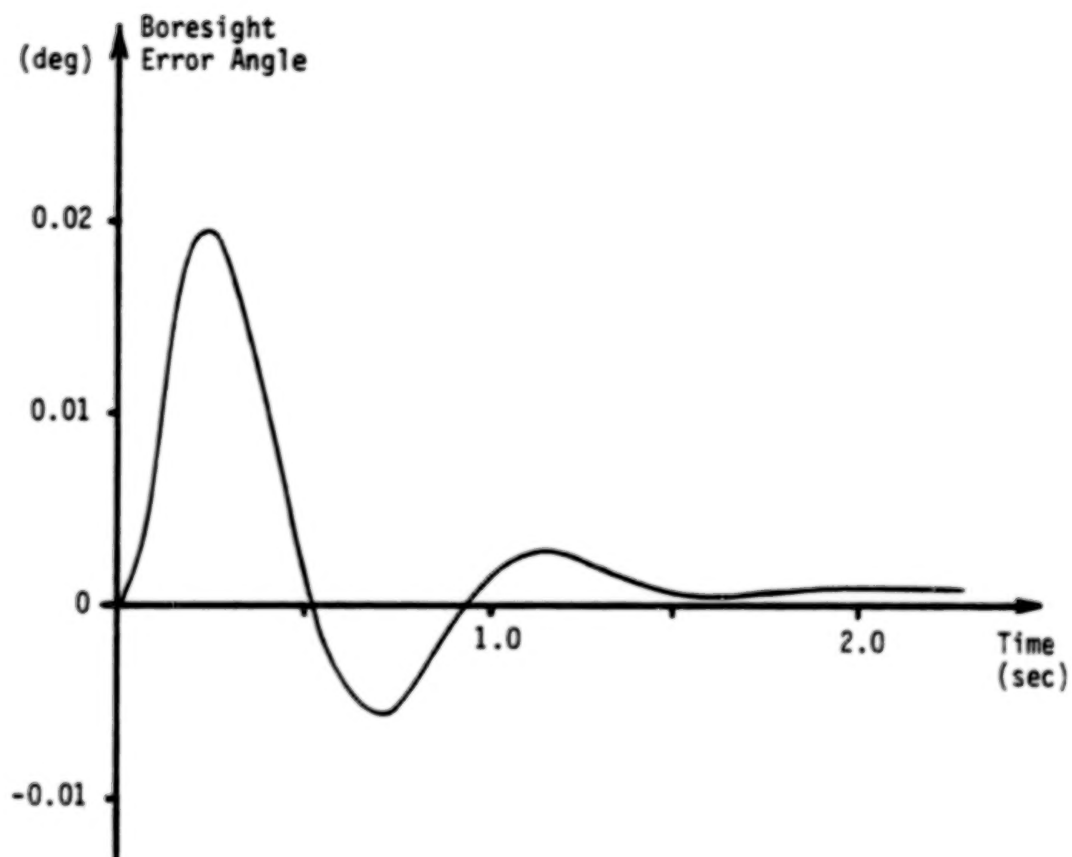


Figure 5. Predicted Boresight Error Response

- Increase structural stiffness, by using stiffer arms and possibly larger diameter pivots (maintaining the current torsional stiffness)
- Reduce mechanism mass by using higher performance materials in the motors and by optimizing the structural components

ACKNOWLEDEMENTS

The author wishes to thank Ford Aerospace and Communications Corporation for its permission to publish this paper.

N84
25092

UNCLAS

SPACELAB 4 - PRIMATE EXPERIMENT SUPPORT HARDWARE

✓ Paul R. Fusco and Richard J. Peyran

ABSTRACT

A squirrel monkey feeder and automatic urine collection system have been designed to fly on the Spacelab 4 Shuttle Mission presently scheduled for January 1986. Prototypes of the feeder and urine collection systems have been fabricated and extensively tested on squirrel monkeys at the National Aeronautics and Space Administration's (NASA) Ames Research Center (ARC). The feeder design minimizes impact on the monkey's limited space in the cage and features improved reliability and biocompatibility over previous systems. The urine collection system is the first flight qualified, automatic urine collection device for squirrel monkeys. Flight systems are currently being fabricated.

INTRODUCTION

The changes in fluid and electrolyte balance that occur during spaceflight are among the most prominent physiological changes induced by weightlessness. Evidence from premanned spaceflights suggest that weightlessness produces an abnormal distribution of body fluids leading to higher than normal excretion of sodium and potassium electrolytes. A new study using squirrel monkeys to examine the mechanisms responsible for the fluid shifts and changes in electrolyte balance is scheduled for the Spacelab 4 Shuttle flight, and will be conducted jointly by NASA/ARC, Harvard Medical School, and the University of California at Riverside. To satisfy the mission objectives, it is necessary to furnish a squirrel monkey cage system that not only provides for the animal's health and well-being, but also provides researchers with an accurate determination of urine output volume and content.

ARC has developed a spaceflight squirrel monkey cage system that will meet all of the mission and experimental objectives (Figure 1). This paper will focus on two of the most challenging and critical subsystems of the cage. Both of these systems have to meet the rigid materials and safety requirements imposed upon flight hardware, and the biocompatibility requirements necessary to maintain the health of the monkey in both 0-g and 1-g environments.

URINE COLLECTION SYSTEM REQUIREMENTS

Discussions between the principal investigators, the animal care consultants, and the engineering design team resulted in the following list of design requirements:

- The system must be biocompatible with male squirrel monkeys and capable of functioning properly for up to 10 days

ORIGINAL PAGE IS
OF POOR QUALITY

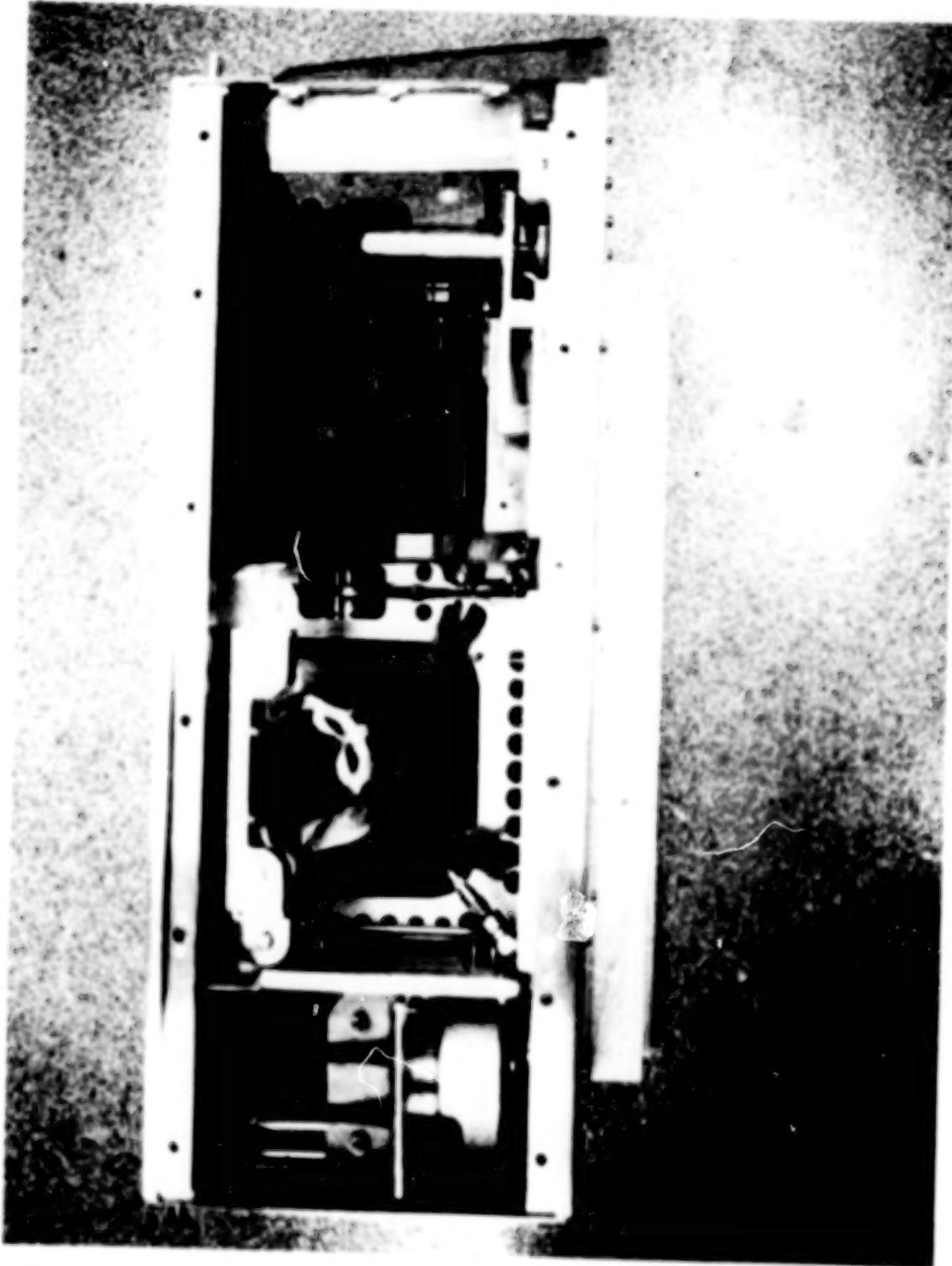


Figure 1. SL-4 Primate Cage Assembly

- The collection system must automatically collect total urine output every 4 hours
- Sample sizes may range from 0-30cc and must be totally collected with not more than 0.2cc of uncollected fluid
- The system must require minimal crew maintenance (approximately 5 minutes per monkey, once every 24 hours)
- The collection system must be compact and fit into an existing space in the primate cage
- The system must be capable of unattended operation for up to 36 hours to meet prelaunch manpower requirements
- The collection system must be capable of functioning in 0-g and 1-g environments
- The system must be lightweight, but capable of surviving extensive vibration testing at high g-levels
- All materials and lubricants must be flight approved

URINE COLLECTION SYSTEM DESIGN

APPROACH

The design of the urine collection system was divided into two integrated areas: design of the monkey-to-collector interface, and design of an automatic collector mechanism. The design of the monkey hardware interface required an evaluation of several design approaches. The most common method used to collect urine, and the one used on previous spaceflights, has been to use indwelling catheters. This approach, however, has some serious disadvantages including a high incidence of urinary infections when the catheter is left unattended for many days. Other problems include discomfort to the monkey, and difficulty with fluid movement in 0-g. As a result, it was decided that every effort should be made to develop an external catheter system that would have little, or no, influence on the monkey's natural urinary functions.

Several different collector mechanism designs were initially developed. Some used stationary collection tubes organized in a rectangular grid with a moveable nozzle that could index to the proper tube at 4-hour intervals. Problems with this approach included the need for multiple motors and a complicated control system to ensure proper indexing of the nozzle. In addition, storage of collection tubes in a flat rectangular grid did not provide efficient usage of the available space. It was determined that the space available could be used more efficiently by a system that employed a stationary nozzle and a round carousel assembly that could rotate nine storage tubes past the nozzle.

SYSTEM OPERATION

The operation of the urine collection system is shown in Figure 2. The monkey urinates at will into an external transfer tube which acts as short-term storage and a connection between the monkey and collection valve. At 4-hour intervals the collection mechanism is activated, which rotates the proper collection container into position and then translates forward. The forward motion moves the collection container towards the collection valve, forcing a needle at the end of the collection valve through the rubber septum in the end of the collection container. The collection containers are evacuated so that they will draw fluid out of the soft, collapsible transfer tube. A small (1.6 mm I.D.) tube connects to the urine valve and runs inside the larger transfer tube to prevent the vacuum from collapsing the transfer tube at the urine valve and sealing off the remainder of the tube. After a 20 second dwell time, the collection mechanism is again activated and the carousel assembly is retracted from the collection valve. The collection valve is spring loaded to close off and prevent any fluid from escaping when the carousel is not in contact with it.

Every 24 hours the flight crew can remove the carousel assembly from the collection mechanism and install fresh, empty collection containers into the carousel. The carousel is then reloaded into the collection mechanism for the next cycle.

TRANSFER TUBE

The design of the transfer tube is shown in Figure 3. The tube fits over the monkey's penis and is supported in place by an additional flange garment which straps to the monkey. The tube is fabricated from silicone rubber and has a wall thickness of approximately 0.25-0.38 mm. The tube was originally fabricated in a mold that required a two-part compound, because air and moisture were sealed out of the mold. Tear strength of the tube, however, was poor. A search for a higher strength, flight acceptable material resulted in the selection of Dow Corning compound #3144 RTV. The difficulty with the 3144 compound, however, was that it required moisture to cure and the mold was virtually sealed. A new fabrication process was developed using a mandrel the exact size and shape of the transfer tube. The 3144 compound was thinned with moisture-free naphtha to a viscosity that could be sprayed. The solution was then sprayed over a slowly rotating mandrel until cured. The finished part was then rolled off the mandrel.

COLLECTION VALVE

The urine collection valve, which provides the interface between the transfer tube and the collection containers, also serves as a penetration through a Lexan partition which seals the cage's instrumentation area from the monkey's area. The valve body forms a 90° angle (Figure 4) to minimize intrusion into the monkey's area of the cage. The valve plunger is spring loaded to provide fluid seal when not engaged with

URINE MANAGEMENT SYSTEM

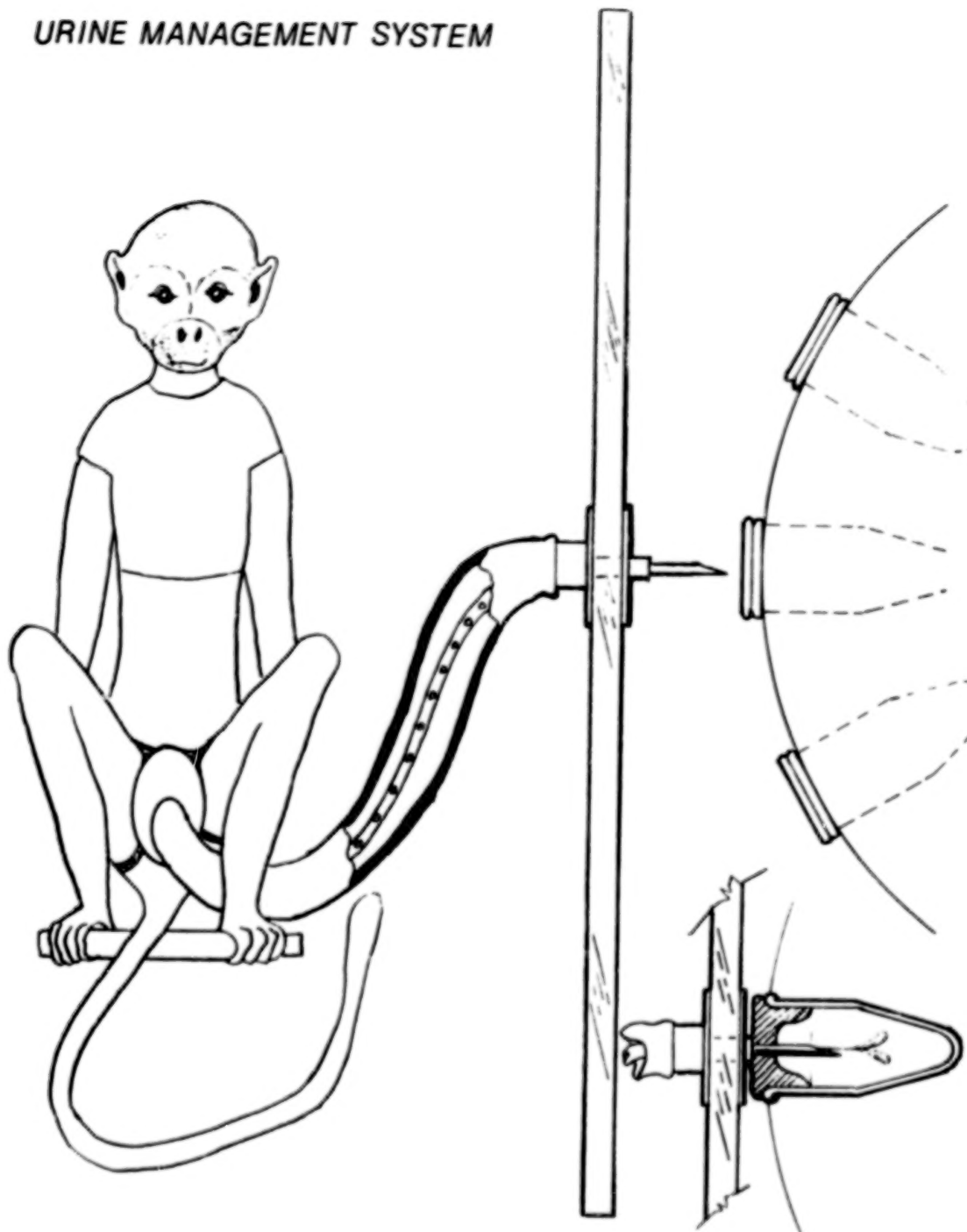


Figure 2. System Operation Schematic

ORIGINAL PAGE 19
OF POOR QUALITY

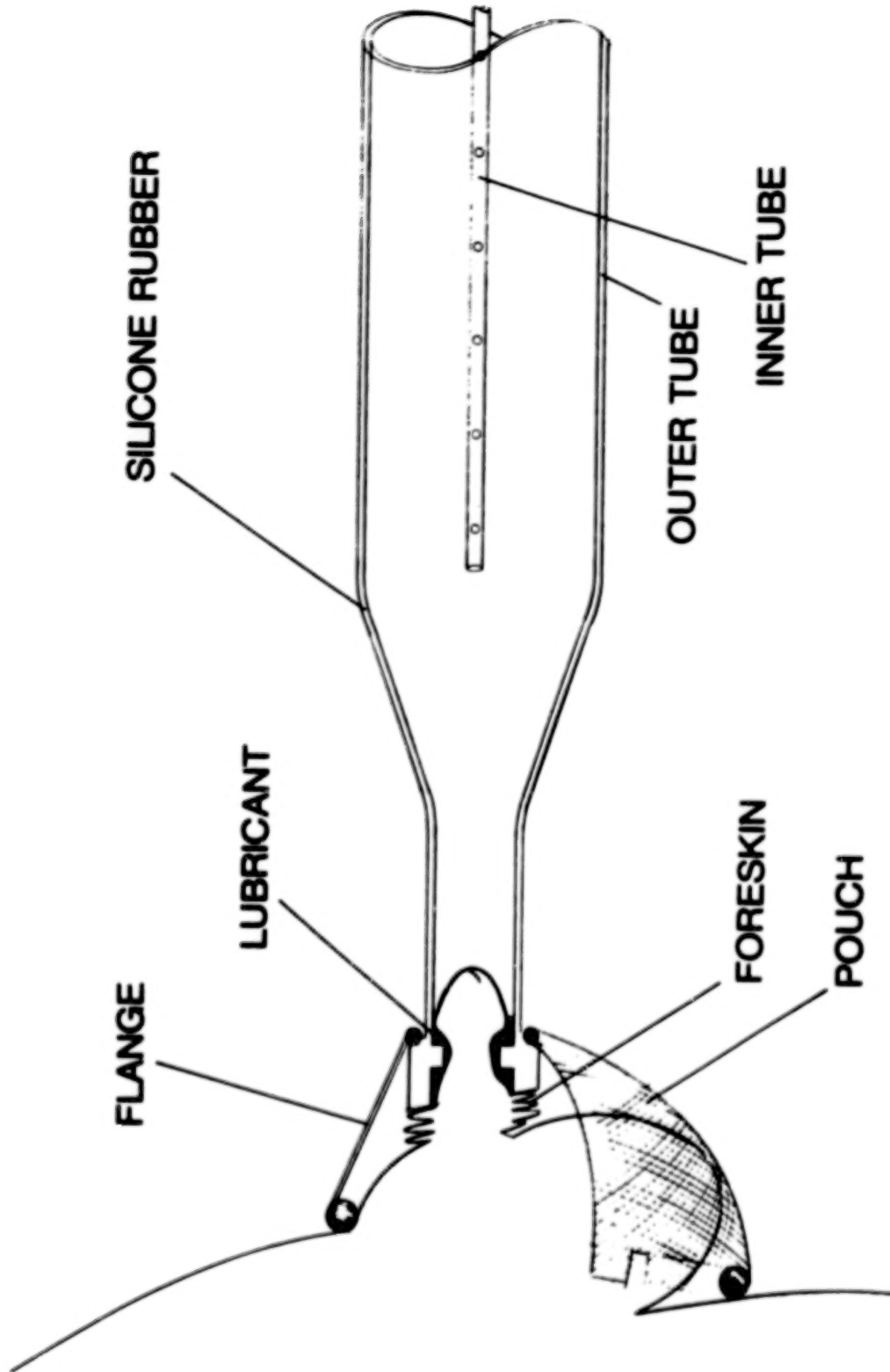


Figure 3. Tube Design

ORIGINAL PAGE 19
OF POOR QUALITY

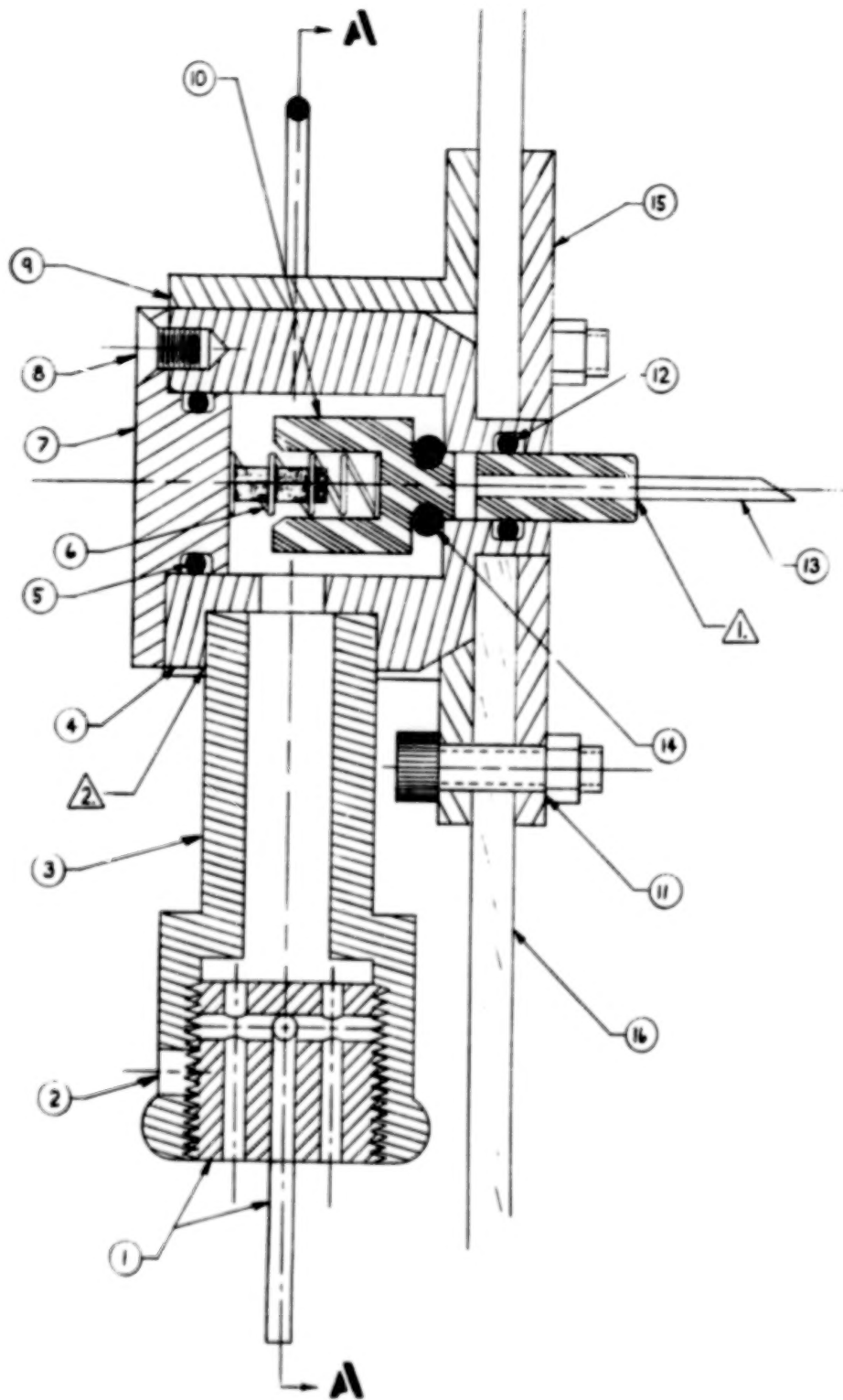


Figure 4. Urine Valve Assembly

a collection tube. A 20-gage needle, brazed into the end of the plunger enables the valve to penetrate the rubber septum on the collection containers.

COLLECTION MECHANISM

The collection mechanism is made up of three subassemblies: the collection containers, carousel assembly, and the carriage assembly. A collection container is shown in Figure 5. The container is made from Pyrex glass with a Lexan collar and a rubber stopper. The total volume of each container is 35cc. Each container is evacuated to approximately 29.0 inches of mercury, which yields a maximum fluid capacity of 33.5-cc. The collar is designed with a circumferential groove as seen in Figure 5, which enables it to be locked into the carousel assembly by a cam activated lock wire.

The carousel assembly shown in Figure 6 is capable of holding nine collection containers. Each container can be individually locked in, or released by rotating a slotted cam actuator. The assembly is made from Lexan with an aluminum geneva gear mounted on one side. An aluminum axle through the center of the carousel sits in three saddle supports on the carriage assembly, and is held secure by a pit pin through the center saddle support.

The carriage assembly is shown in Figure 7 and Figure 8. The purpose of the assembly is to rotate the carousel to the proper location for alignment of the collection valve with a stopper on the desired collection container. The carriage must then move the carousel linearly forward until the needle on the collection valve punctures the rubber stopper on the collection container. After a short dwell time, during which fluid is drawn through the collection valve into the collection container, the carriage moves the carousel back away from the valve. After clearing the tip of the needle the carousel is rotated halfway to the next location.

Initial designs of the carriage assembly called for two motors to accomplish the dual motions of the carousel. One motor would rotate the carousel to the proper location, and a second motor would rotate a lead screw driving the carriage in linear motion. High cost for space-flight electric motors and a complicated control system made this design undesirable. The final design, which couples a scotch yoke mechanism with a nine slot geneva mechanism, was developed which requires only one motor and a simple control system. A schematic of the system is shown in Figure 9a. A 3 rpm ac synchronous motor is directly coupled to the primary gear, which has a cam bearing located 15 mm from its rotational axis. The cam bearing rides in a slot on a stationary part of the carriage. The two parts perform as a scotch yoke mechanism with a total linear travel of 30 mm. Engaged with the primary gear is the geneva drive gear. This gear is the same size as the primary gear so that a 1:1 ratio is maintained. The geneva drive gear was designed to mesh with the nine slot geneva gear mounted on the carousel assembly. As the geneva drive gear makes one full revolution, the carousel

ORIGINAL PAGE 19
OF POOR QUALITY



Figure 5. Collection Container and Carousel

ORIGINAL PAGE IS
OF POOR QUALITY



Figure 6. Carousel Assembly

ORIGINAL PAGE IS
OF POOR QUALITY

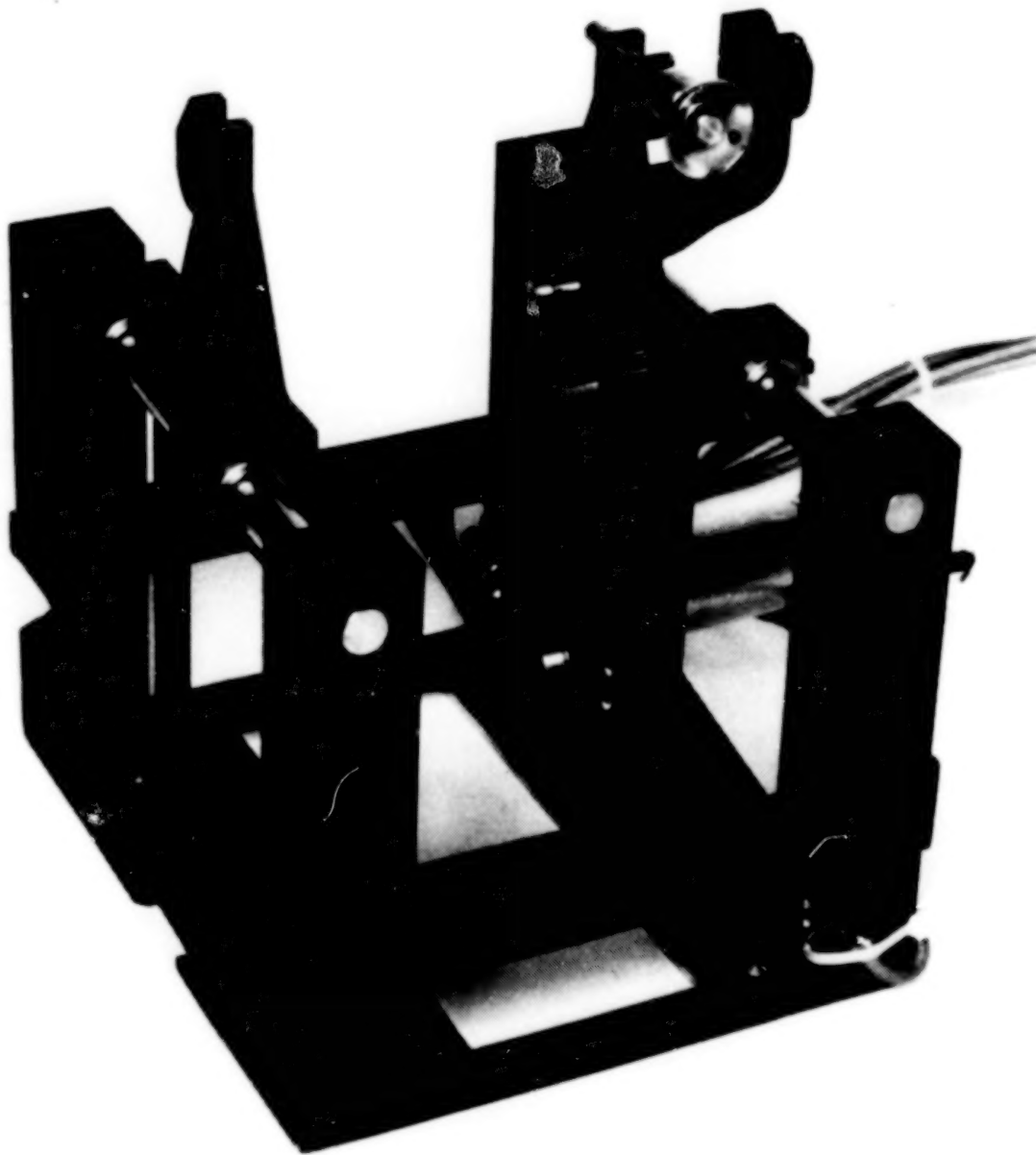


Figure 7. Carriage Assembly

ORIGINAL PAGE 13
OF POOR QUALITY

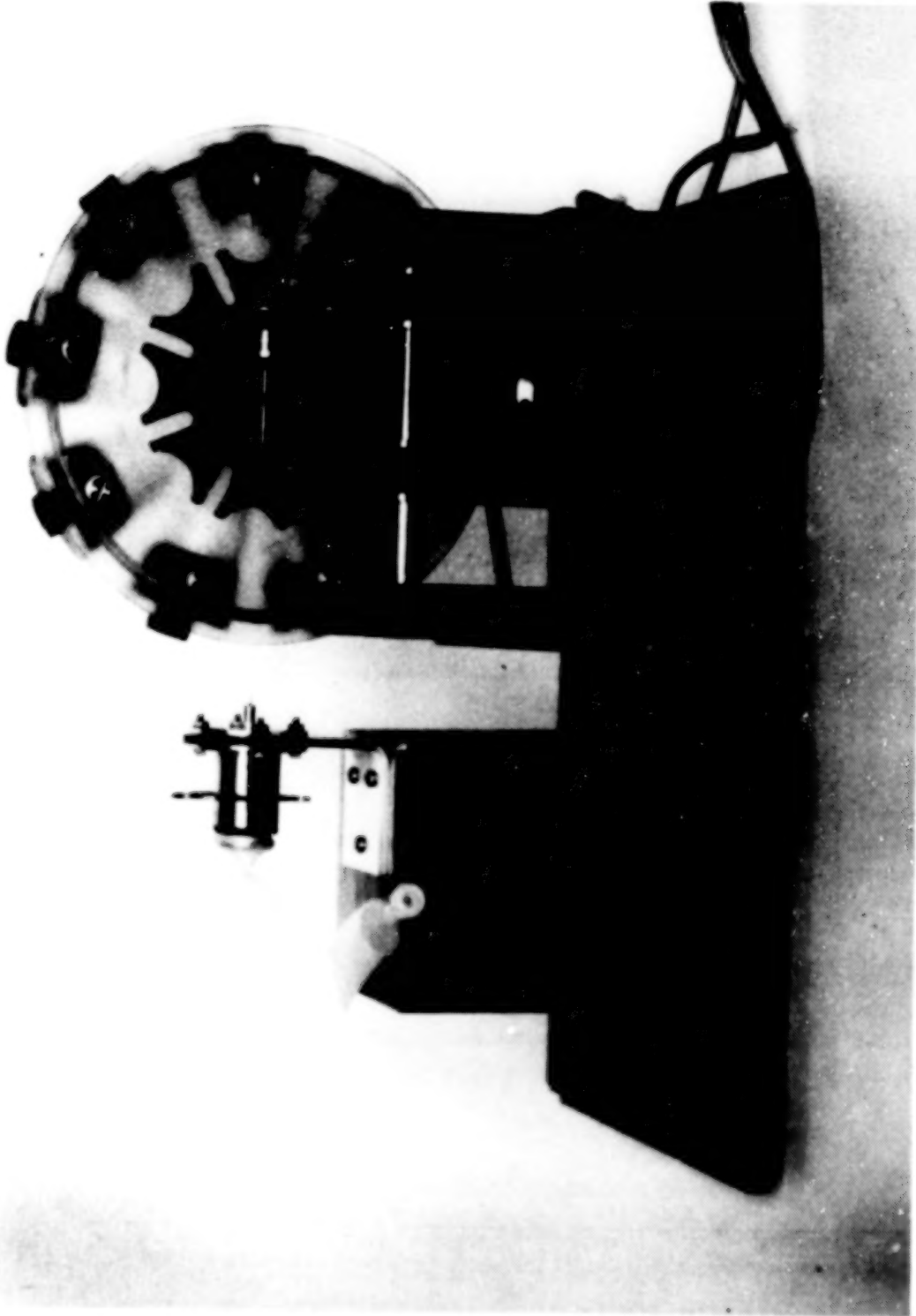


Figure 8. Carriage and Valve Assembly

ORIGINAL PAGE IS
OF POOR QUALITY

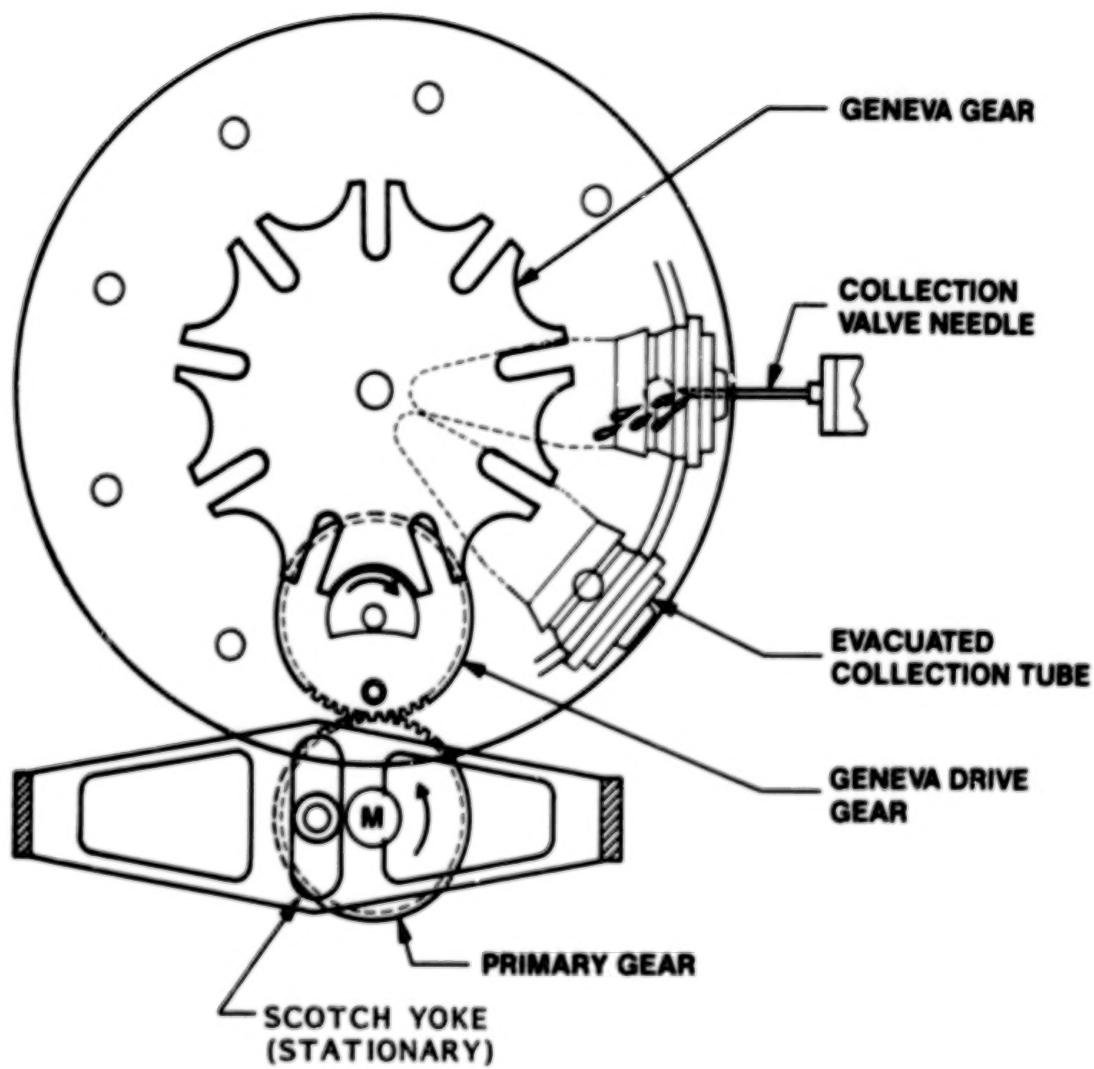


Figure 9a. Carousel Translation, No Rotation

is rotated exactly 40° . Actual rotation of the carousel occurred during only 136° of primary gear rotation. The remaining 224° of rotation is used by the scotch yoke mechanism to provide linear motion of the carousel without rotation.

By correctly timing the two gears it is possible to obtain rotation of the carousel followed by approximately 24 mm of nonrotational, linear travel into the collection valve needle. Figures 2a, 9b, and 9c show the three stages of operation. In Figure 9a, the carousel has moved its full travel into the collection valve. Figure 9b shows the carousel moved back away from the needle and just ready to start rotation. Figure 9c shows the carousel just as rotation is completed and linear movement toward the needle is in progress.

FEEDER DESIGN REQUIREMENTS

In addition to the urine collection system previously described, an effort was directed to create a squirrel monkey-feeding system that met a number of experiment objectives which included the following:

- Cage Integration - The feeder must integrate with the existing Spacelab primate cage.
- Size - Shape and size must minimize impact on the monkey's extremely limited space in the primate cage.
- Capacity - Replaceable food cartridges must hold a minimum of 600 190 mg, spherically shaped, food pellets--the minimum capacity acceptable. Crew time constraints are such that 72 hours could elapse before a feeder cartridge change could be made. The monkey usually consumes approximately 200 pellets per day.
- Biocompatibility - This requirement covers the parts of the design that interface with the monkey and affect his well being. Some of these include quiet feeder operation, a method of holding the food pellet in 0-g prior to the monkey retrieving it when he desires, and a properly designed tap switch for the monkey to advance the feeder on demand.
- Mechanical Design - The design must meet strict design requirements that cover materials requirements, structural design limits, and system reliability.
- Improvements - The feeder needed to be an improvement over previously designed feeders. One problem of some pellet type feeders is the tendency to crumble the pellets so only partial pellets are delivered to the monkey. Also food fines (dust) resulting from broken pellets could jam the feeder and halt its operation. The new feeder minimized these potential problems.

ORIGINAL PAGE 28
OF POOR QUALITY

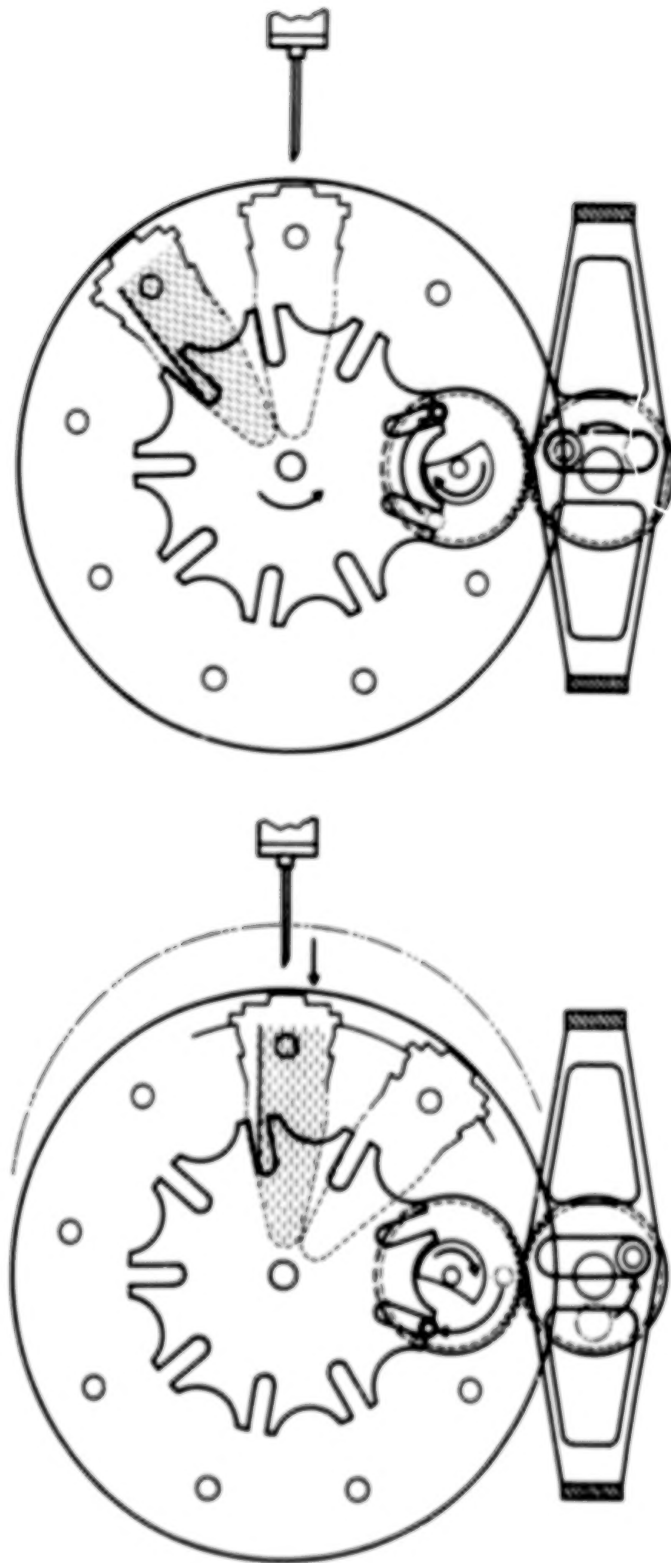


Figure 9b. Carousel Translation and Rotation Figure 9c. Carousel Translation, End of Rotation

FEEDER DESIGN

The Monkey Feeding System designed at NASA ARC meets the design constraints imposed by the experiment and previously outlined. The system delivers one, whole, 190 mg food pellet to the monkey on demand. Food cartridges, each holding 600 pellets, are replaced during the flight by the payload specialist. The food cartridge is removed from the cage by opening the cage door (Figure 10).

The feeder cartridge (Figure 11) incorporates an endless chain made up of stainless-steel barrels, cut from seamless tubing, and joined by Lexan connecting links (Figure 12). A food pellet is loaded into the center of each barrel. The chain is routed through the feeder cartridge around aluminum sprockets with a pitch diameter of 2.72 cm (1.07 in) (Figure 13). On one end of the feeder eight sprockets freewheel; on the opposite end seven sprockets are motor driven to advance the chain. The driven chain sprockets are keyed to shafts which are all ganged to turn together by a system of spur gears (Figure 14). The pinion gear of the feeder drive motor engages a single idler gear, and as the motor turns, the chain advances, driven by seven sprockets. Driving the chain from multiple sprockets minimizes backlash and windup of the system during operation. The feeder motor is mounted permanently in the cage (Figure 15) and remains in place when a cartridge is removed. The motor is a small ac synchronous motor delivering 1.27 N-m (180 oz-in) torque at 3 rpm output speed.

The chain is advanced by the motor on the monkey's demand by a tap switch located in the monkey's compartment (Figure 16). As the chain moves, a passive, spring-loaded toggle removes the food pellets from the chain (Figure 17). The pellet is retained in a transparent, Lexan food receptacle covered with a flexible, Dacron reinforced, Silastic septum (Figure 16). The septum is slotted and the monkey can reach through to retrieve a food pellet when he desires.

A control box, located in the cage, can be adjusted to preset the number of taps required to advance the feeder (1 to 99 taps per pellet). The minimum time between feeder advances can also be set (1 to 99 seconds per pellet). This prevents a hyperactive monkey from emptying the cartridge in a very short time, and allows feeder operation to be adjusted to a particular monkey's behavior.

PROTOTYPE DEVELOPMENT

A one fifth capacity prototype was designed to demonstrate the feasibility of the endless chain feeder concept. This prototype was used to test the chain design, materials selection, and chain assembly procedures. Reliability of the system was checked using actual lab tests with squirrel monkeys (Figure 18) with the feeder mounted on a test stand. Several problems were found in the original design. The chain tended to bind occasionally going around the sprockets, and the pellet

ORIGINAL PAGE IS
OF POOR QUALITY

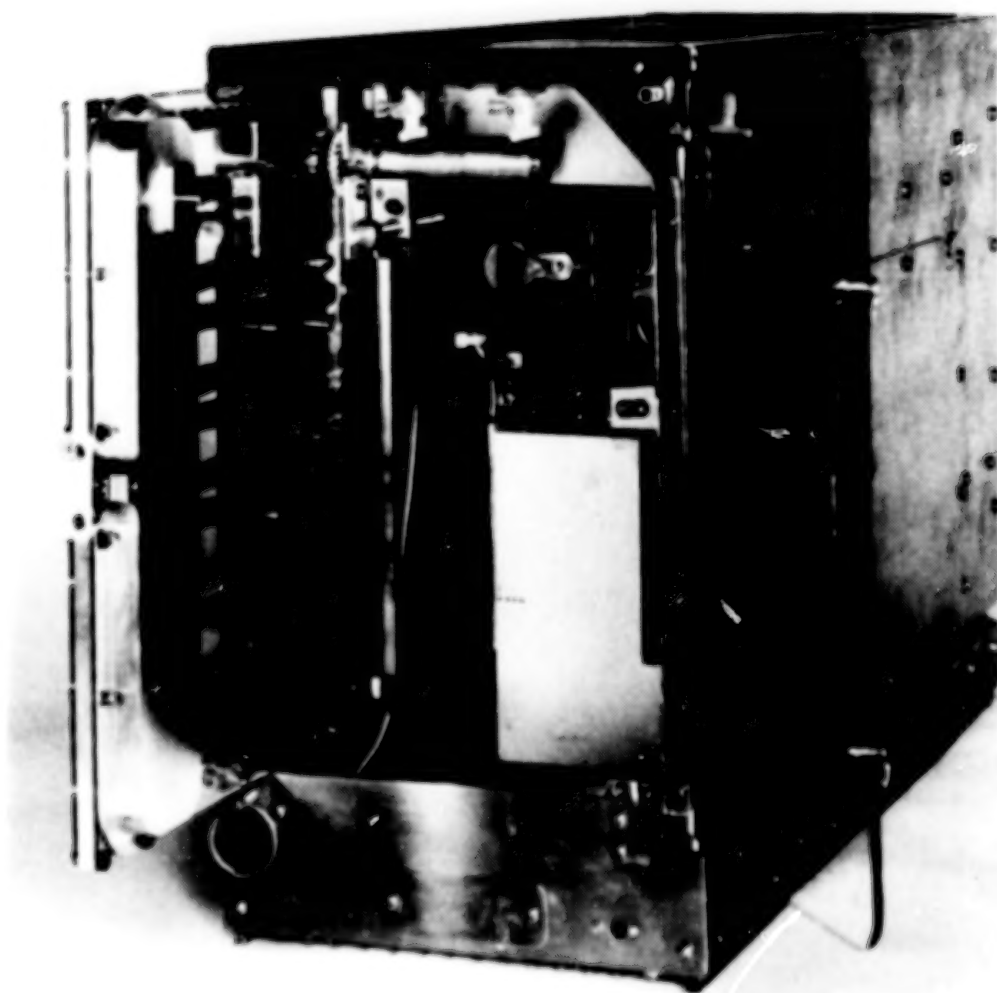


Figure 10. Feeder Cartridge and Cage

ORIGINAL PAGE 19
OF POOR QUALITY

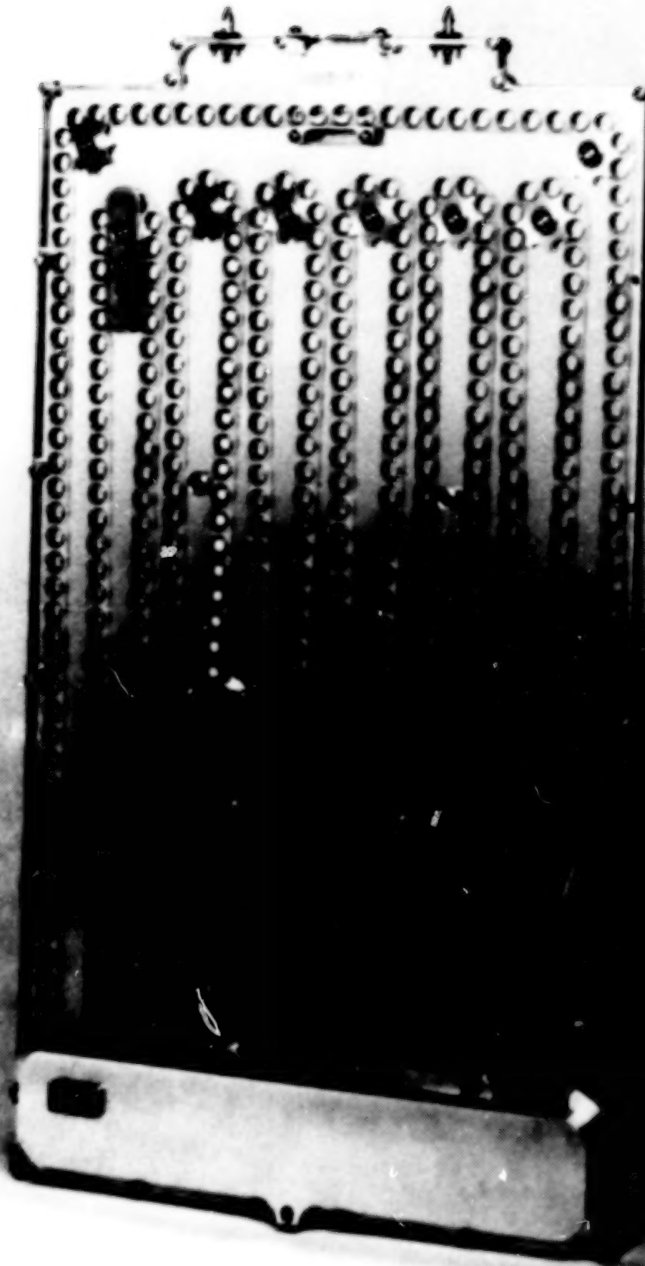


Figure 11. Feeder Cartridge

ORIGINAL PAGE IS
OF POOR QUALITY

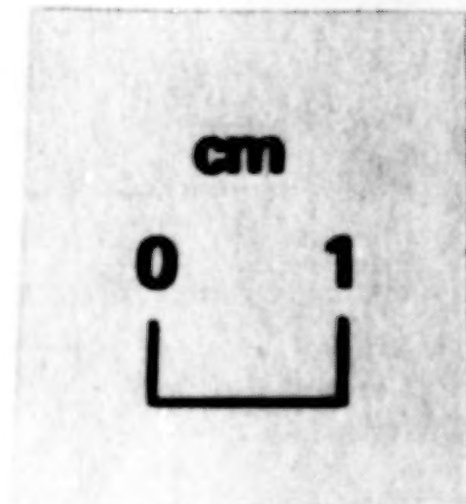
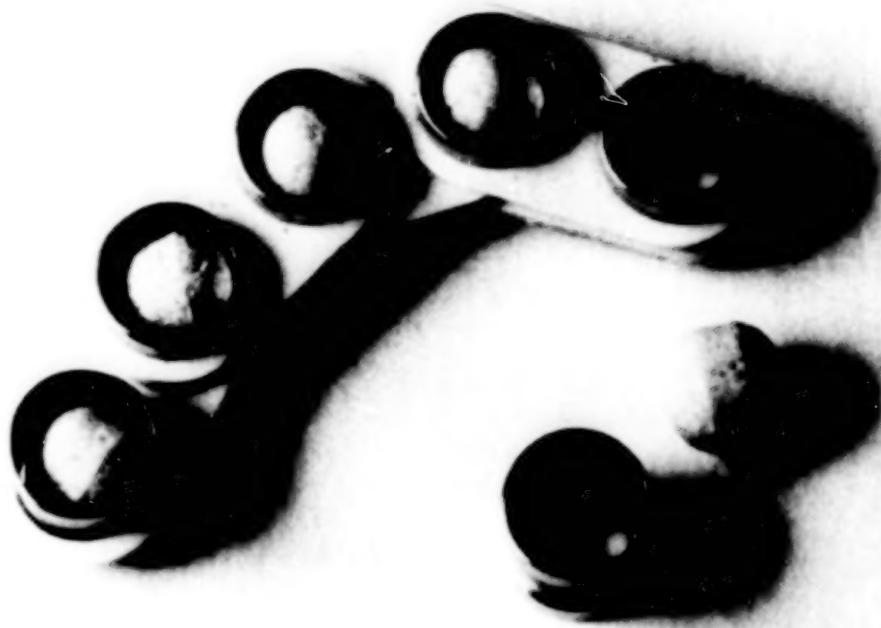


Figure 12. Feeder Chain Details

ORIGINAL PAGE 19
OF POOR QUALITY

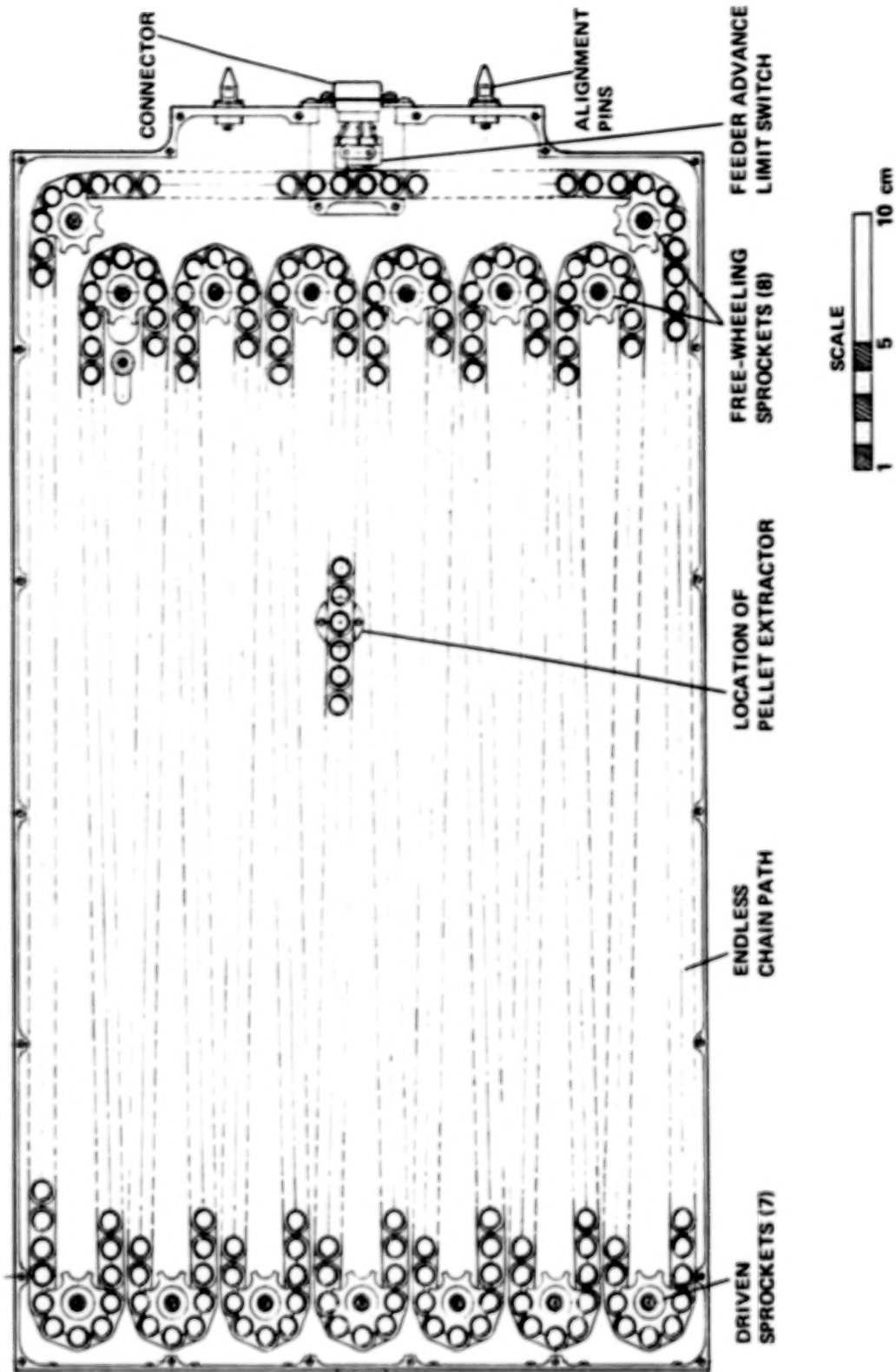


Figure 13. Internal Configuration

ORIGINAL PAGE IS
OF POOR QUALITY

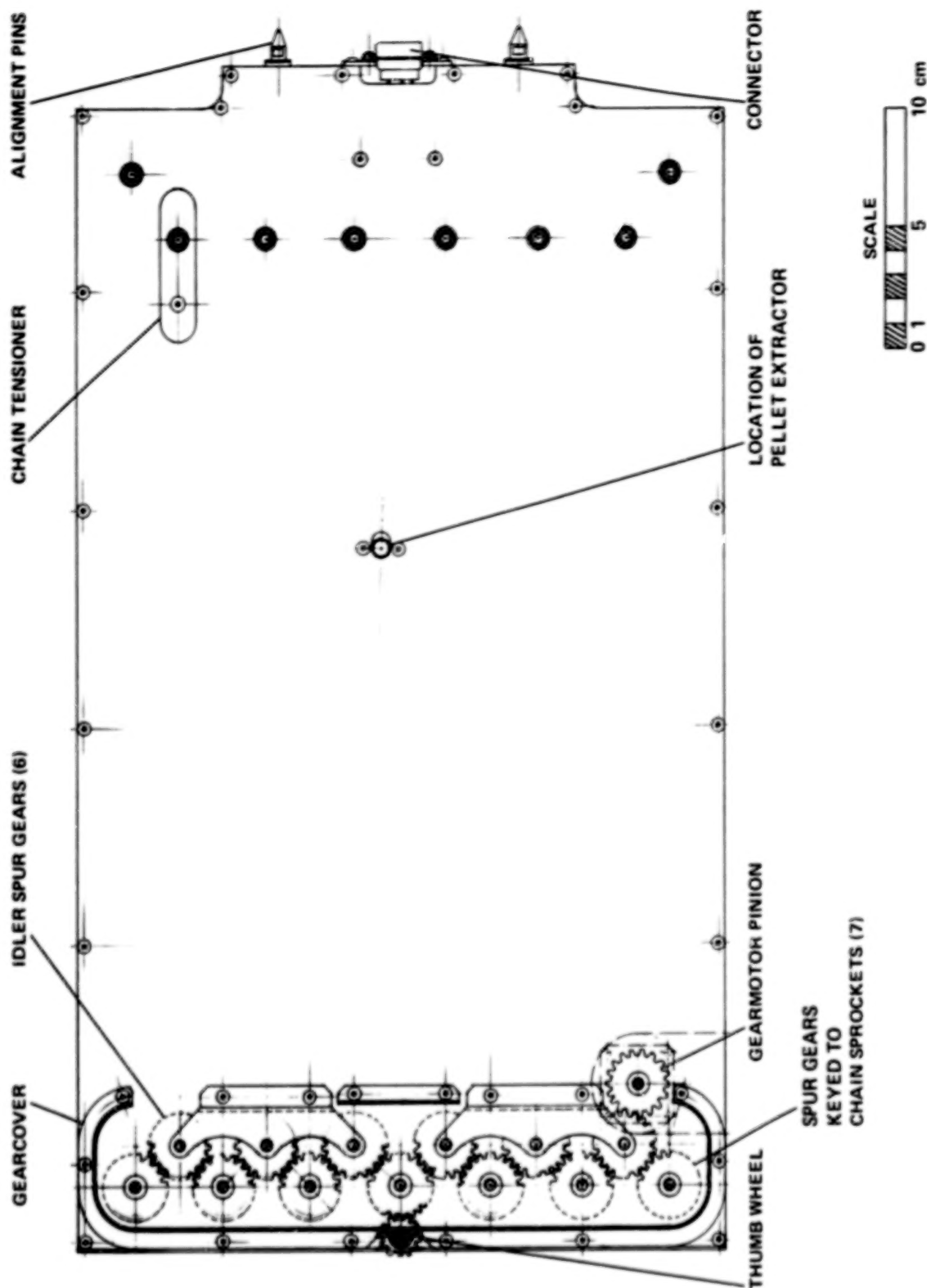


Figure 14. External Configuration

ORIGINAL PAGE IS
OF POOR QUALITY



Figure 15. Feeder Motor Installation

ORIGINAL PAGE 19
OF POOR QUALITY

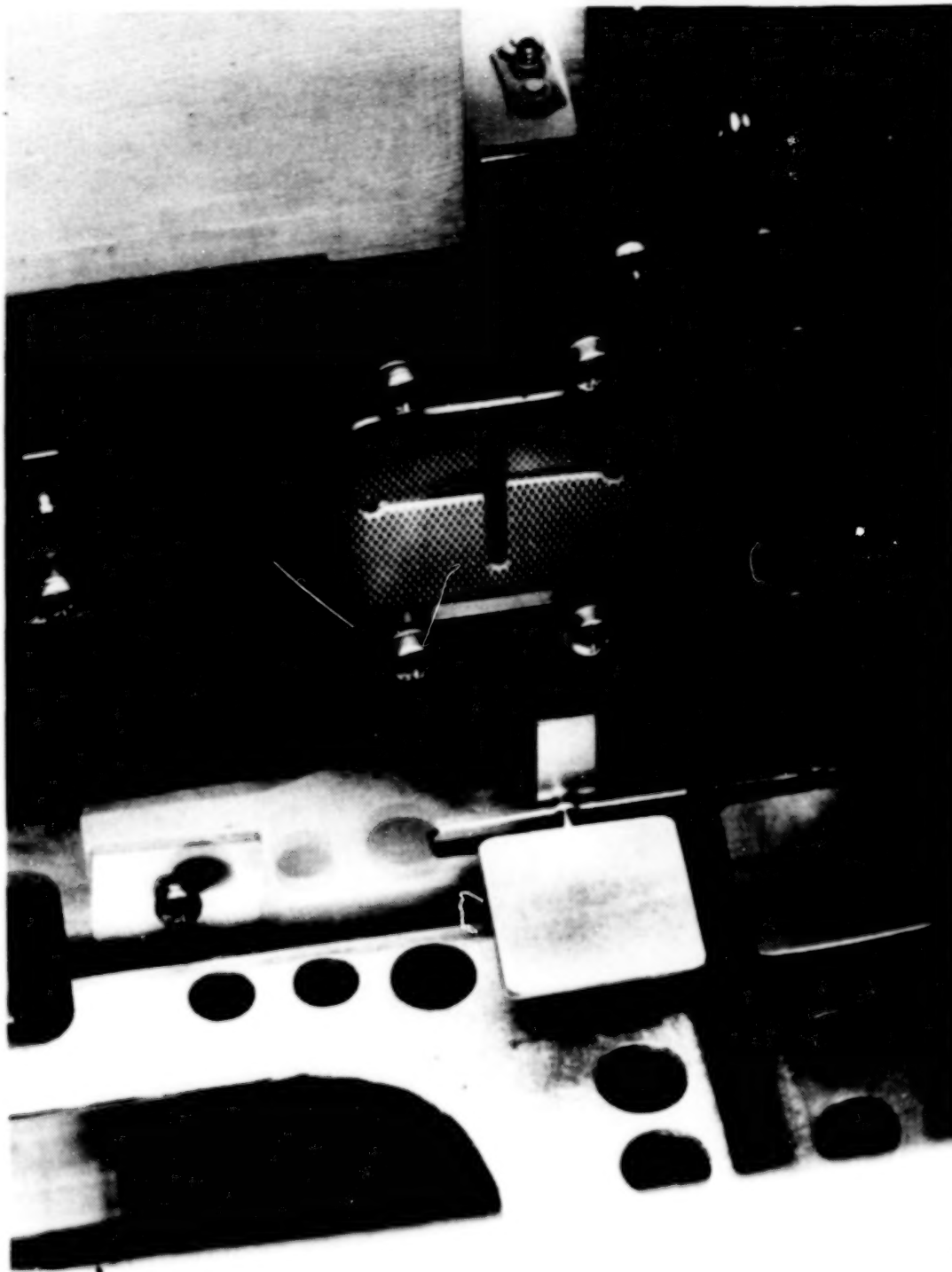


Figure 16. Tap Switch and Food Box

ORIGINAL PAGE IS
OF POOR QUALITY

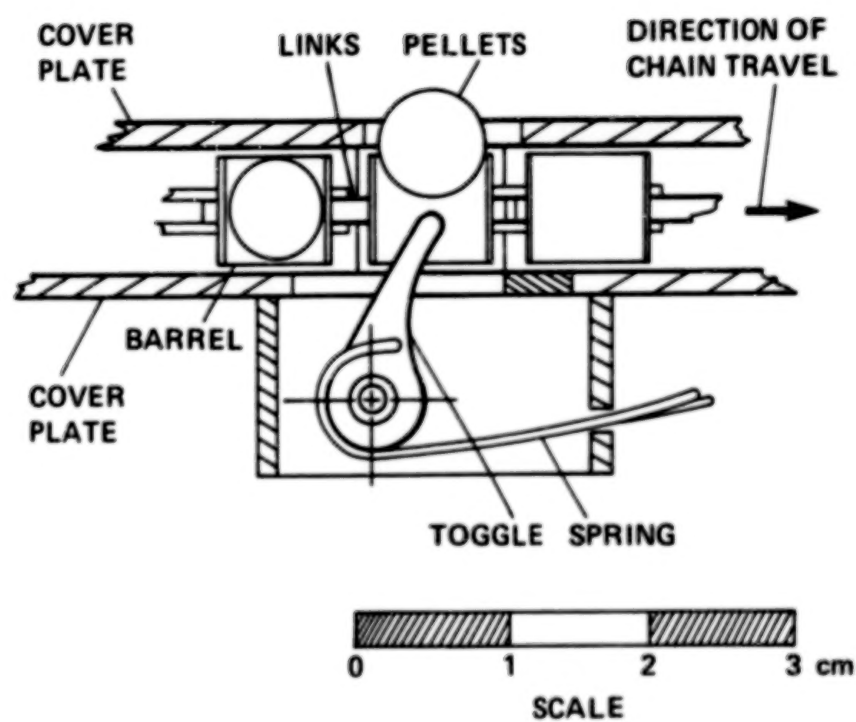


Figure 17. Pellet Extraction System

ORIGINAL PAGE IS
OF POOR QUALITY

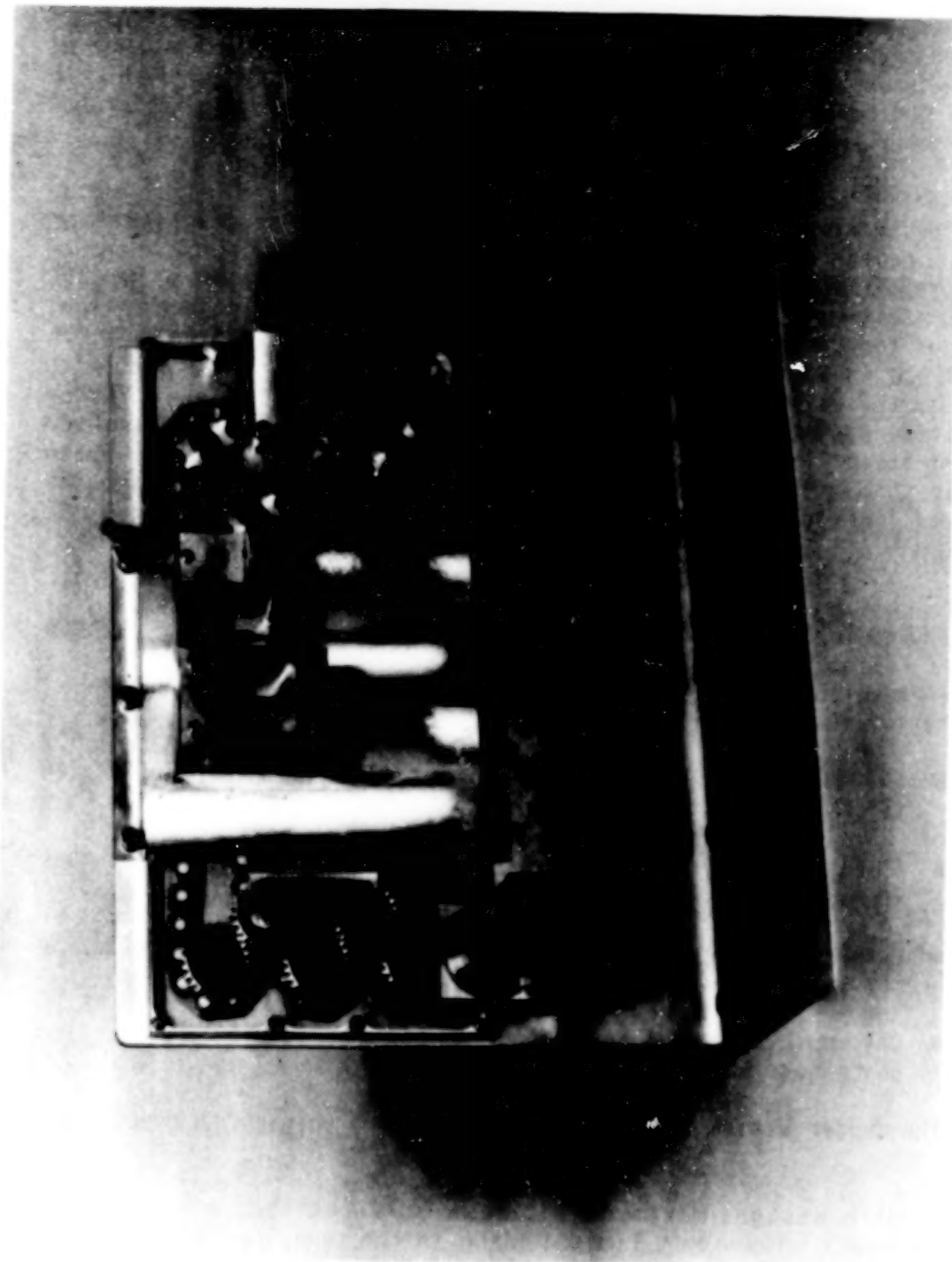


Figure 18. Test Feeder

removal spring broke from fatigue early in the testing. The original chain design consisted of two 0.152 cm (0.060 in) thick links snapped onto each barrel. The links were staggered from barrel to barrel. As the chain was tensioned the barrels tended to cant slightly, impairing their ability to pass around the sprockets. The chain design was revised by replacing the staggered links with a single 0.152 cm (0.060 in) thick link sandwiched between two 0.076 cm (0.030 in) thick links. This made a symmetrical chain which ran smoothly around the sprockets, and allowed the barrel design to remain unchanged. The pellet removal spring was radiused to eliminate a stress concentration that existed at a sharp 90° bend in the original design. With these changes, the prototype feeder performed perfectly in the lab.

Before production of 24 flight feeders, a full size flight prototype feeder was constructed. This feeder was used for cage integration and vibration testing to qualify the hardware for flight. To reduce the cost of fabricating chain links for the production feeders (21,000 links required), an injection mold was developed. The mold has eight cavities for links that are 0.097 cm (0.038 in) thick. Originally 0.076 cm (0.030 in) thick links were molded; however, it was difficult to maintain the tolerances required (+ or -0.0051 cm thick). The thicker links are easier to mold, and a single mold can be used to produce all the chain links required (three 0.097 cm thick links form the chain rather than a single 0.152 cm thick link sandwiched between two 0.076 cm thick links).

CONCLUSIONS

The endless chain feeder system and the urine collection system form a reliable experimental package that meets all the requirements of the Spacelab 4 mission. The urine collection system has several important features, including:

- The first totally automatic urine collection system for space-flight application on squirrel monkeys.
- A leak-proof system that provides up to 10 days service without any observable irritation.
- Compact design and use of only one motor for improved reliability and reduced complexity.
- Carousel assembly makes once-a-day changeouts of collection containers quick and easy.

The feeder design also incorporates several unique features including:

- Slim design (maximum thickness 2.42 cm) that minimizes the impact on monkey's limited space in the cage.

- Each food pellet is separated from other pellets, reducing chafe and excessive food fines (dust) which could accumulate and jam the feeder. In addition, the low contact force on the pellets reduces the possibility of crushing a pellet before delivery to the monkey.
- The food cup, which retains the food pellet until the monkey retrieves it, may be repositioned without significantly changing the feeder design. This will enable the feeder system to be easily adaptable to other cage configurations on future flights.

At present, fabrication of 12 flight urine collection systems and 24 feeders is underway. These units will be used for flight, ground testing, and training.

N84
25093

UNCLAS

DESIGN OF A PRECISION ETALON POSITION CONTROL SYSTEM
FOR A CRYOGENIC SPECTROMETER

By

J. -N. Aubrun*, K. R. Lorell*, D. F. Zacharie*, J. B. Thatcher*

1. INTRODUCTION

The National Aeronautics and Space Administration (NASA) Upper Atmosphere Research Satellite (UARS) will be launched in 1988 to study the distribution of a series of trace elements in the upper atmosphere and to study atmospheric dynamics.¹ The UARS carries on board a cryogenically cooled infrared spectrometer to measure the concentration of a series of chemical species that are important for understanding the ozone layer in the stratosphere. This device, known as the Cryogenic Limb Array Etalon Spectrometer (CLAES), uses a multi-position filter wheel combined with tilt-scanned Fabry Perot etalons to obtain the high resolution required for these experiments.

The CLAES optical system is sealed in a dewar where it is maintained at cryogenic temperatures by a supply of solid hydrogen. Operating temperatures for CLAES range from 130 K at the entrance aperture to 13 K at the focal plane.² Figure 1 is a schematic diagram of the CLAES showing the relative location of the major system components.

In this paper we describe the design and test of a special control system using a unique actuator concept to provide position and scan control for the CLAES etalon. Results of performance tests at cryogenic temperatures simulating the CLAES on-orbit environment will be discussed.

2. PROBLEM DESCRIPTION

2.1 Requirements

The six primary performance requirements for the CLAES etalon position control system are summarized and briefly discussed as follows:

- Precision angular positioning for each of the four etalons
- Rapid step response between adjacent data-taking positions of an individual etalon
- Rapid rotation of the etalon assembly to the next etalon to be used for data-taking
- Minimum dissipation of thermal energy from the actuator to conserve cryogen
- Operation of actuator components in vacuum and 20 K
- Reliable operation over the approximately 2-year mission duration

*Lockheed Palo Alto Research Laboratories, Palo Alto, California

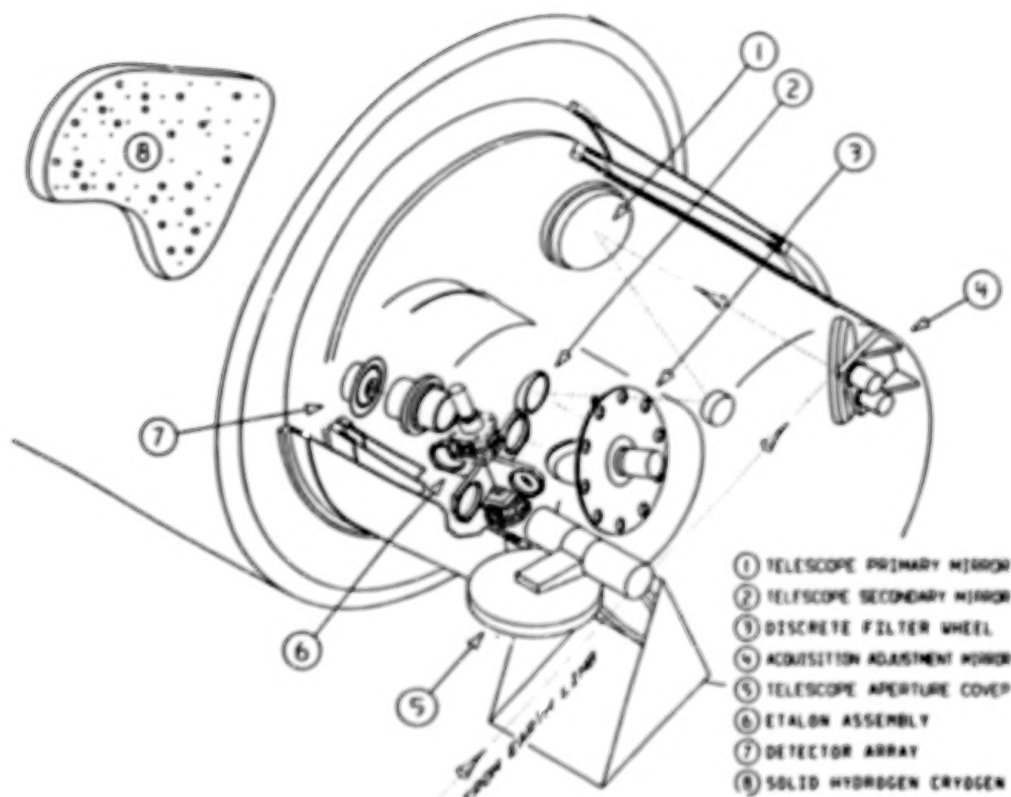


Figure 1. CLAES Baseline Configuration

Individual etalons must be positioned with an accuracy of 0.022° . In a system sensing angular position using a digital encoder, this requirement translates into an accuracy of 14 bits.

The data-taking capability of the CLAES is predicated on the ability to take a new reading every 125 ms. Based on the sensitivity of the focal plane detectors, a period of approximately 30 to 40 ms is available for the etalon to rotate 0.1° to the new data-taking orientation.

In addition to the rapid and precise positioning of an individual etalon in the optical path, it is also essential to reposition each of the four etalons in the incoming beam with as little delay as possible. A goal of 1 s for a 90° rotation has been set for this function.

Minimizing the dissipation of thermal energy is an essential requirement for any long-life cryogenic mission. This is especially important when the heat producing mechanism (in this case, the rotation actuator) is coupled to an optical element whose temperature is also critical. Therefore, the design of the actuator must be such that the resistive thermal energy dissipated during operation is kept in the range of 1 to 5 mW.

Reliable, long-life operation of electromechanical devices in a cryo-vac environment creates a number of constraints on the design of the actuator. In

particular, the brushes, commutator, bearings, and gear trains used in standard servomotors are sources of failure. In addition, careful attention must be paid to tolerances and the potential for differential thermal contraction so that the mechanism will function throughout the temperature range from cryogenic to ambient.

2.2 Potential Solutions

A number of potential solutions are available to meet the previously mentioned requirements. Probably the simplest solution would be to use a small stepper motor and move the etalon assembly in an open-loop mode by counting the number of steps the motor was commanded to move. This technique lends itself to microprocessor control and is easy to implement. Another possible solution is to use a standard dc servomotor with a position feedback loop and drive the etalon assembly through a gear reduction mechanism to provide the desired torque/speed relationship.

The difficulties with both of these and similar approaches are related to meeting the fairly stringent servomechanism requirements while simultaneously providing reliable operation in a cryo-vac environment. For example, some form of gearing is necessary for a stepper motor to have the required angular resolution. Unfortunately, it is not possible to meet the slew requirements with a geared stepper motor because an excessively high-pulse rate (steps per second) would be needed. A geared dc servo motor can meet the resolution and slew rate requirements, but the reliability of a mechanical system with brushes, commutator, gears, and numerous bearings becomes a problem. In addition, the performance of a geared system is always degraded relative to a direct drive arrangement because backlash in the transmission introduces nonlinearities which are difficult to compensate for. Brushless dc motors to avoid many of these problems, especially if configured for direct drive; however, the semiconductors used for the electronic commutation will not operate at cryogenic temperatures.

Therefore, based on the previous discussion, an ideal system would use an actuator with enough torque output to operate in a direct drive configuration. This system would have the continuous positioning ability of a dc servo motor and the rapid slew response of a stepper motor. In addition, the system would use feedback control for precision and repeatability, but would be simple enough to ensure reliability for a long-life mission.

In the following sections, a precision etalon position control system is described that meets the requirements of the CLAES as previously discussed. The system uses commands from a microprocessor to drive a unique actuator that combines the advantages of a stepper motor and a dc servo motor. This low-power unit develops enough control torque so that it can be connected directly to the etalon assembly without the need for intermediate gearing.

ORIGINAL PAGE IS
OF POOR QUALITY

3. ACTUATOR CONCEPT

3.1 Principle

The concept developed for the CLAES etalon wheel actuator was evolved in direct response to the requirements defined in Section 2. The cryovac conditions coupled with long-life mission were strong drivers for an unpowered rotor-direct drive design. High torque and accuracy requirements combined with the need for unlimited angular rotation resulted in a concept that combines the characteristics of stepper motors and dc torquers.

The "stepper" part of the actuator has four stable positions, 90° apart, that correspond to the nominal positions of each etalon. The "torquer" part is obtained by applying to the rotor bidirectional proportional control torques that can continuously move the rotor about its stable position, in the prescribed range of $\pm 15^\circ$. The stepper performs the switching between etalons and the "torque" achieves the precise positioning.

3.2 Magnetic Design

The hybrid stepper/torquer concept can be integrated in a single magnetic assembly as shown schematically in Figure 2. The rotor is a dipolar permanent magnet and the stator consists of four pole pieces that are energized by separate windings. When the windings of two adjacent pieces are producing the same poles, only one rotor position is stable (Figures 3a, 3c, 3d and 3f), achieving the stepper effect. When the windings are driven differentially, bidirectional torques are obtained (Figures 3b and 3e).

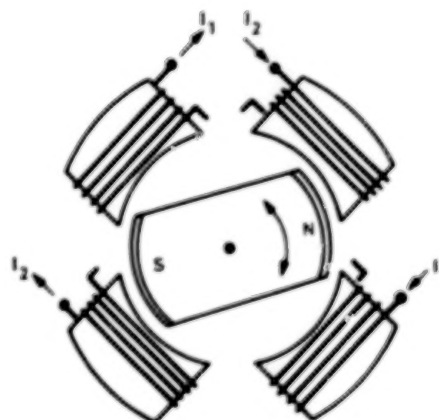


Figure 2. Actuator Magnetic Assembly Concept

Because of the symmetry of the system, the same behavior is obtained about each of the four equilibrium positions. The shape of the pole pieces must achieve three objectives:

- Produce the maximum torque for a given magnetization
- Achieve a rather constant torque/magnetization characteristic within the $\pm 15^\circ$ range
- Make it possible to slew between two adjacent (90°) quadrants

The last two objectives lead to pole pieces that are widely overlapping so magnetic interactions remain present even for large deviations from the

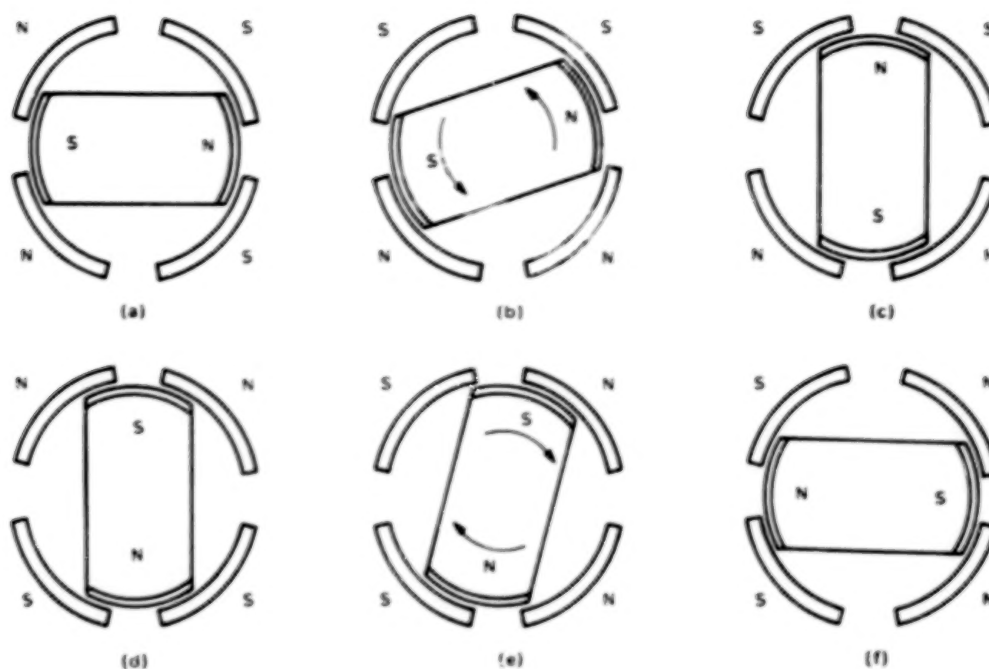


Figure 3. Actuator Stepper and Torquer Nodes

nominal position. The maximization of the torque involves the distance d between two adjacent stator pole pieces (Figure 4). In the case of a linear (translating) rotor, and assuming a constant magnetization, the magnetic force acting on the rotor is a function of the position of the rotor and of the distance d , as well as of the magnetic gap g (distance separating the rotor from the stator). This force can be computed and the results are shown in Figures 5 and 6 corresponding to rotor and stator pole pieces of length equal to 100 gaps. The relative position of the rotor is expressed in units of gaps and the force in normalized units. The curves were computed for several values of the distance d and they indicate that d should be equal to about one-fourth of the stator pole piece length.

The actual magnetic design used the previous ideas, but the geometry of the system was modified from the conceptual concentric design of Figure 2 to a lateral design as shown in Figure 7. This arrangement was preferred for the following reasons:

- Allows a smaller gap between stator and rotor (thus a higher force level) because of a lower differential thermal expansion and sensitivity to bearing accuracy
- Makes it easier to manufacture and replace the permanent magnets
- Results in a more compact design, which is desirable because of the limited space available in the CLAES dewar

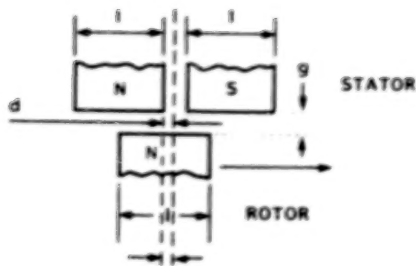


Figure 4. Linear Rotor Model for Pole Piece Optimization

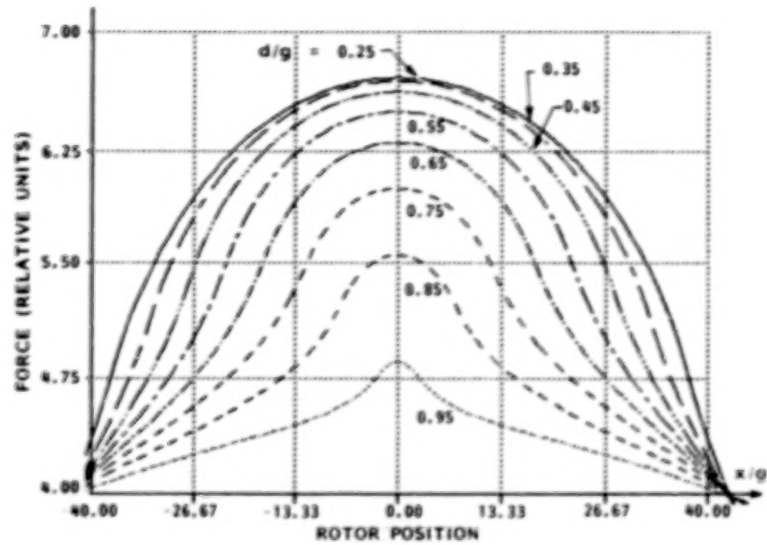


Figure 5. Rotor Forces Versus Rotor Position for Various Values of d/g

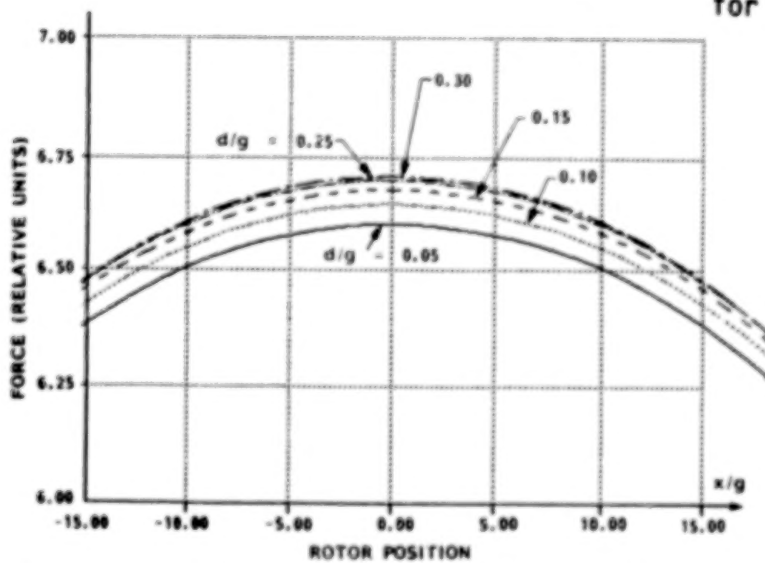


Figure 6. Rotor Force Versus Rotor Position for Various Values of d/g

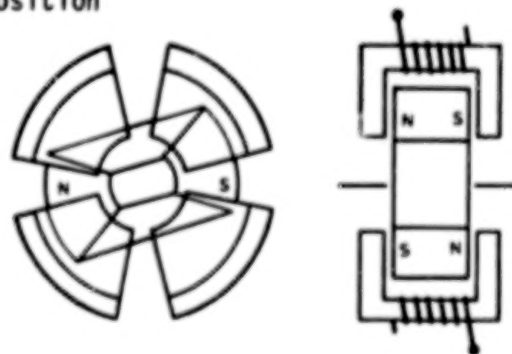


Figure 7. Lateral Magnetic Design

Finally, the windings of the four stator pole pieces are grouped in pairs, because two opposite pole pieces (with respect to the rotor axis) are always of opposite magnetic polarity. Therefore, only two control inputs to the actuator exist: the currents I_1 and I_2 in the corresponding pairs of windings (Figure 2).

3.3 Mechanical Design

The mechanical design of the prototype actuator is shown in the enlarged view of Figure 8. The stator pole pieces are mounted between two aluminum plates connected to each other by steel bolts. The rotor is attached to a stainless-steel shaft supported by BarTemp bearings mounted on the aluminum plates. Belleville washers were used to center the rotor. Alnico permanent magnets are fitted in the rotor and covered with soft iron pole pieces to distribute the magnetization more uniformly. An actual view of the actuator is displayed in Figure 9.

4. ETALON CONTROL SYSTEM CONCEPT

4.1 Control System Overview

The CLAES etalon position control system operates by sensing the angular orientation of the etalon assembly, comparing the measured orientation with the desired etalon angle, and applying a control torque to the assembly to drive the residual error to zero. In addition, rate information is used to damp oscillations and to provide a quick transient response.

The control system has been mechanized in a hybrid configuration with a microprocessor used for generating commands with discrete logic to determine error signals, control phasing, and mode switching and with analog circuitry to provide feedback compensation.

Figure 10 is a schematic diagram of the control system. The etalon angular position (sensed by the resolver) and its angular rate (sensed by the tachometer) are the prime inputs to the control system. The error signal is constructed by comparing the actual and commanded position. The feedback loops include integral, proportional, and rate terms; the actuator produces a torque T_c such that:

$$T_c = K_p (\theta - \theta_c) - K_I \int (\theta - \theta_c) - K_R \dot{\theta} \quad (1)$$

The integral control loop counteracts the effects of mass imbalance, bearing friction, magnetic cogging, and other phenomena that would introduce a static position error.

This control law is activated in each of the four quadrants, and the commanded angle θ_c can be either 0° , 90° , 180° , or 270° with a range of $\pm 15^\circ$ about those values. For a given magnetization or current into the windings, the torque obtained is a function of the angle θ and can be approximated by:

ORIGINAL PAGE 13
OF POOR QUALITY

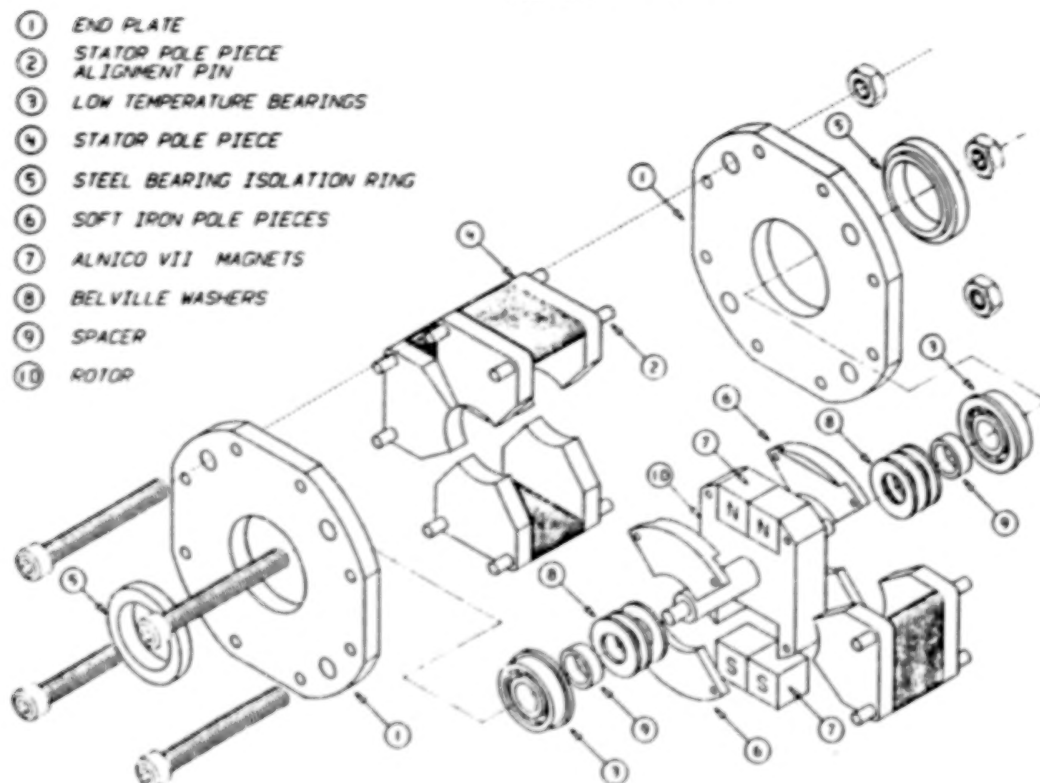


Figure 8. CLAES Etalon Motor Mechanical Design



Figure 9. CLAES Motor View

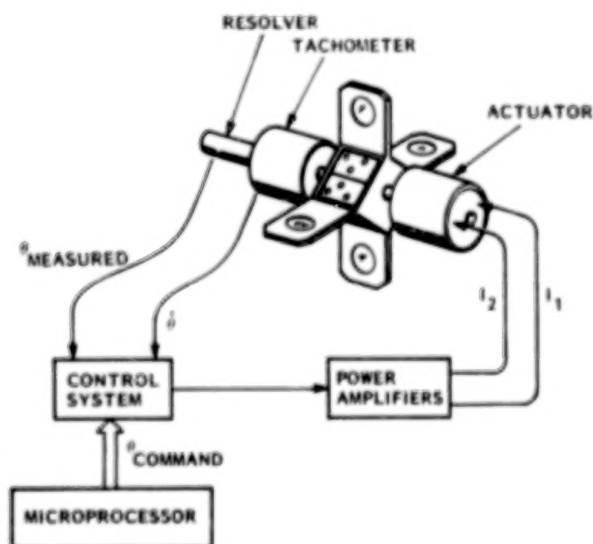


Figure 10. Etalon Control System Schematic

$$T_a = K_a [(I_1 - I_2) \cos \theta + (I_1 + I_2) \sin \theta] \quad (2)$$

where K_a is a constant.

In the control mode defined by Equation 1, I_1 and I_2 are made equal or opposite, depending on the quadrant in which the system is operating. Although the rotor can be commanded to go to the next (or previous) quadrant by setting I_1 and I_2 to the proper value, once a 90° rotation has been obtained, the torque goes to zero and it becomes necessary to switch the signs of I_1 and I_2 to ensure the correct control law. Therefore control of the actuator is handled by three separate control systems:

- A proportional control compensation system described by Equation (1)
- A slew controller providing commands for changing quadrants
- A switching logic controller to set the proper winding connections

4.2 Tachometer Concept

To implement the rate feedback loop described previously, an angular rate sensor is desirable. With a conventional tachometer, the rate signals will have to be switched according to the operating quadrant to ensure the proper sign. The use of conventional tachometers presents the same inconvenience as found in conventional motors, (i.e., moving electrical contacts). In the present case, however, an elegant solution is available by using a tachometer design identical to that of the actuator. Because of the reversibility principle, when the actuator is forced to rotate, currents are created in the windings proportional to the angular rate in such a manner that they create forces opposed to the motion (i.e., the usual back emf effect). Thus rate feedback can be achieved automatically by simply connecting the tachometer windings to the corresponding actuator windings (through electronic compensation and power amplifiers). In this case switching is not necessary because the feedback polarity is always correct. This feature simplifies the electronics and also increases the reliability of the system. Some alignment is required, of course, between tachometer and motor pole pieces, but does not need to be very accurate. For simplicity and cost reduction purposes, two prototype actuators were built, one used as the motor and the other as the tachometer. In a final design the tachometer would be made much smaller.

A schematic of the etalon assembly is shown in Figure 11, including the motor, the wheel, the tachometer, and the resolver.

5. CONTROL LOGIC

The control requirements for the etalon servo can be divided into two categories: slewing and fine control. The slewing mode is used to rotate the etalon assembly rapidly between the four individual etalon elements with a typical slew maneuver requiring a 90° rotation in less than 1 s. Occasionally it may be necessary to make 180° rotations. Fine control of the etalon assembly provides precise positioning of an etalon in the incoming

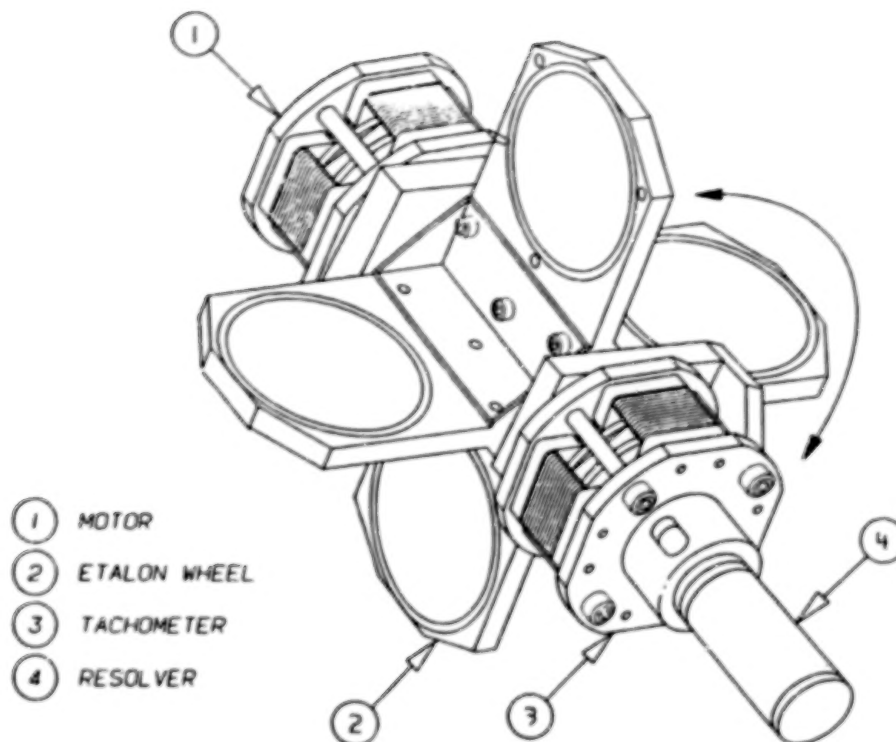


Figure 11. Etalon Wheel Assembly

beam and is also used to make incremental angular position changes as the spectrum is scanned by the focal plane. The etalon is held stationary during a measurement sequence, then rotated by approximately 0.088° so that a new measurement can be made. In addition, the fine control mode is used to rapidly scan the etalon or make large angle changes for repeating a measurement sequence.

The design of the control logic for these two functions is complicated by the way in which the actuator operates for fine control and for slewing. The slewing mode uses the effect of a rotating magnetic field vector to force the rotor to reorient itself in much the same way a synchronous motor operates. During fine control a different control strategy is employed primarily because low-power dissipation is critical. Control torque is generated by a combination of attractive and repulsive forces which are proportional to the magnitude of the error signal. Thus in the fine control mode, force (and current) is not applied unless there is a position error to correct.

Figures 3a, 3c, 3d, and 3f illustrate the change in polarity of the stator pole pieces for a slew of 90° . It is important to note that the rotor aligns itself between two poles, each having identical polarity. The strong force obtained by applying the maximum current to both sets of coils is the reason that the slew mode has the characteristic "snap" motion in which the rotor experiences a rapid acceleration followed by an equally rapid deceleration. Figure 12 shows the switching logic that translates the desired

ORIGINAL PAGE 12
OF POOR QUALITY

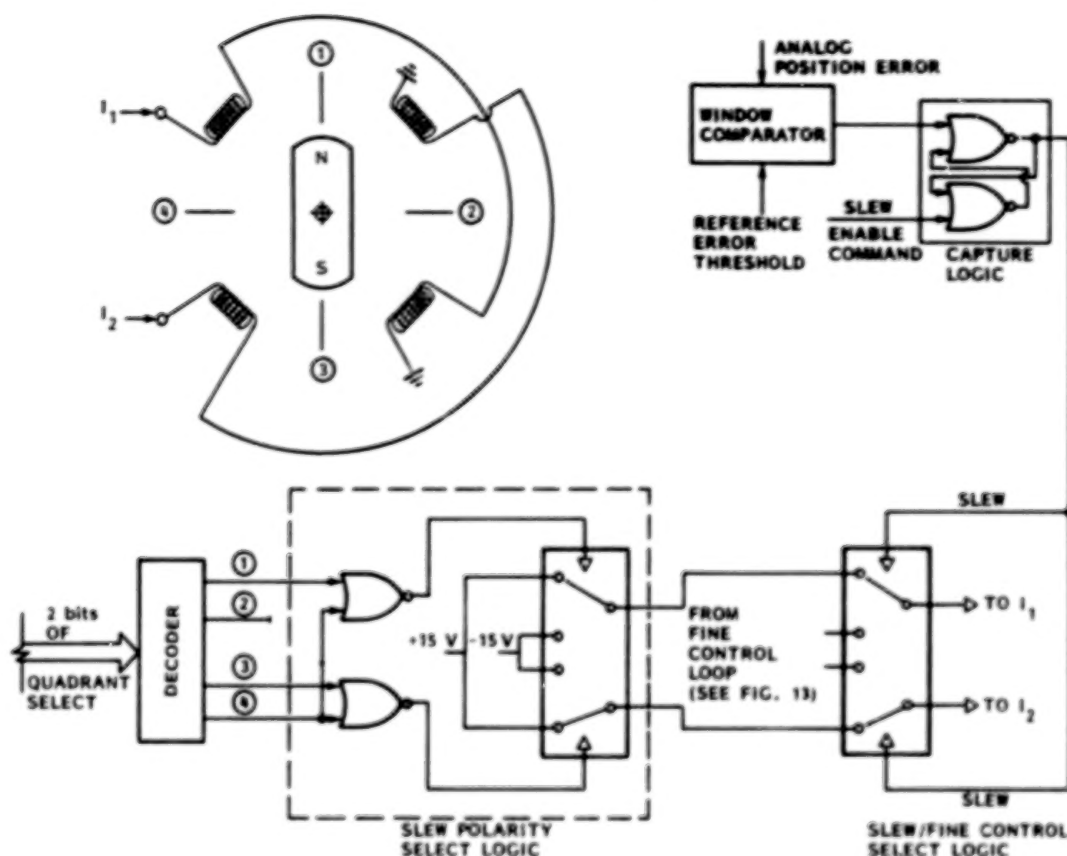


Figure 12. Slew Logic

orientation of the rotor into the correct magnetic polarity for each of the pole pieces. This figure also depicts the logic that senses the completion of a slew maneuver and switches the system to the fine control mode. This logic resets the slew mode so that the system cannot execute another slew unless the microprocessor reenables the slew logic. This feature is important because the threshold detector which senses the completion of a slew maneuver operates by comparing the desired angle with the measured etalon position. If the position error should inadvertently exceed this threshold when the system is in fine control, the slew mode would be reinitiated if the slew logic had not been previously disabled.

A typical magnetic polarity orientation for the stator poles when the system is in the fine control mode is seen in Figures 3b and 3e. The force-generating mechanism is now attractive-repulsive as compared with the slew mode in which it is attractive only. Although it would be possible to operate the fine control mode in the same manner as the slew mode, it would require that a magnetic field be available continuously for the control system to "steer" so that the rotor would be positioned. In the attractive-repulsive scheme, the magnetic field is activated only in proportion to the magnitude (and polarity) of the angular error. If the system is operating exactly

on the desired angular orientation or very close to it, almost no magnetic field is required from the stators. This, of course, means that the power dissipation in the system is kept at a very low level, an important requirement in cryogenic applications.

The use of an attractive-repulsive technique demands that two polarities of control signal be available so that one set of stator coils can generate the attractive component and the other set the repulsive component of the control force. In addition, as the rotor changes quadrants, it is necessary to change the polarities of the control signals to the stators so that the correct overall control system polarity is maintained. The switching logic to command the control signal polarity change is shown in Figure 13. This logic, which is a function of the rotor orientation (i.e., which quadrant the rotor is in), is the electronic equivalent of the mechanical commutator in a dc servo motor. The advantage in the present application is the lack of mechanical parts which are sensitive to both the temperature and vacuum environment, thereby eliminating potential reliability problems.

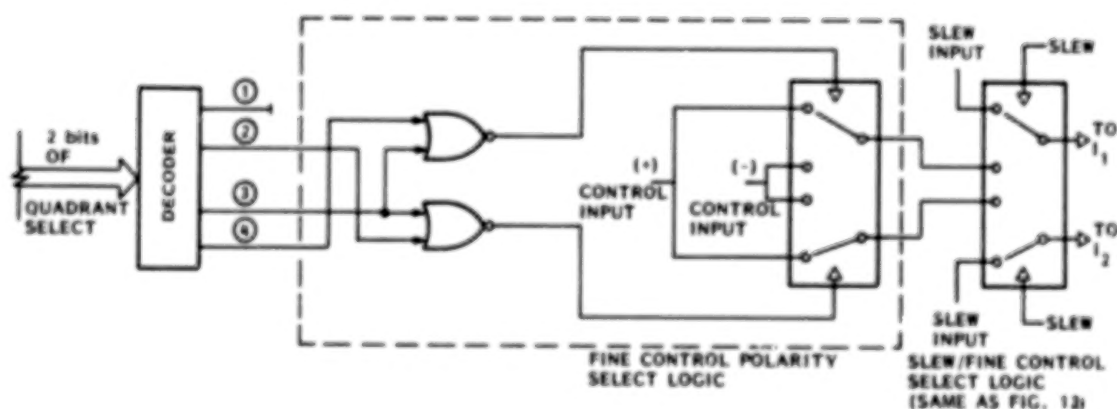


Figure 13. Fine Control Logic

6. CONTROL SYSTEM IMPLEMENTATION

To make best use of the components that were already part of the overall CLAES system design or were known to be reliable for operation at cryogenic temperatures, the etalon control system was designed to use both analog and digital components. For example, the control of other components in the CLAES optical train and the data-taking sequence is provided by a system microprocessor. It was only natural then, to include command generation of the etalon assembly as part of the system microprocessor function. In addition, as discussed in some detail in the previous section, mode switching, control signal polarity, and slew logic are controlled by discrete digital components. The simplest way to implement the control loops, however, was to use analog techniques rather than add another microprocessor and to develop the specialized software required for a digital control loop.

An example of the application of hybrid techniques in the control system design is the use of a 400-Hz resolver to measure the etalon assembly orientation. The output of the resolver is actually converted to 16 bits of digital data and combined with the commanded angle that was generated by the microprocessor to provide a 16-bit angular position error signal. The conversion of analog data into digital data was done because (1) the commanded angle was a digital word, (2) the ready availability of extremely accurate, high performance resolver-to-digital converters that eliminate the need to design and build resolver electronics, and (3) the improvement in performance gained using digital subtraction to generate the error angle rather than analog subtraction.

Figure 14 illustrates the details of the control system mechanization. After the position error has been converted to an analog signal, it is integrated to provide the integral control signal. The position and integral signals are summed with both a positive and negative polarity so that both polarities will be available to drive the actuator.

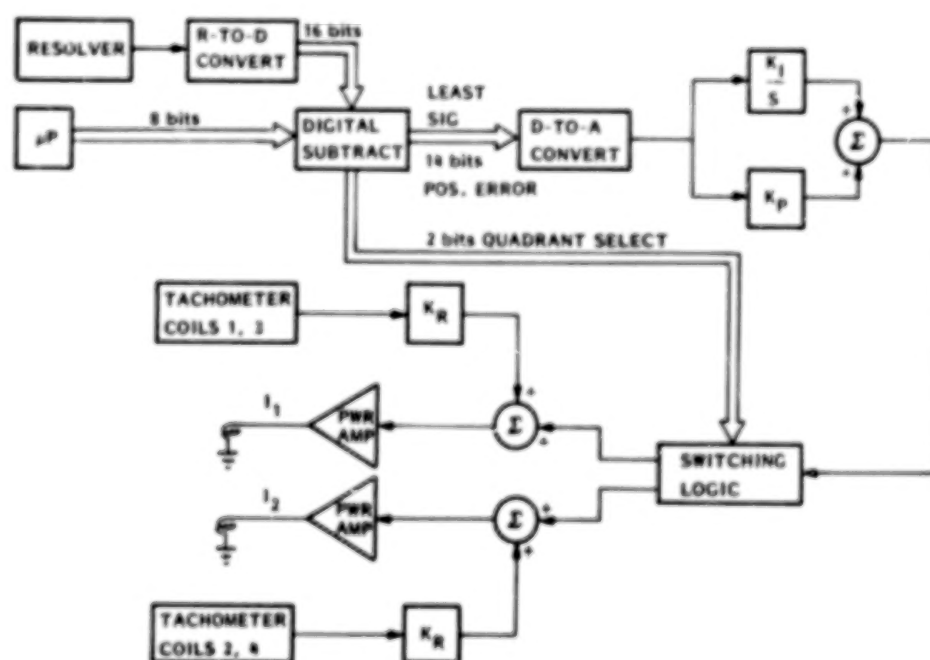


Figure 14. Etalon Control System Mechanization

An interesting feature of the mechanization is the use of polarity switching logic for the position and integral feedback loops but not for the rate (tachometer) loop. This feature is shown in Figure 14 in the summation of the rate signal with the integral plus position error signals which occurs after the polarity switch. The rate signal bypasses the switching logic because the tachometer is electrically identical to the actuator (i.e., the tachometer output changes polarity in exactly the right way to match the requirements of the motor input signal). Because the resolver does not have this polarity

reversal mechanism inherent in its electrical configuration, the position control signals require the special polarity control as described in detail in the previous section.

The motor drive electronics are also shown in Figure 14. The output power amplifiers are of the current-feedback type, which means that they generate an output current proportional to the input signal. Because the control torque developed by the actuator is directly proportional to the current in the coils, it is important to use a current amplifier rather than a voltage amplifier in this application. In the past, this type of mechanization required discrete components; however, advancements in integrated circuit design now permit the use of what is essentially a single chip power op-amp with a current feedback loop to provide the desired function.

The entire set of interface and control electronics fits on two small circuit boards (see Figure 15). One board houses the data latches, address decoders, and R-to-D and A-to-D converters. The other board contains all of the analog control circuitry and switching logic. The power amplifiers are mounted separately because it was initially felt that their higher operating temperatures and cooling requirements would preclude use in proximity to the low-power components. The system runs at such a low average power level (as discussed in the next section), however, that the separation of the output devices proved to be unnecessary.



Figure 15. Control System Electronics

Power for the electronics is provided by ± 15 and 5 Vdc power supplies. In addition, the R-to-D converter requires a 400-Hz signal at 6-Vrms to power the resolver and generate the reference signals within the R-to-D converter. None of the power supply voltages or frequencies (in the case of the 400-Hz signal) are critical, and the system can tolerate 15-percent deviations from the nominal and still function properly.

7. CRYO-VAC PERFORMANCE TESTING

An essential part of the development process for a system like the CLAES etalon position servo is performance testing. In particular, because the environmental conditions are so severe, at least some portion of the performance testing must be done in conditions that simulate actual operation as closely as possible. Because testing in a cryogenically-cooled vacuum chamber is expensive and time consuming, a great deal of preliminary testing and system tuning is accomplished at room temperature in the laboratory. The results presented in this section are a combination of data obtained from both room temperature and cryo-vac tests.

There were two primary objectives to the performance testing; (1) to determine the validity of the control concept and (2) to evaluate the performance of the system in cryo-vac conditions. The room temperature tests were especially important because of the novelty of the hybrid control electronics and the actuator itself. Potential problems associated with cryo-vac operation including bearing stiction, mechanical interference caused by thermal contraction and gradients, and changes in the actuator magnetic properties.

7.1 Control System Tests

These tests were conducted in the laboratory at room temperature and consisted of measurements of step response for small angle increments, time required for 90° slews, and position repeatability and accuracy. Because digital subtraction is used to generate the position error signal, only the position error is available from the control electronics. The absolute position was measured independently by an optical system consisting in a laser beam reflected by a small mirror mounted on the etalon wheel onto a linear photodetector. These tests were useful to tune the control system gains and adjust the slew mode switching threshold.

Figures 16 and 17 show a typical angle increment-decrement sequence in which the etalon is commanded to move 21.1 and 5.27 arc-min, respectively. The transition time for the 21.1 arc min-step was 80 ms and only 20 ms for the 5.27 arc-min step. The latter result betters the CLAES requirement for the etalon assembly to execute this maneuver in less than 25 ms. Quantized motion caused by limit cycling on the resolver's fourteenth and fifteenth bit is apparent in Figure 17.

Slew response was measured by monitoring the position error signal, because there was no convenient means of directly measuring large angles. Mode switching threshold and rate feedback gain were critical for achieving the required performance.

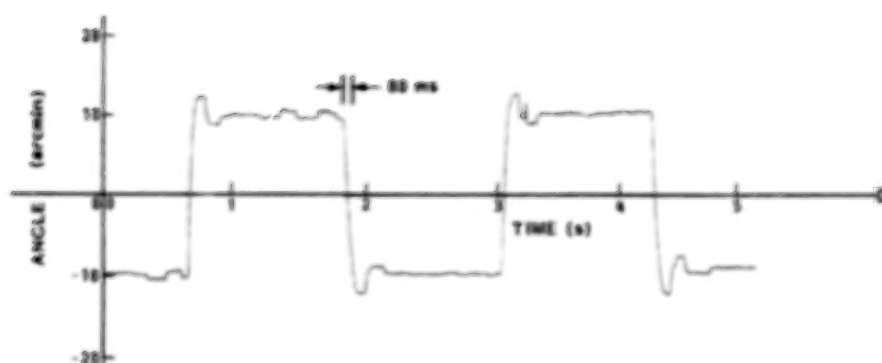


Figure 16. 21.1 arc-min Increment Decrement Sequence at 23°C

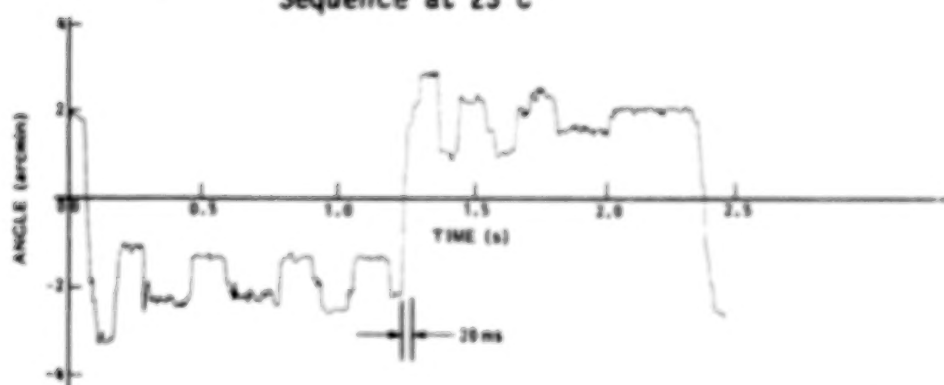


Figure 17. 5.27 arc-min Increment Decrement Sequence at 23°C

7.2 Cryogenic Testing

Cryogenic tests were conducted in a vacuum chamber with liquid nitrogen cooled walls. An overall view of the etalon test assembly can be seen in the photograph of Figure 18. Also seen in the photograph are details of electrical and cryogenic feedthroughs, the liquid nitrogen cooling shroud, and the cold plate to which the system is mounted. Additional cooling was obtained using a gaseous helium refrigerator to bring the temperature of a "cold finger" to about 10K. The close up photograph of Figure 19 shows several insulated copper braids attached to various parts of the system to ensure proper cooling. The entire etalon assembly is insulated from the mounting plate by ceramic standoffs to maintain the low temperature produced by the cold finger. The local temperatures were monitored using special low-temperature platinum resistance thermometers. A glass window allowed some direct viewing of the wheel assembly, making it possible to perform optical measurements using the etalon filters themselves.

The few problems that were encountered during the preliminary tests were principally mechanical in nature. The first attempts to operate at low temperature failed when the rotor assembly stopped responding to commands. Application of maximum current in the motor windings was unable to free the system. Upon disassembly, it was discovered that the bearing races were brinelled. A subsequent analysis indicated that a substantial differential thermal contraction existed between the stainless-steel bearings and the aluminum end-plates in which they are mounted. The solution selected to



Figure 18. Cyro-Vacuum Chamber
Test Assembly

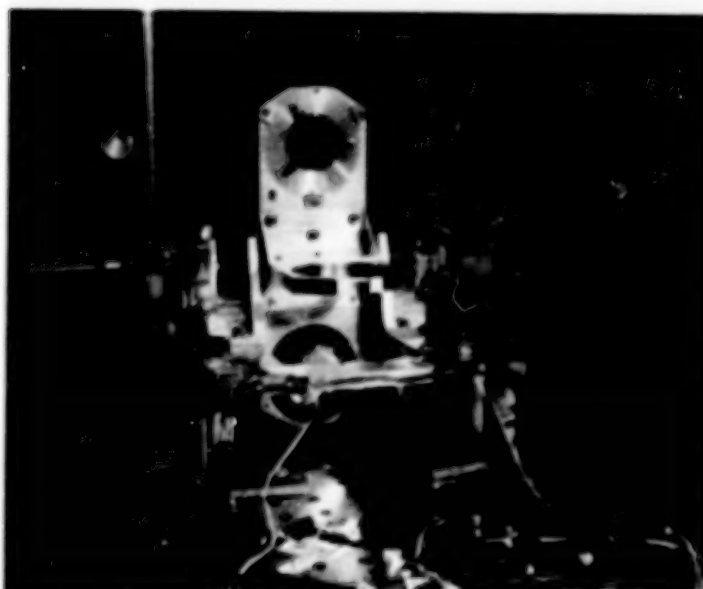


Figure 19. Etalon Wheel Cryo-Vacuum Test Assembly

alleviate this problem was to mount stainless guard rings around the bearings to prevent distortions in the relatively thin outer races.

In subsequent tests, although the bearings were no longer damaged, the motion of the etalon assembly became erratic as the temperature decreased and eventually stopped completely. Two possible explanations were offered: a deterioration in the strength of the permanent magnets with an associated loss of torque output or, more likely, some other source of temperature dependent bearing friction. Magnetic tests were then conducted and new magnets compared with magnets that had been used previously. In various tests these magnets had been subjected not only to thermal cycling, but to large demagnetizing fields as well. No significant difference was noted. The core material of the stator pole pieces was tested independently at 10 K and showed the expected slight increase in hysteresis and saturation magnetization.

It was found that the combination of the static preload on the Belleville washers and their axial compression due to the thermal contraction of the stator pole pieces caused an increase in the axial bearing loads of approximately 20 N per bearing. This resulted in excessive friction torques which the actuator was unable to overcome. A reconfiguration of the washers to remove the room temperature preload solved the problem as long as the actuator was tested alone. Finally, it was determined that distortions in the support structure were causing enough misalignment at cryogenic temperatures to inhibit smooth operation throughout a full 360°. Removing the hard mechanical mounting to the support plate eliminated warping of the etalon assembly.

Subsequent tests were successful for demonstrating full operational capability at 17K. Figures 20 and 21 show the system performing the same angle increment-decrement test as seen in Figures 16 and 17. Although some minor changes in control system gains were required to retune the system for cryogenic operation, the performance is essentially identical to that at room temperature. Performance during slew maneuvers is shown in Figures 22 and 23. In Figure 22, the current pulses to one of the stator pairs is shown during four slews comprising a full 360° rotation. The very low current required to control the etalon assembly between the slews is apparent. This control current, measured at less than 60 mA per stator pair, translates into a steady state power dissipation of 274 μ W (each stator pair has a measured resistance at 17K of 0.038 ohms), which is substantially less than the 1- to 5-mW requirement.

Figure 23 is an expanded view of one of the current pulses that occur during a slew. The current saturates at the driver amplifier limit of 2.3A. The entire maneuver is completed in less than 600 ms, which is comfortably within the 1 s per 90°-slew requirement.

A preliminary reliability test of the system has been completed in which the system was operated continuously in a scan and slew mode for 48 h at 18 K. While this is not as rigorous a test as eventually will be necessary to demonstrate flight qualification, it is an excellent indication that the present design has the potential to operate reliably in a cryo-vac environment for extended periods of time.

8. CONCLUSIONS

This paper has described the development and testing of a control system designed to precisely position etalons in the optical path of a cryogenic spectrometer. One feature of the system which is unique is the etalon assembly actuator, which combines the characteristics of both a stepper motor and a torquer. The successful operation of this system in cryo-vac conditions has been demonstrated for periods of up to 48 h at temperatures below 20K. The system has met or exceeded requirements for position accuracy, slew rate, power dissipation, and operational flexibility. Although the current configuration is not appropriate for flight hardware, it is not anticipated that major changes will be required to develop an acceptable design for the actual flight instrument.

REFERENCES

- 1 Roche, A. E., et al., "Performance Analysis for the Cryogenic Etalon Spectrometer on the Upper Atmospheric Research Satellite," paper presented at SPIE Conference on Technologies of Cryogenically Cooled Sensors and Fourier Transform Spectrometers, San Diego, California, August 1982, pp. 26 to 27.

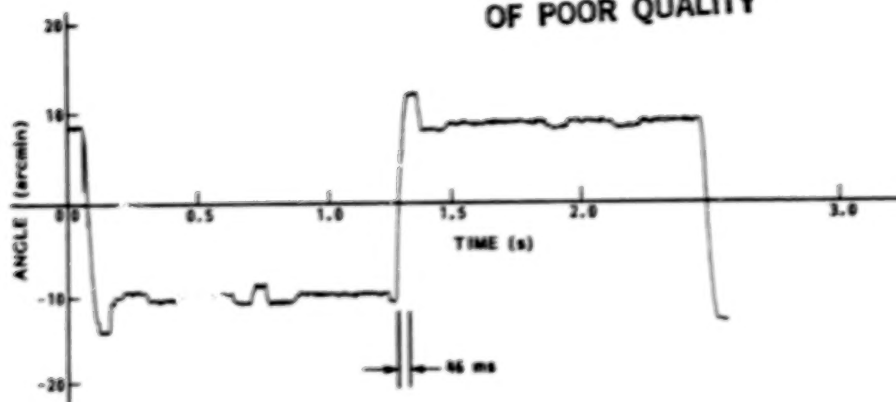
ORIGINAL PAGE 19
OF POOR QUALITY

Figure 20. 21.1 arc-min Increment Decrement Sequence at 17 K

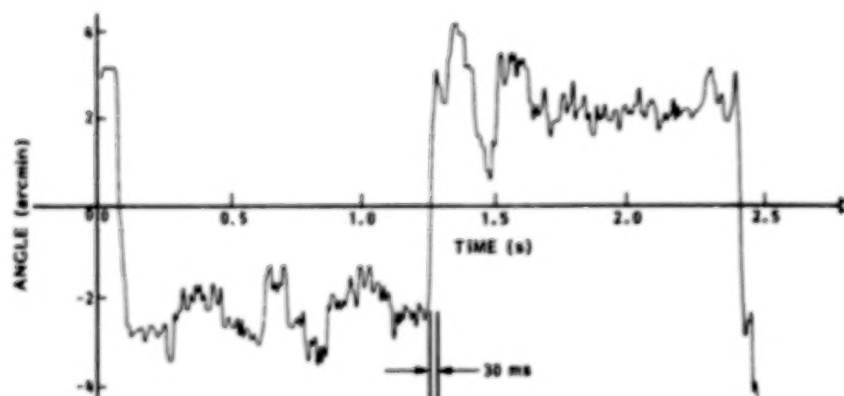


Figure 21. 5.27 arc-min Increment Decrement Sequence at 17 K

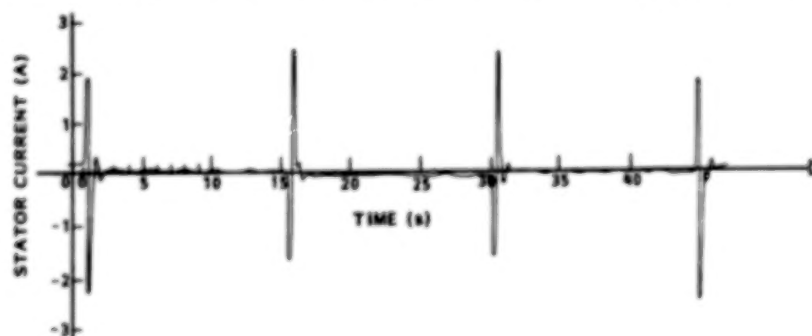


Figure 22. Four 90° Slews at 16 K

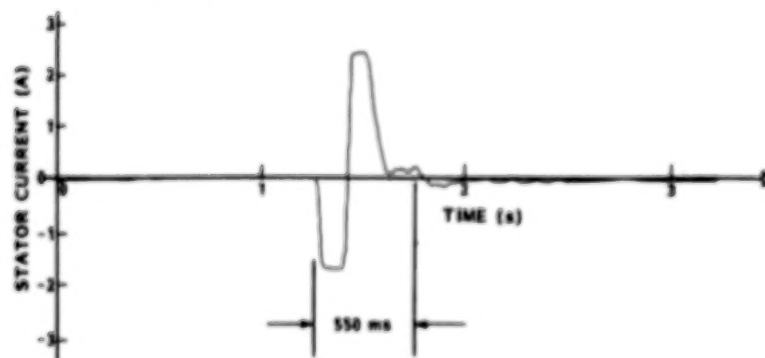


Figure 23. 90° Slew at 16 K

- 2 Naes, L. G., et al., "Two-Year Solid Hydrogen Cooler for the CLAES Instrument," paper presented at SPIE Conference Technologies of Cryogenically Cooled Sensors and Fourier Transform Spectrometers, San Diego, California, August 1982, pp. 26 to 27.

N84
25094

UNCLAS

D16
N84 25094

THE ELECTRON ECHO 6 MECHANICAL DEPLOYMENT SYSTEMS

Stewart C. Meyers *

James E. Steffen, Perry R. Malcolm, and John R. Winckler **

ABSTRACT

The Echo 6 sounding rocket payload was flown on a Terrier boosted Black Brant vehicle on March 30, 1983. The experiment requirements resulted in the new design of a rocket propelled Throw Away Detector System (TADS) with onboard Doppler radar, a free-flyer forward experiment designated the Plasma Diagnostic Package (PDP), and numerous other basic systems. The design, developmental testing, and flight preparations of the payload and the mechanical deployment systems are described.

INTRODUCTION

The Electron Echo 6 program, a joint effort of the University of Minnesota School of Physics and Astronomy with the Sounding Rocket Division of Goddard Space Flight Center, is the sixth in a series of active magnetospheric research payloads. Echo 6 was launched from the Poker Flat Research Range, Fairbanks, Alaska, with a north-northeastward trajectory across auroral arcs. It included two onboard electron accelerators which injected electron beams of up to 40 KeV in energy and 0.25 amperes current as probes into the Earth's magnetosphere. The basic objective of the Echo series is to inject electrons so that they are magnetically guided along field lines to the conjugate point in the southern hemisphere, where they are reflected back to the region near their origin either by magnetic mirroring or by backscattering off of the atmosphere. Analysis of the detected echoes provides valuable information about the structure of the distant magnetosphere and the mapping of its electric field into the ionosphere. In the previous missions (Echo 1, 3, and 4) the echoing electrons have been detected by the beam-emitting payload when their two motions were matched. The evolution of the Echo program has resulted in the development of a multiple remote Throw Away Detector System (TADS) that greatly increases the spatial coverage of the echo detection system and gives more flexibility to the rocket trajectory. The primary emphases of Echo 6 were echo detection using TADS and electric field analysis using a free-flyer forward experiment designated the Plasma Diagnostics Package (PDP).

* Engineering Branch, Special Payloads Division,
NASA Goddard Space Flight Center, Greenbelt, Maryland 20771

** School of Physics and Astronomy, University of Minnesota,
116 Church Street S.E., Minneapolis, Minnesota 55455

FLIGHT PLAN

The scientific launch criteria had three requirements that: the magnetosphere be in an inflated tail like configuration, the local electric field be northward corresponding to an eastward electrojet, and the aurora be in the form of an intermediate intensity arc under the trajectory. The payload launch criteria required that there be no Sun on the payload at apogee, that all payload and ground systems be operational, and that the meteorological conditions be suitable. Because of the short-lived nature of the scientific event, the brevity of the flight, the complexity of the payload, the requirement for the precise placement of the TADs in space, and the necessity of accurate injection of the electrons relative to the magnetic field lines; a rigorous and detailed sequence of payload events was required for the flight plan. (See Figure 1). A series of complex Attitude Control System (ACS) maneuvers had to be coordinated to achieve these requirements. The synchronization of the onboard payload events was controlled by use of six mechanical timers and two electronic programmers. These events are detailed in the time-event sequence of Table 1.

Table 1: Echo 6 Time-Event Sequence

Time Sec	Alt Km	Event Description
-90	0	Systems to internal power
0	0	Terrier ignition, aerodynamic spin-up by fin offset
4	1	Terrier burnout
12	4	Black Brant ignition
44	37	Black Brant burnout, payload rotation at 3.6 rps
60	64	TAD section door ejection
62	68	ACS arm
64	71	Yo-Yo despin to 0.6 rps
66	76	Black Brant Motor separation (250 Kft)
66	76	ACS starts maneuvers to reference orientation
70	82	Nose cone ejection 5 mps relative velocity
80	100	PDP electric field booms unfold and lock
82	102	Detector high voltage enable on PDP and Main section
84	106	PDP deployment, 1.5 mps relative velocity
88	112	ACS despin to zero rps
93	118	ACS alignment to TAD deployment orientation
130	164	TAD spin-ups on and Doppler radars on
140	174	TAD 3 deployment, 10 mps relative velocity
143	177	TAD 1 deployment, 10 mps relative velocity
146	180	TAD 4 deployment, 20 mps relative velocity
149	183	TAD 2 deployment, 20 mps relative velocity
151	184	Electron accelerator system start
155	188	TAD spin-ups off and Doppler radars off
160	190	Electron accelerators on (first pulse)
244	216	Apogee
432	80	ACS off
538	6	Recovery system deployment (20 Kft)

ORIGINAL PAGE 19
OF POOR QUALITY

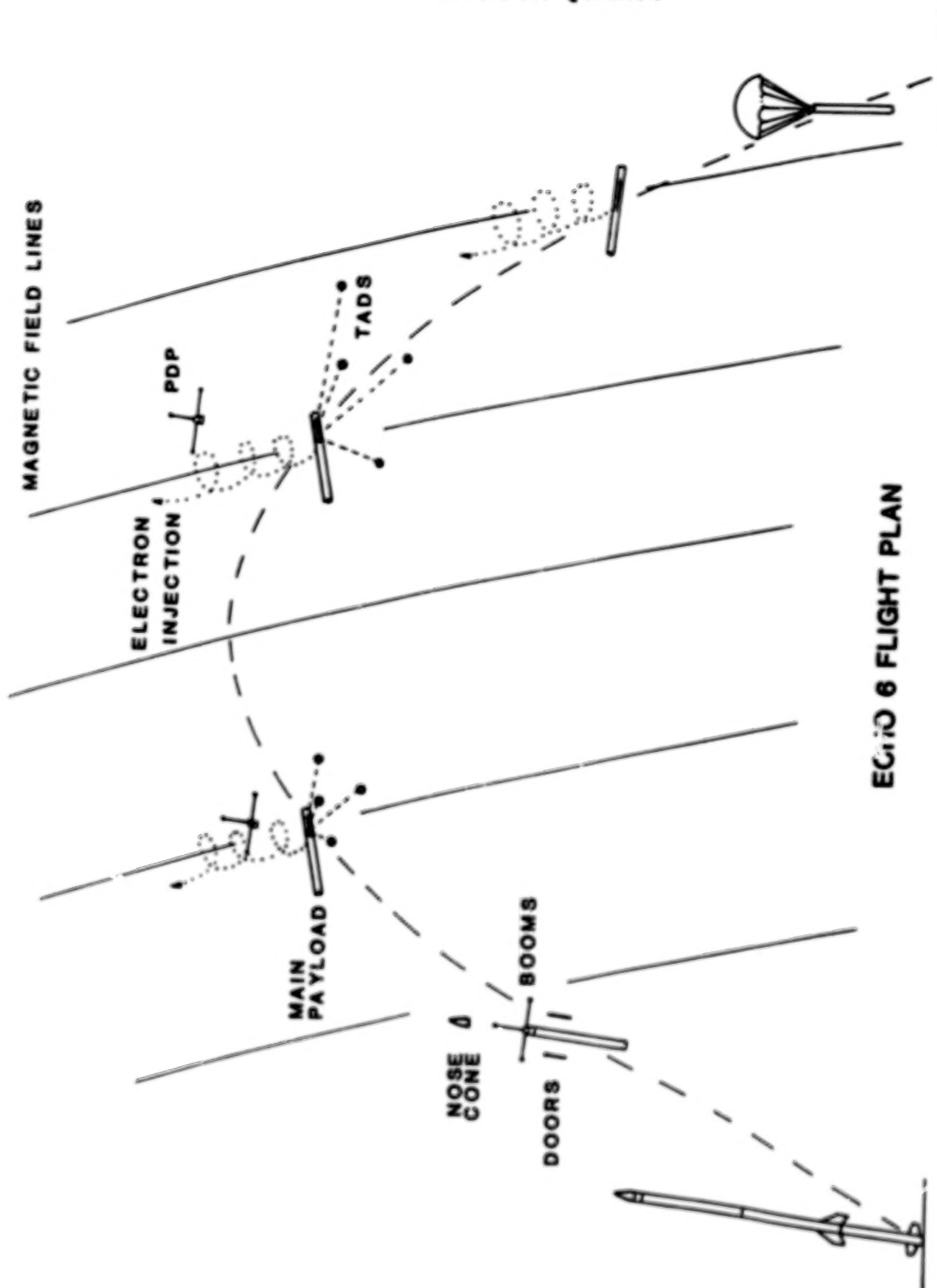


Figure 1. Echo 6 Flight Plan

THE PAYLOAD

Although the TADS was mechanically the most complex aspect of the Echo 6 payload, it was only one of several sophisticated systems that had to function for a successful mission. An index of the mechanical complexity of the entire payload is that 28 electro-explosive devices (squibs) were fired, some simultaneously and some sequentially, to separate the payload into 35 distinct pieces during the flight. To get an overview of this payload, refer to Figure 2 and Figure 3 beginning at the nose and working aft.

The one piece nose cone, which was 1.50-m (60-inches) long with a 3:1 ogive, was retained by a two piece V-band clamp at its base. Two squib actuated bolt cutters were used to sever the band screws, either of which would release the band. An ejection spring, in the tip of the nose cone, pushed off against the top of the payload when the band was cut. (This action is typical of all the payload separation bands.) Ejecting the cone exposed detectors and the electric field booms of the Plasma Diagnostic Package (PDP). The booms were spin deployed when a cable cutter was actuated. The PDP in turn was released by a V-band and was spring ejected forward to expose the electron accelerators and detectors on the forward portion of the main payload. Aft was the electron accelerator battery can containing 220 kg of high-voltage batteries. Further along was the Throw Away Detector section with spin-deployed doors and rocket-propelled TADs.

Aft of the TAD section came the nearly standard sections used on most sounding rocket flights. The telemetry (TM) section supplied both 28-volt power and timing signals to the payload as well as telemetering the data back to the ground. The ACS stabilized and pointed the TADs and electron accelerators. Following was the recovery section which deployed a parachute to decelerate the main payload. Finally, there was the igniter housing which ignited the Black Brant sustainer, despun the whole rocket with yo-yo's to 0.6 rps, and separated the sustainer from the payload. Below the sustainer was the Terrier booster.

The total payload weight was 2310 kg (1050 lbs), of which 2134 kg (970 lbs) reached a burnout velocity of 2020 mps and an apogee altitude of 216 km. The payload, which was 6.5-m (254-inches) long and 0.44 m (17.26 inches) in diameter, sat on top of a 9.8-m (385-inches) long sustainer and booster.

PLASMA DIAGNOSTIC PACKAGE (PDP)

The design of the PDP section of the payload was dictated by the requirement of stowing electric field booms under the nose cone and the need to provide a ground plane for an S-band antenna. (See Figure 4). The core of the section was a 0.61-m (24-inch) long can of which only the top quarter of its volume was used for housing the PDP telemetry system and batteries. To simplify spin balance of the PDP the battery packs were located symmetrically. A set of doors was placed on opposite sides of this section for easy access to the batteries. The remaining empty volume of the can acted as a cover for the forward portion of the main payload containing detectors and the electron accelerator turret. The S-band antenna was located in the middle of the section to provide adequate ground planes on each side. The experiment portion of the PDP mounted to the front of the PDP can and was exposed by the

ORIGINAL PAGE 19
OF POOR QUALITY

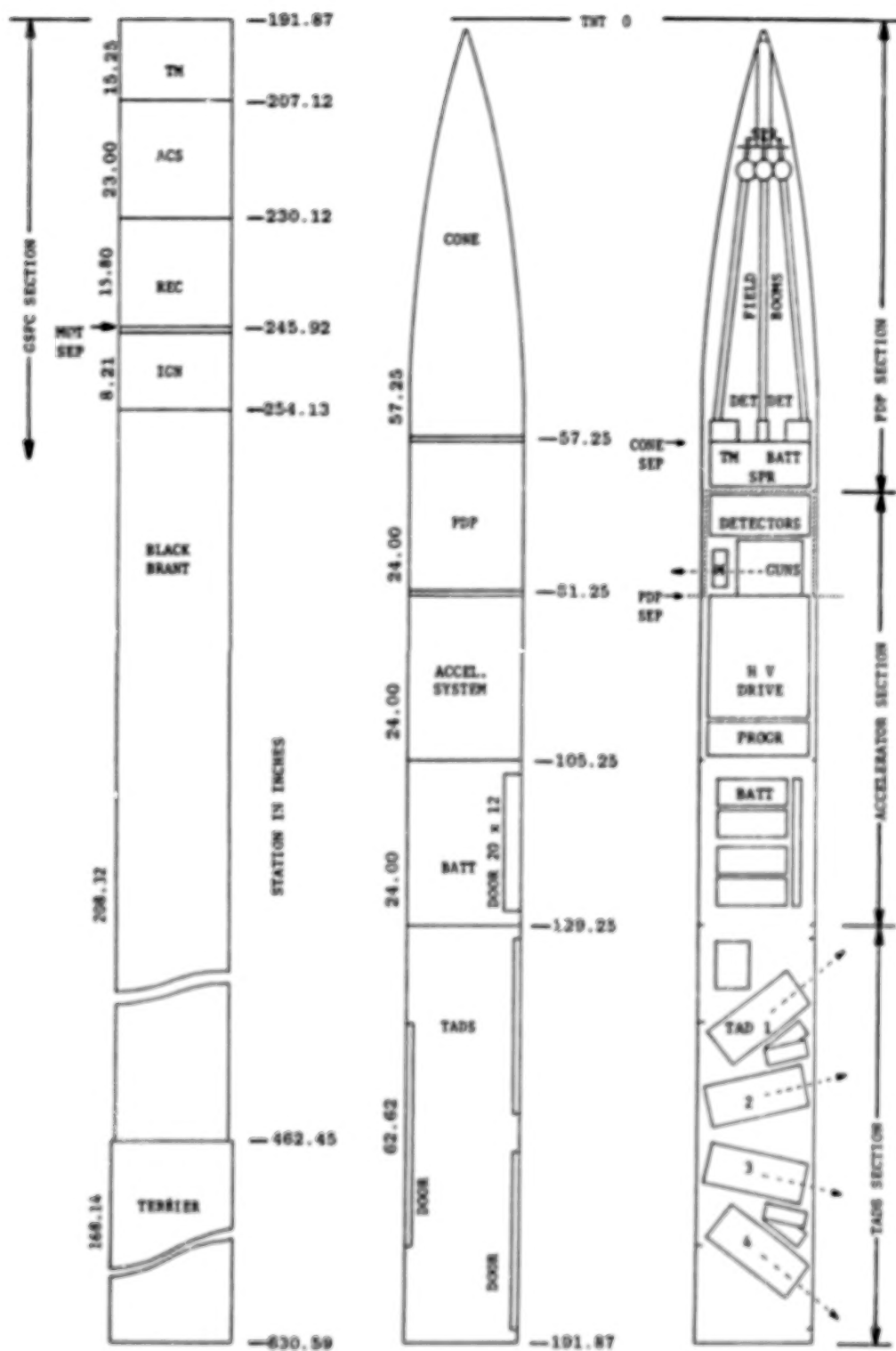


Figure 2. Echo 6 Payload-Vehicle Layout



Figure 3. Echo 6 All-Up Payload (During GSFC Integration)



Figure 4. Echo 6 PDP Flight Configuration (During GSFC Mass Properties)

forward spring ejection of the nose cone. Following the deployment of the nose cone, two sets of orthogonal electric field probes were released from their forward stowed position by the squib action cutting of a cable while the payload was still spinning at 0.6 rps. The four probes were dependent on the centrifugal forces present to torque them 90° into their locked positions perpendicular to the PDP-main payload spin axis. The probes then telescopically and centrifugally extended to almost twice their stored length, separating each pair of conducting spheres on an axis by 3.63 meters. A spring loaded fifth probe was also released and rotated by a torsion spring 180° from its aft pointing stowed position to its locked forward position along the spin axis.

The ejection of the PDP from the main payload was accomplished by a single spring axially located to minimize tip-off at separation. With the 470 lb spring, the PDP achieved a 1.5 mps velocity relative to the main payload. This velocity was measured by a system consisting of a multiturn potentiometer mounted on the main payload and wound with a cord attached to the PDP body.

The ejection spring was designed as a cartridge that could be compressed externally with a loading screw. Once the cartridge was loaded, safety screws were installed and the loading screw removed. This mounting allowed the safety screws to remain in place until just before flight. Access to the safety screws and the velocity pot was through the battery access doors.

Of particular concern was the fact that during ejection relative rotation between the PDP can and the enclosed accelerator turret would destroy the PDP antenna connector that protruded radially inward. A set of rails was added to guide the separation and an antitorque shoe was provided to prevent rotation.

THROW AWAY DETECTOR SYSTEM (TADS)

In previous GSFC programs TADs were deployed by a combination of springs and the centrifugal force created by the spinning rocket payload, resulting in a random dispersion of the TADs away from the main payload. Echo 6 required that the TADs achieve separations of several kilometers from the main payload in a predetermined pattern. Not only was centrifugal deployment too imprecise, but the energy requirements of ejecting four 6 kg TADs at 10 to 20 mps were too high for the safe use of springs. After considering various alternative means of deployment, a rocket propelled, spin stabilized TADs was developed.

The resulting design of the TAD consisted of a cylindrical aluminum tube 0.33-m (13-in) long and 0.14 m (5.5 in) in diameter (Figure 5) containing three solid-state electron detectors, an electrostatic analyzer, a 3-axis aspect magnetometer, power supply, NiCad-battery pack, 50 KHz data encoder, transmitter, S-band antenna, and a small solid fueled rocket motor for propulsion. In essence each TAD was a complete rocket experiment with its own detectors, data system, and means of propulsion.

The TAD propulsion motors were acquired as overaged spin motors from the NASA Delta Program. The motors came in two versions (0.3KS40 and 0.6KS40) both with 88 newtons (40 lbs) of thrust but differing burn times of 0.3 and 0.6 seconds. The two versions provided the capability of propelling the 6 kg (13 lb) TADs to the approximate velocities of 10 and 20 meters

TAD SECTIONAL VIEW

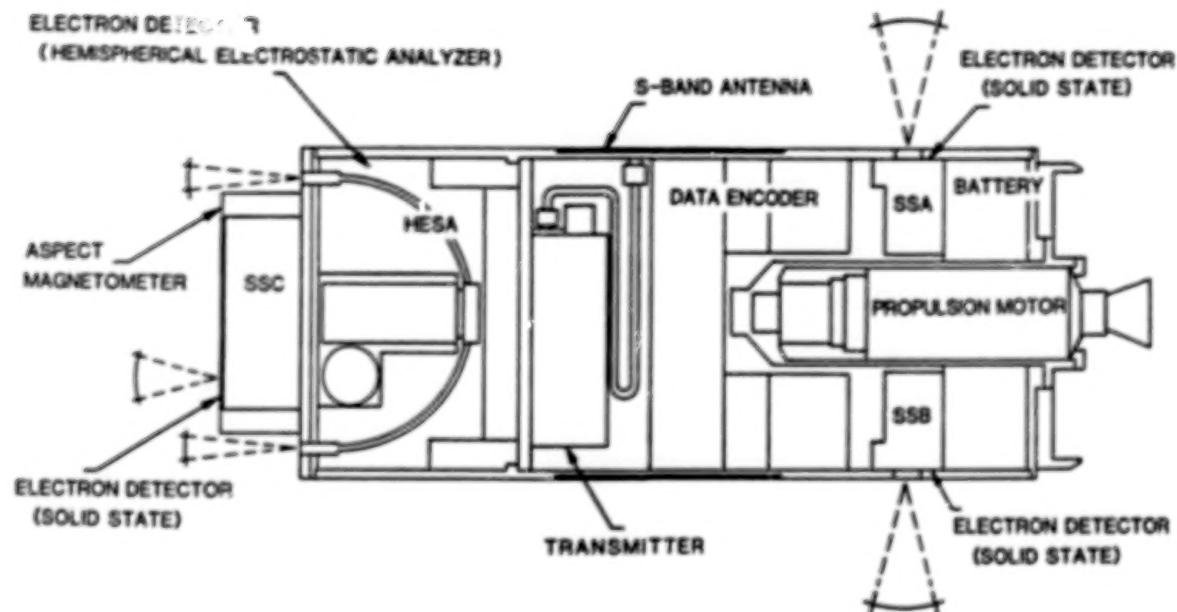


Figure 5. Echo 6 TAD Sectional View

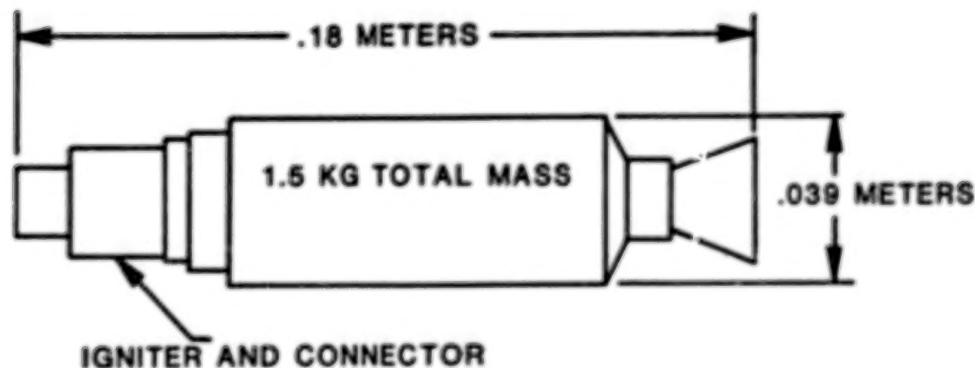
per second. The motors were 0.18-m long and 0.039 m in diameter with an igniter and connector on one end and a small exhaust nozzle on the other (Figure 6). Each motor had a mass of approximately 1.5 kilograms. A test firing of a flight type rocket motor was made at the GSFC propulsion test site, with some exhaust products being noted on the anchoring weights. Concern for the effect that the exhaust plume might have on the payload and undeployed TADs at flight altitude prompted further consideration.

The TAD S-band antennas were adapted from a design used for 0.13 m (5 inch) military projectiles. The antennas were installed as a band around the perimeter of the cylindrical TADs staying within a recess inside the TAD 0.14-m (5.5-inch) diameter thus allowing the TADs to slide smoothly in their launch tubes. The miniature S-band antennas were tested at GSFC to determine their radiation patterns and effectiveness.

To ensure that the TADs remained stable throughout their 300-second flight they were individually spin balanced at GSFC and then spun up in flight to approximately 8 rps prior to their deployment. Spinning reduced the effects of motor burn asymmetry, and balancing to a static limit of 2.0 ounce-inches and a dynamic limit of 5.0 ounce-inches squared kept their coning half angles to within 0.5°.

To spin-up the TADs, launch tubes were contained in the payload by a spool housing supporting two 0.15 m (6 inch) inner diameter sealed ball bearing raceways (Figures 7 and 8). This allowed both the launch tubes and the TADs latched within them to be spun by driving the launch tubes with timing belts connected to vacuum application electric dc motors.

TAD PROPULSION MOTOR



ATLANTIC RESEARCH CORP.
MARC 4C4
0.3-KS-40 AND 0.6-KS-40

Figure 6. Echo 6 TAD Propulsion Motor

On the rear of each spinning launch tube was a latching mechanism that retained each TAD until a bellows actuator was fired by a timing pulse. The bellows actuators not only unlatched the TADs but also activated micro switches that removed safety shorts from the rocket motor igniter leads. This action applied the power which was formerly applied to the actuator across the igniter leads. This technique produced a near simultaneous release of the TADs and ignition of their rocket motors. There were also safety shorting plugs on the rear of each launch tube which shorted out both the bellows actuators and rocket motors during integration.

To interface the functions of the TAD including turnon, checkout, and firing; a 10-band copper slipring with a redundant set of copper-graphite pick up brushes was mounted to the rear of each launch tube. This arrangement included a spring clip socket which the TAD contacted when latched in the launch tube. The flight turnon of the TADs was made through two redundant micro switches that were held off by the walls of the launch tubes. When the TADs exited the tubes these switches enabled the TADs to internal power.

K-band Doppler radar units were used for measuring the TAD velocities after deployment and ultimately their relative displacement as a function of time. The units, operating at 24.15 GHz, were directed at points along the TAD trajectories where the propulsion motors burned out to minimize the reflected noise created by the ionized exhaust. The beat signals resulting from the mixing of the incident radiation and the Doppler shifted reflected signals were tracked by phase lock loop circuits and recorded by TM counters. To increase the effective TAD radar cross section small copper corner reflectors were affixed to the aft end of the TADs.

ORIGINAL PAGE 19
OF POOR QUALITY

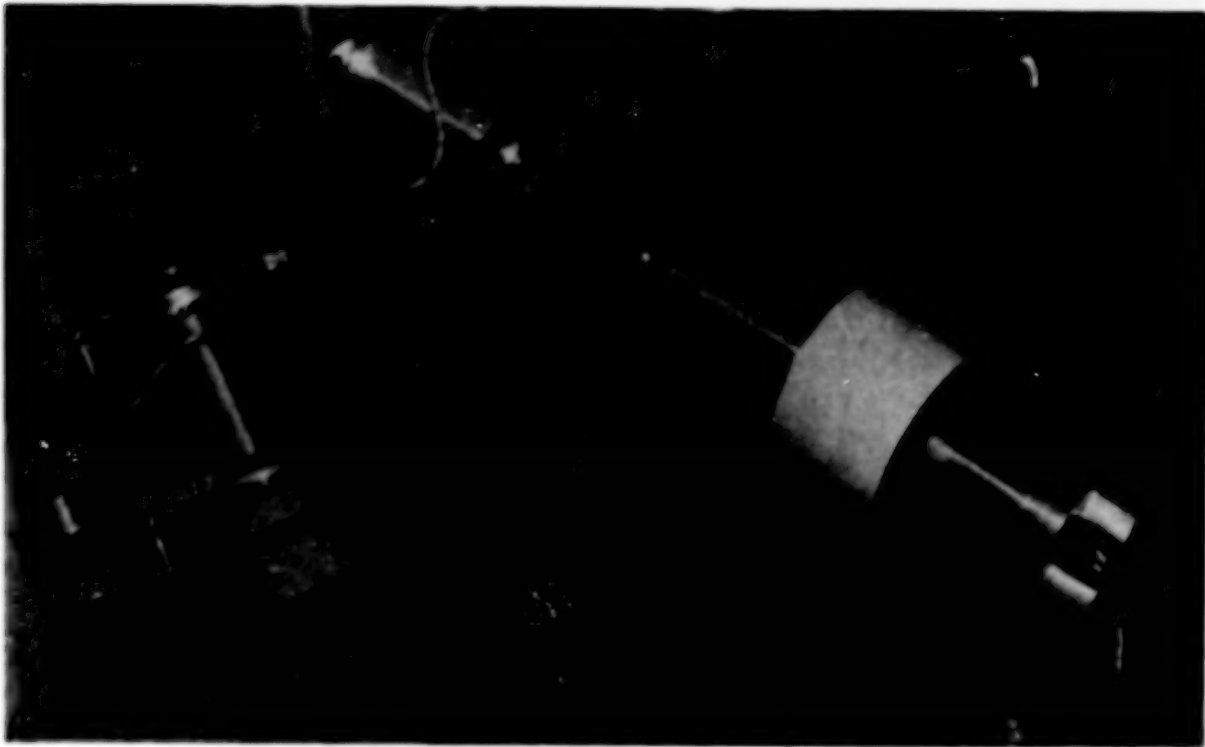


Figure 7. Echo 6 Spin-Up Assemblies with TAD

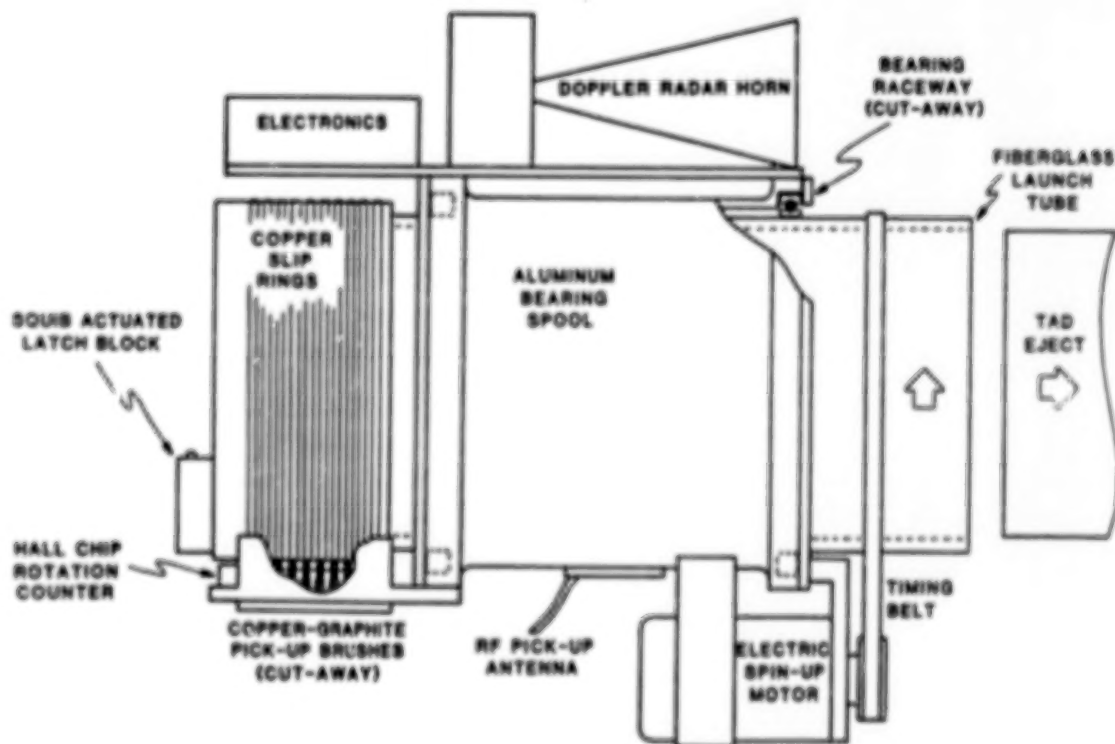


Figure 8. Echo 6 Spin-Up Assembly Sectional View

ORIGINAL PAGE IS
OF POOR QUALITY

Because each TAD has its own telemetry system complete with transmitter and antenna, it was necessary while on the launch pad to energize them and run signal checks while in the launch tubes. The radiation checks were accomplished by making the launch tube out of RF transparent fiberglass. To get the signal out of the rocket skin, a small pick-up antenna was positioned outside of the rotating fiberglass launch tube and the signal transferred through a length of coax cable to some RF BNC pullaways on the skin. This was, in effect, an RF slipring passing the signal to an external "cheater" antenna near the launch pad.

In the flight configuration four spin-up units with TADs were housed in the TAD section (Figures 9 and 10). This section consists of two ringed bulkheads connected by six longerons. Across two sets of these longerons were lightened plates to which the TAD spin-up units mounted. This construction was used because of the need for large openings on two opposite sides of the section. The front opening was to allow the TADs to exit and the other was used to vent the rocket exhaust and allow access for arming the motors before flight.

These openings were covered by doors held in place by a series of latch blocks on both sides bolted to latch bars. These blocks engage hooks on either side of the door. If either latch bar is pulled, the hooks release on that side and the door rolls off about the other side. If both sides were released simultaneously, the door simply moved out radially causing either a leading edge, a trailing edge, or a simultaneous release to occur. The latch bars were pulled by Horex 2900 linear actuators. The rest of the skin of the section which was not devoted to doors had removable panels to allow access to wiring and the latch system.

TEST PROGRAM

One of the first developmental tests of the TAD system was to establish the feasibility of using police radar units for the Doppler measurement of TAD velocities. A dummy TAD was built and powered by a Flight Systems Inc. series F model rocket motor. This motor has thrust characteristics very similar to the Delta spin motors at 1/1000 the cost. The TAD was put on a horizontal guide wire and the motor ignited. The TAD slid down the wire at speeds even exceeding the desired 20 mps and the radar successfully monitored the velocity. For the first spinning ejection test of the TAD and spin unit the model rocket motor was called upon again, assisted by a tether line and counterbalance weight as the TAD was vertically deployed.

Arrangements were also made to test fire a dummy TAD from the spinning launch tube in the 18-meter sphere at the NASA Langley Research Center. The sphere was evacuated, the TAD spun up, the radar turned on, and the firing sequence initiated. Viewing by high-speed cameras showed the TAD travelling very near to its theoretically calculated velocity with no visible evidence of an exhaust plume. The TAD also landed square in the net rigged for it. When the sphere was vented, no evidence of exhaust products was found and the sheet metal exhaust shroud was eliminated.

The integration test and evaluation program consisted of flight vibration, mass properties measurement, and a series of spinning deployments for the main payload and PDP. To begin with, a series of door deployment tests

ORIGINAL PAGE 19
OF POOR QUALITY

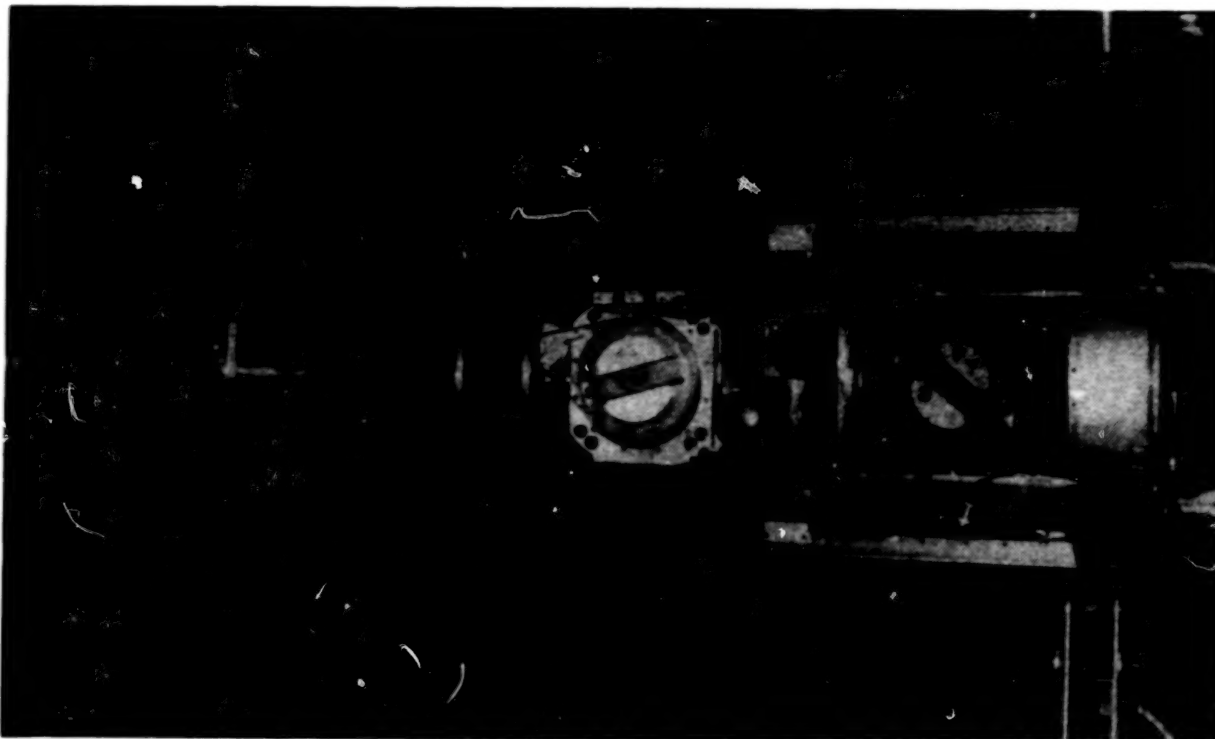


Figure 9. Echo 6 TAD Section Front View

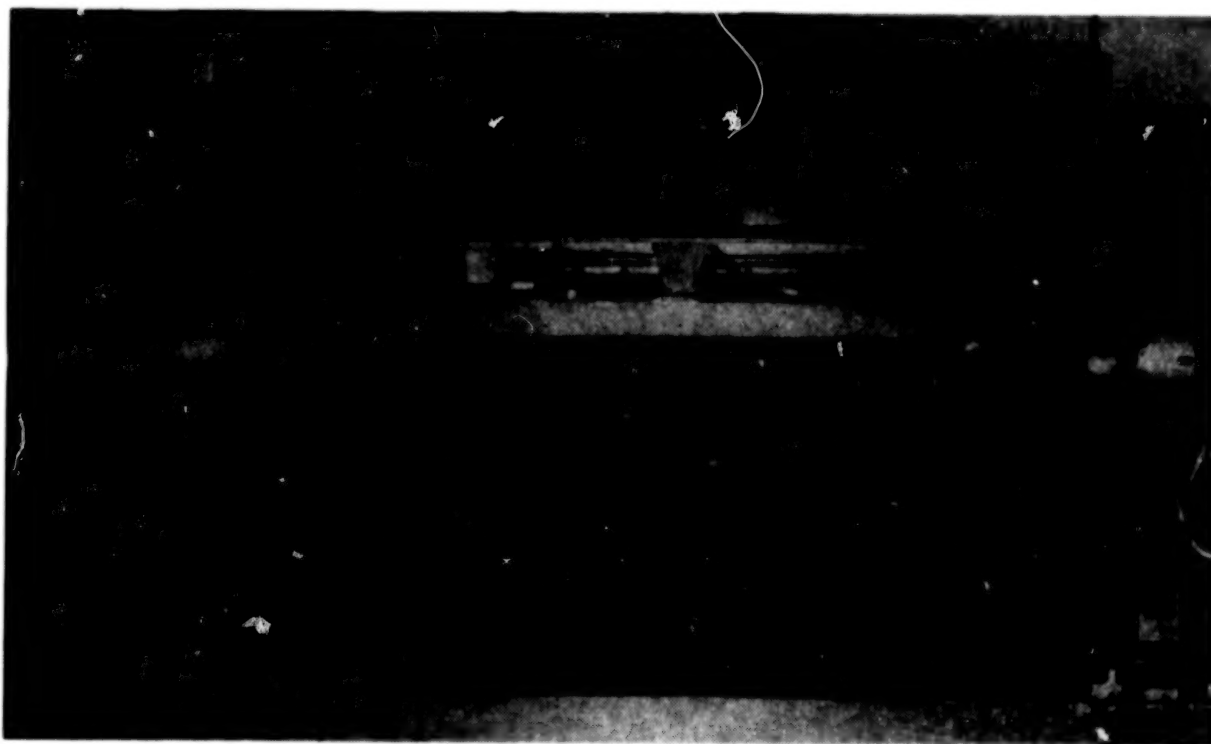


Figure 10. Echo 6 TAD Section Rear View

were conducted to verify the operation of the latch bar system and the three different modes of release. The payload was attached to a spin table and spun up to rates as high as 4 rps (maximum theoretical spin rate of vehicle), the squibs were fired, and the deployed doors were caught in a net. Closed circuit television was used to monitor the action.

The next series of tests were on the PDP. The first, boom deployment, was rather straight forward. The payload was spun up, the squibs fired, and the booms deployed on cue. Then came the spinning separation of the PDP from the accelerator section which was complicated by the requirement for zero gravity simulation. The usual test procedure is to use a counterweight to a line running over a pulley and down to the ejected payload. This method is not suitable for a spinning payload with several 'g's of acceleration. To solve the spin problem, a special low-friction swivel developed for a high altitude parachute was used. This swivel has some belleville washers to unload the bearing under high loads. These washers spring out of the way under low loads to let the low-friction, light-duty bearing spin freely. This free spin was needed on the counterbalance line because of the necessity of avoiding any relative spin between the PDP and the accelerator section. The 2.5 'g' acceleration of the PDP was nullified by running the line through a 3:1 pulley arrangement and by using a counterbalance weight three times that of the PDP. A one-way block was used to snub the system. The deployment test itself, went smoothly. The nose cone had an initial acceleration of 13 'g's. To counteract this, during testing a length of surgical rubber bungee was added to the system to remove the slack from the line during the initial acceleration.

FIELD OPERATIONS AND LAUNCH

The 2 month long, detailed integration of the Echo 6 payload at GSFC culminated with the shipment of the payload and the travel of over 45 support personnel to the Alaska launch site. In February, all the Echo 6 equipment arrived at Poker Flat and the payload was prepared for launch. After the payload had been built up and the experiments given a checkout, the payload was taken to the motor preparation building and mated to the Black Brant sustainer. There the TAD rocket motors were installed with safety shorting plugs attached. The payload with sustainer was then taken to the launch site and combined with the Terrier booster that had been suspended on the launch rail earlier. After completing prelaunch checks, the payload was armed for flight by removing the safety plugs from the back of each TAD, removing all other safety screws and arming the 'g' timers. The deployable doors were reinstalled and secured. Subsequent to a series of delays caused by weather, electrical and mechanical problems, and some minor damage to the launch vehicle, Electron Echo 6 was launched at 06:59:51 on March 30, 1983 UT with the desired launch criteria and geophysical conditions being met.

CONCLUSION

The flight of Echo 6 was mechanically flawless, even in intimate detail. The vehicle propelled the payload to a near nominal trajectory with the predicted final roll rate. The ACS performed its maneuvers to better than its tolerance specifications. The PDP deployment was executed with the proper spin rate and separation velocity. The electric field booms were deployed perfectly. The TAD section doors were ejected, the TADs spun up, fired, and deployed with the Doppler radar measuring their velocities. The main payload

electron accelerator was started on time and injected electrons at the anticipated power according to the preset programmer. The scientific instrumentation on all the sections performed nominally with the six telemetry links from the main payload and free-flyers transmitting, being received, and recorded with excellent signal-to-noise characteristics. In summary, it may be said that the Echo 6 mission performed as anticipated and that the instrumentation made all of the measurements necessary for investigating the major scientific objectives.

This endeavor involved 10's of man years of effort and covered 1 month short of 3 years from inception to launch. The overwhelming success of the mission is a testimony to the extensive cooperation and dedication of the groups involved: NASA Headquarters, NASA/Goddard Space Flight Center, University of Minnesota, General Electric MATSCU, University of New Hampshire, NASA/Wallops Flight Facility, Poker Flat Research Range, University of Alaska, Physical Science Laboratory NMSU, Bristol Aerospace, and numerous other scientists, engineers, contractors, technicians, machinists, and suppliers.

The scientific data analysis is vigorously underway with many exciting results being investigated and reported.

N84

25095

UNCLAS

D17

N84 25095

SEPARATION AND STAGING MECHANISMS FOR THE INDIAN SLV-3 LAUNCH VEHICLE

M. K. Abdul Majeed, K. Natarajan, and V. K. Krishnankutty*

ABSTRACT

This paper describes a unique separation and jettison system for the ascent fairing and a staging system for the apogee motor of the first Indian satellite launch vehicle. Design features, development problems, and mission constraints are discussed in addition to the solutions adopted. A qualification summary is included for each system, and flight results obtained from SLV-3 launches are described.

I. SEPARATION AND JETTISON SYSTEM FOR THE ASCENT FAIRING

INTRODUCTION

The Indian satellite launch vehicle (SLV-3) is a four-stage, solid-propellant space vehicle capable of putting a 50 to 60 kg payload in low-Earth orbit. The ascent fairing, protecting the payload and its apogee motor, must be separated and jettisoned from the vehicle at an altitude of 90 to 100 km during the coasting phase of stage 2. The fairing, a hemisphere-cone-cylinder configuration, is 2.45-m (96-in) long and 0.8 m (31.5 in) in diameter. The material is a phenol-glass honeycomb sandwich of 14.5-mm (0.57-in) thickness.

The separation and lateral jettison system for the fairing is a cold-gas-actuated, hydropneumatic system. The principal components are: four latch modules, two nitrogen gas bottles, high pressure lines, check valves, and tube fittings. A groove joint with spring thrusters was selected for the circumferential separation interface.

MISSION SPECIFICATIONS

For the SLV-3, the following specifications were placed on the fairing release and jettison system:

- The system must ensure collision-free separation from the vehicle during stage 2 motor coast phase at an altitude of 90 to 100 km
- A minimum jettison velocity of 1.5 mps (4.92 ft/sec) will be provided
- Allowable disturbance to upper stage must be ≤ 0.5 deg/sec

*Vikram Sarabhai Space Centre, Indian Space Research Organization, Trivandrum, India

- No contamination or debris is permitted
- System pyros will initiate on an electrical command of 2 Amps with 10-ms duration through snapoff from vehicle
- System weight should be ≤ 18 kg and the fairing interface joint must react vehicle loads
- Because the vehicle assembly must be mounted horizontally in the launcher, the fairing must have load capability in the horizontal position
- A reliability of 0.985 at a confidence level of 85 percent must be demonstrated
- Orientation of the fairing separation plane will be 90° to the vehicle pitch axis and 45° to the launch tower

A combination of four latch mechanisms to clamp the fairing along the longitudinal split line and a circumferential groove joint for the vehicle interface were selected (Figure 1). Separation mechanisms currently available are of a wide variety. A choice was made after extensive evaluation of the merits and demerits of candidate systems. Because a single point actuation and multipoint release system has the highest reliability, the choice was narrowed to a single point actuation of the four latch mechanisms.

The actuation system consists of high pressure nitrogen gas bottles opened by a pyro valve. On initiation, the gas pressure is conveyed to the latch mechanisms through high pressure lines. This gas pressure provides the necessary force at the latching mechanisms to cause release, thereby freeing the fairing halves along the longitudinal splitline.

The joint at the vehicle circumferential interface is shown in Figure 2. This consists of a groove joint--the female groove provided on the fairing end rings, and the corresponding male configuration on the vehicle. This passive separation interface does not require additional release mechanisms. Springs are provided both in the latching mechanisms and groove joint for jettison. At release, the springs impart a lateral velocity of 1.9 mps to each of the fairing halves.

Redundancy has been incorporated in the actuator design by providing two nitrogen gas bottles and by isolating them in the pneumatic circuit by in-line, nonreturn (check) valves. The pressure feed lines are filled with hydraulic oil, MIL-H-5606D, from the check valve onwards for improved event timing.

TECHNICAL DESCRIPTION

The release and jettison system has the following principal subsystems:

- Latch system with springs
- Gas bottle with pyro valve
- Groove joint with springs

ORIGINAL PAGE 19
OF POOR QUALITY

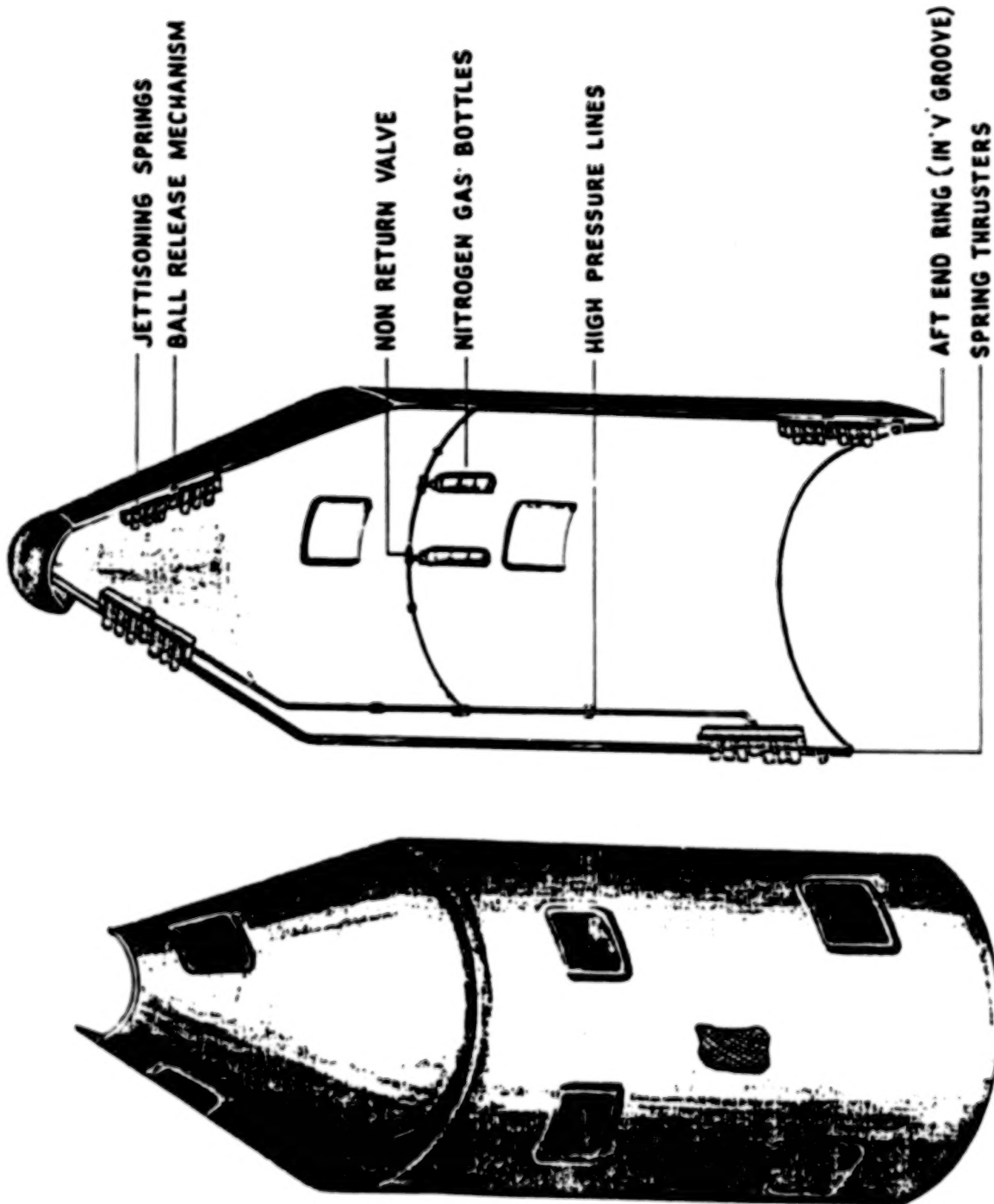


Figure 1. Heat Shield Separation and Jettisoning System Configuration

ORIGINAL PAGE 19
OF POOR QUALITY

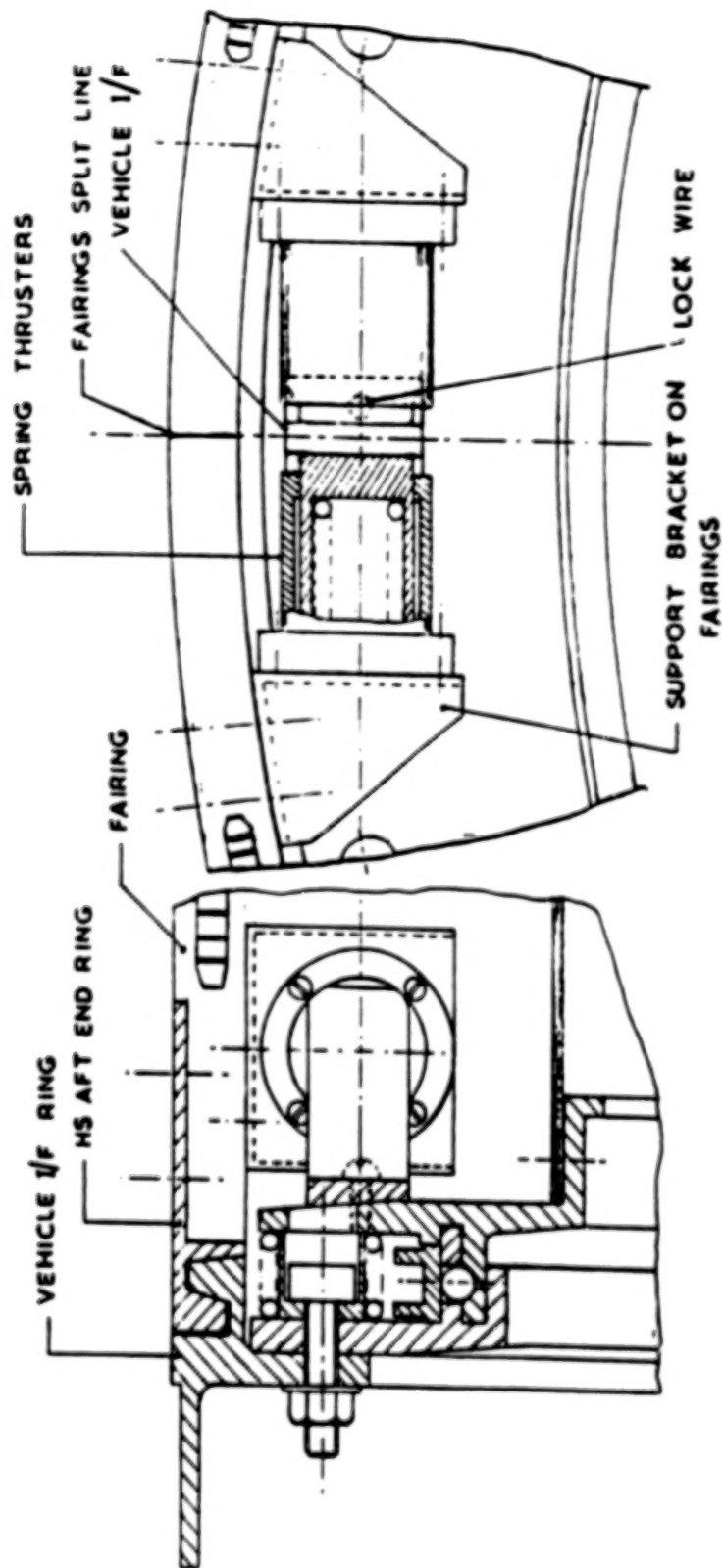


Figure 2. Groove Joint Assembly

Latch System with Springs

The latch system, shown in Figure 3, consists of a ball release mechanism (BRM), and six spring thrusters. Open coiled helical compression springs of 22-mm OD and spring rate of 76.5 N/cm (43.6 lb/in) are used. The springs are arranged symmetrically, three on each side, and a telescopic mechanism is used for loading/unloading. Aluminum alloy angle sections closed at both ends are used as the principal top and bottom latch housings for mounting the units. The housings are provided with floating plate nuts to allow for fastening from outside the fairing, and to accommodate any hole misalignment. The latch, a preloaded assembly, is installed as a module to join the two fairing halves.

The BRM consists of a stud, a hexagonal housing, a spring, and an M-10 bolt for fastening. A piston moving inside the stud is locked by three balls extending through three radial, equally spaced holes drilled in the stud. These steel balls, which project from the stud outside diameter in the locked condition, are seated inside the hexagonal housing. Three 90° conical seats are provided, 120° apart, on the inside bore of the housing. In the locked condition, the housing and the stud of the BRM act as an integral unit and can be bolted to the aluminum alloy housing. On release, initiated by the forward motion of the piston, the balls recede radially inward and their external projections disappear, thereby releasing the bolted hexagonal housing. The balls are contained in the stud on the piston recess and the ball retainer spring prevents their escape. The jettison spring thrusters are bolted to the bottom latch housings and on release impart the required jettison velocity to the fairing halves. The individual thruster spring compressions can be adjusted with close tolerance to maintain the mating plane at the top latch housing. The springs are closely matched with +3 percent tolerance on stiffness. By suitably matching the springs during assembly, the effect of differential force is reduced.

Gas Bottle with Pyro Valve

The gas bottle consists of a cylindrical shell that is 75 cu cm in volume and 40 mm in diameter, with one end spherical and the other end open. The material is aluminum alloy, AA-6351. A releaser that also serves as a filling adapter is screwed into the open end of the bottle. This releaser incorporates a diaphragm that is punctured by a pyro valve. Nitrogen gas at 15 MPa is filled through the releaser filling port.

Groove Joint with Springs

The circumferential groove joint is shown in Figure 2. The female groove is provided in the aft end ring of the fairing and the male groove at the vehicle interface ring. Both rings are made of AISI 4340 alloy steel forged and machined. The joint is dry lubricated with molybdenum disulphide for easy

ORIGINAL PAGE 19
OF POOR QUALITY

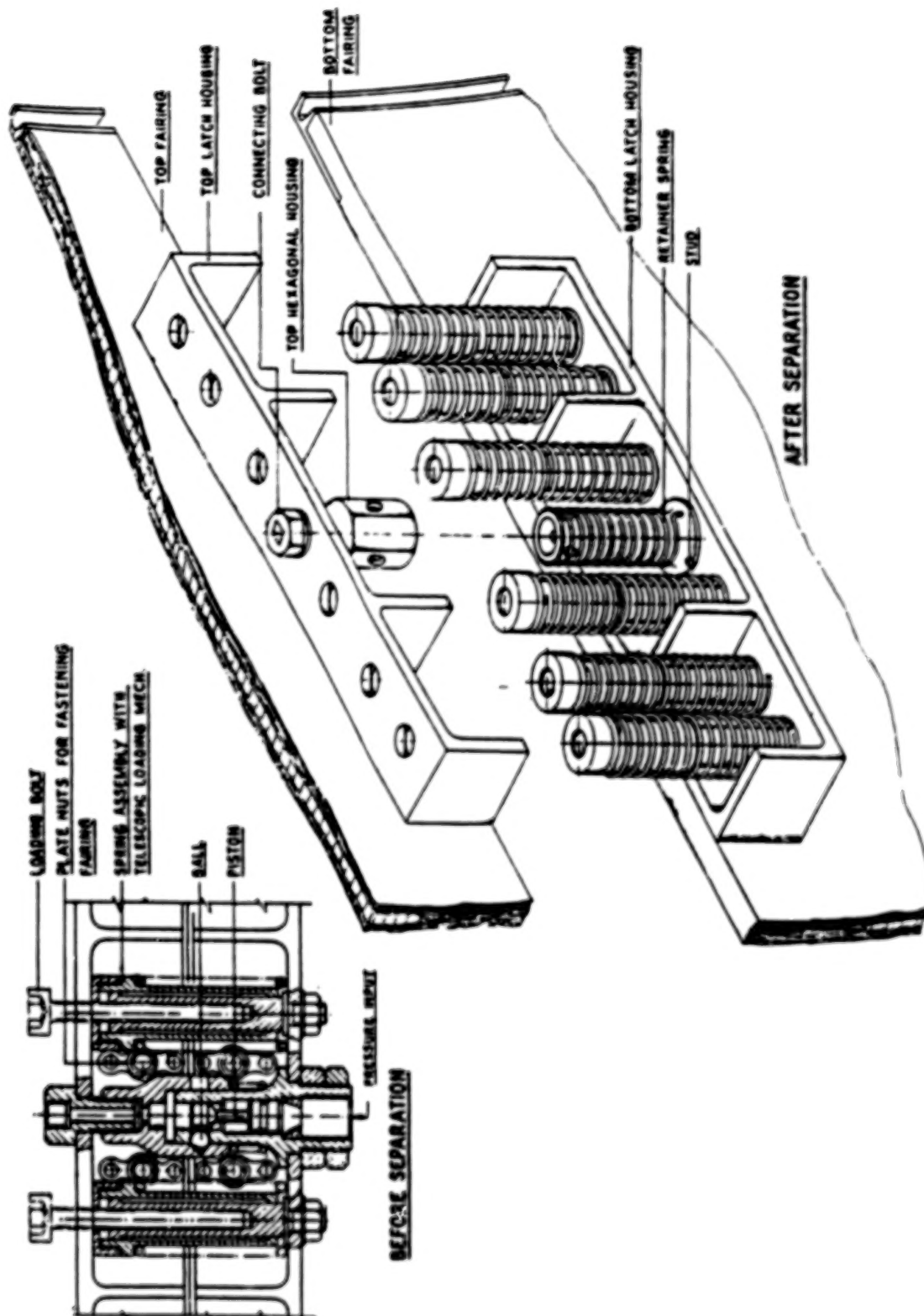


Figure 3. Latch System

assembly and jettison. Four spring thrusters are located at the split plane. These thrusters impart lateral thrust to the fairing halves with respect to the vehicle. After the fairing is assembled to the vehicle, the thrusters are preloaded by removal of a lock wire.

SYSTEM PERFORMANCE

Separation and Jettison System

This system performed as expected, developing a jettison velocity of 1.65 mps (5.4 ft/sec) within an action time of 19 ms. The total system weight was 15.7 Kg. The shock caused by jettison was recorded to be less than 5 g. The latch module had release pressures ranging from 2.8 to 4.0 MPa. The total force exerted by the six thruster springs are 1750 N with a net compression of 38 mm on release. The balls of the BRM are arrested by the retainer springs, thus ensuring no free-flying debris. Figure 4 shows an action photograph of the fairing jettison. Figure 5 shows the latch assembly before and after release.

Pyro Valve

The pyro valve is piston actuated to puncture the aluminum alloy diaphragm of the gas bottle. The functional delay of the valve was within 10 ms. The actuating pressure cartridge had a single initiator and dual bridge wires with the following electrical characteristics:

- No fire current--500 mA; 5-min duration
- All fire current--1 A 50-ms duration
- Recommended firing current--2 A; 10-ms duration

The valve, which was tested to establish a reliability of 0.975 at 85 percent confidence level, is a totally contained system.

Groove Joint with Springs

The groove joint was 800 mm (31.5 in) nominal diameter and was structurally tested to the following loads:

- Bending moment--15,000 N-m
- Axial load--23,000 N
- Shear force-- 6,500 N

The total spring force for each fairing half, acting on this joint, was 270 N. The springs were located 60 mm (2.36 in) from the fairing split plane.

Nonreturn Valve and Compression Tube Fittings

A standard nonreturn valve for 6.35-mm diameter tubing was used in the penumatic circuit. The valve had a rated pressure of 21 MPa and a crack-

ORIGINAL PAGE 19
OF POOR QUALITY

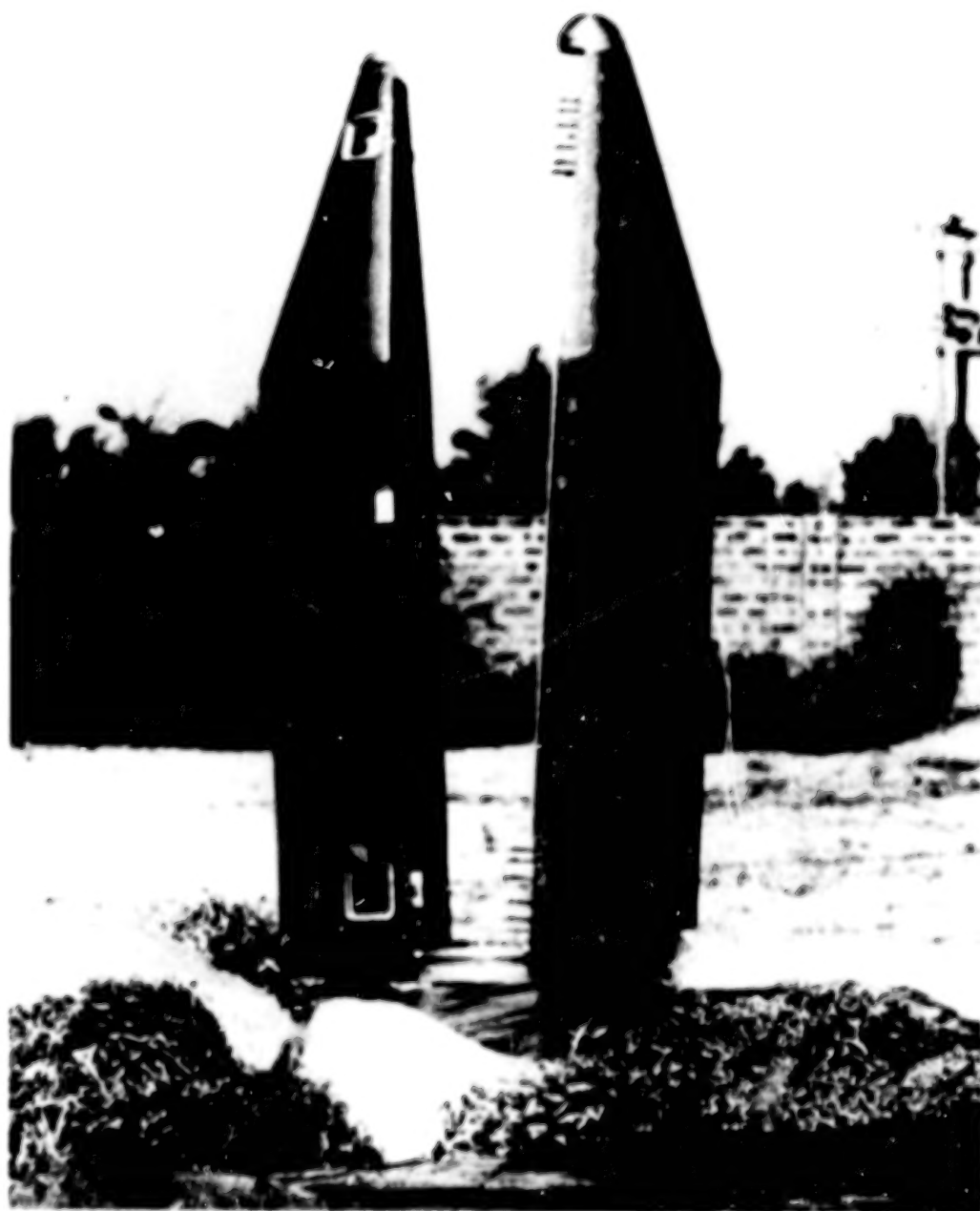


Figure 4. Heat Shield Fairing Jettisoning--In action (1 g condition)

ORIGINAL PAGE 19
OF POOR QUALITY

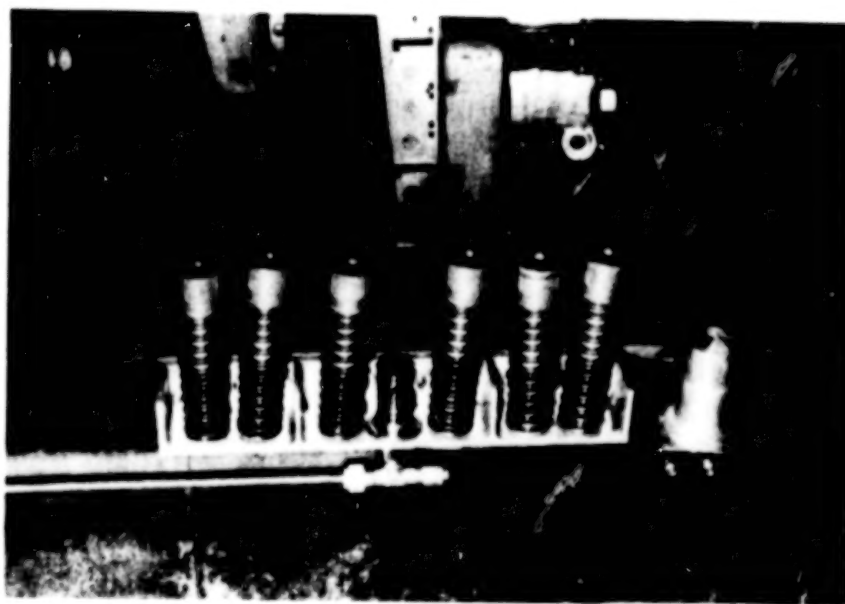
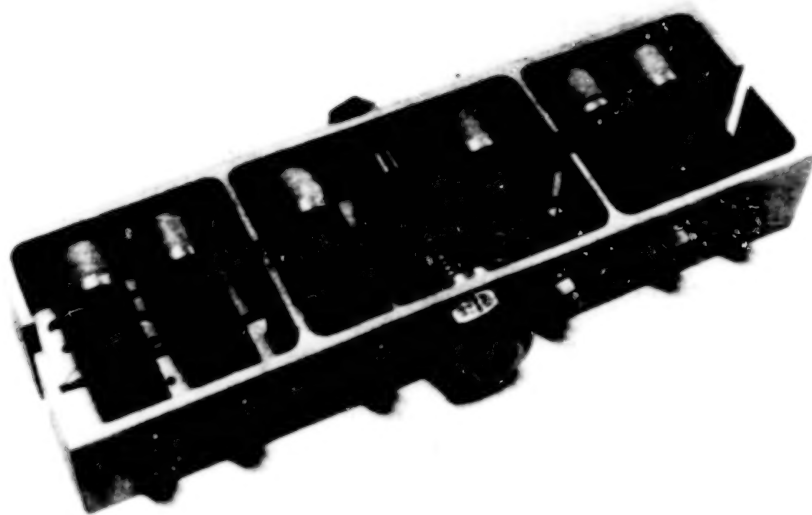


Figure 5. Latch Assembly

ing pressure of 7×10^{-5} Pa. Single ferrule compression tube fittings of ells, tees, and straight connectors were used at the joints of the tubing.

DEVELOPMENT PROBLEMS

Development problems encountered in this system were:

- Achieving precision fabrication of the BRM
- System functional test failures during the initial phase
- Matching of resultant force and center of gravity of FRP fairings

Elaborating on the first problem, the BRM fabrication required high precision, especially in locating the ball-seating holes which carried angular tolerances of ± 5 arc-mins on the 120° spacing. A drilling fixture precise within ± 30 arc-secs was necessary to achieve this. In addition, the inside piston, a moving part, is of case-hardened steel, with a hardness of 55 to 60 Rockwell "C" scale. The piston required concentricity to within 20 microns. Attempts at achieving this precision by grinding on the outside diameter resulted in a high rejection rate. Finally, critical dimensions on the BRM housing required grinding the external flat surfaces. The dimension across the flats was toleranced to 30 microns. This was necessary because the flats served as a reference to control the depth of the ball seating.

The first few functional tests failed because of asynchronous release of the fore and aft latch pairs. Investigation revealed time delays on the order of 20 to 40 ms, which caused the forward pair to release first and the aft pair to fail to release. This time delay was a result of the spring load of the forward pair being transmitted to the aft pair. Because of the load increase on the aft pair, the pressure was insufficient to produce release. Initially, gas bottle pressure was only 7 MPa (70 bars). Two solutions were implemented:

- Reduction of relative release delays of the two pairs of latches by adjusting the locations of the pressure input point
- Increase of actuation pressure to 15 MPa which further reduced the relative delay.

Another problem encountered was the large uncertainty in the location of the center of gravity (c.g.), inherent with FRP fairings. Because of the nature of the groove joint, the resultant force vector is required to pass through the fairing c.g. within a tolerance of $\pm 0/-15$ mm. Location of the resultant force vector above the c.g. would not result in separation, so ballasts were added to adjust the c.g. within the design limits.

RELIABILITY MODELLING

A fairing reliability requirement of 0.985 with 85 percent confidence level was specified by the mission. Apportioning this reliability between

the structure and separation-jettison systems, structural performance should be demonstrated to a reliability of 0.995 and jettison to a reliability of 0.985. The overall confidence level was apportioned according to the following model law:

$$(1 - C) = (1 - C_s) (1 - C_g)$$

where

C = Overall system confidence level

C_s = Structural confidence level (including thermal)

C_g = Separation and jettison system confidence level

Accordingly, the system confidence level of 0.5 was arrived at after fixing the structural level at 0.7. This required that 34 jettison system tests be performed successfully. To satisfy this requirement, the system has undergone 40 successful jettison tests.

QUALIFICATION TESTS

System qualification tests are divided into three categories: functional, structural, and environmental. Table 1 shows the test summary. Table 2 shows the test levels used for environmental simulation. The fairing, after undergoing vibration and shock tests, was functionally tested for jettison. The performance proved normal. A typical one-g trajectory plotted from high speed movie data is shown in Figure 6.

FLIGHT TEST QUALIFICATION

The system was qualified in four flight tests of SLV-3. The system performed successfully in all flight tests. The performance was monitored by means of telemetry from microswitches at each latch, event monitors, and snap-off plugs. The vehicle disturbance rates were within specifications, and the system performed normally.

II. BALL LOCK MECHANISM AS A STAGING SYSTEM FOR APOGEE MOTORS

INTRODUCTION

The apogee motor of the SLV-3 and a satellite weighing 400 kg (881.8 lb) were to be separated from the spent third stage at an altitude of 400 km (248.6 mi). This procedure required that the interstage connecting the apogee motor be axially separated without any collision.

Because of mission constraints on the SLV-3 vehicle, it was required that the separation system impart minimal separation disturbances and a differential velocity of 1 mps while releasing no contamination or debris.

Table 1
Qualification Test Summary

No.	Type of Test	No. of tests	Result	Remarks
1	Functional at • 1 g condition	40	Successful. Velocity 1.65 mps	Jettisoning velocity measured & verified with prediction
	• 0 g condition	3	do	Falling platform facility is used*
2	Structural test	3	Normal	Verified joint rotation of groove joint 1.5×10^{-9} rad/Nm**
3	Environmental tests • Vibration • Shock	3 3	System functioned normal	
4	Flight tests	4	do	Disturbance rates 0.34 deg/sec

*A facility having a platform fall freely guided by columns, thus simulating '0' g

**Improves good category beyond 30 percent of test loads

Table 2
Vibration and Shock Test Levels

Type	Axis	Freq. range	Level	Sweep rate
Sine	ZZ	10 to 50	1.2 mm DA	20 oct/min
	XX & YY	50 to 100 Hz	6 'g'	
		10 to 80 Hz	0.2 mm DA	20 oct/min
		80 to 1000 Hz	2.7 g	
Type	Duration	Band width Hz	PSD g^2/Hz	G rms
Random	2 min	20 to 35	0.0024 to	6.9 g
XX ZZ		350 to 1350	0.04 uniformly	
Axis	2 min	1350 to 2000		
XX & YY		do	0.003 to	7 g
			0.04 uniformly	
Shock pulse-half sine wave	ZZ axis	100 Hz	Shock test level 40 g $\pm 10\%$	3 shocks

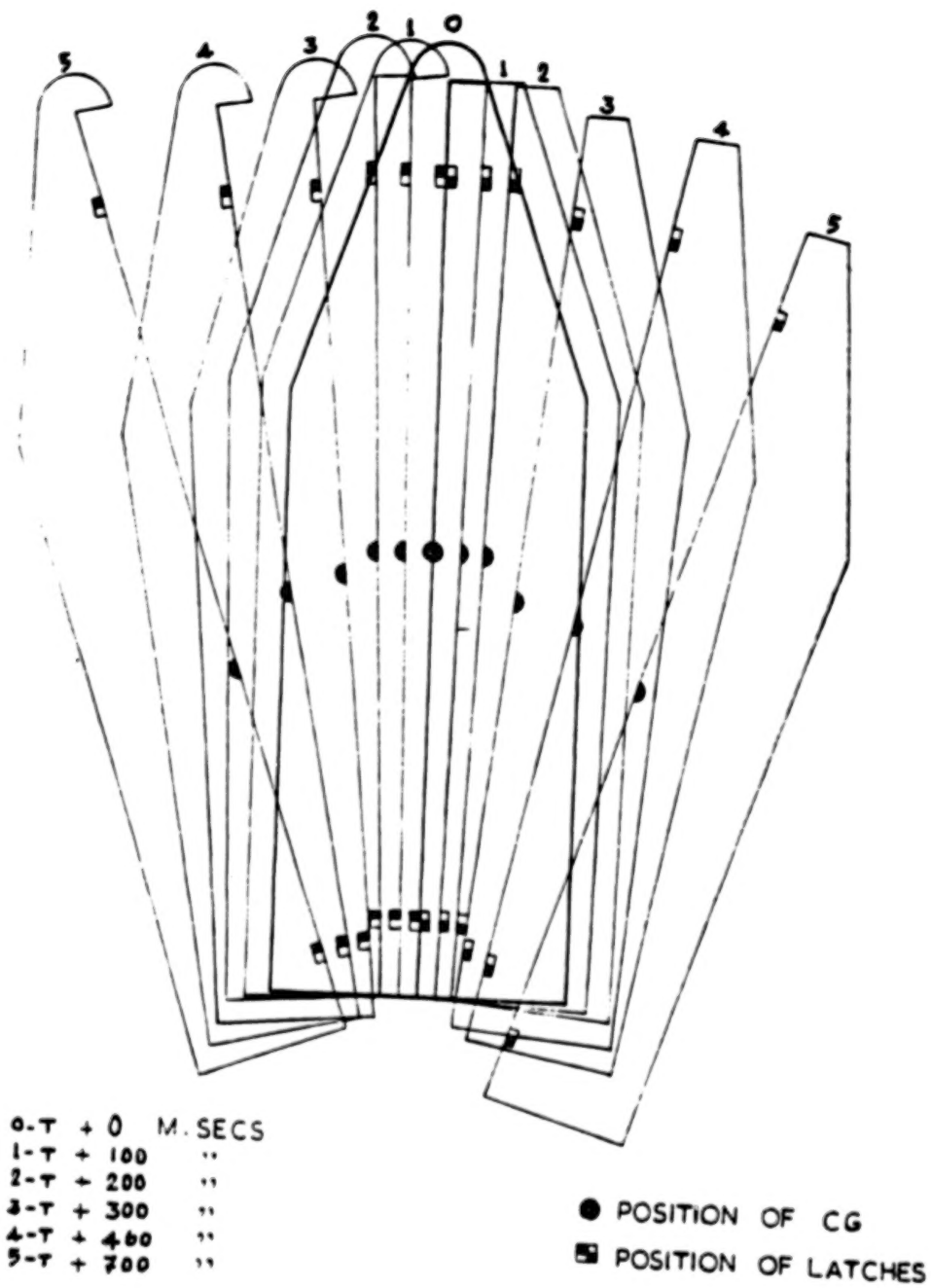


Figure 6. Trajectory of Separated Fairings

A ball lock mechanism was selected as a staging device for this application. The choice was based on its proven reliability on 560-mm (1.84-ft) diameter sounding rocket flights and various trade studies for achieving highest system reliability.

MISSION SPECIFICATIONS

The SLV-3 required the following third stage separation system specifications:

- The system should ensure clean, collision-free separation from the vehicle during the stage 3 motor coast phase
- The system should function at an altitude of 390 to 400 km (242 to 286 mi)
- A minimum of 1 mps (3.3 ft/sec) relative axial velocity is to be provided
- Tipoff rates imparted to the upper stage during separation should be <0.5 deg/sec
- No contamination or debris is permitted
- The system pyros must initiate on electrical command through snapoff from the vehicle (recommended firing current is 2 A for 10 ms)
- The system should meet a reliability of 0.995 at an 85 percent confidence level
- As a structural joint it should be capable of withstanding flight loads and environmental conditions
- The system must be located between the aft end ring of the apogee motor and the forward end ring of the interstage structure
- Size
 - Inner diameter--648 mm (25.5 in)
 - Outer diameter--767 mm (30.2 in)
 - Length--48 mm (1.9 in)
- Allowable weight--7 kg (15.4 lb)
- Electrical interface
 - The mechanism must accommodate six snapoff connectors oriented symmetrically about the vehicle pitch axis

TECHNICAL DESCRIPTION

The ball lock system is shown in Figures 7 and 8. The system consists of upper and lower stage adapter rings held together by steel balls which in turn are held by a retainer ring. The retainer ring is provided with escape holes for the balls. In the locked condition, the holes in the retainer ring are given an angular offset. During release, the retainer ring is rotated by two pyro thrusters (one for redundancy), nullifying the offset. The pyro thrusters are initiated by pressure cartridges on electrical command from the central sequencer of the vehicle. Retainer ring rotation is limited by a stopper.

Helical compression springs positioned between the flanges impart the required differential velocity. The lower stage (outer) ring is provided with

ORIGINAL PAGE IS
OF POOR QUALITY

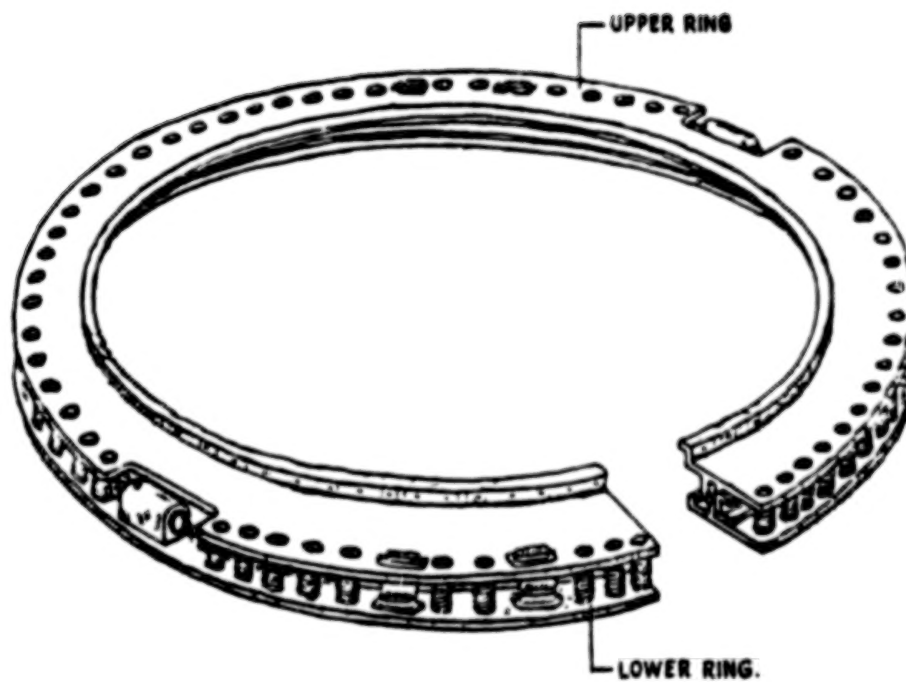


Figure 7. Ball Lock Mechanism Before Separation

ORIGINAL PAGE 19
OF POOR QUALITY

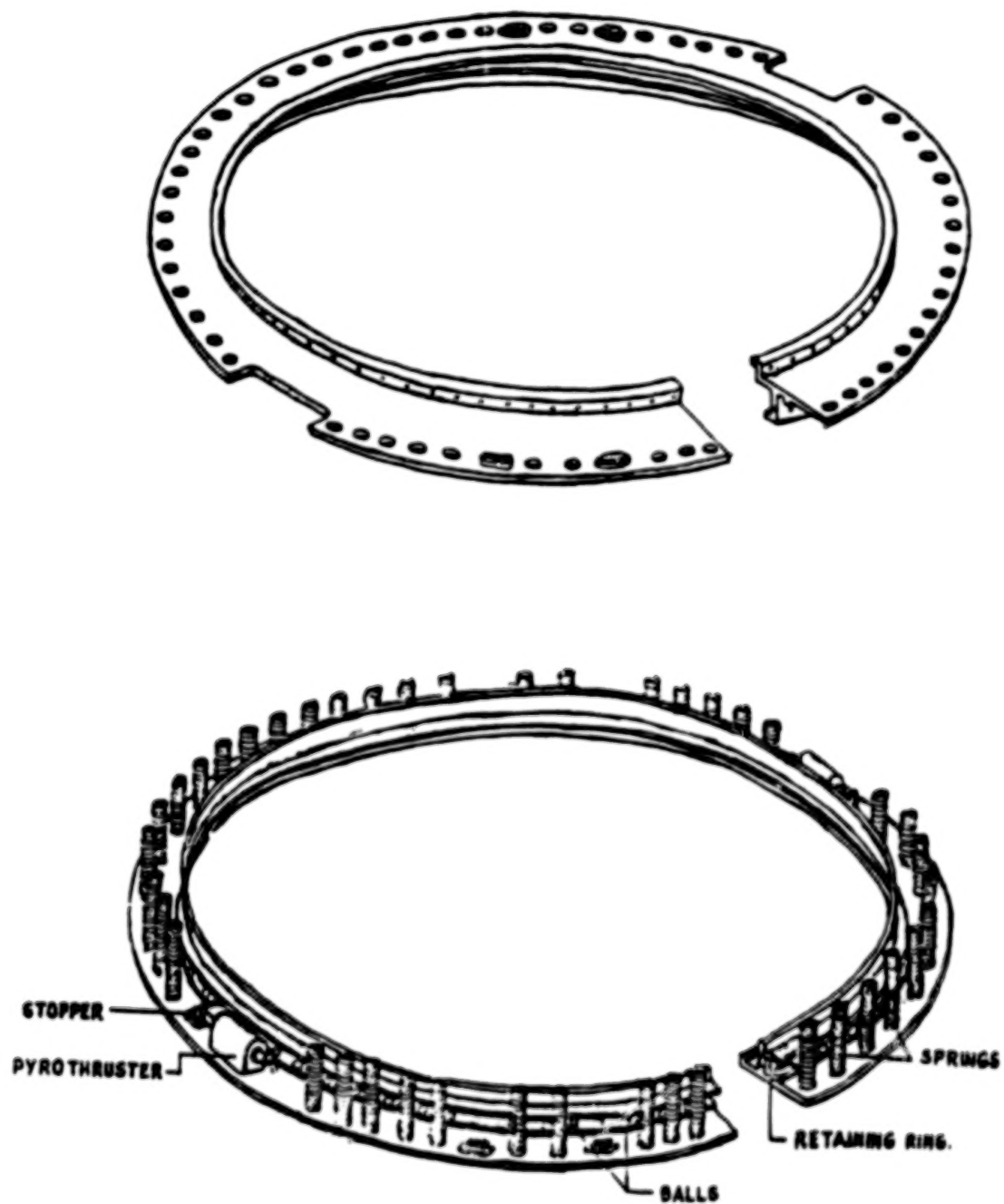


Figure 8. Ball Lock Mechanism After Separation

through holes for the balls in the locked condition and the upper stage adaptor ring is provided with conical ball seats. The radial component of the spring force pushes the balls outward and releases the inner ring, thus ensuring a clean separation.

The adaptor flanges have provisions for fastening the upper and lower flanges. In the locked position, the retainer ring is held positively by shear screws to prevent accidental rotation caused by shock, vibration, and other vehicle loads. The pyro thruster is a piston-cylinder type. The piston provides the necessary ring rotation force through pressure developed by the cartridges inside the cylinder (Figure 9).

DESIGN CONCEPTS

The system was designed for 1.4 times the maximum anticipated flight bending moment. The sections were designed for bending, axial, and shear loads. A margin of safety of 1.5 to 2 was built into this design. The number of balls was selected based on the load on each ball and the corresponding contact stress induced on the conical ball seats. The load on each ball was evaluated from:

$$\begin{aligned} M_u &= \sum F_n \gamma_n^2 \\ &= \sum F_n r^2 \sin^2 \theta_n \end{aligned}$$

where

F_n = Force on the n^{th} ball contact

θ_n = Circumferential angle made by the n^{th} ball

The contact stresses were evaluated based on the coefficient of friction between the aluminum alloy and steel. The joint stiffness was predicted by determining contact deflection. Table 3 shows the calculated deflection and joint rotation.

The functional design was determined by finding the net radial outward component caused by spring force on the ball acting on the retainer ring (Figure 10). The net torque required to rotate the ring is the sum of all the radial component forces multiplied by the friction coefficient between the steel ball and the retainer ring. Because these components are made of hardened steel (the ring hardness is 30 to 35 Rockwell "C" scale), the indentation was very low (0.01 mm) and the friction coefficient was assumed to be in the 0.08 to 0.10 range. The shear screw in the pyro thruster provides functional safety for any accidental release.

ORIGINAL PAGE IS
OF POOR QUALITY

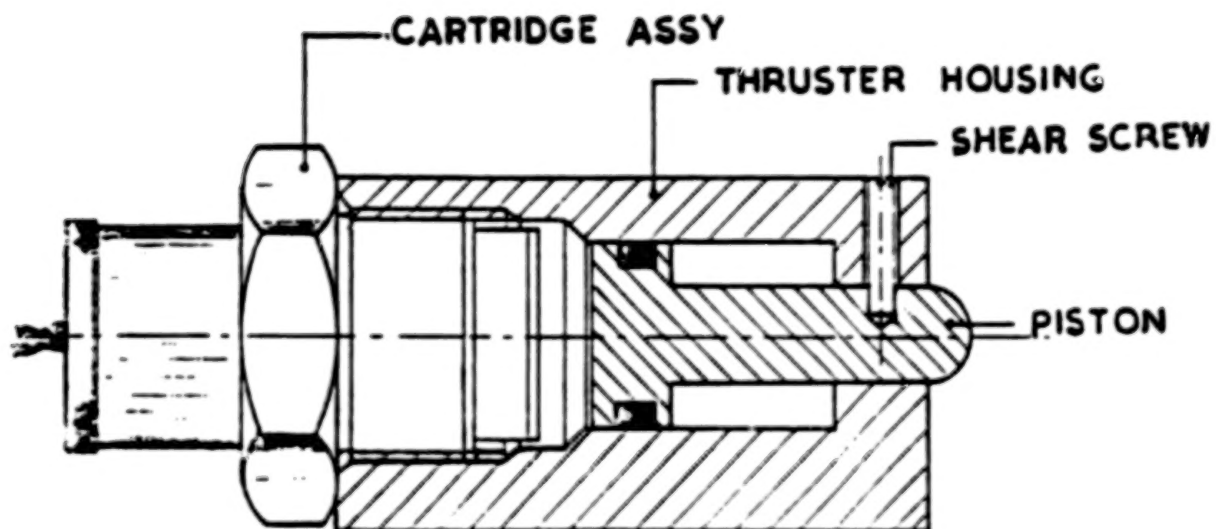


Figure 9. Pyro Thruster

Table 3
Contact Surface Deflections

θ in degrees	Radial distance in mm (inch).	Deflection in mm (inch).	Rotation in radians
90	327.00 (12.87)	0.05559(0.00219)	0.0001700
84	323.43 (12.73)	0.05519(0.00217)	0.0001706
78	312.86 (12.32)	0.05399(0.00213)	0.0001726
72	295.77 (11.64)	0.05203(0.00205)	0.0001759
66	272.90 (10.74)	0.04933(0.00194)	0.0001808
60	245.25 (9.66)	0.04599(0.00181)	0.0001875
54	214.02 (8.43)	0.04204(0.00166)	0.0001963
48	180.59 (7.11)	0.03758(0.00148)	0.0002080
42	146.41 (5.76)	0.03272(0.11129)	0.0002235
36	112.97 (4.45)	0.02757(0.00109)	0.0002440
30	81.75 (3.22)	0.02227(0.00088)	0.0002724
24	54.10 (2.13)	0.01695(0.00067)	0.0003133
18	31.22 (1.23)	0.01180(0.00046)	0.0003780
12	14.14 (0.56)	0.00699(0.00028)	0.0004943
6	3.57 (0.14)	0.00280(0.00011)	0.0007843

ORIGINAL PAGE IS
OF POOR QUALITY

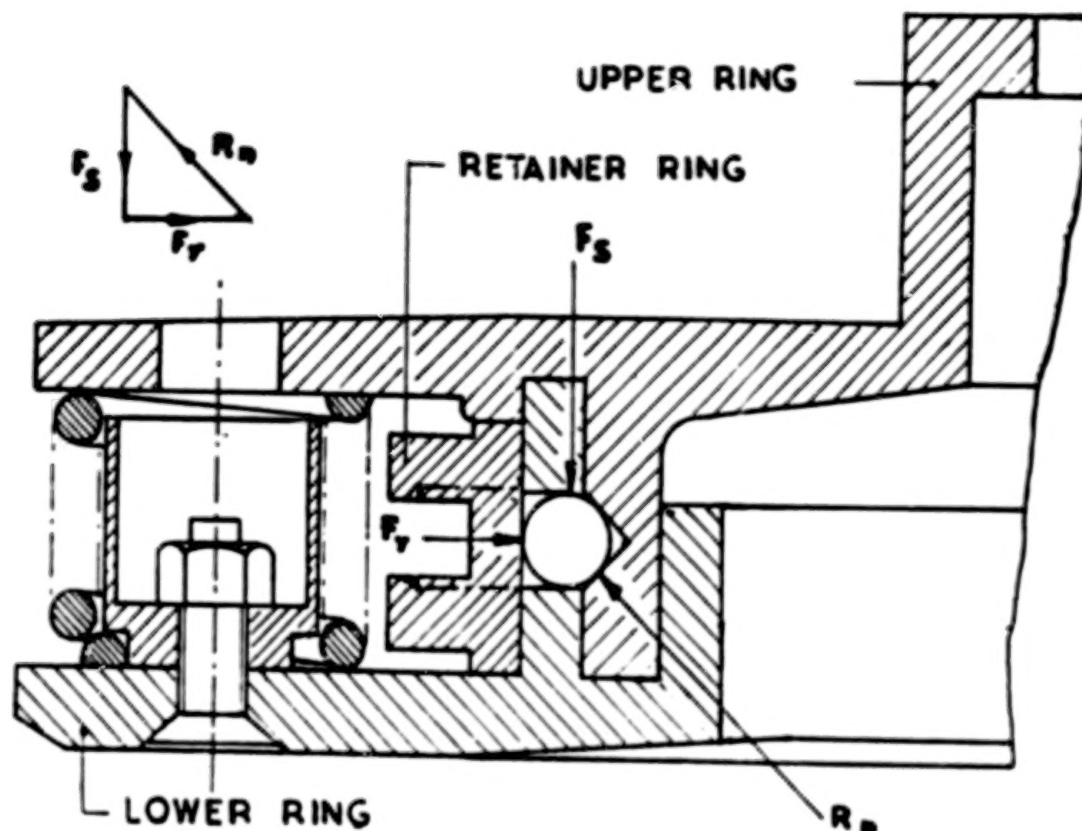


Figure 10. Equilibrium of Forces

The springs for jettison were fully guided during expansion and were screened for a tolerance of +3 percent on stiffness. The dimensional screening ensured identical springs for controlling the net compression. Based on energy and momentum balance, the differential velocity requirement was calculated from the spring energy

$$M_s V_s + M_e V_e = 0$$

$$\frac{1}{2} M_s V_s^2 + \frac{1}{2} M_e V_e^2 = \frac{1}{2} K \delta^2$$

M_s, V_s = Mass and velocity of the upper stage

M_e, V_e = Mass and velocity of the lower stage

K = Total spring constant

δ = Net compression

SYSTEM PERFORMANCE

The ball lock system functioned successfully in separation and jettison of the connecting stages. A differential velocity of 1.2 mps (3.9 ft/sec) was imparted within a time of 15 ms. The measured shock was 3 g and the disturbance rate was 0.14 deg/sec in the roll direction. The system was tested to demonstrate a reliability of 0.995 at an 85 percent confidence level. The system was fully contained and the balls, springs, and retainer ring all remained with the lower stage as designed. No flying loose parts were observed.

The principal diameter of the ball lock system at the separation plane was 696 mm (27.4 in). The system assembly was structurally tested for its joint characteristics. The test loads were:

- Bending moment--11,768 N-m (8,675 ft lb)
- Axial load--56,879 N (12,786 lb)
- Shear force--6,031 N (1,355 lb)

The deflection was 0.07 mm (0.0029 in) and the joint (flexibility constant) was 4.4×10^{-8} rad/N-m (5.02×10^{-9} rad/in-lb). The performance of the joint was within acceptance limits.

The pyro thruster, a piston-cylinder type, had a pressure cartridge of dual-type squibs with electrical characteristics the same as that of the pyro valve of the gas bottle previously mentioned. The cartridge was individually proven for its reliability requirements. Figure 11 shows the assembly of the ball lock system and the pyro thruster.

DEVELOPMENT PROBLEMS

Development problems included: controlling the spring characteristics, dealing with contact stress during dynamic loading, and fabrication of the ball seating, especially controlling the depth.

Matching and symmetrical distribution of springs necessitated selection from a large supply and resulted in higher cost of the system. The contact stress was higher than predicted, and when the same assembly was vibrated and structurally tested, the stiffness of the joint was found to have changed. This problem was solved by providing a hard-chromium coating with a thickness of 20 to 30 microns. The joint stiffness was increased to 4.44×10^{-8} rad/N-m (moderate category). In order to achieve this, a precision fixture was needed. The fixture provided a reference surface and drilling was used to achieve the controlled depth.

QUALIFICATION TESTS

The tests were divided into functional, structural, and environmental tests. The environmental conditions simulated were vibration, shock, and thermal soak.

ORIGINAL PAGE 13
OF POOR QUALITY

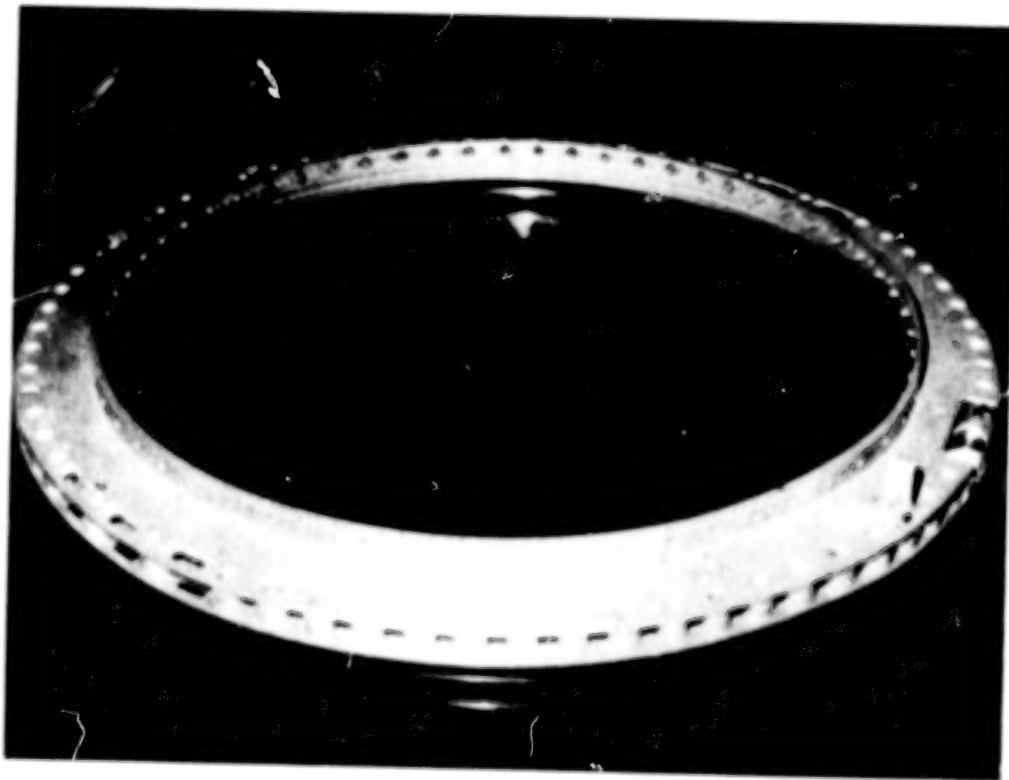


Figure 11. Ball Lock Staging System and Pyro Thruster

ORIGINAL PAGE IS
OF POOR QUALITY

Functional tests were performed both in grounded and free-fall conditions to evaluate the disturbance levels. The functional tests in zero gravity were performed with a simulated mass-inertia model to verify differential velocity and disturbance characteristics. Limitations in the disturbance measurement were caused by the atmosphere and its damping effect on the measured rates. The results showed that the pitch and yaw rates were insignificant, whereas the roll rate had a value of 0.14 deg/sec. In the structural test, the system performed normally, as predicted. The joint stiffness was, according to specification, of moderate class. The vibration and shock tests were stipulated to qualify the system in the functional mode after these environmental loadings. The thermal-soak test was carried out at 70°C with a one-half hour soak to qualify for the expected temperature inside the heat shield during flight. The system function was tested and found normal. A qualification test summary is shown in Table 4.

CONCLUDING REMARKS

The staging and the heat shield systems meet all the mission requirements. These systems have successfully performed their function in all four SLV-3 flight tests. Both systems have excellent performance characteristics of low shock, low-disturbance rates, and complete freedom from contamination. No free-flying debris occurs in these systems. In this respect, these systems fare one order higher compared to a merman band system and so are attractive for launch vehicle applications of a similar class.

Table 4
Qualification Test Summary

Sl.No.	Type	No. of test	Performance	Remarks
1	Functional - 1 g condition	15	Normal	Clean separation.
	- 0 g condition	3	do	Measured disturbance rate in roll 0.14 degree/sec (No significant pitch and yaw rates)
2	Structural	2	As predicted	Joint falls in moderate category
3	Vibration*	1	do	Functioned normal after vibration.
4	Shock*	1	do	do
5	Thermal soak at 70°C	1	Normal	Functioned normal after soak
6	Flight test	4	do	Disturbance rate less than 0.1 degree/sec

*Levels are as per Table 2

REFERENCE

Gluckman, I. B., "Aerospace Vehicle Separation Mechanisms-Selection, Design and Use Considerations," Lockheed Missiles & Space Company, Inc., Fifth Aerospace Mechanisms Symposium, Sunnyvale, California, 1970.

N84
25096

UNCLAS

N84 25096

SMART MOTOR TECHNOLOGY

D. Packard*

D. Schmitt**

ABSTRACT

Current spacecraft design relies upon microprocessor control; however, motors usually require extensive additional electronic circuitry to interface with these microprocessor controls. This paper describes an improved control technique that allows a "smart" brushless motor to connect directly to a microprocessor control system. An actuator with "smart motors" receives a spacecraft command directly and responds in a "closed loop" control mode. In fact, two or more smart motors can be controlled for synchronous operation.

SMART MOTOR TECHNOLOGY

Today's electric motors require substantial additional equipment to achieve "controlled" performance. These additional items may include a power electronics box, a servo electronics box, encoders, tachometers, or potentiometers. The use of these "extras" causes system complexity and cost to increase.

Stepper motors and controls have been introduced as a means of reducing complexity. The simpler stepper systems, however, introduce other undesirable characteristics such as slower speed, higher power dissipation, and output load sensitivity when compared to dc motors and controls.

Recent developments within the motor industry now make it possible to combine advanced brushless-motor technology, microprocessor control, and microprocessor programmability to create a "smart motor." The smart motor possesses internal electronic controls that allow direct interface between the motor and the spacecraft command system. This eliminates the need for expensive, heavy electronic control boxes and external electromechanical devices.

One set of smart motor performance characteristics will now be described. The control techniques to be presented are an outgrowth of the "dual drive actuator" development effort that was presented at the 16th Aerospace Mechanisms Symposium in 1982. The dual drive actuator uses an advanced brushless-motor configuration that will be discussed in detail and then used in describing smart motor characteristics.

The dual drive motor (Figure 1) is produced for the Jet Propulsion Laboratory by Aeroflex Labs of Plainview, New York. The unit contains internal electronic circuitry that provides a rudimentary degree of operating intelligence. This circuitry performs all commutation functions, thereby

*Jet Propulsion Laboratory, California Institute of Technology, Pasadena, California

**Lockheed Missiles and Space Company, Sunnyvale, California

ORIGINAL PAGE 19
OF POOR QUALITY

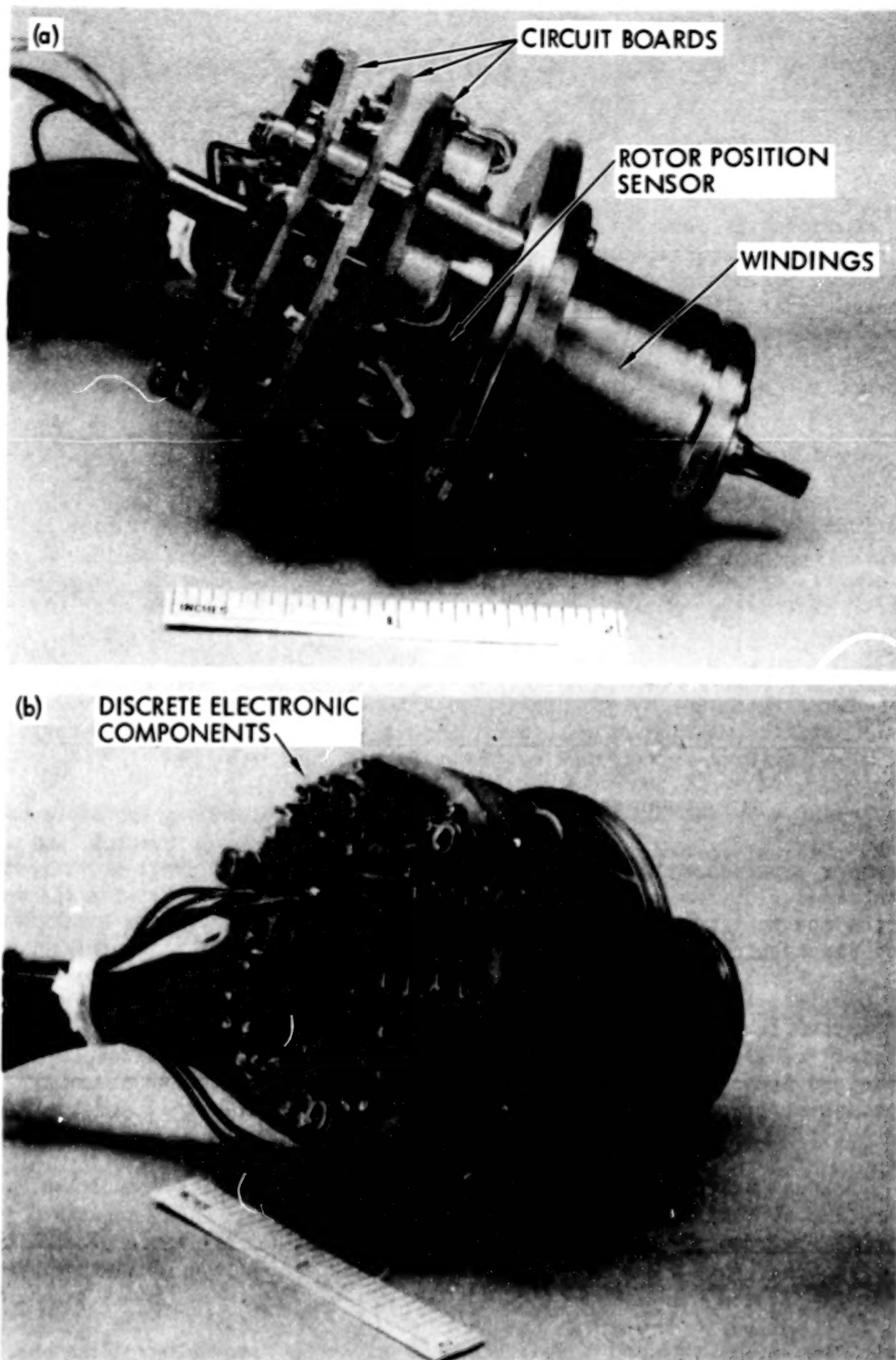


Figure 1. Dual drive motor: (a) side view, (b) rear view (rear cover removed)

providing a "two-wire" electrical interface requiring only reversible dc power for operation.

Figures 2 and 3 show mechanical and electrical design details. The rotor position sensor (Figure 2b) is a noncontacting mechanical assembly that performs the same function as the brush set and commutator in a typical dc motor

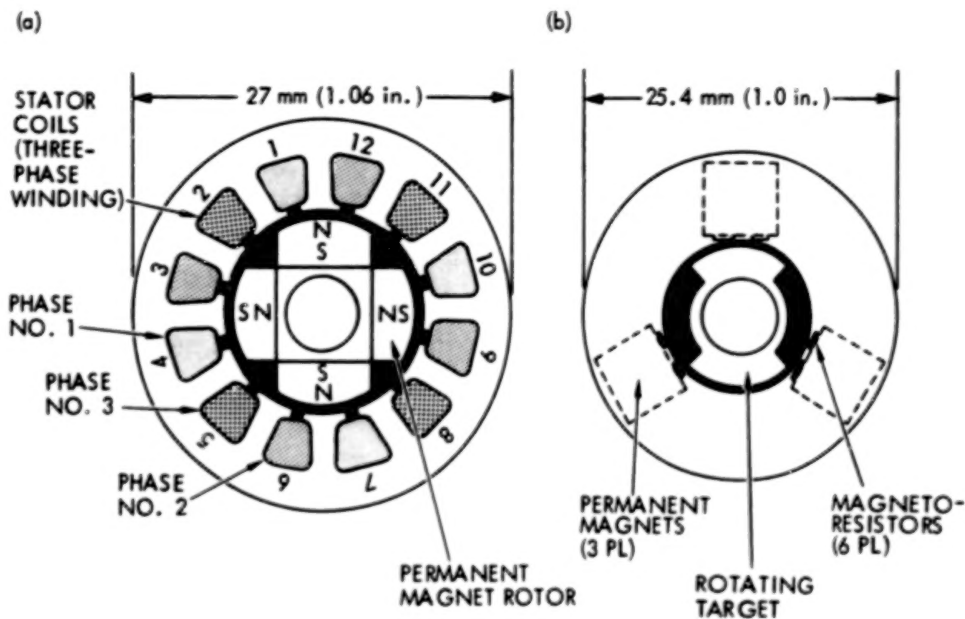


Figure 2. Motor mechanical construction: (a) rotor/stator design, (b) rotor position sensor

Magnetoresistors are the active sensor elements. These are semiconductor resistors that provide an increase in resistance when they are exposed to increased magnetic flux. Thus the proximity of the rotor target to each magnetoresistor governs its relative resistance. The magnetoresistors are connected to form the legs of a bridge network, as the target rotates, a signal is generated from the rotor position sensor for subsequent signal processing. The three magnets create a three-phase signal generated from three independent bridge circuits, thereby producing three-phase control.

A portion of the position sensor circuitry is contained within the mechanical assembly, and the remainder of the circuit is located with the drive control electronics on three printed circuit boards attached to the rear of the motor. The drive control circuit consists of four major electronic subsystems:

- (1) A diode bridge controls the polarity of the reference voltage being applied to the sensor circuit. This voltage polarity reverses when the input power polarity is reversed. The reversal causes a phase change of the switching signals to the amplifiers; however, the diode bridge simultaneously applies a fixed polarity voltage to the amplifiers regardless of the input power polarity (current always flows through the motor in one direction).

ORIGINAL PAGE 19
OF POOR QUALITY

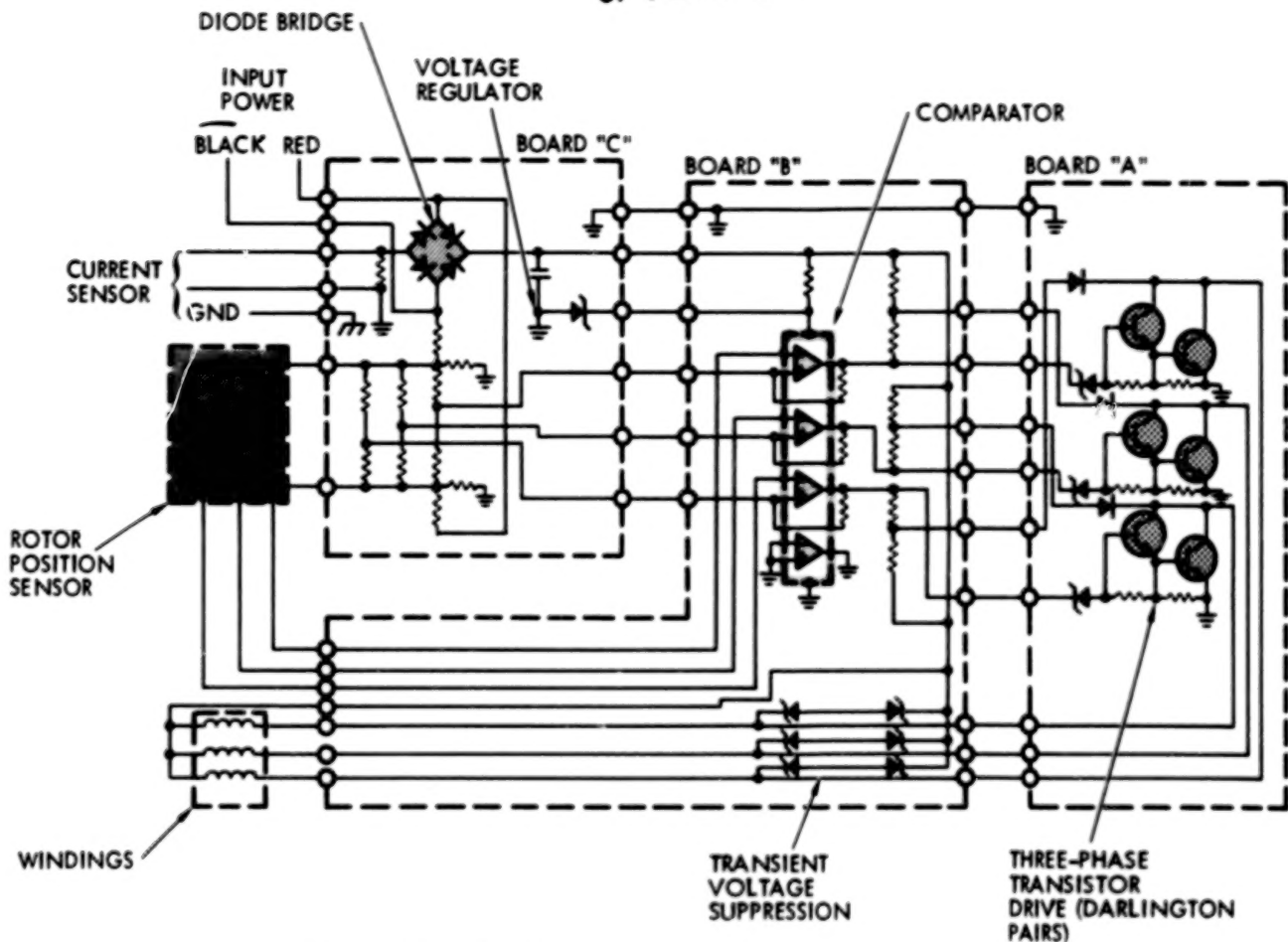


Figure 3. Dual drive motor circuit diagram

- (2) A diode voltage regulation circuit provides a regulated, 15-V power supply to the comparator.
- (3) The comparator receives low-level (50 mV) switching signals from the rotor position sensor and amplifies these signals into higher level switching signals capable of controlling the three-phase transistor drive circuit.
- (4) The transistor drive circuits provide the three-phase (30-V) drive pulses to the windings located in the main motor stator. These drive circuits also contain diode cross-strapping, which precludes simultaneous operation of more than one winding.

The motor that has been described is a direct, highly reliable replacement for aerospace-quality, dc brush-type, permanent magnet motors. The dual drive motor has only rudimentary intelligence, making internal commutation possible. But even with this limited capability, the dual drive motor avoids the shortcomings of brush-type motors (vacuum brush wear and poor heat transfer) while providing their advantages such as a simplified electrical interface, high starting torque, and low-power/high-speed operation.

The key element in the more advanced versions of smart motor technology is based on the fact that commutation means both knowing how to switch and when to switch. Smart motors achieve this electronically through the use of a rotor position signal that is processed within the motor, starting as a low-level, 50-mV signal and ending as a 30-V, high-current drive pulse. The rotor position sensor is a coarse, but accurate incremental encoder and it is possible to "tap into" the motor circuitry through appropriate additional electrical interfaces so that the commutation signal can be processed for use just as the signal from any auxiliary servo component can be processed for closed loop control. The internal motor circuitry can also be tapped at a point that allows direct control by low-level logic signals, typical of the output from a spacecraft command system. This direct control means the total elimination of the drive electronics box usually required on today's systems.

SMART MOTOR FEATURES

Incremental Positioning (Stepping)

The two primary motor types used for spacecraft applications are high-speed dc motors and low-speed stepper motors. Each motor type has certain optimum applications. For example, the stepper motor drive usually provides superior performance when slow-speed operation is desired over a long period of time (e.g., solar array sun-pointing drives). Likewise, the high-speed dc motor (with appropriate gear reduction) provides superior performance when high torque and high speed are required (e.g., acceleration of very large inertias during deployment). Therefore, it would be very useful to have a motor that can be operated as an incremental (stepper) motor or as an analog (high-speed) motor.

The dual drive motor circuit can be used to demonstrate how easily this can be accomplished. "AND" gate circuits may be inserted into the motor circuit between the comparator and the drive transistor pairs (Figure 4). Each "GATE" has multiple inputs and all of these inputs must be simultaneously positive for the comparator drive signal to reach the transistors. This makes commutation control possible from a low-level, external logic command applied to the second input of each gate. The pulse repetition rate of this external command can be adjusted to produce stepping motion at any desired speed within the limits of the motor electrical time constant (L/R).

Motor shaft rotation will begin when both gate inputs become positive and will continue until the comparator switches to the next coil or until the external logic signal is terminated. The advantage of this scheme is twofold: (1) failure to complete a step will not cause a torque dropout because as the sequential external pulses continue, full motor torque will again be developed, and (2) a long external pulse can be used without the danger of excessive power dissipation within the motor because the comparator input to the gate will drop to zero as soon as 60° of shaft rotation occurs, thereby terminating the drive signal to that transistor pair, regardless of the status of the external command.

This technique allows a smart motor to be driven at a selectable pulse rate either by a series of manual commands from a mission specialist or by a

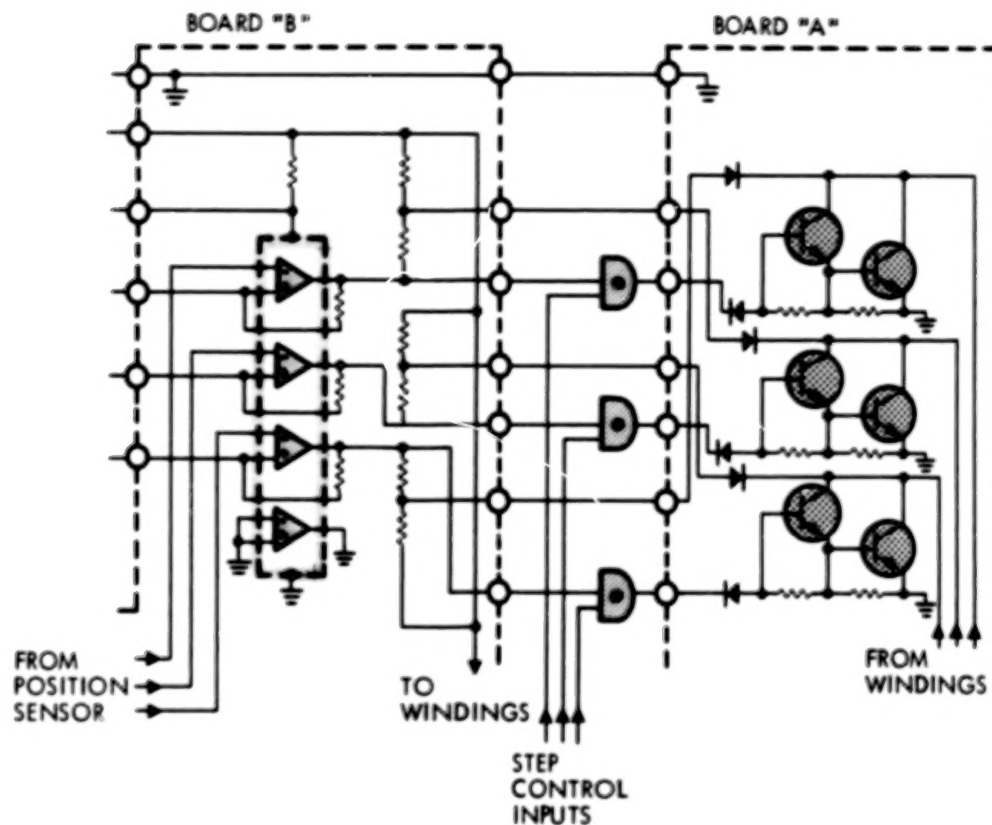


Figure 4. Incremental position control diagram

sequenced command directly from a spacecraft command system. Also, there is never a danger of torque dropout when high-speed rotation is desired because the incremental command can also be supplied as a simultaneous enable signal to all three gates. This action will cause the steppable motor to operate as a normal dc motor. The smart motor can step or run as directed by the spacecraft command system or mission specialist.

Torque Profile Control

Proper operation of stepper motors requires careful attention to the magnitude of friction and inertia in their driven loads. Because energy is added to the driven load to cause motion and must then be removed to stop the motion, stepper motor controllers usually apply a fixed-duration, ramped drive pulse that is preselected to provide the desired performance for a specific load. The pulse duration introduces motion and is applied continuously until motion ceases.

Smart motor designs can accommodate an additional capability to vary the magnitude of each drive torque pulse. This pulse width modulation technique is achieved by using a three-input, three-gate "AND" circuit as shown in Figure 5. Two of the inputs are operated as previously described for incremental motion, and the third input to each gate receives a continuous string of pulses at a frequency to provide a pulse duration greater than the motor electrical time constant, but also significantly higher than the

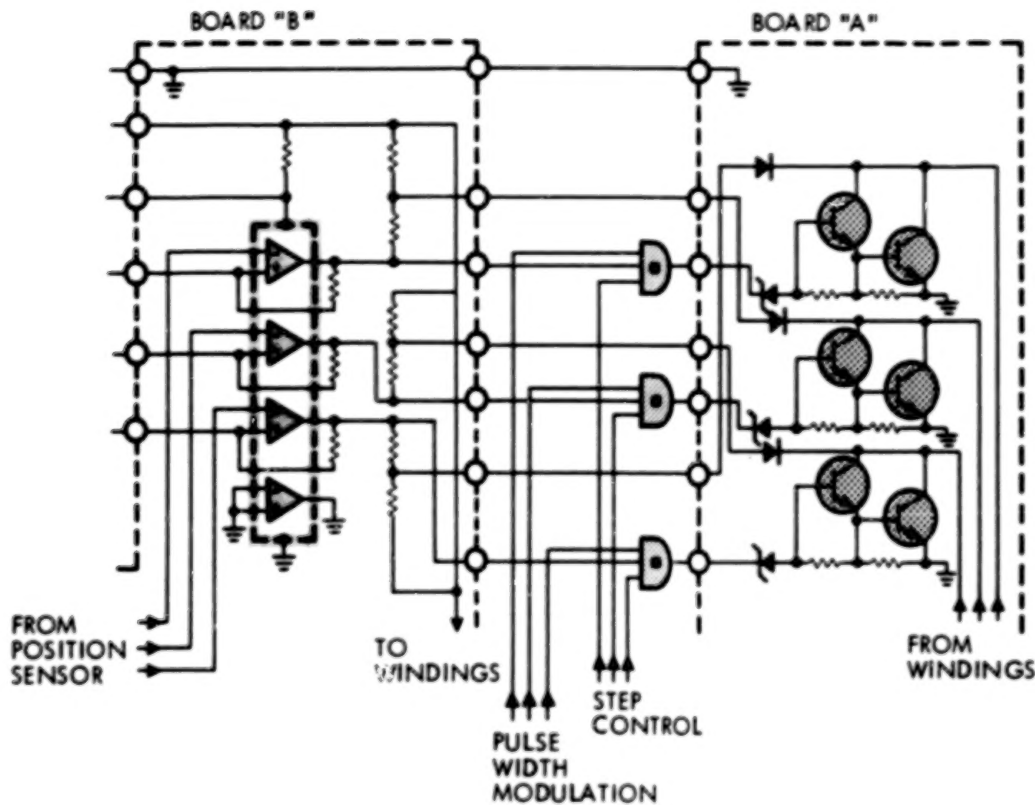


Figure 5. Torque profile control diagram

frequency of the incremental motion command being applied at the second input to each gate. The pulse width duty cycle of the third input determines the total "ON" time for each transistor pair and thereby controls the total amount of energy applied to the load during each step. The torque developed by a motor is directly proportional to current. Therefore, it is possible to use a series resistor within the motor circuit, similar to the dual drive current-sensing resistor, to provide a current feedback signal to the control system. This will provide a direct measure of the torque being generated by the motor. The independently controllable pulse width modulation with current feedback will allow the motor torque profile to be tailored to any desired function within the limits of the motor.

Multiunit Synchronization

Synchronization of the motion of two or more smart motors is also possible and is achieved by simultaneously applying the same step command to each respective smart motor gate (Figure 6). The commutation signals from all motors are then monitored with an external "OR" gate circuit. The output of the "OR" circuit controls the initiation of the next sequential step command, which cannot occur until the monitored commutation signals indicate completion of the previous step for all independent units.

Power will continue to be applied to any motor that has not completed the commanded step. As each individual unit completes the step; however, its

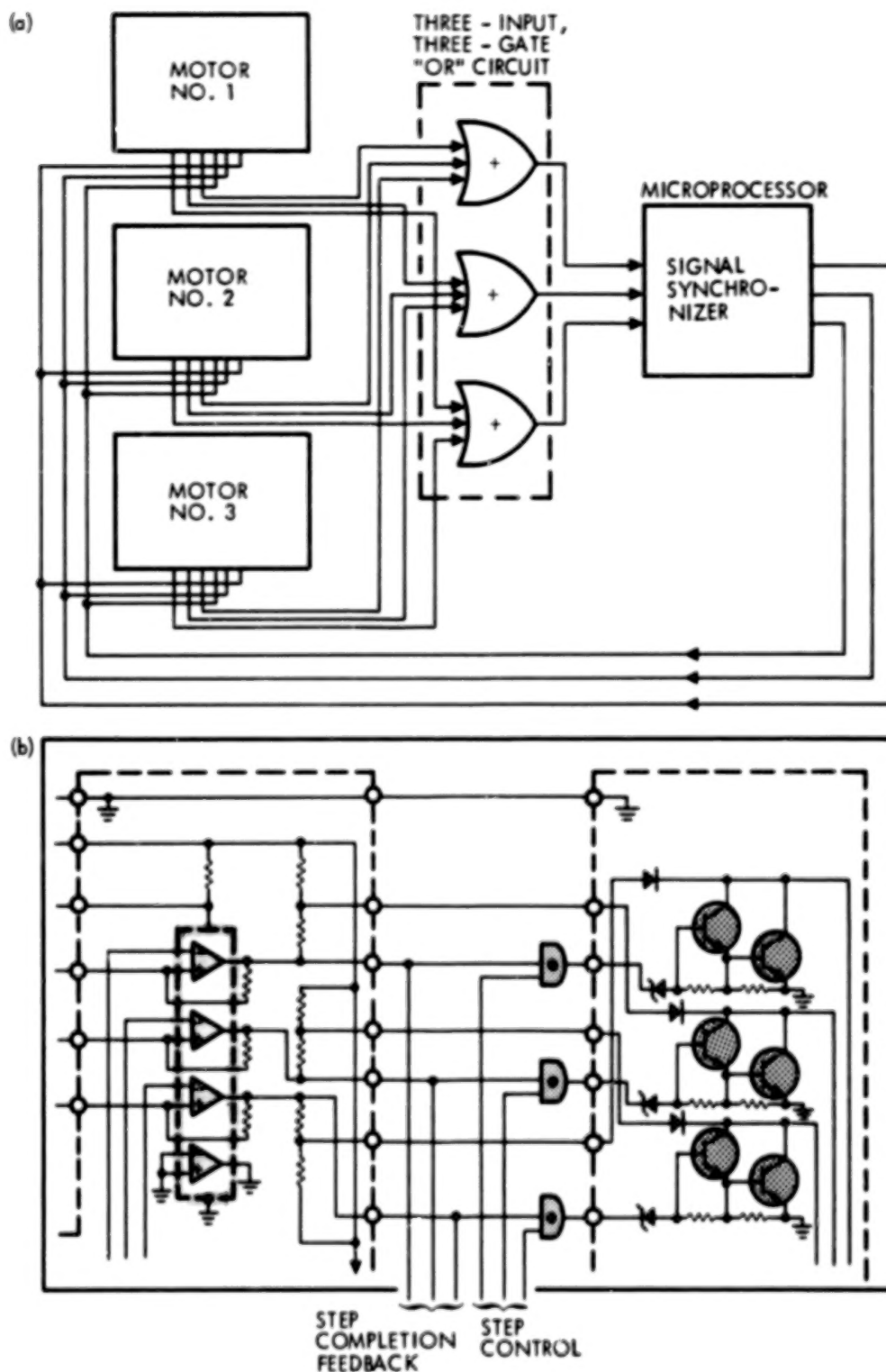


Figure 6. Multiunit synchronization: (a) three-motor diagram, (b) motor internal circuit diagram

position sensor will automatically shut power off and it will wait for the other units to catch up. This permits the use of independent motors with different output loadings yet provides synchronous motion with never more than a single step difference.

Analog Rate Control

Incremental motion control (stepping) of the smart motor, as described above, represents one of the methods of rate control. There are other control techniques that will allow the smart motor to operate as an analog (high-speed) motor with velocity control. Figure 7 shows a control method that

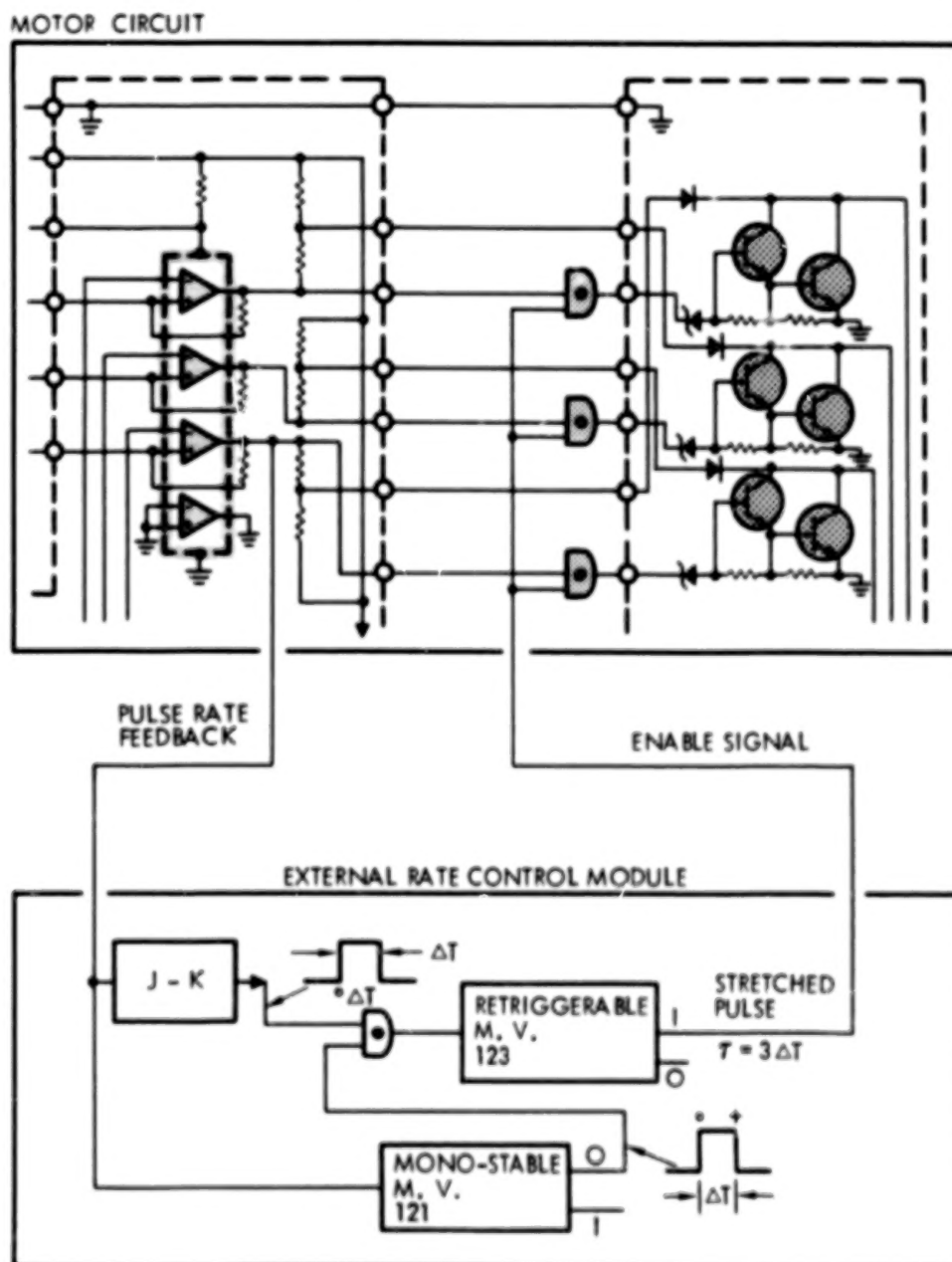


Figure 7. Analog rate control diagram

will control rate with a broad tolerance of approximately 10 percent. This control technique uses the "AND" gate discussed previously and the output signal from one phase of the motor circuit. The motor control provided by this technique will result in a sawtoothed velocity profile. The motor will turn "ON" when a minimum speed threshold is reached and turn "OFF" when a maximum speed threshold is exceeded.

A more precise rate control can be achieved through the use of pulse-width modulation of the driver signal similar to the torque control technique previously discussed. This technique will provide only the power necessary to maintain the desired velocity. With a variable load, the pulse-width modulation will be directly proportional to the load, thereby providing more power with longer driver pulses as the motor speed tends to decrease because of the added load. This high-efficiency method for rate control would be very desirable for large power units.

With pulse-width modulation, the power transistors are still used in the switching mode and are highly efficient. The power applied is directly proportional to the pulse duration. With heavy loads, the pulse width will increase to provide the necessary torque to generate power. Conversely, with light loads, the pulse width will decrease to provide only the power necessary to maintain the velocity.

The use of a pulse-width modulation for power control is suitable for high-accuracy control systems that integrate the error signal with time. Thus, a small error signal integrated over a long period of time will provide a large error signal for rate control.

This technique is easily adapted to high-power systems that need high-efficiency electronics to drive large motors. This design approach can be applied to the motor for large output power levels, yet keep the electronics small in size because of the high efficiency.

Position Control

A simple method (Figure 8) for smart motor position control is to count the output signal from the comparator. This signal, consisting of six pulses from the position sensor for each motor revolution, can be used to determine exactly how many revolutions the motor rotates to a given position.

The granularity of this position control technique is very good. Use of this smart motor in a dual drive having a gear ratio of 880:1 will provide $880 \times 6 = 5280$ position increments per dual drive output revolution. This amounts to more than 2^{12} bits of information per output revolution. Reasonably precise position control can be achieved when output gearing backlash/index errors are minimized and output stiffness is maximized.

For position control, a binary address can be provided corresponding to the desired position to be achieved. If the binary code address is different from the binary code generated from the serial data, the drive pulses will be provided. When the generated binary code equals the binary code address, the drive pulses to the motor will stop and the motor will be at the desired position.

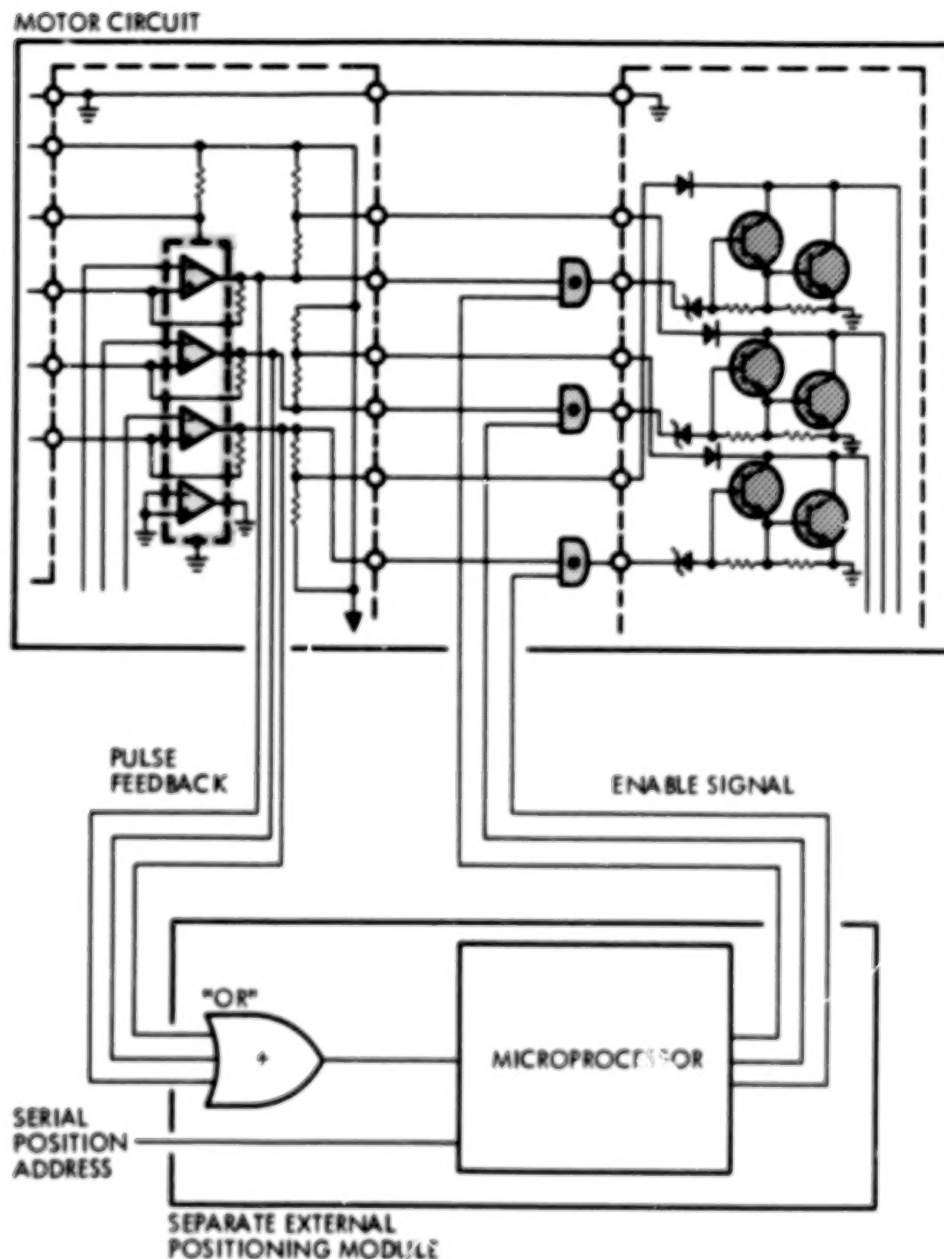


Figure 8. Position control diagram

If the generated binary code is lower than the address code, a drive signal with a given sequence will be provided to the motor and will increase the generated binary code. Conversely, if the desired address is less than the generated binary code, the motor will be driven to decrease the generated binary code to the desired address. The error signal caused by the two binary codes will provide the sequence drive pulse to the motor from the microprocessor, which will consist of three pulses in proper phase sequence. This control technique is an incremental method of establishing position, and the interruption of power will result in loss of data reference. The motor detent torque and gearing static friction, however, will hold the last commanded position until power is restored. (The dual drive gearing can be selected to

ORIGINAL PAGE IS
OF POOR QUALITY

provide no backdriving up to the structural load limit of the gears.) Thus, the last position command can be reentered as the new data reference. If an interruption cannot be tolerated, a small, independent battery power supply can be used to power the position storage register.

Size and Weight

The new smart motor capabilities are achieved by adding components and electrical interfaces to the motor. It is important that these additions do not cause excessive growth of the overall motor size. Figure 9 shows a photograph of the comparative sizes of an actual three-input, three-gate "AND" circuit and a pulse width-modulating circuit. These devices are very small and can be easily accommodated within the motor envelope. Both of these items are commercially available, space-qualified components.

It is also possible to greatly reduce the size of the entire motor circuit by using hybrid circuit technology. Figure 10 shows the potential reduction of motor size provided by hybridization. This hybrid configuration uses "platform" package technology and reduces the electronic packaging volume by a factor of 2.5.

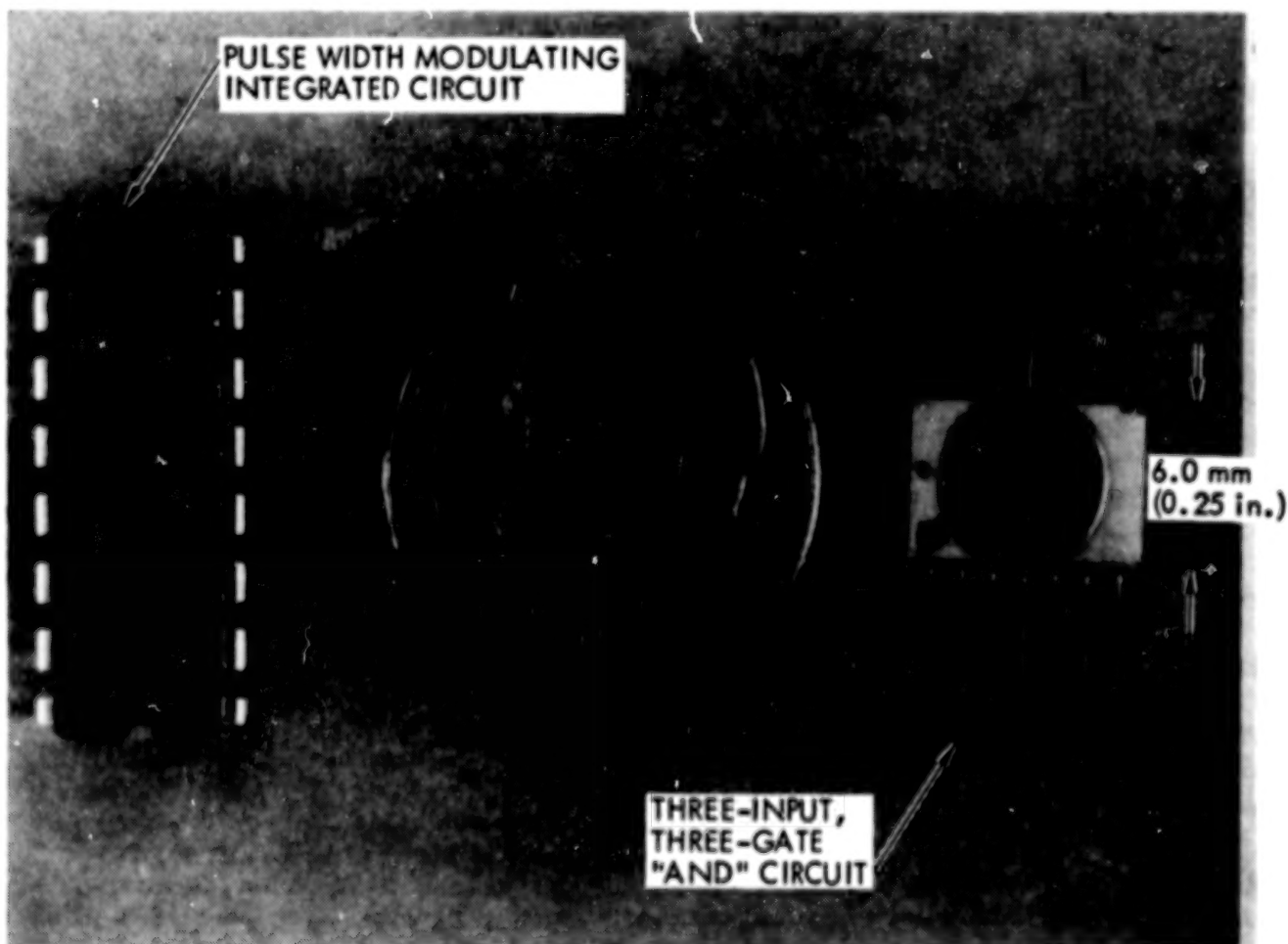


Figure 9. Component configurations

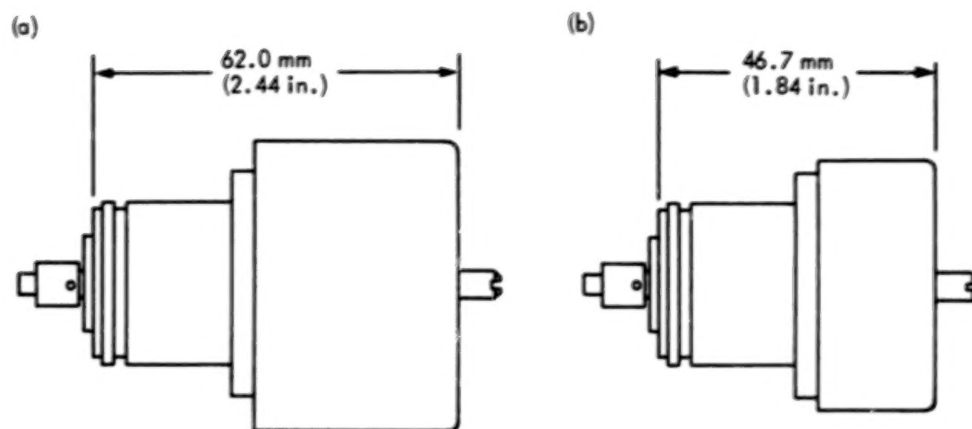


Figure 10. Size comparison: (a) dual drive motor with discrete electronic components, (b) smart motor with hybrid electronics

Expansion of the smart motor technology into higher-power/long-life applications will require consideration of a number of potential improvements. The principal limitations include direction reversing, power dissipation in the circuit components, and stability of the circuitry under "worst-case" environmental conditions.

Direction Reversals

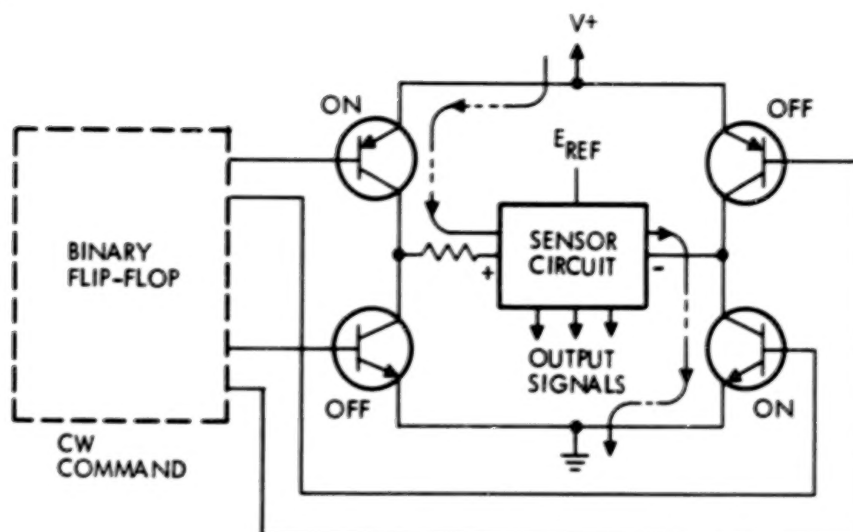
Some applications may require that the motor rotational direction be reversed thousands of times during the normal lifetime of a spacecraft system. The use of mechanical relays is usually considered to be impractical when this amount of switching is needed. An alternate and more reliable switching scheme is possible by modifying the motor current control circuit. The motor's direction of rotation can be reversed using an electronic circuit to reverse the voltage on the position sensor circuit (Figure 11). This will provide direction control and proper phase sequence of the sensor signals. This control technique also has the advantage that the transistors are all operated as switches, either full "ON" or full "OFF," thus making them efficient. It is also important that the "ON-OFF" relationship of the transistor pairs be maintained. This will be ensured if a single component (binary flip-flop) is used to provide both the positive and negative signals simultaneously.

Power Dissipation

The present dual drive motor has a very low operating power level (3 W at no load speed, 13 W at stall) and it was not necessary to optimize the power dissipation of that unit. For larger motors, however, the power dissipation characteristics of the circuit can be significantly improved.

The present motor design uses a switching power transistor configuration called a Darlington Pair (Figure 12). Under worst-case conditions, a voltage drop of 1.7 Vdc can occur across that portion of the motor circuit. This

(a)



(b)

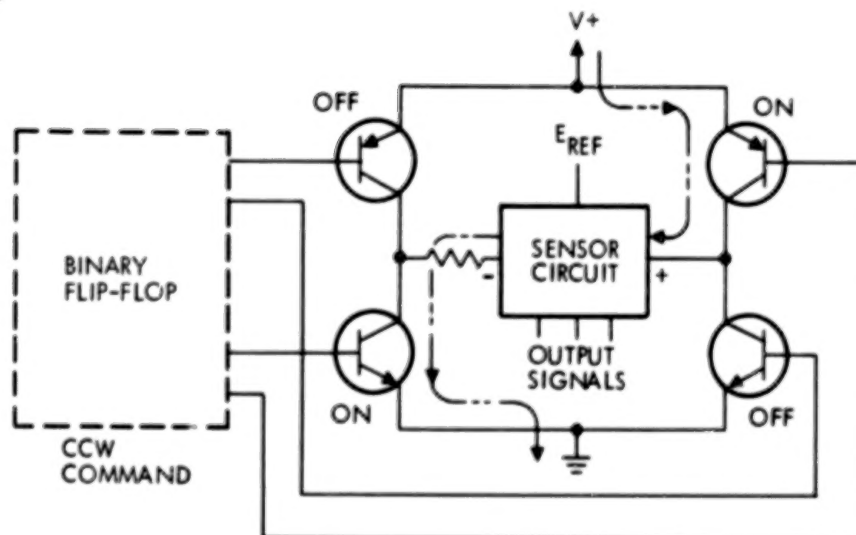


Figure 11. Direction control without mechanical relays: (a) CW command diagram, (b) CCW command diagram

results in increased power dissipation within the transistors and a reduction in output efficiency.

Figure 12 shows an alternate method for power switching. This configuration called a complementary driving circuit, will allow the power transistors to saturate fully. Use of this circuit will result in a greatly improved switching efficiency with a worst-case voltage drop of only 0.2 Vdc, and in a complementary circuit power stress level of approximately 1/8 (12 percent) of the level expected in the Darlington configuration. This significant improvement becomes very important when the higher-power configurations are considered. With the complementary configuration, the transistor environmental temperature can increase significantly without high temperature over-stress.

ORIGINAL PAGE IS
OF POOR QUALITY

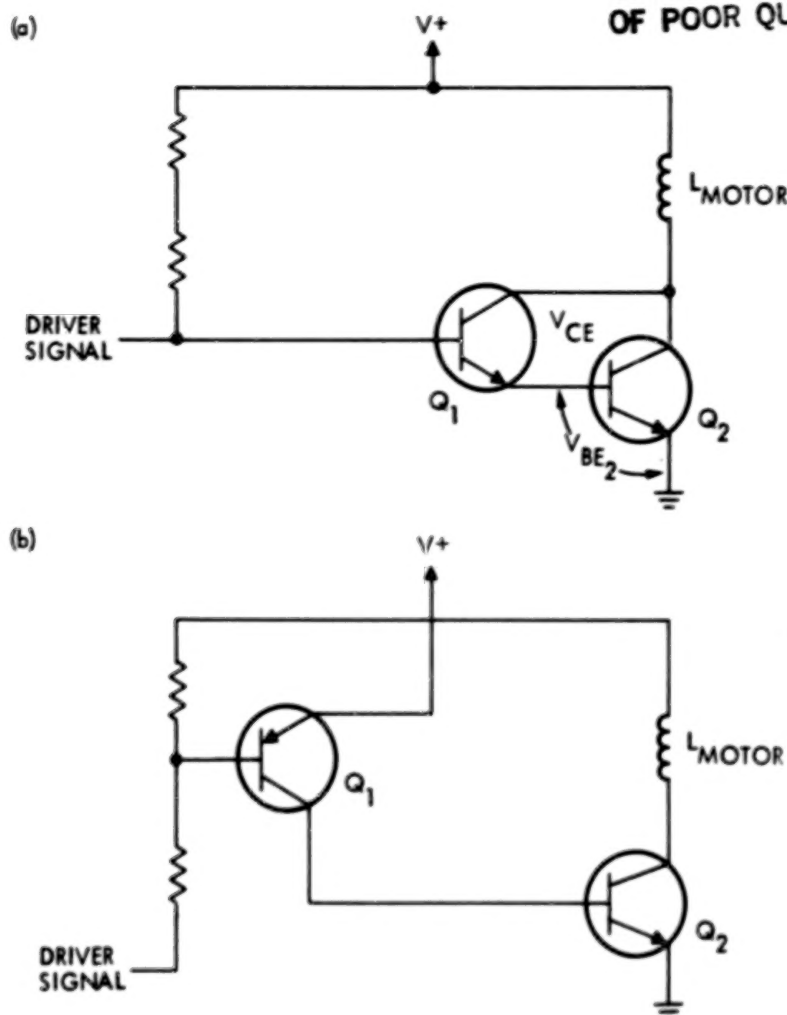


Figure 12. Comparative motor driver circuits: (a) Darlington circuit diagram, (b) complementary circuit diagram

Alternately, the amount of current can be increased by a factor of eight with the same transistor and heat sink configuration. This would permit the use of the same size of transistor to drive a motor about eight times larger than the present configuration. It reduces the requirement for special heat sinks for the power transistor to prevent over-stress conditions. The lower voltage loss in the power transistor also results in a power gain in the motor. This becomes very important when operation is at the minimum voltage condition. There will be as much as 6 percent more power available to the motor simply from the circuit configuration when the voltage is 24 Vdc. This added gain, coupled with the higher power-handling capability, makes the complementary circuit very attractive for higher-power applications.

Circuit Stability

At present, the maximum and minimum operating temperature limits (-51° to $+71^{\circ}$ C) of the dual drive motor are constrained by the voltage stability of the position sensor circuit. A major improvement of the stability can be

provided through the use of a constant current control (Figure 13). This technique provides a constant reference voltage to the sensor circuit regardless of input power variations and achieves control of the sensor circuit current.

The constant reference voltage can be tailored to have a zero temperature coefficient, which will give a more uniform signal output control. In fact, the circuit can be designed to compensate for the negative temperature coefficient of the sensor elements, thereby eliminating the temperature effects on the output signals, and significantly increasing the operating temperature limits of the motor.

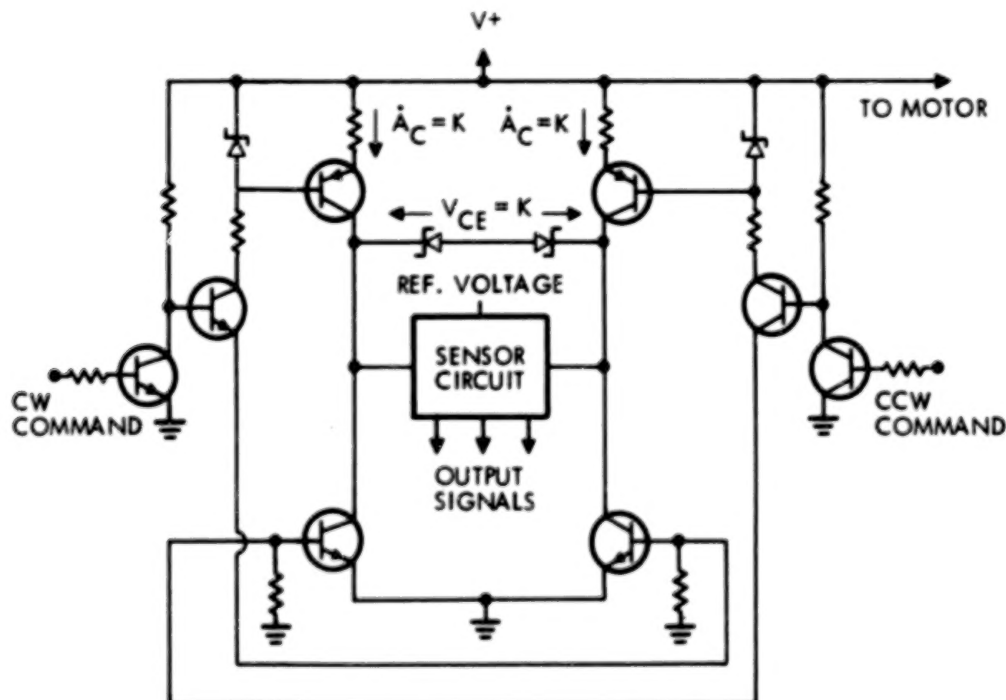


Figure 13. Constant current diagram. Constant current applied to bridge permits uniform E_{REF} independent of source voltage. E_{SIGNAL} is more uniform and independent of source voltage or temperature. $V_{CE(SAT)}$ of switch transistors is very small and almost constant. CW and CCW command change phase of sensor circuit same as in Figure 11.

SMART MOTOR BENEFITS

The benefits of this new technology can be graphically demonstrated by comparing the future "smart drive system" with earlier systems. The NASA/JPL Seasat spacecraft, launched in 1978, contained a drive system that had been developed in the mid-1970s. The Seasat solar array drive system consisted of two rotary drives weighing a total of 10 kg (22 lb) and an electronic control box weighing 5 kg (11 lb). Figure 14 shows a schematic diagram of one of the two electronic circuits contained within the control box. The shaded

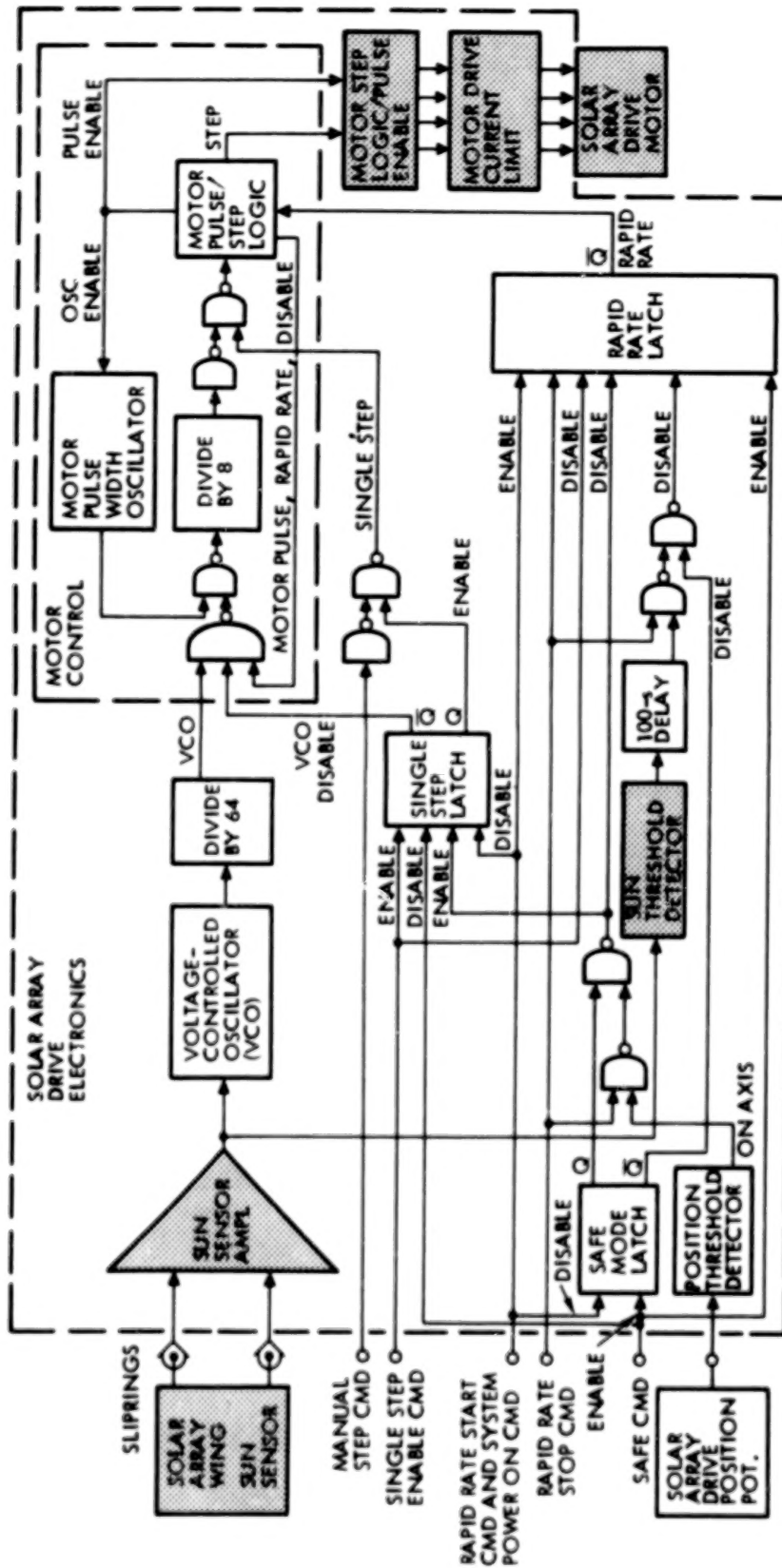


Figure 14. Solar array drive electronics block diagram

portion of the circuit is equivalent to the entire smart motor circuit required to perform the same job. Studies are being conducted of dual drive/smart motor combinations for similar drive systems. It is estimated that the "smart system" will weigh only 2.7 kg (6 lb) total, that the electronic control box can be totally eliminated, and that the total system cost will decrease by a factor of approximately 50 percent.

The versatility of a smart motor has now been presented. The incorporation of a few additional electronic interfaces into the motor greatly increases the capabilities of that unit. These approaches use simple, conventional electronic designs. The innovation is in the synergistic combination of separate technologies.

The current development work at JPL is aimed at facilitating the development of smart motors that will be the maximum number of usable interfaces and capabilities consistent with performance and packaging constraints. JPL is working with the aerospace motor industry to develop and qualify unit configurations that will be usable for widely differing applications. This development is a lengthy task with a number of sequential steps required to perfect the motor design and to ensure that stringent aerospace electronic design standards are met. JPL's motor development program, however, allows sufficient lead time to maximize the usefulness of smart motors. We expect that within 3 to 4 years the motor industry will be a complete line of fully analyzed, fully qualified smart motors available for the complex mechanisms of the future.

ACKNOWLEDGMENT

The research described in this paper was performed by the Jet Propulsion Laboratory, California Institute of Technology, under contract with the National Aeronautics and Space Administration.

**END
DATE
FILMED**

JUL 30 1984